Università degli Studi di Palermo

AREA QUALITÀ, PROGRAMMAZIONE E SUPPORTO STRATEGICO
SETTORE STRATEGIA PER LA RICERCA
U. O. DOTTORATI

PhD Course in Energy and Information Technologies
Department of Engineering
Academic Discipline ING-IND/11 – Building Physics and Building Energy Systems

MODELLING, OPTIMIZATION, AND 3E-ANALYSIS OF DISH-STIRLING CONCENTRATING SOLAR POWER SYSTEMS

DISCUSSANT
ING. STEFANIA GUARINO

PhD COURSE COORDINATOR
PROF. MAURIZIO CELLURA

TUTOR
PROF. ANTONIO PIACENTINO

CO-TUTOR
PROF. VALERIO LO BRANO

CYCLE XXXIV
YEAR OF QUALIFICATION 2022

To *Saro* and *Rosa*

Acknowledgements

This thesis is the result of my research activities as a PhD student in *Energy and Information Technologies* at the Department of Engineering of Palermo University and mainly focused on the dish-Stirling system hosted by the same university. Therefore, first of all, I would sincerely like to express my gratitude to Eng. Christian Chiaruzzi and also the companies HorizonFirm s.r.l, Elettrocostruzioni s.r.l and Ripasso Energy for their cooperation, without which it would not have been possible to install the dish-Stirling solar concentrator on the University campus of Palermo.

I would like to thank my tutors, Prof. Valerio Lo Brano and Prof. Antonio Piacentino, for allowing me to undertake an interesting and stimulating research activity by integrating me into their experienced research group.

My special acknowledgments are for my mentor Prof. Valerio Lo Brano, who has daily enriched my wealth of knowledge by sharing his scientific expertise and his enthusiasm for research with me. I would like to thank, with deep gratitude and affection, Dr Alessandro Buscemi who supported me with full dedication and attention in all research giving me some of his valuable know-how.

I would like to thank my colleagues Dr Francesca Martorana, Researcher Dr Pietro Catrini and Researcher Dr Marina Bonomolo for their precious collaboration but also for their friendship that is dear to me.

In the end, my thanks go to Saro and Rosa, pillars of my family, who taught me the value of honesty and sacrifice and to whom I owe everything.

Thanks to all.

Contents

Introduction

The Earth's atmosphere is a gaseous layer whose composition varies, affecting the climate, since it includes: on the one hand molecular gases that absorb and reflect infrared radiation, as well as ozone that also interacts with ultraviolet radiation; and on the other hand, aerosols that interact with radiation in the visible light spectrum [1]. The interaction of atmospheric gases with radiation in the infrared spectrum ensures that the average annual surface temperature of the Earth is maintained at around 15.5 °C, avoiding temperatures below freezing. This temperature is the result of the energy balance that characterises the Earth's surface, which: receives radiation emitted by the Sun, emits radiation in the infrared spectrum and receives radiant energy re-emitted by the atmosphere again in the infrared spectrum, and in particular by those gases which are responsible for the global climate change, so-called greenhouse gases (GHGs). Indeed, the increase in a specific amount of GHGs in the atmospheric layer results in the energy imbalance at the Earth's surface, leading to a greater amount of energy being absorbed from the atmosphere in the infrared spectrum and thus to global warming.

Among the greenhouse gases occurring in the atmosphere, there are: carbon dioxide (CO_2), methane (CH_4), nitrous oxide (N_2O), and substances with a high ozone-depleting potential (ODP) also called Montreal gases which include chlorofluorocarbons (CFCs), halons, carbon tetrachloride (CTC), 1,1,1-trichloroethane (TCA), hydrochlorofluorocarbons (HCFCs), hydrobromofluorocarbons (HBFCs), bromochloromethane (BCM) and methyl bromide (MB). Finally, although in smaller quantities, the greenhouse gases also include the subproducts of hydrofluorocarbons (HFCs), perfluorocarbons (PFCs) and sulphur hexafluoride (SF_6). Carbon dioxide is the

gas that absorbs less radiant energy than methane and nitrous oxide, and like them, re-emits it with a time delay towards the Earth's surface. However, carbon dioxide is the gas with the highest absolute concentration and longest lifetime in the atmosphere, contributing the most to global warming.

Carbon dioxide has a short-term seasonal variability due to cyclic absorption and release processes involving the oceans and vegetation. More specifically, the factors that can influence the change in the amount of CO_2 in the atmosphere over time are related to both natural processes and anthropogenic activities. The variation in CO_2 concentration in the atmosphere can be determined as the net of positive and negative contributions. The former, which are the processes that lead to an increase of CO_2 in the atmosphere, include combustion of fossil fuels, deforestation and destruction of biomass and soil carbon, respiration by plants, respiration of soil and decomposers, and desorption by the oceans. Instead, the processes that lead to a reduction in the amount of CO_2 in the atmosphere can be attributed to photosynthesis reactions in terrestrial vegetation, adsorption and dissolution in the oceans, and consumption through burial as carbonate and organic matter within limestone and other sedimentary rocks.

Currently, anthropogenic activities engaged in energy production in different power plants through the combustion of fossil fuels are the ones driving the variation of carbon dioxide concentration in the atmosphere, leading to a continuous increase in the long term. Although the disruption of human activities during the Covid-19 pandemic period led to a substantial reduction in climate-changing gas emissions into the atmosphere [2], the global average CO_2 level resumed its rising trend and stood at around 412.4 parts per million at the end of 2021, which is 48.8% above the CO_2 level corresponding to the pre-industrial reference period.

The issue of climate change was the subject of discussion among leaders from all countries of the world at the Conference of the Parties (COP26) in Glasgow in 2021. To accelerate the achievement of the goals of the previous Paris Agreement [3,4], all countries have been invited to commit to securing a global net-zero by mid-century and keep the global average temperature increase significantly below 2 °C, compared to pre-industrial levels by 2050, and more specifically within the upper limit of 1.5 °C [5].

To this end, countries commit to achieving ambitious goals by 2030 focused on:

- promotion of energy production from renewable energy sources;

- phasing out coal power generation and transitioning to clean energy;
- preservation and conservation of forests and limitation of land degradation;
- decarbonising road transport and transition to zero-emission vehicles through rapid electrification of the transport sector;
- reduction of methane emissions produced mainly by the agriculture sector [6].

All countries focus their policies on a global energy transition that consists of increased use of renewable sources for electricity generation and direct use of renewable heat and biomass, direct use of clean electricity in transport and heat applications, improved energy efficiency, and increased use of green hydrogen and bioenergy with carbon capture and storage [7].

Currently, the renewable energy sources with the widest range of applications in the industrial sector are hydroelectric, geothermal, biomass, tidal, wind and solar. Solar energy is used to generate electricity using large-scale power plants or building installations, to produce domestic hot water, to supply space heating or cooling to meet the energy demands of both residential and tertiary users, and to desalinate seawater or brackish water. The most widely used solar technologies for electricity generation are Photovoltaic (PV) and Concentrating Solar Power (CSP) systems, both of which convert solar radiation into electricity but exploit different operating mechanisms and have different conversion efficiencies and investment costs [8].

Specifically, PV systems produce electricity by the photovoltaic effect in special devices, called photovoltaic cells, without any thermodynamic transformations or intermediate mechanical conversion processes. PV cells exploit the special electrochemical properties of semiconductor materials to create a photogenerated current as soon as solar radiation affects the material making up the cell [9]. Solar cells can be classified into three generations. To the first generation belong crystalline silicon-based solar cells (monocrystalline and multi-crystalline), which are the most commercially mature and show conversion efficiencies of up to 26%. The second generation includes thin-film solar cells using materials such as amorphous Si, CdTe, copper zinc tin sulphide (CZTS) and CIGSe. Finally, the third generation includes multi-junction cells, organic solar cells or dye-sensitised cells, whose innovative technology aims to reduce the cost-efficiency ratio [9]. PV systems are advantageous from an environmental point of view, as the generation of electricity is not accompanied by any emissions; from an economic

point of view, because of the low operating costs required; and from a technological point of view, because of the modularity of their size, their ease of use and their potential to be suitable for various applications, such as in space. Nevertheless, the production processes of PV devices, not only are expensive but also require the use of toxic chemical elements such as Cadmium, Selenium or Arsenic [9].

In CSP plants, the solar concentrator essentially consists of a collector, which, through a series of mirrors or lenses, concentrates the collected Direct Normal Irradiance (DNI) onto a receiver, thus obtaining high-temperature thermal energy, which is subsequently converted first into mechanical energy and, then, into electricity [10]. There are four types of solar concentrator systems currently available on the renewable power technologies market, namely: linear Fresnel reflectors, parabolic trough collectors, central solar towers and parabolic dishes (usually equipped with a Stirling engine or a Brayton-cycle micro-turbine) [11]. Of these, the first two types of CSP systems are known as linear-focusing technologies as the sunlight is concentrated from the collector along a receiver tube reaching typical temperatures of around 400 °C. The remaining two types of mentioned CSP systems are known as point-focusing technologies as the radiation is focused on a single point where the receiver is located reaching higher temperatures of around 800 °C and more. Generally, the CSP systems currently being developed are very promising because they are characterised by a low environmental impact, low land consumption and excellent energy performance [12]. However, they have a poor commercial penetration if compared to PV systems. At the end of 2020, more than 760 GW of solar photovoltaic systems were installed worldwide, of which approximately 139 GW were commissioned in 2020 alone [13]. This growth in installed capacity is the highest recorded in that year when compared to all other renewable technologies. CSP installed capacity grew globally between 2010 and 2020, reaching around 6.5 GW at the end of 2020, of which only 150 MW were commissioned in the same year [14]. The share of energy generation by CSP plants increased by 34% in 2019 [15], closely reflecting the growing trend of the global share of renewable generation, which reached 27% in 2019 and 29% in 2020 [16].

Among all, the dish-Stirling system is the least widespread commercially and the least mature from a technological point of view since, firstly, the installation cost of the parabolic dish concentrator is still too high compared to other CSP technologies suffering

the most from the stop of incentives and funding on the renewable energy sector [14] and, secondly, the coupling with a thermal storage system is more difficult to realise [17]. Nevertheless, this technology appears to be the most interesting and promising in terms of high values of solar-to-electric energy conversion efficiency, ease of installation, and modularity and is a viable solution for applications in integrated energy plants [18]. Also, dish-Stirling systems are environmentally reliable not only in terms of emission-free energy generation but also in terms of the level of sustainability observed in the production and installation phases [19].

For both PV and CSP systems, considering the latter not coupled to thermal storage systems, the main factor affecting the reliability and continuity of their electricity production is the aleatory nature of the solar energy source. Of course, the electricity production of such systems has a seasonal trend and closely follows the trend of solar irradiation during the year, peaking during the summer season and dropping to a minimum during the winter months. Furthermore, by reducing the time scale of observation, the daily production period of PV and CSP systems is not continuous but still dependent on the availability of solar radiation and more specifically, the electrical production of these systems depends on the particular climatic conditions at the installation site. Another factor that strongly influences the electrical output and performance of examined solar technologies is the level of soiling of the upper active surface, in the case of PV modules [20,21], and of mirrors, in the case of CSP systems [22].

It follows that, for both PV and CSP systems, it is essential to have models that are sensitive to the main factors influencing their operation and able to predict electricity production reliably and efficiently. The development of accurate and dynamic energy predictive models could be a key issue to consolidate and promote the deployment of these systems, driving a rapid and robust transition from coal energy production toward energy generation from renewables without CO_2 emissions. Firstly, a correct energy assessment of power plants would allow outlining the right direction for optimisation and improvement, especially of promising and not yet fully mature technologies such as CSP, towards cost-efficiency reduction. Secondly, accurate knowledge of the energy performance of no-coal power plants would allow making a realistic evaluation of their

economic recoverability, making the investment safe and encouraging more cautious investors also.

Outlines of this doctoral thesis

A brief outline of the contents addressed in the various sections of this thesis is given here. In *Chapter 1*, a descriptive overview of the four different types of concentrated solar power technologies currently available in the generation technology market will be given.

In *Chapter 2*, an insight into parabolic dish concentrating solar power technology will follow i.e., a detailed description of its subsystems and operation. Then, focusing on dish-Stirling concentrating solar technology, the energy balance of this system will be defined and analysed. Finally, in the same chapter, the reference dish-Stirling system will be presented, including the technical-descriptive illustration of the system, the description of the experimental measurement campaign, and the climatic characterisation of the installation site.

Chapter 3 will focus on the modelling of dish-Stirling systems: firstly, the linear energy model used to evaluate the electricity production of the dish-Stirling system and validated on experimentally collected data will be introduced, being the starting point for the subsequent models developed and discussed in this same chapter; secondly, a new and efficient algorithm for calculating the electricity production of dish-Stirling systems that uses, as input data, no longer a set of hourly solar data but the hourly frequency distribution of the DNI characteristic of the chosen installation site will be exposed; finally, the model, based on artificial neural networks, developed to predict the electricity production of dish-Stirling systems will be outlined and discussed here.

In the following chapters, various studies and energy, economic and environmental analyses of the dish-Stirling system will be addressed, with the aim of optimising energy generation and exploring other possible ways of operating this system.

In *Chapter 4*, the optimisation study of the dish-Stirling system will be presented, varying the size of the parabolic reflector according to the level of DNI characteristic of the selected installation site. It will then be discussed and demonstrated how this

technological advancement together with an incentive mechanism, with a variable incentive tariff over time, can contribute to reducing the LCOE of dish-Stirling systems, boosting their market competitiveness compared to other CSP systems.

Then, in the next two chapters, the operation of the dish-Stirling system in cogeneration mode will be analysed in order to exploit the thermal energy recovered at low temperature through the Stirling engine cooling system.

More specifically, in *Chapter 5*, the energy and environmental benefits that can be obtained by integrating a cogenerative dish-Stirling concentrator into the energy systems used to satisfy the air conditioning demand of an office building will be assessed. To this end, two typical reference energy systems will be explored, which include: first, a natural gas boiler for heating and air-cooled chillers for cooling periods; second, a reversible heat pump for both heating and cooling.

In *Chapter 6*, a combined heat and power plant implementing a dish-Stirling collector field, seasonal geothermal storage and a water-to-water heat pump system will be proposed. The operation of such a cogenerative plant layout will be simulated in the Transient System Simulation Tool (TRNSYS) environment and analysed from an energy, economic and environmental point of view.

Finally, *Chapter 7* will evaluate the reference dish-Stirling existing plant, installed at the university campus in Palermo (Italy), with a Life Cycle Sustainability Assessment.

Chapter 1

Overview of concentrating solar power systems

This chapter deals with concentrating solar power technologies used in power plants. Starting with a description of the main types of concentrating solar power systems currently available on the market and of emerging innovative ones, their principle of operation, functioning conditions and main industrial applications are illustrated.

1.1 Technologies for concentrating solar energy

Concentrating solar power systems convert only the direct component of solar radiation into thermal energy through the use of a series of properly oriented lenses or mirrors. Thus, this high-temperature thermal energy can then be used for direct or indirect uses such as electricity generation. In the latter case, high-temperature thermal energy is transferred to a working fluid that performs a thermodynamic cycle to produce mechanical energy, for example, in a conventional Rankine-cycle thermal power plant. Finally, an electric generator carries out the last stage of conversion from mechanical energy to electricity.

In general, CSP systems consist of five main sub-systems which are:

- The concentrating mechanism or collector, consisting of a series of mirrors or lenses with high reflectivity, is the primary optic of the system that captures the incident DNI and concentrates it on the receiver;
- The receiver is the subsystem that receives the solar radiation concentrated there and transfers it to the working fluid used for subsequent thermodynamic processes, acting as a heat source;
- The power conversion unit, which is the subsystem that includes all those plant components involved in the conversion of energy from thermal to mechanical and then to final electricity;
- The solar tracking system, single-axis or biaxial, which orients the collector so that the incident sun's rays are as perpendicular as possible to the reflective surface of the primary optics;
- The thermal storage system, if present, is used to store part of the thermal energy produced during the hours of sunshine to allow continuous operation (even at night) of the power plant.

The metric used to describe the quality of the concentration mechanism of a CSP system is the concentration ratio, which can be defined from an optical and geometric point of view. The optical concentration ratio (C_o) is determined using Eq. (1.1):

$$C_o = \frac{G_r}{G} \tag{1.1}$$

where G_r is the irradiance at the receiver surface and G is the incident solar irradiance usually referring to the peak of the solar irradiance distribution at the reference location. Instead, the geometric concentration ratio (C_g) is defined as the ratio of the aperture area of the collector (A_c) to the receiver area (A_r) as shown in Eq. (1.2):

$$C_g = \frac{A_c}{A_r} \tag{1.2}$$

The CSP systems that achieve the best concentration of direct solar radiation are essentially those with reflecting surfaces of paraboloid shape or parabolic cross-section, as they allow the parallel incident radiation to be concentrated at a single point on the

focal axis. Depending on how the primary optic concentrates the collected solar radiation on the receiver, it is possible to classify the different solar concentrating technologies into linear-focusing or point-focusing ones. The first group includes linear Fresnel reflectors and parabolic trough collectors (see *Figure 3 – a, b*), in which the solar collector, although different in shape and design, concentrates the solar radiation on a receiver tube that extends in a longitudinal direction along with the collector. Whereas the second group includes central receiver towers and paraboloidal dishes (see *Figure 3 - c, d*), in which the primary optics are such that the incident sun rays are concentrated on a single point where the receiver system is mounted.

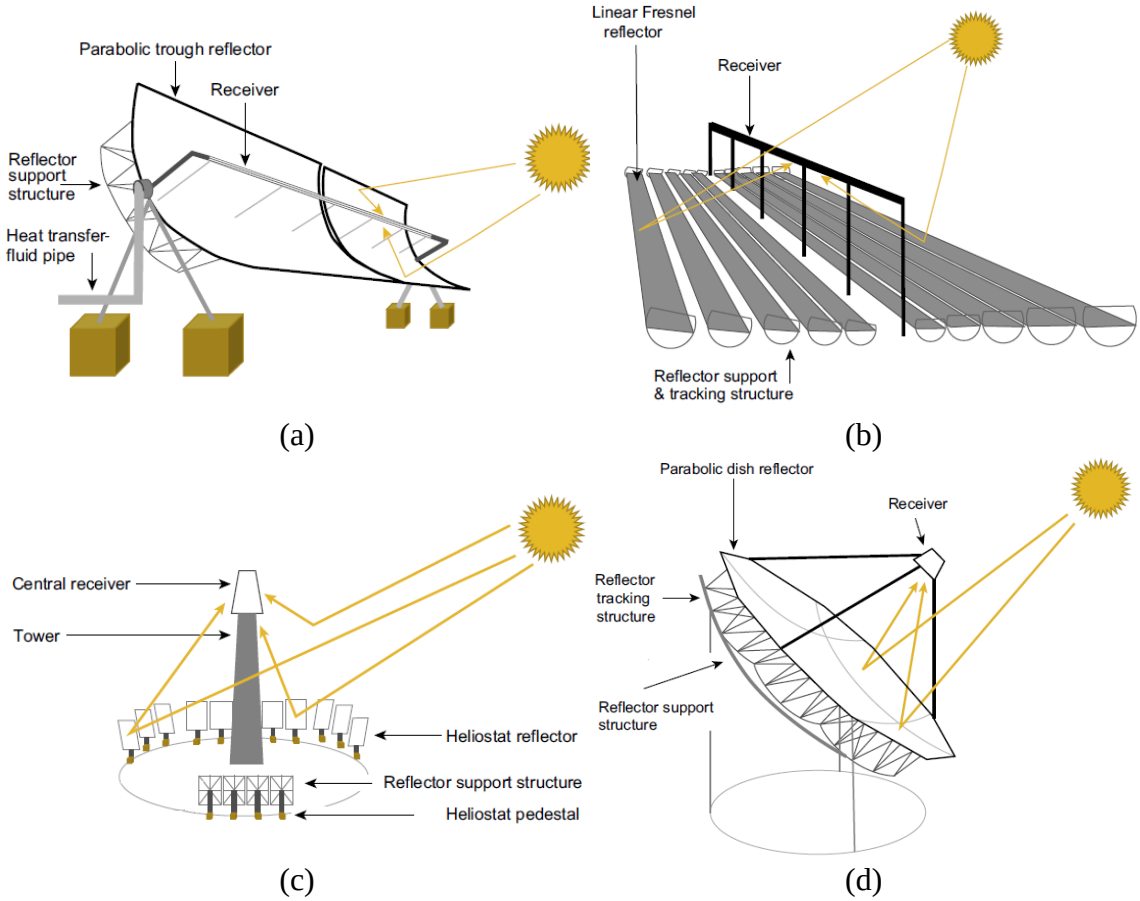

Figure 1. Schematic representation of a solar field: (a) parabolic trough collector, (b) linear Fresnel reflector, (c) central receiver tower (d), and paraboloidal dish [23].

1.1.1 Parabolic trough collectors

Parabolic trough collectors consist of a parabolic cross-section reflector, which reflects and concentrates solar radiation onto a tubular receiver placed along the focal line. The collector field consists of a large number of troughs that are arranged in parallel rows aligned on a north-south axis and are equipped with a single-axis tracking system that allows rotation from east to west throughout the day so that the solar radiation is continuously focused on the receiver tube [24]. The receiver, rigidly connected to the support structure and moving with it, consists of a metal tube coated with a selective material characterised by a high absorption coefficient in the solar radiation spectrum and a low emissivity in the infrared radiation spectrum, in order to minimise optical losses towards the environment. The metal tube in question is also enclosed within an evacuated coaxial glass tube, in order to minimise convective heat loss and trap the infrared radiation emitted by the receiver. Several receiver tubes are connected one after the other with appropriate joints made of highly elastic material resistant to high temperatures, and able to absorb thermal expansion.

Figure 2. Mojave, a 250-MW parabolic trough CSP plant in California with a nominal annual generation of 617,000 MWh (Source: https://www.energy.gov/lpo/mojave)

The heat transfer fluid used in this type of plant is usually molten salt or synthetic oil, which can reach temperatures of up to 400 °C. The high-temperature heat thus absorbed is then stored in a thermal energy system of molten salts, which exchanges heat with a secondary working fluid (water-steam) which allows the generation of mechanical energy and then electricity by performing appropriate cyclic thermodynamic transformations. The geometric concentration ratio of these systems is low ranging between 25 and 100 [24], but they are nevertheless the most widely used technology in the world. *Figure 2* below shows the biggest parabolic trough CSP plant in the world, which is placed in California across the Mojave Desert and has a generation capacity equal to 250-MW and a nominal annual generation of 617,000 MWh.

1.1.2 Linear Fresnel reflectors

Linear Fresnel reflectors (see *Figure 3*) have a collector consisting of flat or slightly curved mirror facets arranged according to the Fresnel lens principle. Each facet has its inclination, which increases as the distance from the receiver tube increases, and together they concentrate the solar radiation collected along the focal axis. In addition, each facet has an independent single-axis tracking system that allows it to rotate along the east-west direction. The receiver tube is a fixed metal tube that develops along the focal axis of the reflector. Compared to linear parabolic concentrators, here the receiver is placed at a greater distance from the reflector, and this implies a lower conversion efficiency from the collected solar radiation. For this reason, the receiver may consist of a second reflection surface to minimise the lost solar radiation. The pressurised water is usually used as a heat transfer fluid for direct steam production at a temperature of up to 500 °C. Concentrators of this type can also be equipped with multiple receivers and, in this case, the mirrors are installed with an alternating inclination so that some concentrate on one receiver and the rest on the other.

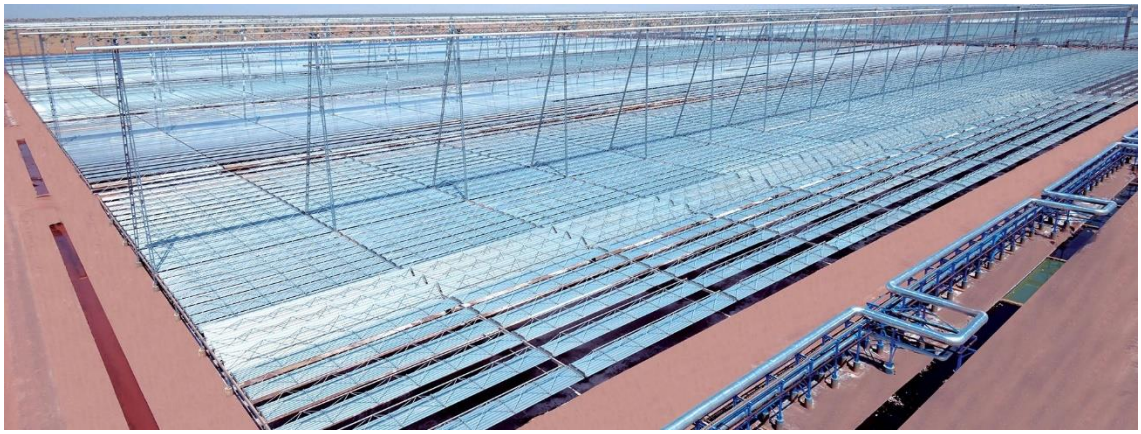

Figure 3. The largest CSP plant in Asia (Dhursar) with a peak output of 125 MWp and 792 linear Fresnel reflectors (source: https://www.lntecc.com/projects/infrastructure-for-renewables/125-mwp-csp-plant-at-dhursar/)

1.1.3 Central receiver towers

Central tower systems use flat collectors, called heliostats, placed around the tower and equipped with a bi-axial tracking system. The solar radiation collected by heliostats is concentrated at a focal point at the top of the tower where the receiver is located. The height of the tower can be over 100 m and increases as the heliostat field increases. The heat transfer fluid circulating in the receiver removes the heat by reaching high temperatures (565 °C in the case of molten salts and 800-1000 °C in the case of pressurized gas or air) and the thermal energy thus available can be used either directly in chemical processes or indirectly in thermodynamic cycles for the ultimate production of electrical energy, following thermal exchange with a secondary fluid. In the latter case, thermal storage systems are coupled to the plant. *Figure 4* below shows Ivanpah, the largest central receivers tower plant in the world, which is located in the Mojave Desert of Southern California and is characterized by a capacity of 392 MW and a nominal annual generation of 940,000 MWh.

Figure 4. Ivanpah, the largest tower solar CSP plant with a generation capacity of 392-MW located in the Mojave Desert of Southern California (Source: https://www.energy.gov/lpo/ivanpah)

1.1.4 Paraboloidal dishes

Of all solar concentration technologies, parabolic dish technology has the highest optical efficiency, the highest concentration ratio and the highest energy conversion efficiency. Parabolic dish systems concentrate direct solar radiation collected by a paraboloid-shaped collector on a focal point where the receiver is located. Inside the receiver, the heat transfer fluid (hydrogen, helium or air) absorbs the thermal energy obtained from the solar concentration and delivers it to the power conversion unit for subsequent energy conversion stages. To this aim can be used external combustion engines such as Stirling engines, gas turbines, reciprocating steam engines or organic Rankine engines. *Figure 5* shows the Maricopa Solar Project, which is a paraboloidal dish demonstration CSP plant located in Peoria, Arizona (USA). This plant has a generation capacity of 1.5 MW and comprises 60 dishes coupled to Stirling engines, achieving an annual solar-to-electricity efficiency of 26%.

Figure 5. Maricopa Solar Project 1.5 MW in Arizona (source: http://www.feliciabellows.com)

1.2 World-wide dissemination of CSP technologies

According to data collected by SolarPACES (Solar Power and Chemical Energy Systems) and provided by National Renewable Energy Laboratory (NREL), the installed capacity of operating CSP systems worldwide currently amounts to 6.49 GW [25], of which parabolic trough collector systems and central receiver tower systems account respectively for about 75% and 20%. The remaining smaller fraction of installed capacity concerns systems with Fresnel reflectors. The factors that make parabolic troughs preferable to other CSP technologies are essentially the lower total installed cost, the possibility of installing systems on an industrial scale, the ease of being coupled to a thermal storage system by being able to extend the production period into the night and the advantage of having a reduced focal distance. Central tower systems are the second most popular CSP technology after parabolic troughs because they are more expensive but still advantageous as they feature higher concentration ratios, significantly higher operating temperatures and therefore higher conversion efficiencies. Finally, regarding parabolic dish technology, the same data [25] show that there are currently only non-

operational plants with a total installed capacity of about 3 MW in the United States. This CSP technology, therefore, appears to be the least commercially mature, despite its excellent energy performance [14,26].

Overall, the most recent data for the year 2020 [14] show that the installed capacity of CSP systems has increased more than 5 times more than the installed capacity in 2010 (1.2 GW). Moreover, the Levelized Cost of Energy (LCOE) from CSP has decreased over the same decade by 71.6%, from 0.381 USD/kWh (0.334 €/kWh) to 0.108 USD/kWh (0.095 €/kWh) [14]. Nevertheless, CSP technology is still not very competitive compared to photovoltaic and wind technologies, which dominate the renewable electricity generation market. Technological development focused on the optimisation and improvement of conversion efficiencies, combined with the activation of suitable incentive mechanisms could lead to economies of scale such that the total installed cost of CSP technologies could be reduced, increasing their commercial penetration.

Nomenclature

A_c	Aperture area of the collector [m²]
A_r	Aperture area of the receiver [m²]
C_g	Geometric concentration ratio [-]
C_o	Optical concentration ratio [-]
G	Solar flux over the aperture (insolation) [W/m²]
G_r	Average solar flux over the receiver [W/m²]

Acronyms

CSP	Concentrating Solar Power
DNI	Direct Normal Irradiance
LCOE	Levelized Cost of Energy
NREL	National Renewable Energy Laboratory
SolarPACES	Solar Power and Chemical Energy Systems

Chapter 2

Dish-Stirling solar concentrator

In this chapter, a detailed examination of parabolic dish solar concentrator systems follows, along with a description of the constituent subsystems and their operation. With particular attention to dish-Stirling systems, the energy balance of this technology is then defined and analysed, dividing it into two macro-sections, one dedicated to the energy balance of the parabolic trough concentrator and the other to the energy balance of the power conversion unit. The closing part of the chapter is focused on the dish-Stirling system installed at the university campus of Palermo (Italy), to which all the studies addressed and presented in the following chapters will refer.

2.1 Introduction to parabolic dishes

Parabolic dish systems, characterised by the highest concentration ratios of up to 3000 [27], exploit the excellent geometric and optical properties of the paraboloidal mirror to concentrate direct solar radiation on the receiver, obtaining thermal energy at high temperatures from which the final energy vectors can be derived. Among all CSP

systems, the parabolic dish concentrator is the most efficient technology in the conversion of solar energy into thermal energy [28], especially when they are installed in locations with high DNI levels [29] since direct sunlight is the main meteorological parameter that most affects the energy yield of such systems [30]. However, parabolic dish systems have some limits and critical points, including the high initial investment cost required and the difficulty of coupling a thermal storage system [28]. Nevertheless, parabolic dish systems can be used in many applications [31], such as: in micro-cogeneration to generate heat and electricity simultaneously [32]; in integration with heating, ventilation and air conditioning technology to fulfil the heating, cooling, electricity and domestic hot water demands of a residential building [33]; in integration with thermal energy storage [34] or hybridisation using other RES [35]; in standalone power generation to bring electricity to remote rural areas [36]; in centralised power generation [37]; and in potable water production [38] and water pumping [39].

2.2 Fundamentals of parabolic dishes

As can be seen in *Figure 6*, a parabolic-dish type CSP system consists of:

- a paraboloidal reflector, whose surface shape is geometrically obtained by the revolution of a bidimensional parabola around its axis;
- a power conversion unit responsible for converting high-temperature thermal energy into electricity;
- a cooling system as a heat sink for the heat engine possibly integrated with the concentrator.
- a biaxial tracking system to correctly orient the paraboloidal reflector depending on the current position of the sun.

Usually, the paraboloidal reflector is made up of an assembly of several mirrors, which have a double curvature and can be facets of different geometry, but in any case, they have a glass or plastic upper surface with a very high reflection coefficient. Each facet of the paraboloidal reflector concentrates the solar beam radiation arriving at it in a direction parallel to the axis on a precise point corresponding to the aperture area of the receiver.

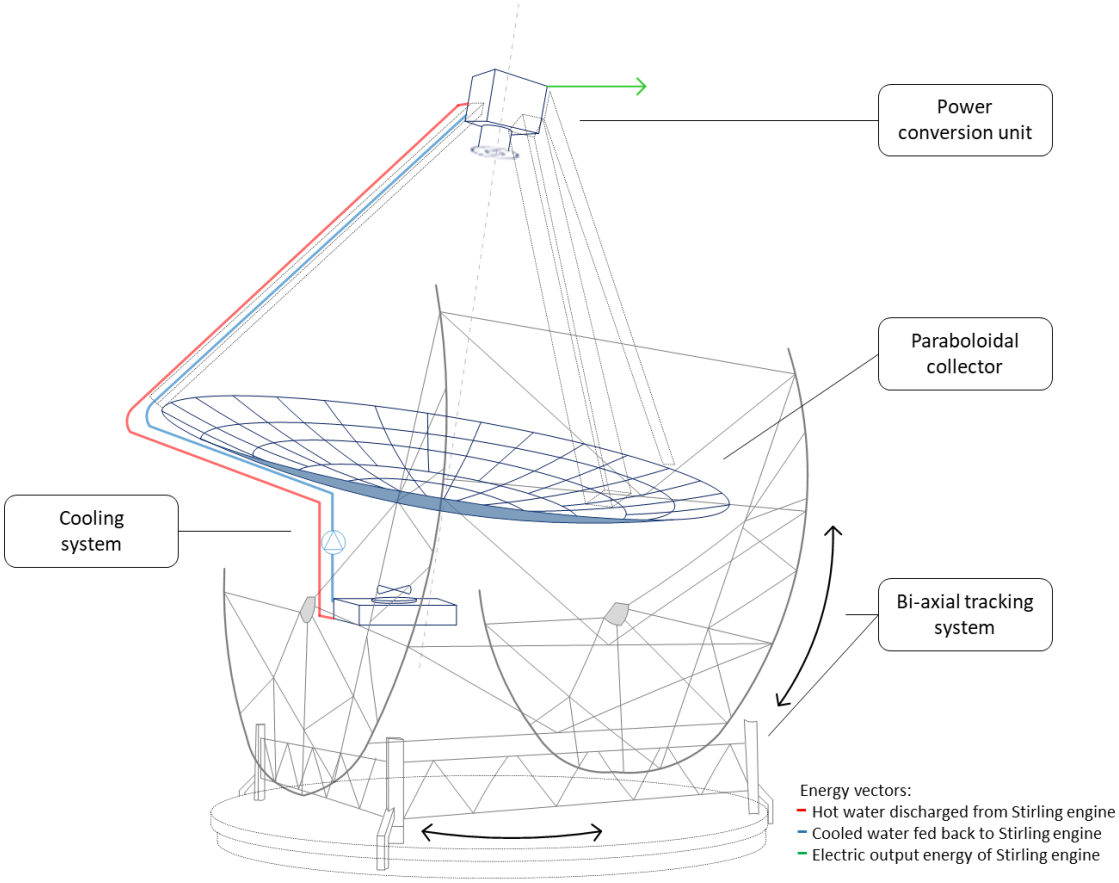

Figure 6. Schematic representation of a parabolic dish plant equipped with an azimuth-elevation tracking system.

The dimensions of the paraboloidal reflector, such as diameter and effective reflecting area, are determined as a function of the motor output power and by considering a direct normal irradiance of 1000 W/m². Usually, commercial parabolic dish concentrators can have a diameter of up to about 18 m and an area of up to 245 m² [28]. The position and aperture area of the receiver on the focal axis depends on the geometry of the parabolic concentrator [40]. Specifically, the distance between the focal point and the vertex of the paraboloid (see *Figure 7*) is the focal length (f) that can be derived using the equation below:

$$f = \frac{d_c}{4 \cdot tan\left(\frac{\varphi_r}{2}\right)} \tag{2.1}$$

where, as shown in *Figure 7*, d_c is the diameter of the dish concentrator and φ_r is the rim angle [41]. The rim angle is the geometric variable that defines the geometry of the combined concentrator/receiver system, as it is the angle measured at the focal point from the axis of the paraboloid to the tail of the dish (see *Figure 7*). The receiver is designed to absorb a large amount of irradiance concentrated on it by the mirrors that make up the dish and, thus, it is affected by optical losses but also by convective and radiative thermal losses to the external environment. Such heat losses increase as the aperture area increases [42]. The diameter of the aperture area of the receiver (d_r) is defined as follows:

$$d_r = \frac{f \cdot \theta}{\cos(\varphi_r) \cdot \cos(1+\varphi_r)} \tag{2.2}$$

where, θ is the acceptance angle is the angle at which all the beam irradiance reflected by the dish is collected in a short tracking time under worst-case conditions (see *Figure 7*) [43].

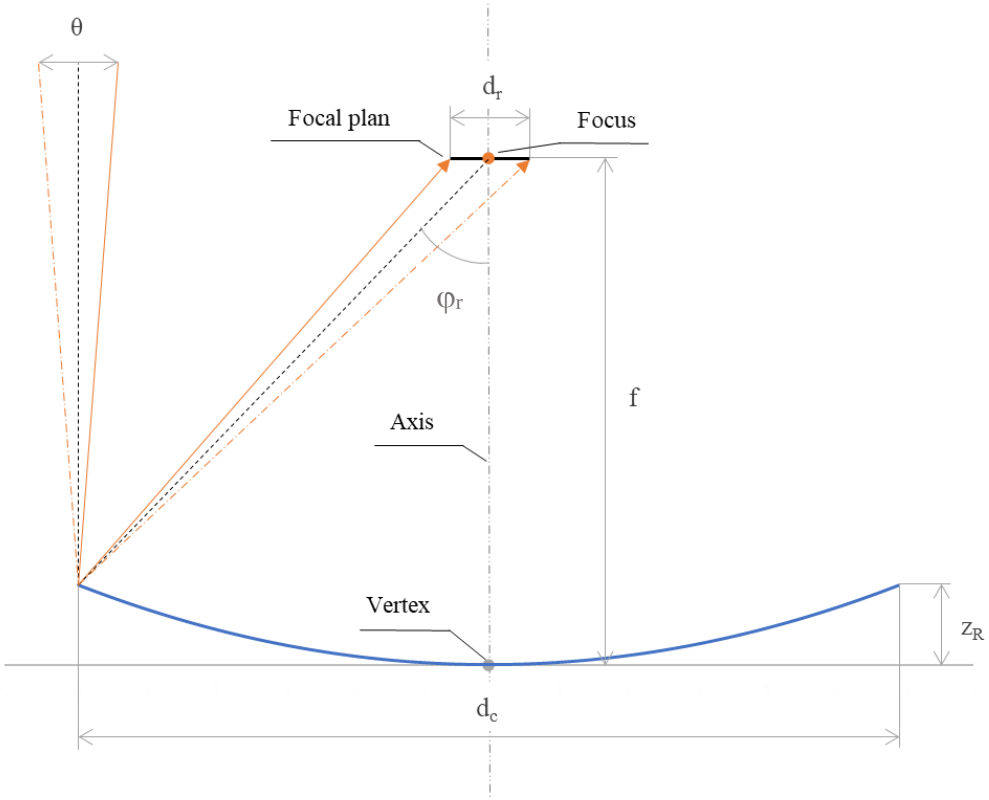

Figure 7. The geometry of the combined receiver-concentrator system.

The high values of efficiency in converting solar energy into thermal energy at the receiver are certainly thanks to the optical and geometric properties of the concentrator, but also to the precision with which the biaxial tracking system is able to follow the sun as it moves across the sky during the day. As indicated in *Figure 6* the biaxial tracking system can allow two independent rotational movements to the reflector: one around a rotation axis perpendicular to the ground plane to correct the azimuth angle of the dish, the other around a rotation axis parallel to the ground plane to track the sun at solar elevation. Alternatively, the solar tracking system can also be a polar-equatorial type according to which, the reflector rotates simultaneously around an axis parallel to the Earth's rotation axis with the same velocity and around a rotation axis perpendicular to the polar axis to adjust the declination angle of the dish. In both cases, the tracking system aims to keep the vertex of the paraboloid, the focal point and the sun aligned in the same direction.

Several factors adversely affect the optical efficiency of the solar concentrator, such as the quality and shape of the reflective surface, the accuracy of the tracking system in aligning the axis of the dish parallel to the direction of the sun's rays, and the cosine effect. Cosine losses are due to the imperfect alignment between the concentrator and the position of the sun, which results in a reduction of the apparent surface area exposed to solar radiation, due to the reduction of the cosine of the angle of incidence. In the case of parabolic dish concentrators, being equipped with a high-precision biaxial tracking system, these types of losses are extremely low compared to other forms of concentrators, and the only losses are due to the cosine effect are due to the curvature of the mirrors making up the dish.

While on the one hand, the reflector must be able to concentrate solar radiation while minimising optical reflection losses, on the other hand, the receiver must absorb the maximum concentrated solar radiation and minimise both radiative and convective thermal energy losses. To this effect, the aperture area of the receiver must be as small as possible and more specifically, taking into account that the point-focusing concentration can never be perfect in practice, it has to cover the set of focal points on which the various mirror facets concentrate the solar radiation.

The high-temperature thermal energy efficiently obtained at the receiver, if not used directly as process heat in industrial plants [44], is transferred to a working fluid for conversion into mechanical or electrical energy.

2.3 Power conversion unit and auxiliary equipment

Thanks to their high achievable operating temperatures, parabolic dishes are able to provide the energy input required in thermodynamic cycles for energy conversions such as Brayton, Rankine or Stirling ones. Therefore, such systems are generally coupled to gas or steam turbines or Stirling engines to generate mechanical power.

2.3.1 Receivers

The receiver is the subsystem that absorbs the maximum amount of concentrated solar radiation and transfers the resulting thermal energy to the heat transfer fluid for subsequent energy conversion processes. The receiver consists of a thermally insulated cavity to minimise thermal losses and has a small enough aperture area to include all the points on which the various mirrors making up the reflector concentrate direct solar radiation. The absorber is placed immediately behind the opening of the receiver cavity.

Depending on how the absorber of the receiver transfers the absorbed heat to the working fluid, it is possible to distinguish directly illuminated tube receiver (see *Figure 8.a*) and heat pipe receiver (see *Figure 8.b*). In the first case, direct solar radiation is concentrated on the surface of a series of small tubes through which the working fluid flows. Heat pipe receivers, on the other hand, use a liquid metal that vaporises by exchanging heat with the surface of the absorber and then condenses on the surface of the tubes inside which the working fluid circulates.

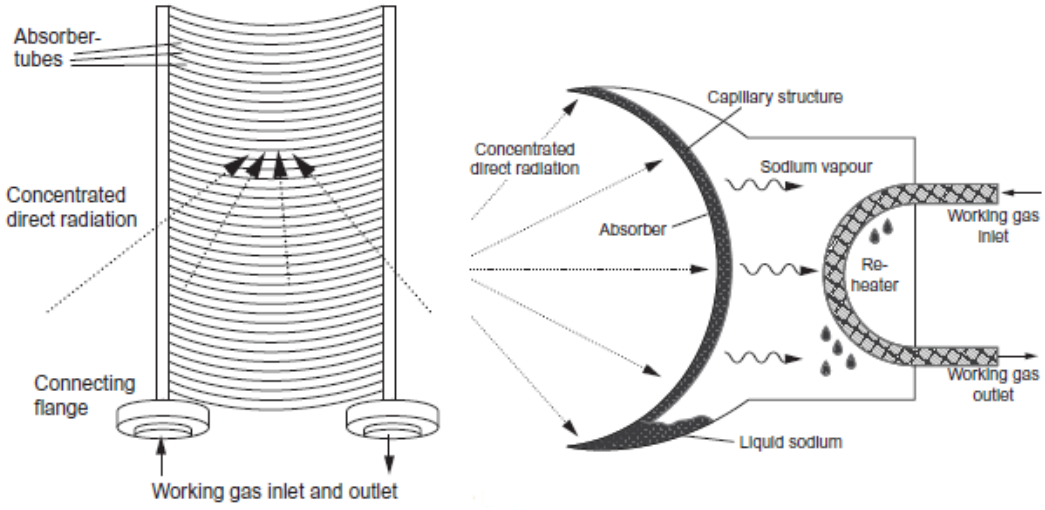

(a) (b)

Figure 8. Different types of the receiver: (a) directly illuminated tube receiver and (b) heat pipe receiver [45].

2.3.2 Brayton engine

Parabolic dish concentrators which use the thermodynamic Brayton cycle for energy conversion are usually coupled to an open loop in which air is the working gas. The ideal Brayton cycle consists of four basic processes: isentropic compression, isobaric heat supply, isentropic expansion and isobaric heat rejection. In solar systems, the receiver transfers high-temperature thermal energy to the air, which is previously compressed and preheated by recovering waste heat from the exhaust air at the end of the expansion. The gas turbine then allows the generation of mechanical energy which is then converted into electricity through an alternator, except for the mechanical energy needed for the compression process [46]. With a typical pressure ratio of around 2.5 and a turbine inlet temperature of around 850 °C, the thermal-to-electricity conversion efficiency of Brayton engines coupled to solar dishes is over 30% [47].

2.3.3 Stirling engine

Brayton engines are widely used in parabolic dish CSP systems and are preferred because of their low cost, the ease of hybridisation of the system and the potential for

improving system performance by heat regeneration [48]. Nevertheless, parabolic dishes driven by Stirling engines are much more popular, mainly because of their better thermal-to-mechanical energy conversion performance, which exceeds 40% [49]. Stirling engines can be kinematic and free-piston [50]; in the former, the pressure variation of the working gas is converted into mechanical power at the crankshaft using a connecting rod-crank system that connects the pistons in alternating motion inside the engine. In free-piston Stirling engines, the crankshaft is replaced by an internal spring system with a system of internal springs connected to the respective displacer and working piston, the movement of which is based only on the pressure variation of the working gas without any other driving mechanisms [51].

More specifically, the working fluid follows the Stirling thermodynamic cycle and evolves between two temperature levels, expanding and compressing within the hot and cold chambers of the engine, respectively. The ideal regenerative Stirling cycle consists of four thermodynamic transformations (see *Figure 9*):

- Isothermal expansion 1–2: once the maximum temperature of the cycle corresponding to point 1 has been reached, the fluid begins an expansion in the hot cylinder at an ideally constant temperature, thanks to the continuous addition of high-temperature heat from an external source.
- Isochore cooling 2–3: at the end of the expansion, the fluid is returned to the regenerator where, at a constant volume, it is pre-cooled before being conveyed to the cold cylinder.
- Isothermal compression 3–4: the evolving fluid is compressed inside the cylinder, which is ideally maintained at the minimum temperature of the cycle by the continuous rejection of heat;
- Isochore heating 4–1: once the pressure corresponding to point 4 of the cycle is reached, the fluid passes to the regenerator, where it is preheated at a constant volume until it reaches the maximum temperature of the cycle in the hot cylinder.

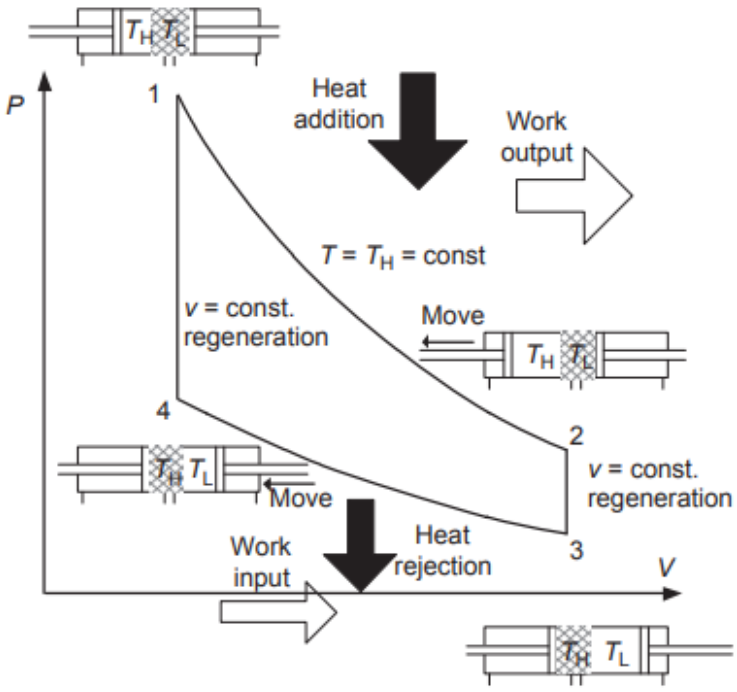

Figure 9. P-V diagram of the ideal Stirling cycle [52].

The Stirling cycle is therefore a cycle that evolves between two temperature levels, and the regenerator is the component that enables high efficiency to be achieved, close to the Carnot cycle evolving between the same temperatures. It is a regenerative type heat exchanger, consisting of a material with a high thermal capacity, capable of storing the heat released by the expanded fluid (pre-cooling) and then transferring it to the same fluid after compression (pre-heating).

In practice, the Stirling cycle suffers from various types of losses, such as mechanical losses due to the presence of viscous friction between the sliding mechanical components, pressure losses due to leakage of the working fluid, the impossibility of realising isothermal heat exchanges between the hot source and the cold source, incomplete heat exchanges in the regenerator due to its finite size and the limited duration of the heat exchange, or the impossibility of eliminating dead space in the cylinders. The main elements of a Stirling engine are as follows:

- the hot chamber, in which the working fluid expands as a result of a temperature increase by an external heater;
- the cold chamber, in which the fluid is compressed after being cooled by a cooling system;

- the engine piston, which actively carries out the compression and expansion operations;
- the displacer, which, where this is present, simply allows the fluid to migrate from the hot chamber to the cold chamber, either through a special duct or by leakage through the space between the piston and the cylinder, and finally
- the regenerator.

A working fluid suitable for use in a Stirling engine should be characterised by: good thermal properties for efficient heat exchange on the hot and cold sides of the engine, chemical compatibility with the materials used to ensure their long-term integrity, a viscosity that minimises friction losses, easy availability and low environmental impact. Listed in ascending order of performance, fluids such as air, nitrogen, helium and hydrogen meet these requirements.

2.3.4 Other equipment

To ensure that the Stirling engine operates continuously over time, the characteristic temperature difference of the thermodynamic cycle must be maintained constant. Therefore, while a heat exchanger supplies the high-temperature thermal energy on the hot side of the engine, a cooling system must be able to dissipate the waste heat on the cold side of the engine in order to maintain the minimum temperature of the thermodynamic cycle. The cooling system typically used in Stirling engine applications is an air-to-water heat exchanger that exchanges with the external environment.

Another auxiliary element with which the Stirling engine is equipped is the alternator since the Stirling engine only converts thermal energy into mechanical energy. The conversion of mechanical energy into final electrical energy is carried out using an alternator fitted on the same crankshaft of the Stirling engine.

2.4 Energy balance of a dish-Stirling system

According to *Figure 10*, showing the simplified diagram of all the energy flows involving a dish-Stirling system, all the quantities in terms of input and output power

concerning the main subsystems, the solar concentrator and the Stirling engine, are described below.

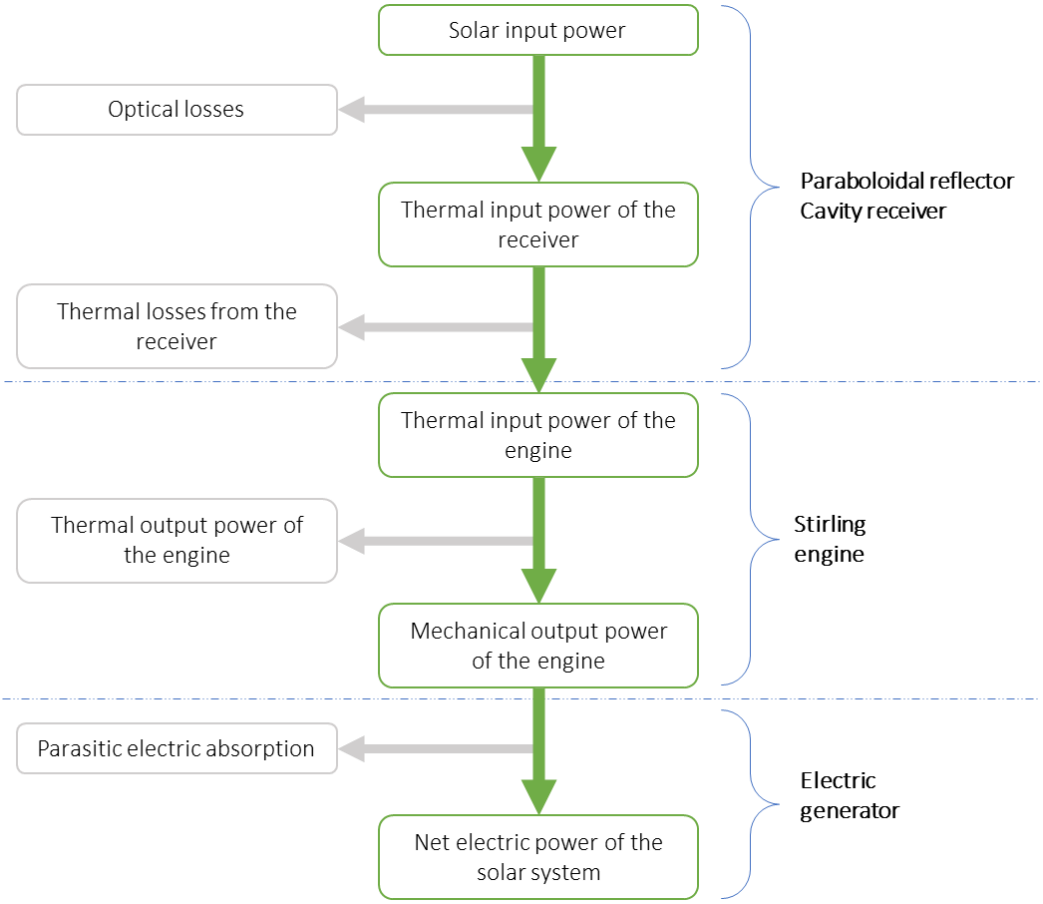

Figure 10. A simplified diagram of energy flows involving a dish-Stirling system

2.4.1 Energy balance of the concentrator

As previously mentioned, concentrating solar power systems convert only the direct component of solar radiation into other forms of energy and the solar power arriving at the paraboloidal reflector, indicated as $\dot{Q}_{sun}$ and expressed in W, can be expressed as in *Equation (2.3)* below:

$$\dot{Q}_{sun} = I_b \cdot A_n \tag{2.3}$$

where, I_b is the solar beam radiation (or DNI) expressed in W/m^2 and A_n is the effective useful surface of the paraboloidal reflector, in other words, it is the aperture

surface of the dish reduced both by the surface affected by shading due to the structure supporting the power conversion unit and to this latter and by the non-reflective surface corresponding to the gaps between one facet and the other and any frames of the same facets. The function of the combined system comprising the paraboloidal collector and the receiver is to convert the collected DNI into high-temperature thermal energy. however, not all the solar power arriving at the reflector can be usefully converted, because both the reflector and the receiver are affected by optical inefficiencies. From an optical point of view, the factors that could lead to power losses are essentially linked to the optical properties of the reflector surface of the collector and the absorber surface of the receiver, and to defocalisation phenomena, namely misalignment between the focal axis and the sun rays due either to errors in the solar tracking system or to wind-induced vibrational stress. To account for these optical losses, the optical efficiency of the concentrator (η_o) can be defined as in *Equation (2.4):*

$$\eta_o = \rho \cdot \alpha \cdot \gamma \cdot \eta_{cle} \tag{2.4}$$

where, ρ indicates the reflectance of the mirrors making up the paraboloidal dish, α is the absorbance of the absorber surface of the receiver, γ is the intercept factor related to the inaccuracy of the alignment between the focal point of the paraboloid and the position of the sun, and η_{cle} is the cleanliness index of collector surface. This last coefficient takes into account the level of cleanliness of the mirrors, which can be reduced (from the maximum value of 1 when mirrors are perfectly clean) due to soil and dirt deposits carried by wind or rainfalls, or to condensation phenomena that may occur in the early hours of the day. Therefore, the power that is effectively concentrated and absorbed by the receiver, denoted as $\dot{Q}_{r,in}$, can be expressed as in *Equation (2.5)*:

$$\dot{Q}_{r,in} = \eta_o \cdot \dot{Q}_{sun} \tag{2.5}$$

In the energy balance of the concentrator system, it is also necessary to take into account the thermal power losses by radiation and convection that occur from the opening area of the receiver to the external environment. In fact, as a result of solar concentration, the internal surface of the cavity receiver reaches a much higher temperature than the

outside ambient air. The thermal power dissipated by the receiver, indicated as $\dot{Q}_{r,out}$, can be determined as a sum as in *Equation (2.6)*:

$$\dot{Q}_{r,out} = \dot{Q}_{rad} + \dot{Q}_{conv} \tag{2.6}$$

where, $\dot{Q}_{rad}$ and $\dot{Q}_{conv}$ indicate radiative and convective thermal power losses, respectively. The first term concerning the radiative heat losses can be defined as in *Equation* (2.7):

$$\dot{Q}_{rad} = \varepsilon_r \cdot \sigma \cdot A_r \cdot \left(T_r^4 - T_{sky}^4\right) \tag{2.7}$$

where ε_r is the emissivity of the inner surface of the cavity receiver, σ is the Stefan–Boltzmann constant, A_r is the aperture area of the cavity receiver, T_r and T_{sky} are the inner surface receiver and effective sky temperatures expressed in Kelvin, respectively. In particular, the effective sky temperature depends on atmospheric conditions and is usually deduced through empirical relations such as the following equation, in which T_{air} is the external ambient air temperature:

$$T_{sky} = 0.0552 \cdot \left(T_{air}\right)^{1.5} \tag{2.8}$$

The second term of *Equation* (2.6), concerning the convective thermal power losses of the receiver, can be defined by *Equation* (2.9) below:

$$\dot{Q}_{conv} = h_r \cdot A_r \cdot \left(T_r - T_{air}\right) \tag{2.9}$$

where, h_r is the convective heat transfer coefficient of the cavity receiver.

Finally, the high-temperature thermal power obtained at the receiver from the solar power input to the reflector, which is also the input power of the Stirling engine, can be defined as the difference below:

$$\dot{Q}_{S,in} = \dot{Q}_{r,in} - \dot{Q}_{r,out} \tag{2.10}$$

In addition, by using Equations (2.5), (2.7), and (2.9), the input power of the Stirling engine can be rewritten as follows:

$$\dot{Q}_{S,in} = \eta_o \cdot I_b \cdot A_n - A_r \cdot \left[h_r \cdot \left(T_r - T_{air} \right) + \varepsilon_r \cdot \sigma \cdot \left(T_r^4 - T_{sky}^4 \right) \right] \tag{2.11}$$

At this point, it is possible to define the thermal efficiency of the concentrator $\left(\eta_c\right)$ as the ratio between the output high-temperature thermal power of the receiver and the input solar power of the paraboloidal reflector, obtaining:

$$\begin{cases} \eta_c = \dfrac{\dot{Q}_{S,in}}{\dot{Q}_{sun}} \\ \eta_c = \eta_o - \dfrac{1}{I_b \cdot C_g} \cdot \left[h_r \cdot \left(T_r - T_{air} \right) + \varepsilon_r \cdot \sigma \cdot \left(T_r^4 - T_{sky}^4 \right) \right] \end{cases} \tag{2.12}$$

It can be seen from the *Equation (2.12)* that the thermal efficiency of the concentrator is an increasing function of the geometric concentration ratio of the concentrator $\left(C_g\right)$.

2.4.2 Energy balance of the power conversion unit

The high-temperature thermal power absorbed by the cavity receiver is delivered to the Stirling heat engine to be converted into mechanical power at the crankshaft, which can be defined as follows:

$$\dot{W}_S = \eta_S \cdot \dot{Q}_{S,in} \tag{2.13}$$

where, η_S is the thermal-to-mechanical energy conversion efficiency of the Stirling engine. Moreover, while the receiver continuously supplies the thermal power on the higher temperature side of the Stirling engine, a cooling system allows waste heat to be removed from the lower temperature side of the engine. This thermal output power of the engine can be defined by difference as in *Equation (2.14)*:

$$\dot{Q}_{S,out} = \dot{Q}_{S,in} - \dot{W}_S \tag{2.14}$$

Then, the alternator converts this mechanical power into electricity. Specifically, taking into account the mechanical-to-electric energy efficiency of the alternator $\left(\eta_e\right)$, its gross electric output power, indicated as $\dot{E}_g$, can be written as in *Equation (2.15)*:

$$\dot{E}_g = \eta_e \cdot \dot{W}_S \tag{2.15}$$

In addition, considering the electrical power essentially absorbed by the solar tracking system $\left(\dot{E}_{p,t}\right)$ and the cooling system $\left(\dot{E}_{p,d}\right)$ of the Stirling engine, the net electrical power output of the dish-Stirling system can be defined from the gross electrical power by excluding these parasitic power absorptions as follows:

$$\dot{E}_n = \dot{E}_g - \left(\dot{E}_{p,t} + \dot{E}_{p,d}\right) \tag{2.16}$$

In conclusion, the instantaneous solar-to-electric efficiency for all dish-Stirling systems $\left(\eta_{DS}\right)$ can be determined as the ratio between the net electrical output power of the dish-Stirling system and the solar input power of the paraboloidal reflector, as written in the equation below:

$$\eta_{DS} = \frac{\dot{E}_n}{\dot{Q}_{sun}} \tag{2.17}$$

2.5 The reference dish-Stirling system

2.5.1 Description of the dish-Stirling reference plant of Palermo (Italy)

The dish-Stirling reference system, shown in *Figure 11*, is the commercial solar concentrator demonstration plant installed on the University campus in Palermo (Italy) in 2017, thanks to the collaboration between the companies HorizonFirm S.r.l with Dr Eng. Christian Chiaruzzi and Elettrocostruzioni S.r.l., involved in the installation and operating phases of the plant, and the Swedish company Ripasso Energy which manufactured the dish-Stirling system. The most relevant technical data on the CSP unit installed at the facility site at the University of Palermo has been summarised in *Table 1* below.

Table 1. Main technical features of dish-Stirling reference plant

Parameter	Value	Unit
Paraboloidal reflector		
Net aperture area of the dish collector (A_n)	101	m²
Aperture area of the receiver (A_r)	0.0314	m²
Focal length	7.45	m
Geometric concentration ratio	3217	-
Reflectivity of clean mirror (ρ)	0.95	-
Power conversion unit		
Peak electric output (DNI equal to 960 W/m²)	31.5 @ 2300 rpm	kW_e
Type of Stirling engine	4 cylinders double acting	
Displaced volume	$4 \cdot (95 \cdot 10^{-6})$	m³
Max operating pressure of hydrogen	20	MPa
Temperature of the receiver (T_r)	720	°C

The Ripasso Energy dish-Stirling unit has a net peak electric output power of 31.5 kW_e (at a DNI value of 960 W/m²) and produces alternating current electricity which is fed into the national grid. The paraboloidal reflector is characterised by an aperture area with a diameter of 11.86 m, a rim angle of 43.4° and an edge depth of 1.18 m. Such dish is made up of an assembly of 104 mirrors, different in shape and size, distributed on five concentric rings and characterized by a sandwich structure with a glass upper surface such as to give the mirror high reflectivity coefficient equal to 0.95. Moreover, each mirror has a double curvature and is calibrated to concentrate the incident DNI at a focal length of 7.5 m, on a focal point corresponding to the small aperture of the receiver cavity having a diameter of 0.02 m.

The power conversion unit (see *Figure 12*), which includes the receiver, the Stirling engine and the electric generator inside a steel box, is fixed on the focal point through a tripod anchored to the reflector support structure.

Figure 11. The dish-Stirling reference system installed at the university campus in Palermo (Italy)

Figure 12. Power conversion unit of the CSP reference plant

The cavity receiver acts as a high-temperature heat source needed by the thermodynamic transformations of the Stirling cycle by transferring the absorbed thermal power to the working fluid evolving on the hot side of the engine. The highly efficient *Ripasso* Stirling engine is an updated version of the original model (USAB 4-95) licensed from *Kockums AB* in 2008. Some data concerning the performance of the original USAB 4-95 Stirling engine, working with a temperature of 720 °C, can be found in [53]. In the past, this engine was installed on different dish-Stirling models, among which are: the MDAC systems located at different test facilities in the USA (1984-1985) [54] and the SES MPP systems (2008), one of which is located at the Sandia National Laboratories test site in New Mexico, USA [49]. These plants represent precursors to the evolved versions that *Ripasso Energy* has firstly realised in recent years at the *Ripasso* test site at Upington, South Africa. In November 2012, the *Ripasso* South African plants set the current world record of energy conversion efficiency from solar-to-electric at 32%, making the *Ripasso* dish-Stirling a state-of-the-art system in the *CSP* sector [28].

This Stirling engine consists of four double-action cylinders and is equipped with regenerators to maximise the efficiency of the conversion from thermal to mechanical energy. In addition, the cold side of this Stirling engine is cooled through a circuit in which a mixture of water and glycol flows removing waste heat on the cold side. the waste heat is then discharged into the environment by a dry-cooler mounted on the back of the reflector and attached to the support structure. The working fluid evolving in the Stirling engine of the reference system is hydrogen, which reaches the nominal operating conditions of 720 °C and 20 MPa. At these pressure and temperature levels, as can be seen in the diagram of *Figure 13*, hydrogen has the lowest dynamic viscosity values if compared to other common working fluids such as air or helium, minimising dynamic fluid friction losses [55].

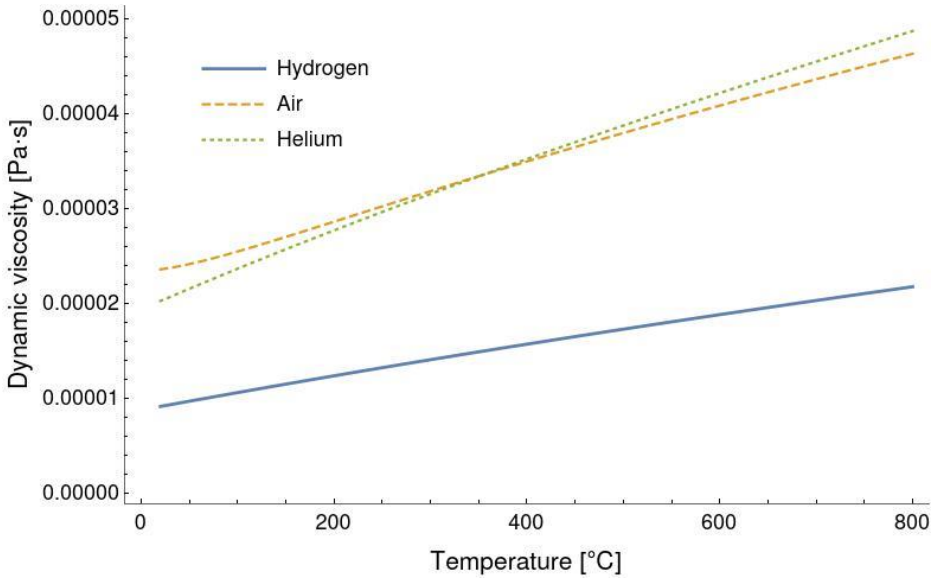

Figure 13. Dynamic viscosity for hydrogen, helium and air versus temperature with the pressure of 20 MPa

Lastly, the concentrator is equipped with a high-precision biaxial tracking system that makes it possible to follow the position of the sun throughout the day [19] by correcting its azimuth and elevation angle through the action of two independent motors controlled by two actuators. Specifically, these motors move two parts of the tracker structure that are: a carousel structure that is anchored at four points to a track on the base of the concentrator and turns in an azimuthal direction and a cradle structure that rotates according to the elevation position of the sun (see *Figure 14*). The reinforced concrete base shown in *Figure 14* supports the entire dish-Stirling system which has a total weight of 8 tonnes and occupies a ground area of 500 m^2.

Figure 14. Supporting structure of the dish-Stirling reference system

2.5.2 Experimental measurement campaign

During an operating period of the dish-Stirling reference system of 165 days ranging from 5 January 2018 to 2 July 2018, the monitoring system acquired 14,256,000 records (on a second-by-second basis). During this period, although the full operation of the solar plant was interrupted several times due to the maintenance and testing stages planned for the demo plant, it was possible to record, for 3,960 hours, the performance of the system under different conditions of solar irradiance, air temperature and cleanliness of the mirrors. All variables observed and recorded by the monitoring systems of the CSP plant include information about the operating state of the plant, climate conditions and solar position.

2.5.3 Climatic characterisation of the installation site of the reference system

The geographical coordinates specifying the installation site of the reference dish-Stirling system are Long. 13° 20’ 43’’ E - Lat. 38° 06’ 17’’ N.

Figure 15. The location of the reference dish-Stirling system (Palermo, Italy)

The climate of Sicily is typical of the Mediterranean, being dry, with hot and very long summers, mild and rainy winters, and highly variable intermediate seasons. On the coasts, especially in the south-west and south-east, the climate is more affected by African currents, making the summers very hot. Especially in summer, Sirocco events are very frequent. During the winter season, in the inland areas, temperatures are slightly colder, characterising the Mediterranean climate with conditions typical of a continental climate. The metropolitan city of Palermo, Sicily's capital, has a Mediterranean climate with mild, wet winters and hot, dry summers. In winter, the average temperature ranges between 8 and 14 °C and rarely drops to 0 °C. Phenomena such as snow and fog are extremely rare. Sometimes it is even possible to measure 25 °C in January. Rainfall, which is mainly concentrated in October and March, is generally light or moderate, rarely intense. The average temperature during the summer varies between 21 and 28 °C. In summer, temperatures reach 33 °C, but temperatures of 42 °C have also been recorded. The average humidity is about 70% during each season [56].

Figure 16. Direct normal irradiation map of Italy

As mentioned in the previous sections, all CSP technologies convert only the direct component of global solar radiation into thermal energy and electricity, and observing the DNI map of *Figure 16* prepared by Solargis for the World Bank, it can be possible to see that Sicily is the region of Italy with the highest level of radiation and is, therefore, the most suitable region for the installation of these systems. According to the same data source, Palermo is characterized by an annual direct normal irradiation equal to 1731.5 kWh/m².

Nomenclature

A_n	net surface of the paraboloidal reflector [m²]
A_r	aperture area of the cavity receiver [m²]
C_g	geometric concentration ratio of the concentrator [-]
d_c	diameter of the dish concentrator [m]
d_r	diameter of the receiver aperture [m]
$\dot{E}_g$	gross electric output power of the dish-Stirling system [W]
$\dot{E}_n$	net electrical power output of the dish-Stirling system [W]
$\dot{E}_{p,d}$	electrical power absorbed by the cooling system of the engine [W]
$\dot{E}_{p,t}$	electrical power absorbed by the solar tracking system [W]
f	focal length [m]
h_r	convective heat transfer coefficient of the cavity receiver [W/(m²·K)]
I_b	solar beam radiation [W/m²]
$\dot{Q}_{conv}$	convective thermal power losses at the receiver [W]
$\dot{Q}_{rad}$	radiative thermal power losses at the receiver [W]
$\dot{Q}_{r,in}$	thermal power concentrated and absorbed by the receiver [W]
$\dot{Q}_{r,out}$	thermal power dissipated by the receiver [W]
$\dot{Q}_{S,in}$	thermal input power of the Stirling engine [W]
$\dot{Q}_{S,out}$	thermal output power of the Stirling engine [W]
$\dot{Q}_{sun}$	solar power arriving at the paraboloidal reflector [W]
T_{air}	external ambient air temperature [K]
T_r	inner surface receiver temperature [K]
T_{sky}	effective sky temperature [K]
$\dot{W}_S$	mechanical output power of the Stirling engine [W]

Greek letters

α	absorbance of the absorber surface of the receiver [-]
γ	intercept factor [-]
ε_r	emissivity of the inner surface of the cavity receiver [-]
φ_r	rim angle of the dish concentrator [°]
θ	acceptance angle of the concentrator [°]
ρ	reflectivity of the clean mirrors [-]
η_c	thermal efficiency of the concentrator [-]
η_{cle}	cleanliness index of collector surface [-]
η_{DS}	instantaneous solar-to-electric efficiency for all dish-Stirling systems [-]
η_e	mechanical-to-electric energy efficiency of the alternator [-]
η_o	optical efficiency of the concentrator [-]
η_S	Stirling engine thermal-to-mechanical energy conversion efficiency [-]
σ	Stefan–Boltzmann constant [W/(m²·K^4)]

Acronyms

CSP	Concentrating Solar Power
DNI	Direct Normal Irradiance
RES	Renewable Energy Source

Chapter 3

Modelling of a dish-Stirling solar concentrator

This chapter deals with the modelling of dish-Stirling systems aimed at assessing their energy production as a function of all those factors, both operational and climatic, which may influence their operation. First of all, the energy model that linearly relates the net electric power produced by the system and the direct normal irradiance is described. This energy model, validated on data collected experimentally during the operating period of the dish-Stirling plant installed at Palermo, represents the starting point for the subsequent models developed and discussed in this chapter. Secondly, a new and efficient algorithm for the calculation of the dish-Stirling systems electricity production by using, as input data, not a set of hourly solar data, but the hourly frequency distribution of the DNI characteristic of the chosen installation site is presented. Finally, the model for predicting the electricity production of a dish-Stirling system based on artificial neural networks is defined and explained and tested and validated using real experimental data.

3.1 A validated energy model of a solar dish-Stirling system considering the cleanliness of mirrors

Among several numerical models used to evaluate the energy production of dish-Stirling systems based on real performance data from operating dish-Stirling plants [57], [58], [59], [60], the Stine model and its subsequent evolutions are the most widely used [61], [62]. These empirical models are based on the observation that there is usually a linear correlation between DNI and the electrical power generated by dish-Stirling plants when the collector mirrors are clean [57], [58], [54] and the coefficients of the correlation can be calibrated using function test data on a full day with clear skies. These constants can be further corrected to take into account the effect of air temperature changes and degradation of optical efficiency due to soiling of the collector mirrors [61], [57], [58].

The research group established in Palermo shows in [22] how data collected during the monitoring programme of the dish-Stirling plant built at a test site at the University of Palermo (Sicily), described in *Paragraph 2.5.1 "Description of the dish-Stirling reference plant of Palermo (Italy)*", were used to experimentally assess the main factors influencing the performance of these systems. The tests performed on this plant are particularly interesting because there are few demonstrative dish-Stirling plants installed in the Central Mediterranean region and there is, therefore, no evidence of the effects of the particular micro-climate of this region on the performance and maintenance operations of this type of plant. This geographical area is characterised by rather high levels of DNI [63], particularly during the warmer periods of the year. However, cloud decks associated with typical mid-latitude depressions and frontal passages are evident during cold periods of the year. In addition, desert dust transport events are frequent in this area. Dust transport occurs almost every day in different parts of the Mediterranean, especially during spring and summer [64], [65], [66], [67]. Both the frequent passage of clouds in the winter season and the dust deposition on collector mirrors in the spring and summer seasons can reduce the performance of dish-Stirling systems, yet these effects are often difficult to predict and manage. Using operating data measured on days when the concentrator mirrors were clean, our research group elaborated a physical-numerical model based on a simplified energy balance of the collector (according to a well-

established technique for modelling the CSP system performance [68]), taking into account the part-load efficiency curve of the Stirling engine [53]. Assuming further reasonable simplifying hypotheses, based on the experimental evidence, it has been possible to linearise the model obtaining a physical interpretation of the empirical coefficients of the model proposed by Stine. In addition, we compared the performance measured for the dish-Stirling system with soiled mirrors with that expected from the model with clean mirrors, for the same conditions of DNI and air temperature, using a technique proposed in the literature to assess the effect of module soiling on the energy production of photovoltaic systems [69]. Using this method, it has been possible to define an average daily cleanliness index of the system for each day during the monitoring period and the evolution of this index has been compared with the history of rains and dust deposition events recorded in the same period for the area where the plant is installed [70].

3.1.1 Analysis of experimental data acquired during the operation of the dish-Stirling reference system

The research group in Palermo started their study from the analysis of the experimental data collected during the operating period of the dish-Stirling reference plant (see *Paragraph 2.5.1 "Description of the dish-Stirling reference plant of Palermo (Italy)*) that occurred between 11 January 2018 and 2 July 2018. According to weather, such data were divided into two groups; days when the collector mirrors were clean or not. In fact, during the period in which the experimental data were recorded, the dish-Stirling plant was subject to numerous rain cycles of various intensities and Sirocco events with associated variable levels of dust deposition. For this reason, it was assumed that most of the records analysed correspond to conditions where the collector mirrors were naturally characterised by different levels of dirt. On the other hand, a total of 13 days were selected from the total data set on which the mirrors were also classified as clean in relation to the particular conditions occurring on the previous days: the first 4 days between 18 January and 2 February immediately after the removal of the protective films from the mirrors and at a time when frequent rainfall kept them clean; another day on 30 May after washing of the mirrors that took place on 23 May; and finally another 8 days between 16 June and 2 July when the mirrors were particularly clean as a result of

the heavy rainfall that took place on 14-15 June. On most of the other days, except for these 13, the effect of dust deposition on the surface of mirrors was often observed, such as on 6 March, as a result of a significant Saharan dust transport event (Sirocco) occurring from 28 February to 5 March.

According to the approach suggested by Sandia National Laboratories for the analysis of the performance of dish-Stirling plants [58], the data of net electric power, corrected for the effect of the ambient temperature, has been correlated with the corresponding values of direct solar irradiation. Concerning the correction factor for the air temperature, it has been noted that the selected data corresponding to clean mirrors was well-correlated by a linear relation representing the upper limit of the experimental point cloud and all the other data has shown that the plant performance was lower compared to that of the first group with similar values of DNI. From these observations, it has been deduced that a large majority of the reported production losses during the testing campaign were caused by the soiling of the mirrors and only marginally by other factors such as sun-tracking errors, the fast passage of clouds, engine transients, etc. In order to quantify these effects on the optical efficiency of the system, we have used the method proposed by Stine [57] through the introduction of a reductive factor to the slope of the linear function between the correct net electric output power and DNI.

3.1.2 A linear model of dish-Stirling electric power generation

Starting from the energy balance of the Stirling engine (see *Paragraph 2.4 "Energy balance of a dish-Stirling system"*) and according to the analysis of the real data of partial load operation of the original USAB 4-95 Stirling engine (working with T_h = 720 °C) [53] and the performance of the Stirling engine of the SES plant [62], we have decided to approximate with a linear regression the curve between the thermal input power $\left(\dot{Q}_{S,in}\right)$ and the mechanical output power $\left(\dot{W}_S\right)$ of the engine as:

$$\dot{W}_S = (a_1 \cdot \dot{Q}_{S,in} - a_2) \cdot R_T \tag{3.1}$$

Where a_1 and a_2 are the two positive fitting constants and R_T is the ratio of a reference temperature T_0 to the current ambient temperature T_{air} (both expressed as Kelvin degrees):

$$R_T = \frac{T_0}{T_{air}} \tag{3.2}$$

This last correction factor was introduced, inspired by what was proposed in the Stine model [61], [57] and similar ones [58], to take into account the effect of variations in outside temperature on the efficiency of the Stirling engine.

Rewriting the terms of Equation (2.16) by using both Equations (2.15) and (2.11) of the energy balance of the dish-Stirling system (see Paragraph 2.4 "Energy balance of a dish-Stirling system") and Equation (3.1), it is possible to find the linear correlation between the net electrical power output of the dish-Stirling plant $\left(\dot{E}_n\right)$ and DNI $\left(I_b\right)$ as follows:

$$\dot{E}_n = \left(\eta_e \cdot \eta_o \cdot a_1 \cdot A_n \cdot R_T\right) \cdot I_b - \left[\eta_e \cdot \left(a_1 \cdot \dot{Q}_{r,out} + a_2\right) \cdot R_T + \dot{E}_p\right] \tag{3.3}$$

The model described by *Equation (3.3)*, once calibrated with the real operating data, can be applied in order to predict the net electric power output of the dish-Stirling system taking into account:

- the changes of the direct normal irradiation and external temperature
- the optical efficiency (by the parameters of Equation (2.4))
- the effect of mirror soiling (by the cleanliness index in Equation (2.4))
- the thermal losses from the receiver (by the parameters of Equation from (2.6) to (2.9)), assuming the receiver temperature is constant during the operation of the plant
- the expression of the thermal efficiency of the Stirling engine as a function of the partialisation of the thermal input loads (by *Equation (3.1)*) and external air temperature (by *Equation (3.2)*)
- the parasitic powers of the tracking and cooling systems of the PCU (by Equation (2.16))

Moreover, referring to the dish-Stirling reference system, it is possible to predict the power production over a long time through the numerical model described by the *Equation (3.3)* assuming a constant average value of cleanliness coefficient $\left(\eta_{cle}^{ave}\right)$ and considering that both the power absorbed by the parasitic components $\left(\dot{E}_p^{ave}\right)$ and the

receiver temperature $\left(T_r^{ave}\right)$ remains approximately constant as observed experimentally [22].

$$\dot{E}_n = \left(\eta_e \cdot \eta_o \cdot \eta_{cle}^{ave} \cdot a_1 \cdot A_n \cdot R_T\right) \cdot I_b - \left[\eta_e \cdot \left(a_1 \cdot \dot{Q}_{r,out} + a_2\right) \cdot R_T + \dot{E}_p^{ave}\right]$$
$$\text{where: } \dot{Q}_{r,out} = A_r \cdot \left[h_r \cdot \left(T_r^{ave} - T_{air}\right) + \varepsilon_r \cdot \sigma_{SB} \cdot \left(T_r^{ave\,4} - T_{sky}^4\right)\right] \tag{3.4}$$

Table 2 shows the parameters of the numerical model described so far and also specifies the operating limits (lower $\left(\dot{Q}_{S,in}^{\min}\right)$ and upper $\left(\dot{Q}_{S,in}^{\max}\right)$) of the Stirling engine of the reference concentrator in terms of the high-temperature thermal power it is able to convert into mechanical power.

Table 2. Model parameters defined for the dish-Stirling plant of Palermo

Parameters	**Value**	**Unit**
Receiver aperture area A_r	0.0314	m^2
Clean mirrors optical efficiency η_o	0.85	-
Receiver convective coefficient h_r	10	$W/(m^2 \cdot K)$
Receiver effective emissivity ε_r	0.88	-
Parameter a_1 of *Equation (3.1)*	0.475	
Parameter a_2 of *Equation (3.1)*	3.319	kW
Average Receiver temperature T_r^{ave}	720	°C
Reference temperature T_0	25	°C
Max engine thermal input power(*) $\dot{Q}_{S,in}^{\max}$	85	kW
Min engine thermal input power(*) $\dot{Q}_{S,in}^{\min}$	11	kW
Electrical efficiency of the *PCU*, η_e	0.924	-
Average parasitic absorption $\dot{E}_p^{ave}$	1.60	kW
Average cleanliness index η_{cle}^{ave}	0.85	-

(*) Maximum and minimum values of the Stirling engine thermal input power have been determined at an air temperature of 25 °C and with clean mirrors at 960 and 155 W/m², respectively.

In conclusion, the numerical model described by Equations (3.3) and (3.4) represent the state of the art for dish-Stirling systems modelling and, calibrated on a single clear sky day, allows for accurate predictions of the net electrical power output. As it is possible to see in Figure 17, where are diagrammed the electric power output values predicted by the model against those measured experimentally when the mirrors were clean, a square-R equal to 0.97 was obtained.

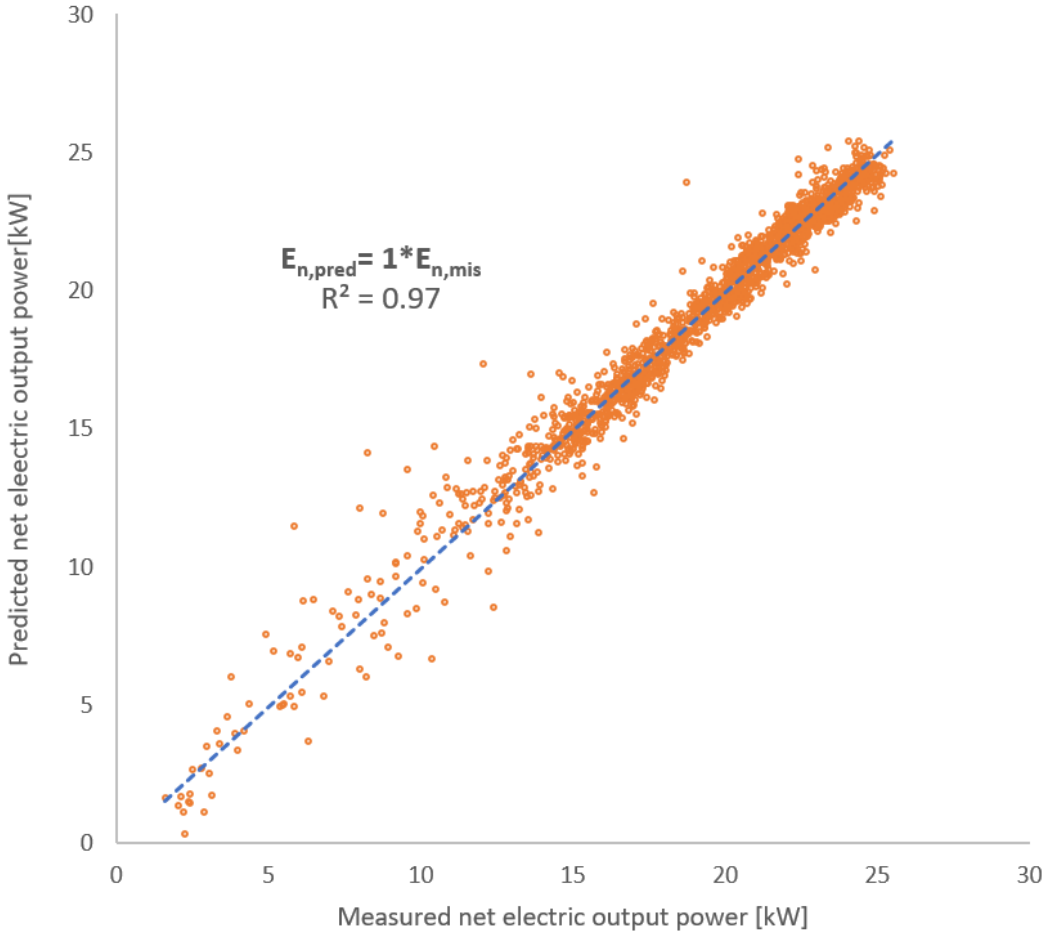

Figure 17. Measured versus predicted net electric output power for the days on which the collector mirrors were clean.

3.2 A new simplified algorithm to assess electricity production from DNI frequency histograms

Usually, the available energy models calculate the electric output power of dish-Stirling systems as a function of the DNI, the external air temperature and the soiling level of the collector mirrors [61]. Of these, the solar beam radiation which characterizes each plant installation site [71] is the factor that most influences both the system sizing [72] and the prediction of its energy output [73]. Most of the popular models used for DNI assessment are based on the estimation of both the global horizontal irradiation and the diffuse fraction of the solar radiation, the latter often determined from the clearness index [74]. Alternatively, using different models it is possible to estimate the beam irradiance directly from satellite images [75]. Through these different approaches, it is then possible to stochastically generate hourly synthetic DNI time series [76] that can be used to perform hourly simulations useful for calculating the annual energy produced by dish-Stirling systems.

A new simplified calculation algorithm allowing the energy production assessment of dish-Stirling systems using the frequency histogram of 1-hour DNI data series as input is proposed. As will be discussed in *Chapter 4* that follows, this method could present a useful application in the optimization of dish-Stirling systems for macro geographical regions for which it would be possible to elaborate statistically a single typical average frequency histogram of a 1-hour DNI series.

3.2.1 Explanation of the simplified calculation method

As described in the previous subsection, the electrical output of a dish-Stirling system essentially depends on both the level of direct normal irradiance and the outdoor temperature value. In this regard, the accuracy of predicting the long-term energy production of a CSP system does not exclusively depend on the reliability of the numerical model, but also on the representativity of the DNI data used as input. Unfortunately, an accurate elaboration of a DNI time series, representative of the long-term average conditions for a given location, is far from simple [77]. Different solar databases make available climate information for a specific location, for instance,

Meteonorm [78] and PVGIS [79]. Meteonorm is a reliable source of meteorological parameters providing a typical meteorological year (TMY) for any location in the world. However, DNI values extracted from this synthetic data can differ significantly from ground measurements [80]. On the other hand, PVGIS is a European solar data information system that is used to assess the energy production of photovoltaic systems. This data is based on images provided by the Meteosat East geostationary satellites [81], and, therefore, may be inaccurate on cloudy days [82]. However, using the TMY generated by a solar database, it is possible to define two different series of hourly values of solar beam radiation (I_b) and external air temperature (T_{air}) for a specific location.

The climate data of a location can be used to assess the net electrical outputs of the dish-Stirling systems using a simplified approach summarized in the flowchart in *Figure 18*. Starting from the hourly series of the two meteorological input variables (I_b and T_{air}), represented by box (a) of *Figure 18*, it is possible to elaborate hourly frequency histograms through the binning procedure that is described in box (b) of the same figure.

According to this data binning procedure, the range of I_b values of the input dataset of box (a) can be divided into a series of consecutive non-overlapping bins, all having the same width ΔI_b [W/m^2]. Thus, as indicated in box (b), the following quantities can be calculated for each bin:

- n_{I_b} [h], representing the number of records falling into the bin. That is, the number of hours during which I_b occurred with values included within the extremes of the definition of the bin.
- $\overline{T}_{air}$ [°C], representing the average of all the T_{air} values corresponding to records having an I_b value falling into the bin. These different values of T_{air} in each bin are related to the fact that, during the year, there are hours characterised by the same level of direct normal irradiance but different air temperature values.
- $\overline{I}_b$ [W/m^2], which is the mid-point value of the extremes defining the bin width.

- E_s [kWh/m^2] represents the total amount of the solar direct normal energy that can be calculated by multiplying $\bar{I}_b$ by n_{I_b}.

By observing the flowchart in *Figure 18*, it is easy to see that these values resulting from the binning procedure (box (b)) represent the input data for the simplified procedure briefly described in box (c). In other words, this simplified method allows the energy calculation using the hourly frequency distributions of direct normal irradiance (and the corresponding $\bar{T}_{air}$ values) as input. To this aim, starting from the triplets $\left(\bar{I}_b, \bar{T}_{air}, n_{I_b}\right)$ defined for each bin with of procedure described by box (b), it is possible to calculate the net electric output power $\left(\dot{E}_t\right)_{sim}$ corresponding to each bin using *Equation (3.4)*. Finally, for each bin, the net electric output energy $\left(E_t\right)_{sim}$ values are obtained by multiplying the bin value of $\left(\dot{E}_t\right)_{sim}$ by the corresponding n_{I_b} value.

The simplified approach is particularly advantageous, from an application point of view, whenever, for a certain location, an hourly frequency distribution of the DNI is available even when the original hourly-based data series is not. The latter, for example, may be the case when frequency histograms of direct solar radiation are defined synthetically, through either statistical or analytical methods, to represent the average solar radiation conditions of a studied macro-region. In these cases, it is not even strictly necessary to know the exact value of $\bar{T}_{air}$ corresponding to each bin of I_b and it is sufficient to assume a constant value equal to the annual average air temperature of the specific geographical location. The model described by *Equations (3.3)* and *(3.4)*, in fact, shows that the net electricity production of a dish-Stirling system is only slightly sensitive to variations in temperature and mainly depends on the intensity of direct normal irradiance. As will be shown in the next *Chapter 4*, the simplified method is, also, particularly convenient, in terms of the immediacy of the calculations, whenever it is necessary to optimise the design of dish-Stirling collectors as a function of the hourly frequency distribution of direct radiation, especially considering that the linear model used for electricity production simulations (described by *Equation (3.4)*) can be easily recalibrated to simulate the electrical output of different dish-Stirling systems [22].

Finally, when the period to which the historical climate data series refers is sufficiently long (e.g. 10 years) it is possible to calculate, for each defined bin and for a given location, the annual average values of the hourly frequency $\overline{n}_{I_b}$, the solar direct normal energy $\overline{E}_s$ and the net electric output energy calculated by the simplified $\left(\overline{E}_t\right)_{sim}$ approach (as shown in box (d) in *Figure 18*). The accuracy of the new simplified algorithm for evaluating the energy production of a dish-Stirling system is demonstrated in *Chapter 4*, where the results obtained with the latter approach will be compared with those obtained with an approach based on hourly data of solar beam radiation and air temperature.

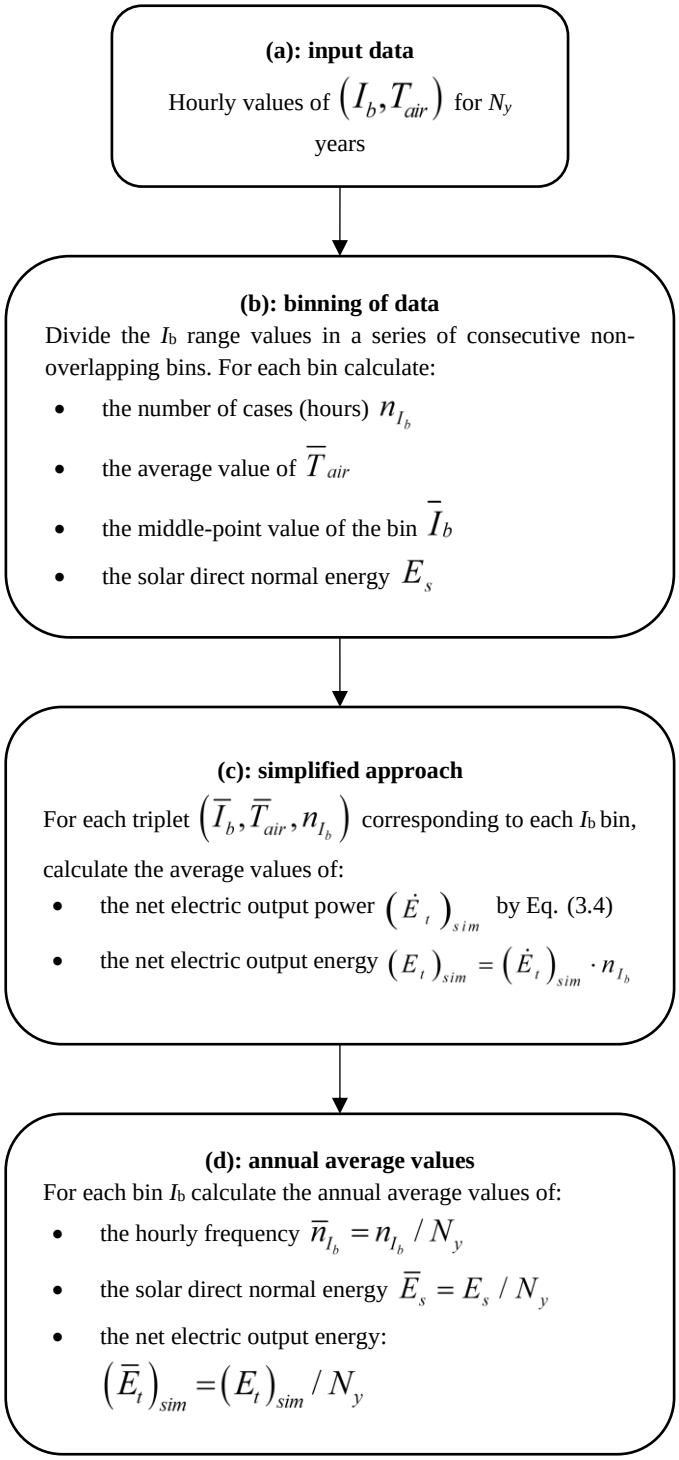

Figure 18. The flowchart of the simplified calculation algorithm

3.3 *Artificial neural networks to predict electricity production of a dish-Stirling system by using real experimental data*

Several studies propose the energy modelling of solar power systems by Artificial Neural Networks (ANN) as an alternative to the analytical models developed and present in the literature. ANNs represent a valuable intelligent method for optimising and predicting the performance of buildings [83] and of various solar energy systems, such as solar collectors, solar-assisted heat pumps, solar air and water heaters, photovoltaic/thermal (PV/T) systems[84], [85], solar stills, solar cookers and solar dryers [86].

Referring to concentrating solar power systems, [87] assesses the energy performance of a dish-Stirling system considering its installation in Natal-RN, Brazil, and investigating four hybrid methods, including the Adaptive Neuro-Fuzzy Inference System (ANFIS) and Multiple Layer Perceptron (MLP), both trained with Particle Swarm Optimization (PSO) or Genetic Algorithm (GA). [88] compared the performance of two analytical methods and one based on neural networks to assess the hourly electrical production of a parabolic trough solar plant (PTSTPP) located in Ain Beni-Mathar in eastern Morocco. Simulations conducted using an annual series of operating data showed that the performance of the ANN model was better than that of the analytical models analysed. [89] demonstrates the effectiveness of a model based on a feed-forward artificial neural network optimised with particle swarm optimisation to predict the power output of the solar Stirling heat engine, using first input data from literature and then experimental data.

In this part of the thesis, different Artificial Neural Networks (ANN) are investigated and trained to predict the energy performance of an existing demo dish-Stirling solar concentrator installed on the university campus in Palermo. To this aim, employing the open-source platform TensorFlow, two different classes of feedforward neural networks, Multi-Layer Perceptron (MLP) and Radial Basis Function (RBF), were developed and validated using a set of experimental input data collected during the real operation period of the cited system. The two different classes of networks were tested by varying the number of neurons (depth and computing resources involved) and other sensitive parameters in order to identify the best possible architecture. Finally, the

predictive performance of the networks was compared with a previously developed analytical model.

3.3.1 Novelties

The aleatory nature of the solar energy source and the need to have available power generation plants that ensure the dispatchability of the resource and make the energy supply secure, drive toward the development of reliable energy prediction tools. Especially in the case of plants not yet fully mature from the commercial point of view, such as dish-Stirling plants here investigated, their diffusion cannot disregard the development of a predictive model that considers the most influencing environmental and technical variables.

The work described below is characterized by some notable innovative aspects that integrate the latest scientific knowledge in this field.

- The numerical models investigated are based on a collection of experimental data obtained from the real operation of a prototype dish-Stirling solar concentrator installed at the campus of the University of Palermo. The direct availability of such data, in the case of the aforementioned technology, is not common and several studies are exclusively theoretical, such as in [90], [91], [92], and [93]. Also, in the case of the application of artificial intelligence techniques, sometimes the data used are mainly obtained from other analytical or numerical models and not from experimental measurement campaigns [87].
- One of the most important characteristics of the following research is that the tools that were used to develop the proposed models are explicitly stated and belong to the category of open-source software (Python and TensorFlow), ensuring absolute replicability of the algorithms by the scientific community. This feature is not particularly common in previous literature, in fact, even if tools are declared, it is still not possible to faithfully reproduce the models as they lack a multitude of details typical of proprietary software, such as in [94], [88], and [89].
- To allow users to replicate and possibly upgrade the proposed models, our work provides among the supplementary material all the necessary

instructions to perform a reliable prediction, which can be carried out from a single input record or a set of input data records. In addition, the accurate description of each coding step allows even an inexperienced programming user to quickly learn how to use the proposed methodology.

- Finally, a further innovative element with respect to other models already available consists in the use of an input parameter representing the level of cleanliness of the mirrors. Such parameter has been shown to be among the most influencing the energy production of the system [22].

The combination of such innovative features could make this research an effective tool able to encourage the promotion of dish-Stirling systems among other CSP technologies.

3.3.2 The Experimental set-up

This research proposes a neural approach to predict the electric energy production of a dish-Stirling solar concentrator at a specific selected installation site. The reference system and its real operational data that were considered for the development of a neural prediction model is the demo commercial dish-Stirling solar concentrator installed on the university campus of Palermo which was described in *Paragraph 2.5 "Reference dish-Stirling system".*

As mentioned in *Paragraph 2.5.2 "Experimental measurement campaign"*, during 165 days ranging from 5 January 2018 to 2 July 2018, the monitoring system acquired 14,256,000 records (on a second-by-second basis). Obviously, a large proportion of these records relate to events when the plant was not operating because they correspond to the night periods or day periods affected by weather conditions that were unsuitable for plant operation or to periods when the plant was under maintenance. The records relating to the remaining events were further aggregated with a simple average operation by single minutes, thus obtaining 7,971 records (data on a minute basis). The main observed and recorded variables by the monitoring systems of the CSP plant are listed and briefly described in *Table 3.*

Table 3. All monitored variables of the CSP system

Parameter	Description	Unit
Clean day	Number of days since the last mirror cleaning event	-
Direct Normal Irradiance	Beam solar radiation incident per unit area by the reflector	$W \cdot m^{-2}$
Global Horizontal Irradiance	Global solar radiation incident per unit area by the reflector	$W \cdot m^{-2}$
Diffuse Horizontal Irradiance	Diffuse solar radiation incident per unit area by the reflector	$W \cdot m^{-2}$
Ambient Temperature	Outdoor air temperature	°C
Average Wind Speed	Average wind speed on site	$m \cdot s^{-1}$
Wind Speed	Wind speed on site	$m \cdot s^{-1}$
Wind Direction	Wind direction on site	degree
Humidity	Relative humidity of external air	%
Air Pressure	Outdoor air pressure	mbar
Solar azimuth	Instantaneous position of the Sun respect to the south direction	degree
Solar elevation	Instantaneous position of the sun respect to the horizontal plane	degree
Total CSP net power output	Instantaneous power output of CSP less parasitic consumption	W

In *Figure 19*, some preliminary statistical analyses on some of the most important variables of the original dataset are presented. The Pearson coefficient (ρ_p) illustrated in *Figure 19* shows that the net electrical power output of the dish-Stirling system is strongly correlated with the DNI.

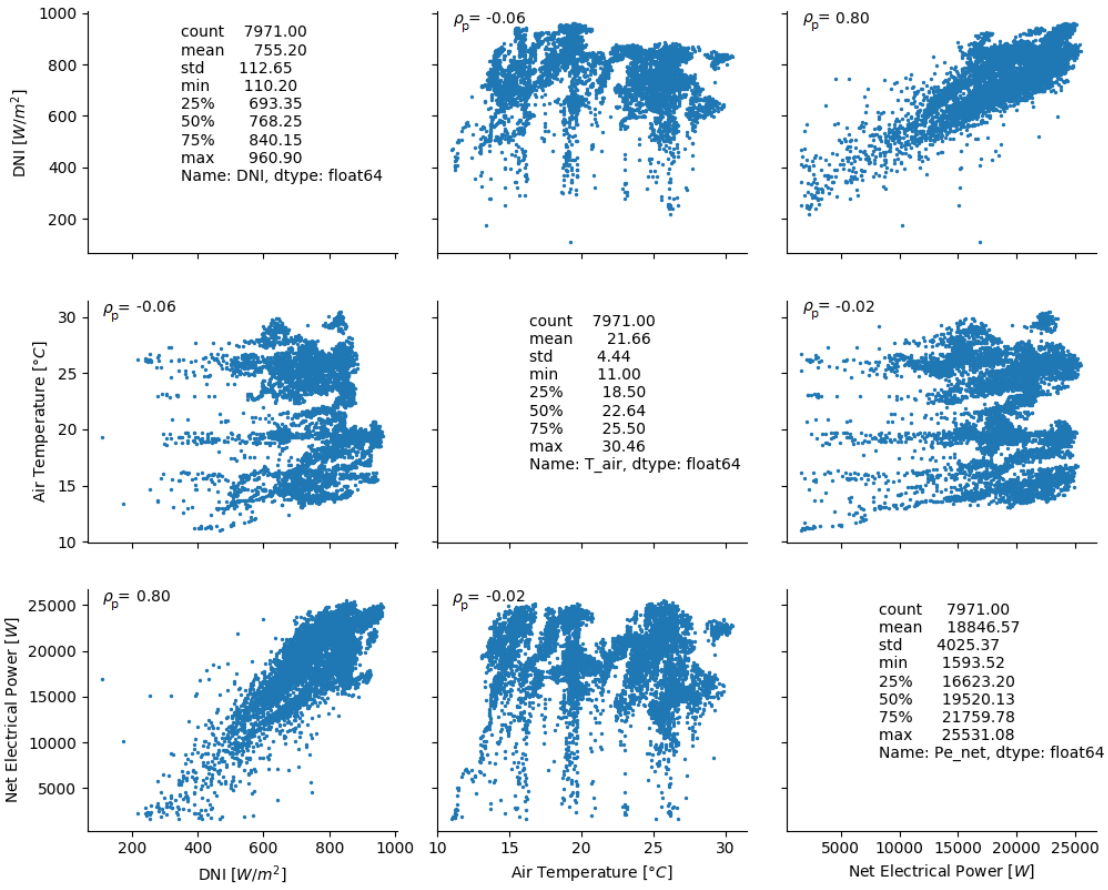

Figure 19. Statistical analysis of the original dataset

3.3.2.1 Outlier removal procedure

As is usually the case, any population of samples or data can exhibit large deviations, meaning anomaly points or individual data points that deviate significantly from the rest of the distribution data. These data points are called outliers. The presence of outliers in a dataset can be due to a variety of factors, such as the experimental nature of the same data, human or measurement instrument errors, or wrong data handling; therefore, they are to be considered normal. In order to prevent outliers in the dataset from affecting the performance of any model to be developed, it is common practice to preliminarily identify and remove them to reduce the variability of the input dataset. Outliers can be either univariate or multivariate, depending on whether it is possible to identify them by observing a distribution of values in a single-dimensional space or an n-

dimensional space. Obviously, in the latter case, the removal of outliers requires the training of an appropriate model able to replace the human brain. Several techniques are useful for detecting outliers in a dataset, of which the most widely used is the Z-score. The Z-score method uses standard deviation to identify outliers in a dataset with a Gaussian distribution (or whose distribution is assumed to be Gaussian). Such a statistical quantity is a measure of how the observed data deviates from the most probably occurring data in the dataset, in other words, the mean of the data. Referring to a Gaussian distribution of the data, the standard deviation (σ) is defined by relation (a) in *Equation (3.5)* below:

$$\begin{cases} \sigma = \sqrt{\dfrac{\sum_{i=1}^{N}\left(x_i - \overline{x}\right)^2}{N-1}} & \text{(a)} \\ \overline{x} = \dfrac{1}{N}\sum_{i=1}^{N} x_i & \text{(b)} \end{cases} \tag{3.5}$$

where: N is the number of records in the dataset, x_i is the *i*-th record in the dataset, and $\overline{x}$ is the mean of the data (see relation (b) in *Equation (3.5)*). Thus, the Z-score (z) can be calculated by *Equation (3.6)* as:

$$z = \frac{x_i - \overline{x}}{\sigma} \tag{3.6}$$

In our case, the Z-score technique was applied considering three variables from the dataset, which are: the DNI, the net electric output power, and the outdoor air temperature. According to the Gaussian distribution of the data, all records falling within the range of extremes were considered. The resulting filtered dataset includes 7417 records, approximately 93% of the originally available valid data.

3.3.2.2 Statistical analysis of input datasets

To describe and define the dataset purified of outliers, a statistical analysis was carried out investigating the quantities that are listed and explained in *Table 4*. These quantities were calculated for each variable of the original dataset without outliers, including 7417 records, and are summarised in

Table 5 below.

Table 4. Summary of all used statistical quantities

Statistical quantity	Description	Formula
Arithmetic mean	the sum of a set of values divided by the number of values in the set	Eq. 2.b
Variance	measures how much a set of values quadratically deviates from its arithmetic mean	$\sigma^2 = \frac{1}{N}\sum_{i=1}^{N}(x_i - \overline{x})^2$
Standard deviation	a measure of how much a set of values deviates from their arithmetic mean	Eq. 2.a
Standard error	a measure of how much the sample statistic (i.e. sample mean) deviates from the actual population mean	$se = \frac{\sigma}{\sqrt{N}}$
Skewness	a measure of the asymmetry of the probability distribution of the data	$\frac{N}{(N-1)(N-2)}\frac{1}{\sigma^3}\sum_{i=1}^{N}(x_i - \overline{x})^3$
Kurtosis	a measure of the thickness of tails or the flattening of a probability distribution	$\frac{(N+1)N}{(N-1)(N-2)(N-3)}\frac{\sum_{i=1}^{N}(x_i - \overline{x})^4}{\sigma^4} - 3\frac{(N-1)^2}{(N-2)(N-3)}$

Table 5. A preliminary statistical analysis of the dataset without outliers (number of samples = 7417)

Variable	Max value	Arithmetic mean	Variance	Standard deviation	Standard Error	Skewness	Kurtosis
Clean day	131	46.61	1533	39.15	0.45	0.74	-0.95
Direct Normal Irradiance	957.17	774.63	7399.4	86.02	0.99	-0.14	-0.75
Global Horizontal Irradiance	1118	765.95	27869	166.44	1.94	-0.73	-0.49

Variable	Max value	Arithmetic mean	Variance	Standard deviation	Standard Error	Skewness	Kurtosis
Diffuse Horizontal Irradiance	512.2	157.06	4022.8	63.43	0.73	1	1.85
Ambient Temperature	30.46	21.77	18.93	4.35	0.05	-0.26	-1.12
Average Wind Speed	10.29	2.87	1.76	1.33	0.01	1.12	2.94
Wind Speed	11.43	3.13	2.08	1.44	0.02	1.23	3.38
Wind Direction	340.65	145.32	5576.3	74.67	0.87	0.94	-0.59
Humidity	71	52.15	90.45	9.51	0.11	-0.19	-1.06
Air Pressure	1026.1	1006.7	34.85	5.90	0.06	0.57	1.87
Solar azimuth	265.05	167.99	2512.3	50.12	0.58	0.17	-1.20
Solar elevation	75.42	54.04	217.07	14.73	0.17	-0.35	-1.05
Total CSP net power output	25531	19516	9.65E+6	3107.8	36.08	-0.36	-0.63

The full input dataset of 7417 samples is always randomly split to obtain an input dataset for the training/validation process of the neural networks and another input dataset to be used for the test process of the same neural networks: the training/validation dataset includes 85% of the original data; the test dataset resembles the other 15%. Preliminary statistical analysis of the data made it possible to evaluate the correlation coefficients between each of the variables covered and the results are exemplified by *Figure 20*.

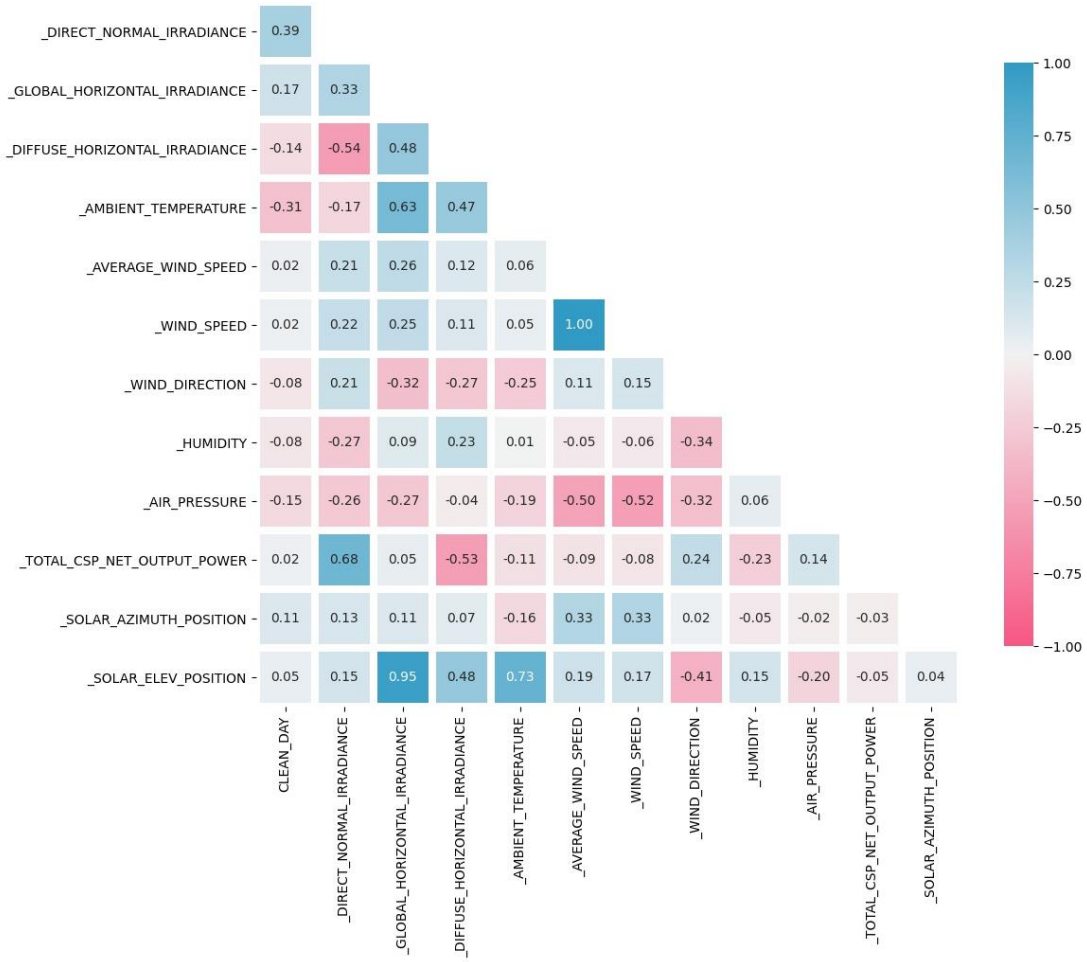

Figure 20. Correlation matrix of variables of the original dataset without outliers (Pearson correlation coefficient)

To avoid any form of direct influence or manipulation in order to improve the predictive performance of the developed neural models, training/validation and test data sets are autonomously extracted by the software in random mode from the set of data monitored on our prototype system. Therefore, no filter or algorithm was applied for the above splitting operation except for the removal of outliers. In this sense a punctual data used for the training/validation of the network will never be used to validate the results and vice versa. Although, in theory it could happen that a point data is used for the training/validation phase and the one immediately following in time it is used for test, it is necessary to underline that we have not applied algorithms specifically indicated for time series. The data, before being used, are in fact purposely remixed eliminating any

temporal succession. In addition, the operation of the dish-Stirling is characterized by an extreme and fast variability due to a continuous variability of weather and solar parameters.

3.3.3 Artificial neural network models

3.3.3.1 Machine learning deployment using TensorFlow and Python

In recent years, the use of neural network technologies and algorithms applied to physical and engineering problems has become increasingly common, and software companies have made increasingly sophisticated tools available for analysing complex systems. However, such software has often required the user to have detailed knowledge of artificial intelligence, which has slowed the spread of these interesting methodologies. The cost of purchasing such software has been another limiting factor for the spread of machine learning techniques. The diffusion of open-source libraries characterised by high reliability and effectiveness has facilitated the success of this ground-breaking technology. In this context, Google's TensorFlow 2 library represents an extremely powerful free tool, but at the same time, it is characterised by extreme ease of use for the production of machine learning algorithms in several programming environments [95]. For the development of the models described below, it was used Python code language, which is very well suited to some of the particular functionalities of TensorFlow 2 [96], such as saving and restoring the state of a neural network in order to predict at a time following the training of the network itself [97]. Python is a programming language developed in the 1990s that is particularly suited to the development of applications that rely on numerical computation. It is free of charge and is available for a wide range of operating systems, a feature that has made it particularly popular in academic circles [98], [99]. All the machine learning models described below, therefore, use libraries and environments that are completely free and reusable, for absolute transparency and replicability of the results.

3.3.3.2 Artificial neural networks

The Artificial Neural Network (ANN) is a powerful tool whose sophisticated rationale is inspired by the way the human brain analyses and elaborates information

[100]. ANNs are largely used for modelling, prediction, assessment, and optimisation of the performance of many different engineering technologies, which often require the solving of complex and non-linear problems, such as solar energy systems. Essentially, ANNs are learning machines made up of different processing elements, also called neurons. Starting from input information, ANNs elaborate output signals and transfer them to other processing elements through interconnections according to the network topology. Indeed, each neuron can receive connections from others or even from itself. The signals are propagated and scaled by weights characteristic also of the interconnection. Finally, a processing element sums all of these signals and produces an output signal that is a non-linear function of the sum (see *Figure 21*) [101].

In this part of the thesis, from all the different types of ANNs, the Multilayer Perceptron (MLP) and the Radial Basis Function (RBF) models were selected. These models, suitable for solving classification problems, are defined as feed-forward networks since the interconnections between the neurons do not form loops, but the propagation of the signal is unidirectional (running from the input neurons to the output neurons of the network).

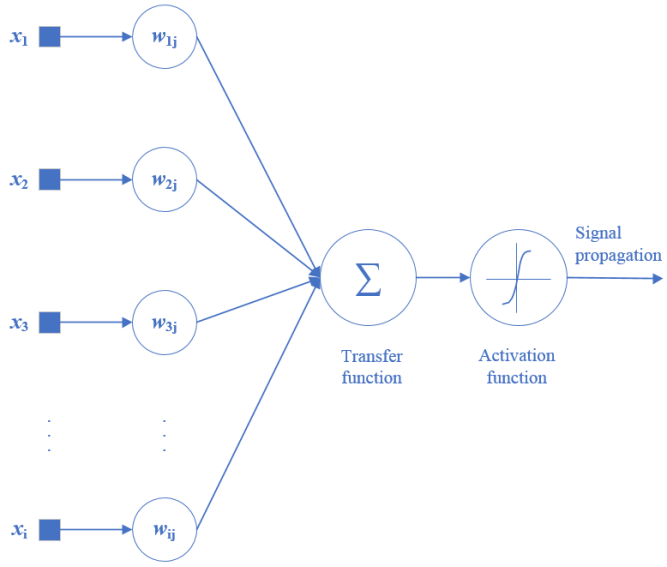

Figure 21. Simplified scheme of an artificial neuron

The MLP neural network (see *Figure 22*.a) consists of several layers in which the neurons are ordered, namely: an input layer comprising the neurons that receive the input information to the network; several hidden layers, so-called because their activation

functions are not directly accessible from outside of the network; and finally, an output layer that transmits the final output signal. Each neuron of the hidden layer attributes a bias that it adds to the sum of the weighted signals received from the neurons of the input layer and passes the results through a non-linear transformation. This last result becomes the input for the second hidden layer or for the output layer that replicates the same operations. The resulting transformed output from each neuron of the output layer is the output of the network. The network needs to be trained using an algorithm that adjusts the weights and biases in order to reduce global error [101]. The output ($\varphi_i(x)$) of each neuron of the hidden layer and the network output (y) are mathematically described by *Equation (3.7)* as:

$$\begin{cases} \varphi_i(x) = \zeta\left(\sum_k a_{ik} x_k + b_i\right) \\ y = \sum_i w_i \varphi_i \end{cases} \tag{3.7}$$

where: ζ is a non-linear function, a_{ik} is the weight of the first layer, x_k is the input information, b_i is the bias, and w_i is the weight of the output layer.

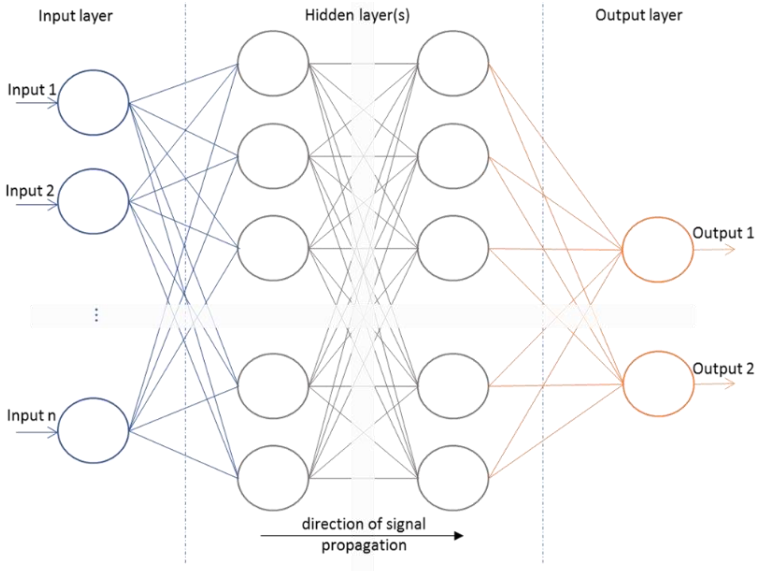

(a)

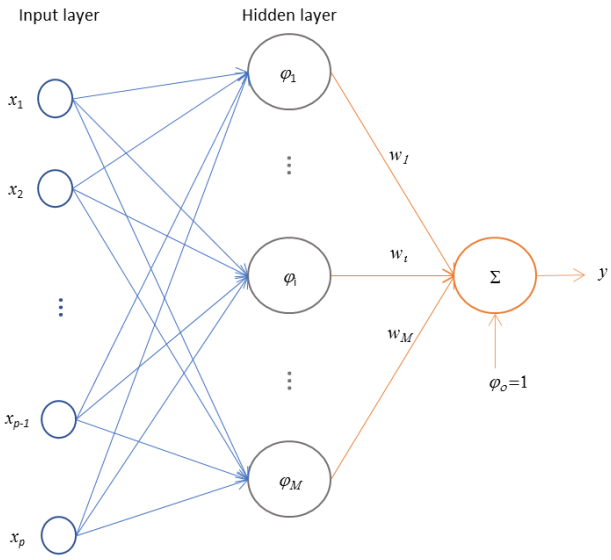

(b)

Figure 22. General architectures of ANNs: MLP (a) and RBF (b).

The architecture of a general RBF network (see *Figure 22.b*) consists of an input layer, a hidden layer and an output layer. Each neuron of the hidden layer has a vector of parameters called centre ($\boldsymbol{x}_i$), which is compared with the input vector ($\boldsymbol{x}$) of the network producing a radial-symmetric response [102]. The responses of the hidden layer are also scaled by the connection weights (w_i) to the output layer and then combined to generate the output of the network [103]. The output ($\varphi_i(\boldsymbol{x})$) of each neuron of the hidden layer and the network output (y) are mathematically described by *Equation (3.8)* as:

$$\begin{cases} \varphi_i(\boldsymbol{x}) = g\left(\left|\boldsymbol{x}-\boldsymbol{x}_i\right|\right) \\ y = \sum_i w_i \varphi_i \end{cases} \tag{3.8}$$

where $g(.)$ could be a Gaussian function [101].

Keras layers are the basic building blocks of neural networks in Keras, the opensource framework used in our research. A layer consists of a tensor-in tensor-out computation function (the layer's call method) and some state, held in TensorFlow variables (the layer's weights). While Keras offers a wide range of built-in layers, they do

not cover every possible use case. Indeed, Radial Basis Function layer was achieved by customising the already available layers in Keras [95,104].

3.3.4 Development of neural network models

This section defines the models and the description of the neural network architectures, both MLP and RBF, which were used for the prediction of the energy producibility of the analysed dish-Stirling plant. As indicated in *Table 6*, for both types of ANN models, the total net output power of the CSP is the only output variable of the networks, and two different datasets were defined for the input variables to these same networks: the first including twelve variables (long dataset) and the second one including only two variables (short dataset). It is important to highlight that the identification of a restricted group of variables, to be used in the training/validation phase, was carried out after a preliminary sensitivity analysis of the energy performance of the plant with respect to the environmental and operating conditions of the technology, also taking into account the physical features of the phenomena occurring in a CSP plant, such as the one investigated.

Two possible types of input datasets are presented in the research described here: long and short. The long dataset consists of all significant variables made available by our monitoring system. The short dataset, on the other hand, considers only the two climate variables that are necessary from the physical point of view to describe the energy balance and the related analytical model of dish-Stirling. The two possible datasets therefore delimit the widest interval within which the input variables can be selected.

For both MLP and RBF models, several neural network architectures characterised by different levels of depth were tested for each of the two datasets of variables defined. Specifically, the performance of each network architecture was investigated for four different depth levels, varying the number of neurons in the layers and the number of layers making up the neural network. Therefore, a total of 16 networks were trained, of which 8 were of the MLP type and the other 8 of the RBF type.

Table 6. Input and output variables of datasets implemented in both MLP and RBF neural network models

Long dataset	**Short dataset**
Input variables	
1. Direct Normal Irradiance	1. Direct Normal Irradiance
2. Ambient Temperature	2. Ambient Temperature
3. Clean day	
4. Global Horizontal Irradiance	
5. Diffuse Horizontal Irradiance	
6. Average Wind Speed	
7. Wind Speed	
8. Wind Direction	
9. Humidity	
10. Air Pressure	
11. Solar azimuth	
12. Solar elevation	
Output variables	
1. Total CSP net power output	1. Total CSP net power output

From this point on, for ease of writing and to better identify the different neural networks examined, each of them has been associated with the nomenclature X-Y-N, in which: X is a letter that indicates the level of depth of the network, which can be superficial (S), medium-deep (M), deep (D) or very deep (V); Y is an acronym that can be MLP or RBF depending on the type of neural network implemented; N is a number that can be equal to 2 or 12 depending on how many input variables were used. *Table 7* summarises the main characteristics of all 16 neural networks tested to predict the energy producibility of the dish-Stirling plant, reporting for each network: the number of layers, the number of neurons in each layer, and the total number of parameters involved in the training process.

Table 7. The main characteristics of all 16 neural networks tested

ANN code	Number of layers	Neurons	Trained parameters
S-MLP-2	4	2+20+5+1	181
S-MLP-12	4	12+50+10+1	1351
S-RBF-2	4	2+20+5+1	181
S-RBF-12	4	12+50+10+1	1351
M-MLP-2	4	2+40+20+1	971
M-MLP-12	4	12+150+30+1	6691
M-RBF-2	4	2+40+20+1	971
M-RBF-12	4	12+150+30+1	6691
D-MLP-2	5	2+140+300+80+1	66891
D-MLP-12	5	12+140+300+80+1	68461
D-RBF-2	5	2+140+300+80+1	66891
D-RBF-12	5	12+140+300+80+1	68461
V-MLP-2	8	2+130+200+400+700+100+50+1	462897
V-MLP-12	8	12+130+200+400+700+100+50+1	464371
V-RBF-2	8	2+130+200+400+700+100+50+1	462901
V-RBF-12	8	12+130+200+400+700+100+50+1	464371

3.3.5 Definition of performance measures

With the aim of assessing the quality and reliability of the neural models developed, several statistical indices were calculated starting from the test dataset, including the determination coefficient R-squared (see *Table 8*), which provides a synthetic measure of the goodness of the approximate function. This index can assume a value between 0 and 1 and indicates how far the predicted values deviate from the expected ones. Moreover, starting from the test dataset again, the Mean Absolute Error (MAE) (see *Table 8*) was produced for each trained neural network. The MAE is the average of the absolute differences between the prediction and the actual value of the

output variable of the neural network, providing information on the average magnitude of errors in a set of predictions, regardless of their direction.

Also, a statistical analysis of the resulting residuals was carried out after the test process of each neural network. Being residuals, (e_i) the set of differences was obtained by subtracting the actually measured values from those predicted as the output variable of the networks. The following quantities were then evaluated to examine the frequency distribution of these residuals: the mean value, the size of the test dataset (count), the standard deviation value, the minimum and maximum values, and quartiles at 25% (first quartile, Q_1), at 50% (second quartile, Q_2), and 75% (third quartile, Q_3). In order to graphically compare all the developed neural networks in terms of the accuracy of predicting the energy production of the dish-Stirling plant, the following graphs were produced for each of them:

- A histogram of residuals showing the distribution of residuals obtained by comparing the values of the electrical output power of the dish-Stirling system predicted against that measured. From this comparison, the mean (μ) and standard deviation (σ) values of the residuals were calculated and displayed. In general, it is expected that the distribution is centred on the value 0 and is close to a Gaussian distribution. However, in this graph, it is also possible to graphically compare the probability density distribution obtained with a normal distribution having the same mean value and the same standard deviation value.
- A Q–Q (quantile-quantile) plot, that is a probability plot, in which the probability distributions of the residuals obtained after the test process is compared with a normal distribution by plotting their quantiles against each other.
- A predicted versus measured graph showing points of coordinates expected and actual measured electrical output power values. In this graph, it is possible to appreciate, through the coefficient of determination R-squared (R^2), the spatial distribution of the points with respect to the bisector of the first quadrant, which represents an ideally perfect regression.

Table 8. Statistical quantities calculated on residuals

Statistical index	Symbol	Formula or definition
Coefficient of determination	R^2	$1-\frac{\sum_i e_i^2}{\sum_i (y_i-\mu)^2}$
Mean Absolute Error	MAE	$\frac{\sum_{i=1}^{C} \lvert y_i - m_i \rvert}{C}$
Count	C	Size of the test dataset
Mean	μ	$\frac{1}{C}\sum_{i=1}^{C} e_i$
Standard deviation	σ	$\sqrt{\frac{\sum_{i=1}^{C}(e_i-\bar{e})^2}{C-1}}$
Minimum	min	$\min(e_i)$
Maximum	max	$\max(e_i)$
Quartile at 25%	Q_1	Value for which the cumulative percentage frequency of the sample is at least 25%
Quartile at 50%	Q_2	Value for which the cumulative percentage frequency of the sample is at least 50%
Quartile at 75%	Q_3	Value for which the cumulative percentage frequency of the sample is at least 75%

3.3.6 Results and discussion

3.3.6.1 Performance of neural networks model

In general, in the scientific literature, when neural networks are used as function approximators, it is very common to use RBF-type architectures [102]. However, neural networks with MLP-type architecture are an excellent function approximator because they can replicate any type of mathematical function [101]. As can be noted from *Table 9*, which summarises all the statistical variables calculated to assess the prediction accuracy obtained by the 16 neural networks developed, the results showed that the modelling approach through RBF did not prove to be the most efficient in this analysis.

Conversely, neural networks based on an MLP-type architecture always led to better results, both when varying the level of depth of the network and when varying the number of input variables to the neural network.

Table 9. Values of all statistical quantities calculated on residuals resulting from the test process of all 16 neural networks tested

ANN code	R^2	MAE	μ	σ	min	max	Q_1	Q_2	Q_3
S-MLP-2	0.57	1597.8	-191.4	2038.6	-8113.1	5141	-11198.2	-22.4	1234
S-MLP-12	0.92	599.8	68.0	872.8	-4827.7	6164.7	-323.1	107.1	509.5
S-RBF-2	0.55	1650.5	7.4	2065.1	-6563.9	4908.6	-1320.3	173.2	1474.1
S-RBF-12	0.80	964.1	19.5	1341.9	-7987.8	8043.8	-630.6	46.7	705.9
M-MLP-2	0.63	1325.1	-148.2	1891.9	-8370.4	4382	-777.2	9.8	946.7
M-MLP-12	0.94	465.9	-5.5	720.8	-7290	3536.8	-281.3	59.5	390.9
M-RBF-2	0.62	1375.5	-250.7	1956.2	-8494.6	4800.2	-909.3	35.7	836.6
M-RBF-12	0.85	795.1	-62.9	1167.7	-5386.1	5695.8	-583.8	-44	451.2
D-MLP-2	0.72	1059.4	-99.4	1633.2	-7544.2	6653.0	-634.6	-17.8	576
D-MLP-12	0.95	419.7	-58.4	653	-6596.8	3117.6	-335	-21.1	285.7
D-RBF-2	0.70	1047.2	-39.3	1671.5	-7516.9	6034.8	-506.8	44.4	585.1
D-RBF-12	0.94	458.5	-87.1	695.7	-5627.9	6163.3	-362.4	-15.6	317.5
V-MLP-2	0.76	904.8	-124.6	1546.9	-9183.2	6220.4	-518.4	-28.1	385.2
V-MLP-12	0.98	306.9	-50.9	421	-3050.8	2484.5	-275.2	-45.0	205.4
V-RBF-2	0.73	936.2	91.7	1615.2	-8514.5	7946.0	-421.5	22.1	476.2
V-RBF-12	0.95	420	-66.7	682	-5950.3	7282.2	-353.6	-29.4	241.3

Furthermore, for the same type of architecture (MLP and RBF) and the number of input variables, it can be seen from *Table 10* that increasing the depth of the network and, in parallel, increasing their complexity (in terms of the number of neurons) generally

leads to better performance but longer training times (see *Table 9*). For this reason, the authors did not consider appropriate to experiment even more complex network architectures.

Table 10 shows the total time it took to train the different models and the speed evaluated in training epochs per second. Furthermore, it is important to underline that too many input parameters can theoretically degrade the predictive performance of a neural network and require excessive computational resources. In order to consciously guide the reader in the choice of the number of input variables, we have for the sake of argument provided in *Table 10* the time required for proper training of each neural model presented. Naturally, once properly trained, the networks are able to perform prediction virtually instantaneously.

Table 10. Training time and velocity of all 16 neural network tested by an i7 CPU with 32 GB of RAM

ANN code	Elapsed time [s]	Velocity [epoch/s]
S-MLP-2	1662	0.487
S-MLP-12	2607	0.500
S-RBF-2	711	0.555
S-RBF-12	454	0.603
M-MLP-2	1558	0.217
M-MLP-12	1221	0.300
M-RBF-2	1613	0.203
M-RBF-12	1074	0.458
D-MLP-2	1595	0.333
D-MLP-12	1215	0.341
D-RBF-2	2505	0.385
D-RBF-12	1662	0.480
V-MLP-2	15731	0.507
V-MLP-12	5848	0.506
V-RBF-2	21877	1.653
V-RBF-12	5078	0.327

The coefficients of determination (see R^2 in *Table 9*) calculated for neural networks using synthetic input datasets (short datasets including two input variables) fall within a range of values between 0.55 and 0.76. On the other hand, the neural networks using 12 input parameters (long dataset of input variables), specifically including the variable providing the number of days since the last cleaning event of the reflecting mirrors (Clean day – see *Table 6*), allow the achievement of much better results in terms of R-squared, falling in the range of values between 0.80 and 0.98. Generally, the best performance tested neural networks have the following codes: V-MLP-2 and V-MLP-12. Of these, the first neural network uses the short dataset with two input variables, and the second neural network uses the long dataset with 12 input variables. However, both of the selected best neural networks have an MLP type architecture.

Referring to the best-performance neural network with the code V-MLP-2, Figure 23, Figure 24 and Figure 25 show: the frequency distribution of the residuals, the plot of the distribution of the quartiles of the residuals with respect to normal, and the plot of the predicted values compared to the measured ones, respectively. The quantile-quantile (q-q) plot is a graphical technique to compare the shapes of distributions. Specifically, by observing the frequency distributions of the residuals and quartiles (see Figure 23 and Figure 24), it is possible to appreciate how close these distributions are to normal ones. In Figure 23 and Figure 26 in blue are indicated the probability densities of residuals; the dashed yellow line indicates the shape of the theoretical normal distribution.

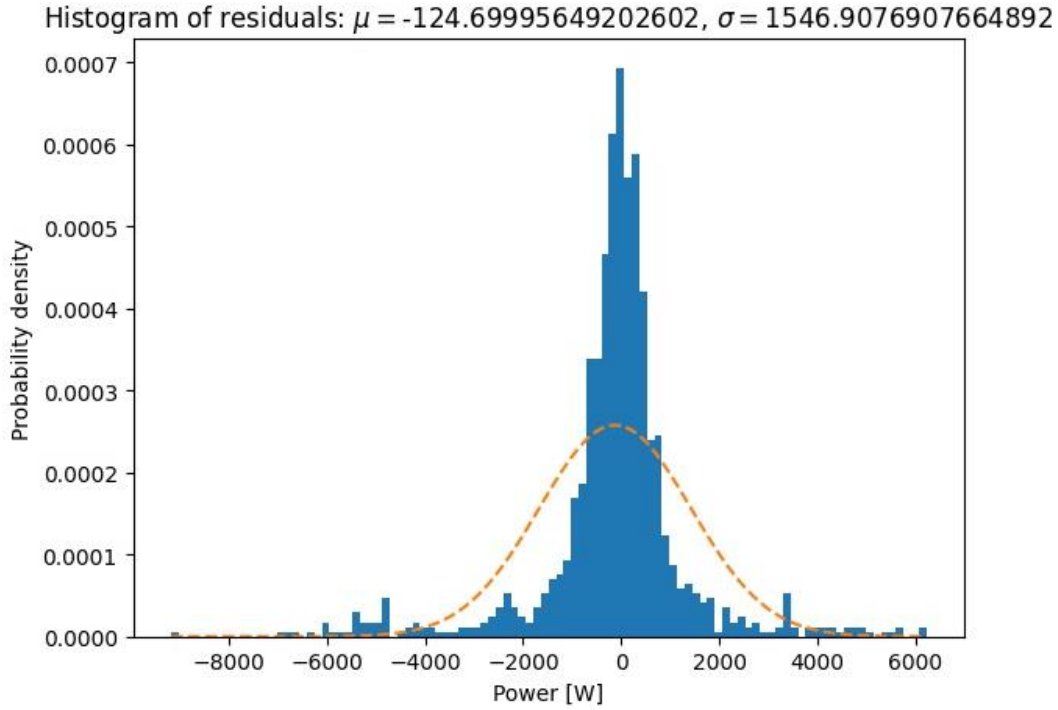

Figure 23. Histogram of residuals showing the probability density distribution of residuals resulting from the test process of V-MLP-2

In *Figure 24* and *Figure 27* in blue are indicated the probability plot of predicted values; the continuous red line indicates the shape of the theoretical optimum distribution.

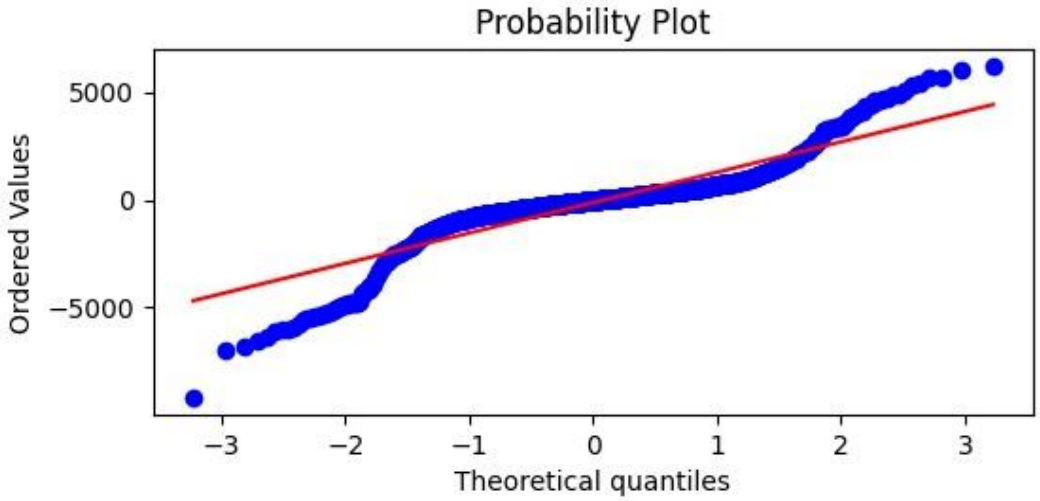

Figure 24. A Q–Q (quantile-quantile) plot resulting from the test process of V-MLP-2

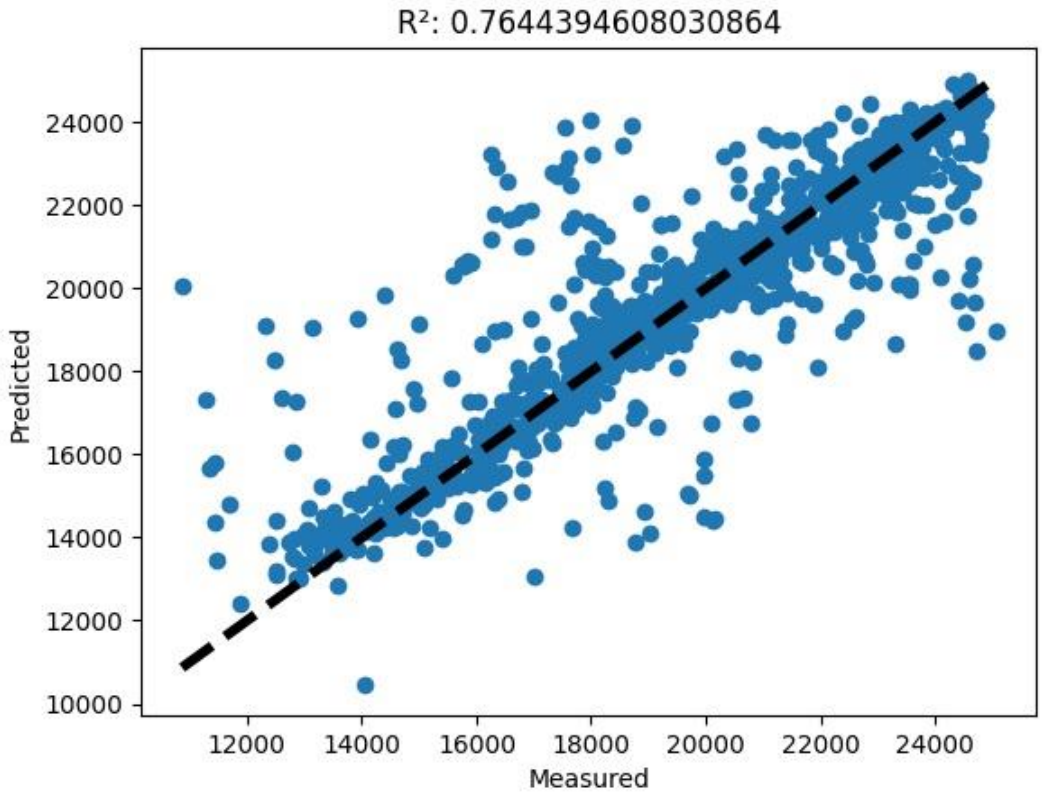

Figure 25. A predicted versus measured power output [W] resulting from the test process of V-MLP-2

Similar to what was carried out for the best performance neural network with 2 input variables, the same graphs (see Figure 26, Figure 27, and Figure 28) were also produced for the best performance neural network that uses the long dataset of input variables, which is also the best of all developed ANNs. It is possible to appreciate how both the frequency distribution of residuals (see Figure 26) and the distribution of quartiles (see Figure 27) closely approximate the normal distribution, ensuring high reliability of the model in predicting the net electric output power of the dish-Stirling system.

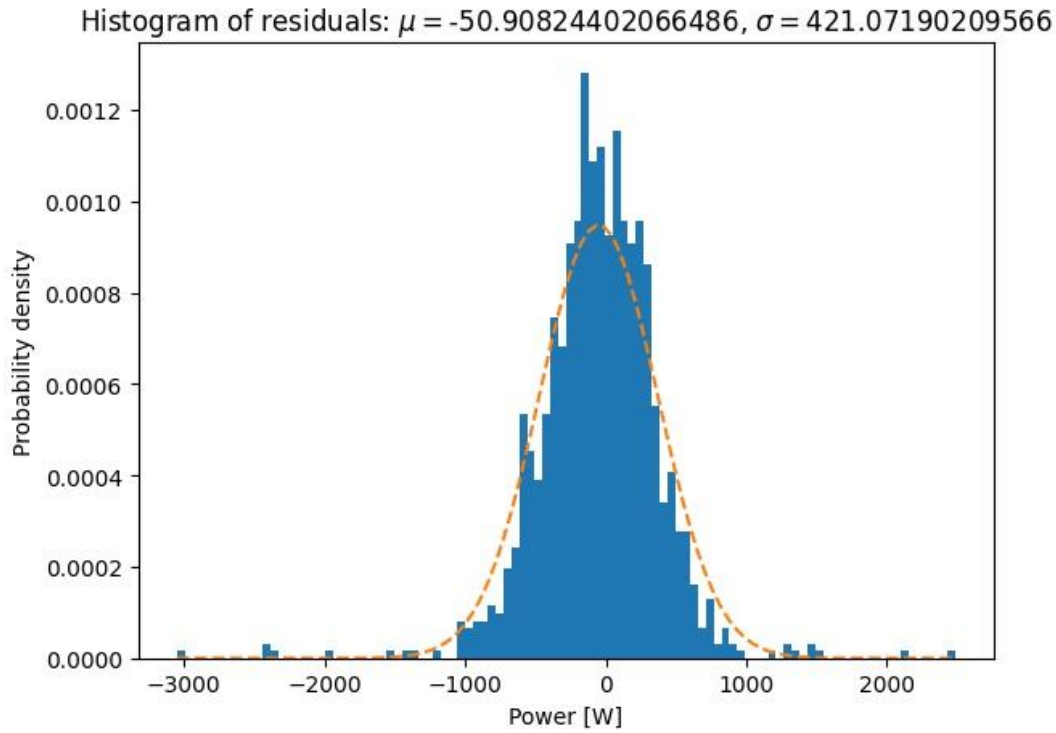

Figure 26. Histogram of residuals showing the probability density distribution of residuals resulting from the test process of V-MLP-12

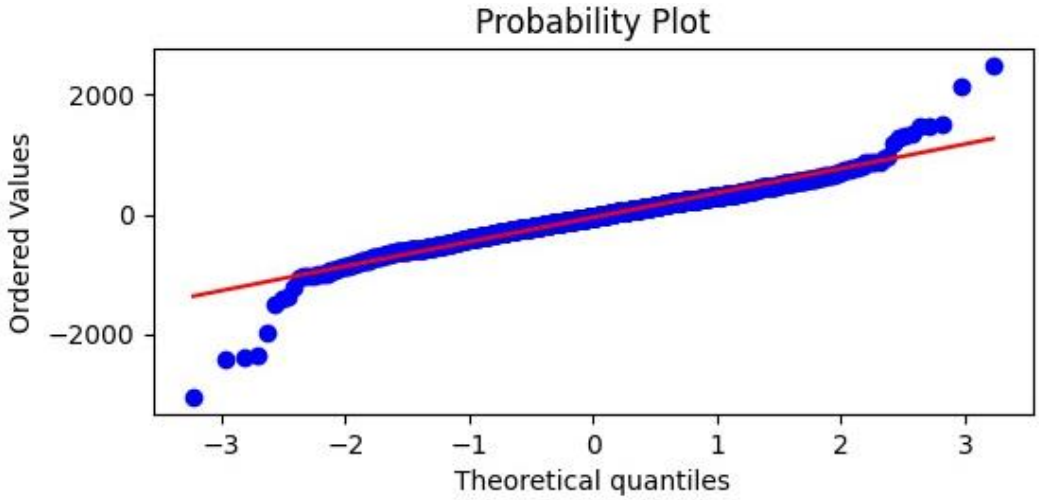

Figure 27. A Q–Q (quantile-quantile) plot resulting from the test process of V-MLP-12

Finally, *Figure 25* (above) and *Figure 28* below, showing the predicted values of the net electric output power of the dish-Stirling system versus those measured (blue

points), clearly demonstrates the high accuracy of the developed and proposed predictive models (the dashed black line indicates where the points of a perfect forecast should lie).

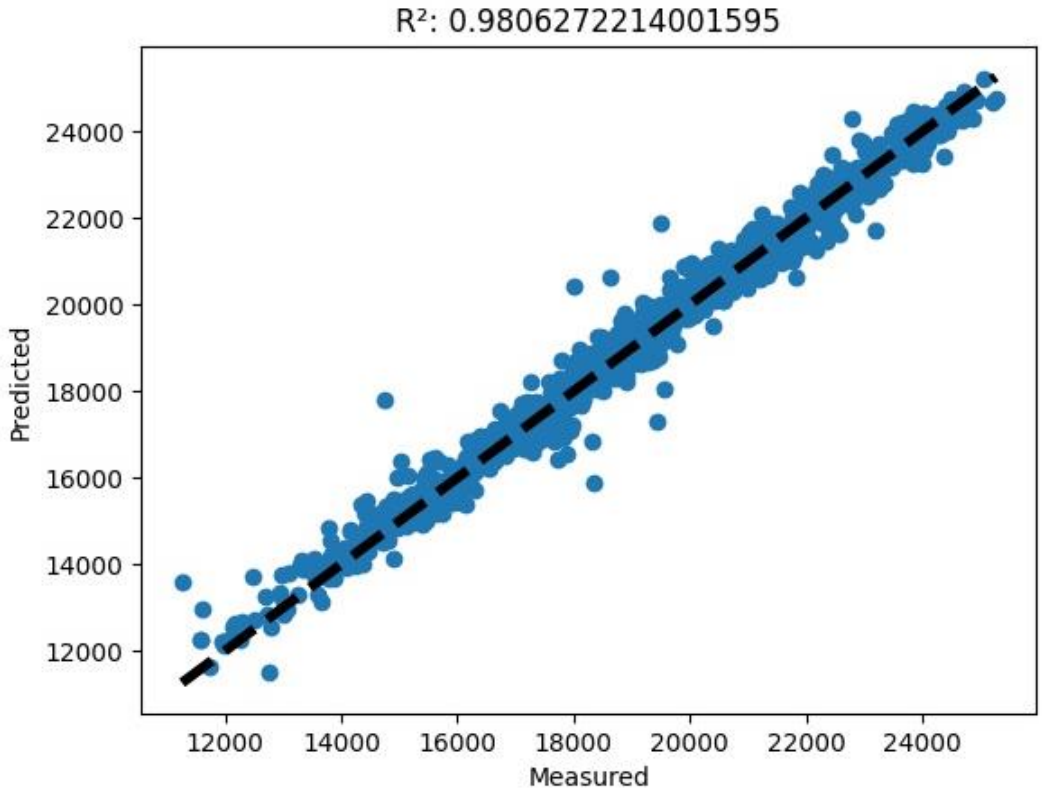

Figure 28. A predicted versus measured graph resulting from the test process of V-MLP-12

3.3.6.2 Comparison with an analytical model

In order to better characterise the predictive performance of the neural models presented above, we compared the results achieved with those obtained through the application of a very recent analytical model based on the same initial experimental data described in *Paragraph 3.1 "A validated energy model of a solar dish-Stirling system considering the cleanliness of mirrors"* [22]. It should be noted that the stochastic nature of the algorithms used makes the input dataset for the neural network, both for the training/validation and test phases, a subset of that used to test the performance of the aforementioned analytical model. In the best conditions, as it is possible to see in *Figure 29* below, both models, the analytical one and the neural one, hit the target of correctly

calculating the energy production of a dish-Stirling plant, with a slight prominence of the neural model that, as already anticipated, gives a determination coefficient of 0.98.

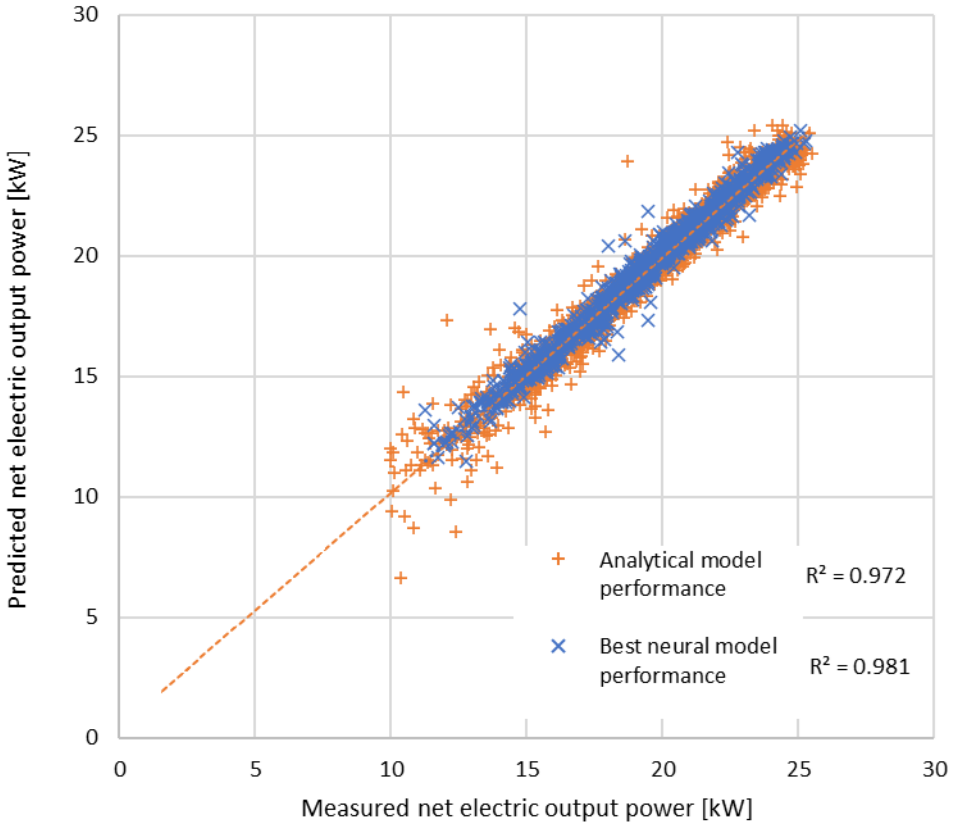

Figure 29. Performance comparison between analytical and the best neural network models, V-MLP-12 [22]

As it is easily observable from the *Figure 29*, the number of the points in the diagram predicted vs measured referable to the neural model is inferior to that referable to the analytical model. This condition derives from the fact that, in order not to overestimate the predictive performances of the neural model, only the points belonging to the test dataset were used, that is only 15% of the total. As regards the analytical model, instead, all the available points have been correctly used. Although it is theoretically possible to apply the analytical model only to the points belonging to the test dataset of the neural network, this procedure is impractical and of doubtful utility since the test dataset is selected in random mode and changes every time the training/validation script of the neural network is executed and for each neural network. The reader should also note that the outlier removal procedure in fact removed from the initial experimental

dataset the data concerning the low-power regimes of the dish-Stirling plant. These data were considered outliers because they were characterised by particularly extreme and fast irradiance variations, typical of extremely disturbed cloud cover days. On the other hand, the low generated power values in the range 2-11 kW induced by rapid variability of cloud cover would in any case be unreliable as starting data because they would be disturbed by continuous restarts of the Stirling engine driven by the related electric motor.

3.3.7 Conclusions about the use of artificial neural networks

The analysis here presented aims to test and optimise a forecasting model for the energy performance of a dish-Stirling solar concentrating plant based upon the use of artificial neural networks. Contrary to most of the models already tested in the most recent literature in this scientific sector, the data used for the training/validation phase of the networks are real data coming from a monitoring campaign of a real working plant on the university campus in Palermo. Neural networks of different architectures and sizes were also tested to better understand the link between the complexity and quality of the obtained results. All the different tested network architectures were trained alternately with 2 inputs (in the case of only standard data such as DNI and external temperature being available) and 12 inputs (in the case more complete climatic data are available). A further reason for the novelty is the introduction among the input variables of information regarding the cleaning of the reflector mirrors, never before tested in this type of model. The results made it possible to appreciate the good performance of the MLP models compared to the RBF models, traditionally characterised by better performance in the approximation of functions. Compared to a modern analytical model already developed, the best of the developed neural models obtained an even higher determination index between expected and calculated results, with a value equal to 0.98. The comparison is not therefore to be considered singularly but it is useful to understand how a sophisticated neural network can be equivalent and sometimes superior to analytical models. Results confirm the maximum reliability of the developed ANN models. A neural model already trained together with the same input data used are made available as attachments in “Supplementary data”. Together with the digital neural model is directly provided the script in Python language, allowing maximum transparency of the algorithms described

in the research work. The availability of the dataset and the used Python scripts allow, thanks to the exclusive use of open software, maximum transparency and replicability. Finally, it should be noted that the results of the best of the neural networks tested (V-MLP-12) are better, in terms of coefficient of determination than one of the most advanced and performing analytical models already developed. Further improvements in the performance of the neural network models could be achieved by using different activation functions and different optimisers (fine-tuning), using the python script and dataset provided as a complement to this study.

Nomenclature

a_1	slope of the linear relation between $\dot{W}_S$ and R_T [-]
a_2	intercept of the linear relation between $\dot{W}_S$ and R_T [W]
a_{ik}	weight of the first layer in a MLP neural network
A_n	net surface of the paraboloidal reflector [m²]
A_r	aperture area of the cavity receiver [m²]
b_i	bias value
C	size of the test dataset
e	mean value of residuals
e_i	i-th value of residuals
$\dot{E}_n$	net electrical power output of the dish-Stirling system [W]
$\dot{E}_{n,pred}$	predicted value of net electrical power output of the system [W]
$\dot{E}_{n,mis}$	measured value of net electrical power output of the system [W]
$\dot{E}_p^{ave}$	average power absorbed by the parasitic components [W]
$\dot{E}_p$	total parasitic absorption power [W]
E_s	solar direct normal energy corresponding to each I_b bin [kWh/m²]
$\overline{E}_s$	annual average values solar direct normal energy [kWh]
$(E_t)_{sim}$	annual electric output energy from simplified approach [kWh]
$\left(\overline{E}_t\right)_{sim}$	average annual electricity from the simplified approach [kWh]
$\left(\dot{E}_t\right)_{sim}$	annual electric power output from the simplified approach [W]
g	Gaussian function
I_b	solar beam radiation [W/m²]
$\overline{I}_b$	the middle-point value of the I_b bin [W/m^2]
N_y	number of years of the time series of meteorological data
N	number of records in the dataset
n_{I_b}	number of cases falling into each I_b bin [h]

$\overline{n}_{I_b}$	annual average values of n_{I_b} [h]
m_i	*i*-th of the measured values
R^2	coefficient of determination
R_T	temperature correction factor [-]
Q_1	first quartile of the frequency distribution of residuals
Q_2	second quartile of the frequency distribution of residuals
Q_3	third quartile of the frequency distribution of residuals
$\dot{Q}_{r,out}$	thermal power dissipated by the receiver [W]
$\dot{Q}_{S,in}$	thermal input power of the Stirling engine [W]
$\dot{Q}_{S,in}^{max}$	maximum thermal input power of the Stirling engine [W]
$\dot{Q}_{S,in}^{min}$	minimum thermal input power of the Stirling engine [W]
se	standard error
T_0	reference temperature [K]
T_{air}	external ambient air temperature [K]
$\overline{T}_{air}$	average air temperature of each I_b bin [K]
T_h	heat input temperature of the engine working fluid [K]
T_r^{ave}	average receiver temperature [K]
T_{sky}	effective sky temperature [K]
w_i	weight of the output layer
$\dot{W}_S$	mechanical output power of the Stirling engine [W]
$\overline{x}$	mean of the data
$\boldsymbol{x}$	vector of input data to the neural network
$\boldsymbol{x_i}$	vector of parameters of each neuron of a hidden layer
x_i	*i*-th record in the dataset
y	output signal from the neural network
z	Z-score

Greek letters

ΔI_b	width of each I_b bin [W/m^2]
ε_r	emissivity of the inner surface of the cavity receiver [-]
$\phi_i(x)$	output signal of each neuron of the hidden layer
η_{cle}^{ave}	average value of cleanliness coefficient [-]
η_e	mechanical-to-electric energy efficiency of the alternator [-]
η_o	optical efficiency of the concentrator [-]
ρ_p	Pearson correlation coefficient [-]
σ	standard deviation
σ_{SB}	Stefan–Boltzmann constant [W/(m²·K^4)]
ζ	non-linear function
μ	mean of the values of residuals

Acronyms

ANFIS	Adaptive Neuro-Fuzzy Inference System
ANN	Artificial Neural Networks
CPV	Concentrating PhotoVoltaics
CSP	Concentrating Solar Power
DNI	Direct Normal Irradiance
GA	Genetic Algorithm
MAE	Mean Absolute Error
MLP	Multiple Layer Perceptron
PCU	Power Conversion Unit
PSO	Particle Swarm Optimisation
PTSTPP	parabolic trough solar plant
PV	Photovoltaic
PVGIS	Photovoltaic Geographical Information System
RBF	Radial Basis Function
TMY	Typical Meteorological Year

Chapter 4

Optimization of a dish-Stirling solar concentrator

This chapter deals with the study of optimising the power generation of the dish-Stirling system, exploiting the fundamental idea of adapting the extension of the parabolic reflector according to the level of DNI characteristic of the selected installation site. It has therefore been discussed and demonstrated how this technological advancement combined with an incentive mechanism based on a time-varying incentive tariff can be reflected in the market by reducing the LCOE of dish-Stirling systems and increasing their competitiveness compared to other CSP systems that are more widely used.

4.1 Introduction

Data issued by the National Renewable Energy Laboratory (NREL) shows that the CSP plants currently operating or under development all around the world have a total peak power of about 10 GW [105]. Around 62% of these plants are parabolic trough systems, 34% are solar towers and about 4% are Fresnel systems. Approximately 6 GW, equally distributed between the parabolic trough and solar tower systems, refer to plants

equipped with thermal storage having a capacity of more than 8 hours. This data is consistent with the fact that parabolic trough collectors have reached higher commercial maturity earlier [8] and that more recently the number of solar tower systems is growing considerably [105]. Moreover, a comparison in terms of the Levelized Costs of Electricity (LCOE) [106] of these two technologies shows that solar towers are currently more economically viable (LCOE = 0.09 €/kWh) than parabolic trough collectors (LCOE = 0.21 €/kWh) [107]. Interestingly, dish collector systems, usually equipped with Stirling engines [108], are almost completely absent from the aforementioned CSP power generation scenarios, despite this technology holding the record for solar-to-electric peak conversion efficiency [109]. In most cases, in fact, dish-Stirling concentrators are still part of pilot projects [8]. These projects have demonstrated that dish-Stirling concentrators are characterised by a high level of modularity [110] and present a relatively low land occupancy compared to the other CSP systems [109]. Owing to these special features, dish-Stirling systems have been used in several applications, including [31]: heat and power micro-cogeneration [32], heating, ventilation and air conditioning of residential [33] and tertiary buildings [111], power generation in remote rural areas [36], potable water production [38], water pumping [39] and hybridization with other renewable energy sources [35]. In [112] a new hybrid system was proposed, where solar energy collected by a dish-Stirling system can be indirectly used in a high-efficiency power engine in form of syngas to increase electricity production.

The low commercial penetration of dish-Stirling systems in the renewable solar power generation market can be partially attributed to the fact that these systems are more difficult to combine with thermal energy storage [34] with respect to the other CSP systems. Furthermore, the presence of a thermal storage system would reduce the cost of electricity produced thanks to the continuity of operation during night-time hours [113]. However, as shown by the analysis of the installed plant data [105], dish-Stirling concentrators are not widespread among the CSP plants without energy storage either (about 40% of the total installed plants). The fact that Stirling engines are not produced on a large scale and have a relatively high initial cost [114] is certainly another strong barrier to the commercial penetration of this technology [28]. In around 2001, an interesting concept to increase the profitability of these systems [115] was proposed with the Schlaich Bergermann und Partner (SBP) EuroDish collector installed in Spain for

demonstration use [116]. This pilot system, with a peak output power of 10 kW_e corresponding to a DNI level of 800 W/m^2, was optimised as a function of the DNI hourly frequency distribution typical of the installation location. This technological improvement was realised by both enlarging the reflector size and using a fan cooler for the dissipation of the surplus of thermal energy absorbed by the collector cavity receiver during the few hours of the year when the DNI level exceeds the value of 800 W/m^2 [49]. Nonetheless, these technological developments have not been sufficient to increase the diffusion of dish-Stirling systems in the last two decades. Appropriate incentive policies [117] could encourage greater commercial penetration of CSP systems [118,119] by activating economies of scale that can reduce the initial costs of this promising renewable technology [120] and speed the dish-Stirling technology toward grid parity [121]. However, a correct and reliable assessment of the energy production of these systems is a necessary step to design a dedicated specific incentive scheme.

A novel strategy to encourage greater commercial diffusion of dish-Stirling systems is outlined and proposed in this part of the thesis. This strategy combines the optimization of the collector size to the solar radiation conditions of the installation site with the definition of a new incentive scheme. Concerning the optimization of the collector size, an approach similar to that proposed for Euro Dish systems was followed in this thesis. Since no relevant information was found in the literature for this case, a new numerical approach was defined to assess the energy production of a dish-Stirling system equipped with a fan cooler installed inside the receiver. To this aim, a recent numerical dish-Stirling simulation model [22] was expanded by introducing the term representing the input solar energy surplus to be dissipated into the energy balance of the receiver. This quantity was properly expressed as a function of both the nominal peak thermal input power of the Stirling engine and the current DNI levels. The proposed model allows the optimization of the concentrator mirror size considering both the Stirling engine characteristics and typical solar radiation conditions of the plant location.

Using the new simplified calculation algorithm described in *Paragraph* 3.2 "*A new simplified algorithm to assess electricity production from DNI frequency histograms*" allows for assessing the energy production of dish-Stirling systems based on the frequency histogram of 1-hour DNI series. This method could present a useful application in the optimization of dish-Stirling systems for macro geographical regions

for which it would be possible to elaborate statistically a single typical average frequency histogram of a 1-hour DNI series.

Finally, as a fundamental part of the outlined strategy defined within this part of the thesis, a novel incentive scheme, with a time-varying feed-in tariff is proposed for dish-Stirling systems. This scheme is based both on a realistic hypothesis of a reduction in the plant installation cost over time, based on the analysis of historical data from CSP technologies and on the assumption of constant payback time values for plants built during the incentivised period. This proposed incentive mechanism aims to find a trade-off between the interests of CSP investors and those of the local governments providing the incentive. Thus, the proposed incentive scheme can be seen as an interesting contribution to national energy policies for this type of renewable technology mainly because this approach can be generalised to different geographical locations.

The proposed energo-economic strategy was tested for dish-Stirling systems located in the central Mediterranean area. To this aim, six different plant configurations hypothetically installed in seven different locations were considered. For each location, two different input solar data sets were used as input (Meteonorm and PVGIS - Photovoltaic Geographical Information System). The results of these analyses made it possible to evaluate both the LCOE and the optimised feed-in tariff function for this geographical location.

4.2 Methodology for an energy assessment of an optimized concentrator

In this section, the physical-mathematical model used to carry out the energy analyses of the different studied dish-Stirling concentrator configurations is presented. For each location selected in this study, two different solar databases were chosen in order to extract the hourly series of the numerical model input variables. Afterwards, two different calculation approaches were defined to evaluate the electric energy outputs of the 42 studied cases.

4.2.1 A model considering the surplus of energy input on the receiver

The optimization of the dish-Stirling system by resizing the parabolic reflector implies that a greater thermal power is concentrated and absorbed by the receiver and

consequently a greater thermal power is available to the Stirling engine, at the same level of DNI. This makes it necessary to account for the operating limits of the engine by adding a new term in the reference energy model that represents the surplus thermal energy that must eventually be disposed of. To perform optimization analyses of dish-Stirling components taking into account the main parameters governing the efficiency of the system, reference was made to the numerical model described in *Paragraph 3.1.2 "A linear model of dish-Stirling electric power generation"*, which linearly correlates the mechanical output power of the Stirling engine and the high-temperature thermal power supplied to the hot side of the same engine by the receiver [22].

For this purpose, the linear model expressed by *Equation (3.1)* can be extended by rewriting the thermal power $\dot{Q}_{S,in}$ delivered to the Stirling engine as:

$$\dot{Q}_{S,in} = \left(\eta_o \cdot \eta_{cle} \cdot A_n\right) \cdot I_b - \left(\dot{Q}_{r,out} + \dot{Q}_{rej}\right) \tag{4.1}$$

where the newly defined term $\dot{Q}_{rej}$ [W] represents the heat power that can be rejected from the receiver by a hypothetical cooling fan. This latter term was added to the energy balance since some dish-Stirling models, such as the SPB EuroDish system [49], allow the receiver temperature to be controlled by a cooling fan dissipating the surplus of solar energy input. This device is activated whenever the thermal input power to the engine is higher than an upper limit value $\dot{Q}_{S,in}^{\max}$ which depends on the engine characteristics. This limit value is reached when I_b exceeds a maximum value that can be calculated by the following equation:

$$I_b^{\max} = \frac{\left(\dot{Q}_{S,in}^{\max} + \dot{Q}_{r,\text{out}}\right)}{(\eta_o \cdot \eta_{cle} \cdot A_n)} \tag{4.2}$$

that is deduced from *Equation (4.1)*, by imposing $\dot{Q}_{rej}$ equal to zero. It is noteworthy that $I_b^{\max}$ depends not only on the reflector and engine characteristics but also on the ambient temperature T_{air} (from the dependence of $I_b^{\max}$ from $\dot{Q}_{r,\text{out}}$). Thus, the thermal power that can be dissipated by the receiver fan cooler can be calculated as a function of I_b ad T_{air}, by the following relation:

$$\dot{Q}_{rej} = (\eta_o \cdot \eta_{cle} \cdot A_n) \cdot I_b - \left(\dot{Q}_{S,in}^{\max} + \dot{Q}_{r,\text{out}} \right) \tag{4.3}$$

which is deducted from *Equation (4.1)* by imposing $\dot{Q}_{S,in}$ equal to its maximum value $\dot{Q}_{S,in}^{\max}$. The operation of the Stirling engine is also limited by a minimum value of thermal input energy $\dot{Q}_{S,in}^{\min}$, below which the engine does not start. In a similar way to that described above for *Equation (4.2)*, the minimum value of beam solar irradiance useful for the system operation can be deduced from *Equation (4.1)* as:

$$I_b^{\min} = \frac{\left(\dot{Q}_{S,in}^{\min} + \dot{Q}_{r,\text{out}} \right)}{(\eta_o \cdot \eta_{cle} \cdot A_n)} \tag{4.4}$$

which, as previously explained, is also a function of the external temperature T_{air}

.

Taking into account the new term describing the surplus of thermal power delivered to the receiver by an enlarged reflector, the net electric power output of the dish-Stirling system $\left(\dot{E}_n \right)$ described by *Equation (3.4)* can be rewritten considering *Equation (4.1)* as follows:

$$\dot{E}_n = \left(\eta_e \cdot \eta_o \cdot \eta_{cle}^{ave} \cdot a_1 \cdot A_n \cdot R_T \right) \cdot I_b - \left\{ \eta_e \cdot \left[a_1 \cdot \left(\dot{Q}_{r,out} + \dot{Q}_{rej} \right) + a_2 \right] \cdot R_T + \dot{E}_p^{ave} \right\} \tag{4.5}$$

where: $\dot{Q}_{r,out} = A_r \cdot \left[h_r \cdot \left(T_r^{ave} - T_{air} \right) + \varepsilon_r \cdot \sigma \cdot \left(T_r^{ave\,4} - T_{sky}^4 \right) \right]$

The energy model described by the set of *Equation (4.5)* was used to perform the hourly-based simulations of the electric power outputs of the 42 analysed plants as a function of the changes of both the beam solar irradiance and air temperature, using the model calibration parameters defined for the dish-Stirling reference system of Palermo and summarised in *Table 2*. For all studied cases it was possible to calculate the instantaneous solar-to-electric energy conversion efficiency using the equations described above as follows:

$$\eta_{sol-ele} = \frac{\dot{E}_n}{I_b \cdot A_n} \tag{4.6}$$

Finally, the annual value of the solar-to-electric efficiency can be calculated as:

$$\bar{\eta}_{sol-ele} = \frac{E_t}{DNI_e \cdot A_n} \tag{4.7}$$

where: E_t is the annual electricity production of the dish-Stirling system and DNI_e [kWh/(m²·year)] is the annual effective direct solar irradiation.

The latter quantity is obtained by integrating over time only the direct solar irradiance values greater then $I_b^{\min}$.

4.2.2 Assessing of energy production: hourly-based approach and simplified approach

As already mentioned in the introductory part of this chapter, the performance of an optimized dish-Stirling solar concentrator was analysed to test the increase in electricity production for different reflector configurations and different installation locations, which essentially depends on both the level of direct normal irradiance and the outdoor temperature value. Thus, in order to evaluate the electricity production of a generic configuration of such a system, two different solar databases for the generation of synthetic files containing meteorological information for a specific location and two different calculation models were used. These methods are summarised in the flowchart in *Figure 30*.

By using both the TMY generated by Meteonorm [78] and PVGIS [79] solar data elaborated from 10 years of satellite measurements (2007-2016), it was possible to define two different series of hourly I_b and T_{air} values for each of the 7 studied Mediterranean locations. These data sets are the input data for both calculation methods used (as can be seen in box (a) of *Figure 30*), of which: the hourly-based approach refers to the analytical model described by the *Equation (4.5)* and the simplified approach is the one already described in *Paragraph 3.2 "A new simplified algorithm to assess electricity production from DNI frequency histograms"* in *Chapter 3*. Both used methods include the new term defined in *Paragraph 4.2.1 "A model considering the surplus of energy input on the receiver"* for calculating the surplus of the thermal power concentrated at the receiver through an enlarged reflector.

According to the first approach, the hourly series of the two meteorological input variables (I_b and T_{air}), represented by box (a) of *Figure 30*, are used to directly calculate the corresponding hourly series of the net electrical output power $\left(\dot{E}_n\right)_{hor}$ values by means of the electric power production model described by *Equation (4.5)* (see box (b) in *Figure 30*). Thus, in the flowchart in *Figure 30* the hourly-based approach is simply described by the two boxes (a) and (b). Then in order to effectively represent the hourly input values from box (a) and the output values from box (b), hourly frequency histograms were elaborated through the binning procedure that is described in box (c) in *Figure 30*. According to this data binning procedure, the range of I_b values of the input dataset of box (a) was divided into a series of consecutive non-overlapping bins, all having the same width ΔI_b [W/m^2]. Thus, using both the data of box (a) and the $\left(\dot{E}_n\right)_{hor}$ values from box (b), the following quantities were calculated for each bin:

- n_{I_b} [h], representing the number of records falling into the bin. That is, the number of hours during which I_b occurred with values included within the extremes of the definition of the bin;
- $\overline{T}_{air}$ [°C], representing the average of all the T_{air} values corresponding to records having an I_b value falling into the bin. These different values of T_{air} in each bin are related to the fact that, during the year, there are hours characterised by the same level of direct normal irradiance but different air temperature values.
- $\overline{I}_b$ [W/m^2], which is the mid-point value of the extremes defining the bin width.
- E_s [kWh/m^2] represents the total amount of the solar direct normal energy that can be calculated by multiplying $\overline{I}_b$ by n_{I_b};
- $\left(E_t\right)_{hor}$ [kWh], which is the net electric output energy that is calculated by summing the hourly values of $\left(\dot{E}_n\right)_{hor}$ that fall in the bin. In other words, the addends of this sum are the output values of box (b) corresponding to those I_b values which belong to the bin.

Unlike the first approach, the simplified method (described by box (d) in *Figure 30*) requires, as input data, the result values of the binning procedure of box (c). In other words, this second method allows the energy calculation using the hourly frequency distributions of direct normal irradiance (and the corresponding $\overline{T}_{air}$ values) as input. To this aim, starting from the triplets $\left(\overline{I}_b, \overline{T}_{air}, n_{I_b}\right)$ defined for each bin with of procedure described by box (c), it is possible to calculate the net electric output power $\left(\dot{E}_t\right)_{sim}$ corresponding to each bin by means of *Equation (4.5)*. Finally, for each bin, the net electric output energy $\left(E_t\right)_{sim}$ values are obtained by multiplying the bin value of $\left(\dot{E}_t\right)_{sim}$ by the corresponding n_{I_b} value.

The simplified approach is particularly advantageous, from an application point of view, whenever, for a certain location, an hourly frequency distribution of the DNI is available even when the original hourly-based data series is not. The latter, for example, may be the case when frequency histograms of direct solar irradiance are defined synthetically, through either statistical or analytical methods, to represent the average solar radiation conditions of a studied macro-region. In these cases, it is not even strictly necessary to know the exact value of $\overline{T}_{air}$ corresponding to each bin of I_b and it is sufficient to assume a constant value equal to the annual average air temperature of the specific geographical location.

The model described by *Equation (4.5)*, in fact, shows that the net electricity production of a dish-Stirling system is only slightly sensitive to variations in temperature and mainly depends on the intensity of direct normal irradiance. The simplified method is, also, particularly convenient, in terms of the immediacy of the calculations, whenever it is necessary to optimise the design of dish-Stirling collectors as a function of the hourly frequency distribution of direct radiation, especially considering that the linear model used for electricity production simulations (described by *Equation (4.5)*) can be easily recalibrated to simulate the electrical output of different dish-Stirling systems [22].

When the time period to which the historical climate data series refers is sufficiently long (e.g. 10 years) it is possible to calculate, for each defined bin and for a given location, the annual average values of the hourly frequency $\overline{n}_{I_b}$, the solar direct

normal energy $\overline{E}_s$ and the net electric output energy calculated both by the hourly-based $\left(\overline{E}_t\right)_{hor}$ and the simplified $\left(\overline{E}_t\right)_{sim}$ approaches (as shown in box (e) in *Figure 30*). By comparing the latter two quantities, it was possible to verify the accuracy of the newly proposed simplified method compared to the hourly-based approach.

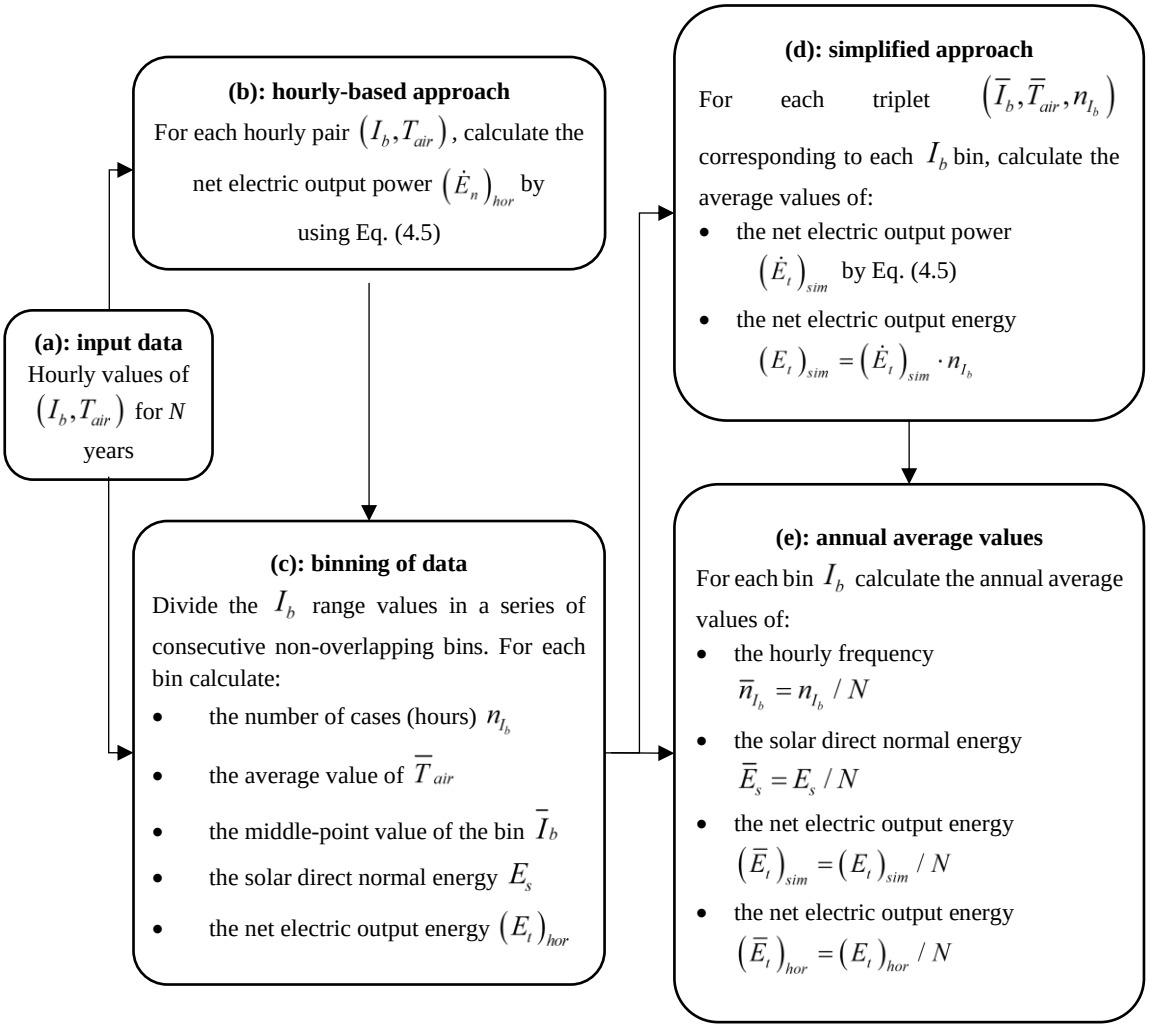

Figure 30. The flowchart of the calculation approaches

4.2.3 LCOE analysis and definition of a new incentive scheme

In this subsection, both the methodology for carrying out the LCOE analyses and the definition of a new incentive scheme for dish-Stirling systems are presented. Based on the results of energy analyses carried out with the numerical approaches described above, the LCOE analyses were developed assuming a trend of reduction over time of the system installed costs. This trend, gauged as a result of the effect of economies of scale, was hypothesised using the installed cost data of the other CSP systems available in the literature for the last decade [107]. Then considering the same cost reduction trend, a new incentive scheme was defined and validated using both the net present value (NPV) and the discounted payback time (DPBT) as economic indicators. The LCOE of an electrical generation system is, in general, defined as the present value of the cost of the produced electricity taking into account the plant lifespan and the costs of construction, operation and maintenance and fuel consumption. [122]. In this study, the following LCOE expression was used [107]:

$$LCOE = \frac{\sum_{t=1}^{n} \frac{I_t + M_t + F_t}{(1+r)^t}}{\sum_{t=1}^{n} \frac{E_t}{(1+r)^t}} \quad \left[\frac{€}{\text{kWh}_e}\right] \tag{4.8}$$

where:

- I_t [€] is the investment cost occurring in the year *t*
- M_t [€] is the Operation and Maintenance (O&M) costs occurring in the year *t*
- F_t [€] is the fossil fuel cost
- E_t [kWh] is the amount of electricity produced in the year *t*
- r [-] is the interest rate used for discounting expenditures and revenues
- n [year] is the lifetime of the power plant under consideration
- t is the *t-th* year of the lifetime of the power plant.

The investment costs I_t considered for the LCOE analyses are those occurring at year zero (I_0). These costs include those of the transport and installation of the system and those of the unit components (the collector mirrors, the PCU, the solar tracking system, the supporting structure, the foundation, the weather station, the electric

equipment, and the cooling system). No economic subsidies or incentives were considered in I_t.

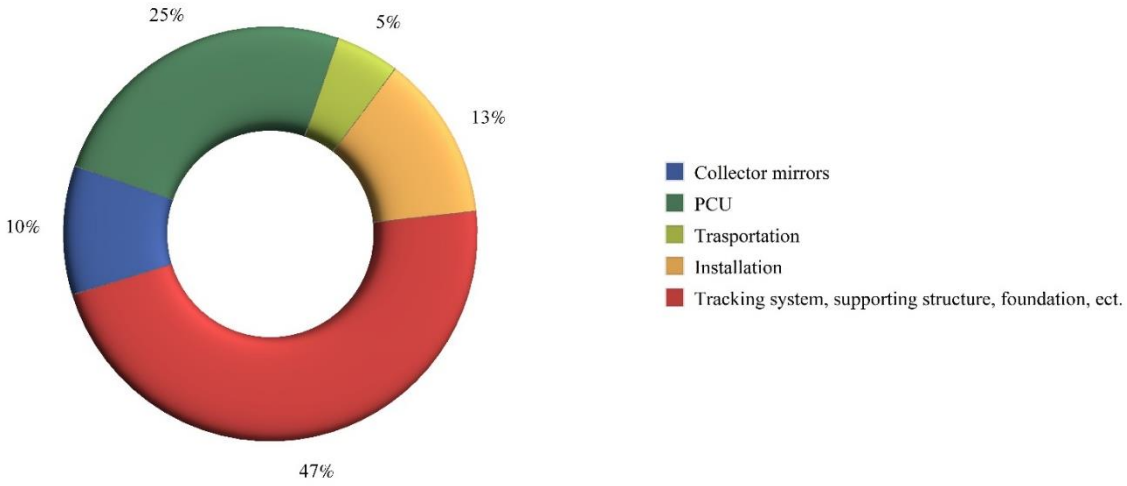

Figure 31. Percentage breakdown of total installed costs for the Palermo dish-Stirling unit

The I_t of the dish-Stirling unit of Palermo, corresponding to the basic configuration of the 6 units analysed, was assessed considering the real costs afforded for the construction of this plant. The percentage breakdown of the total installed costs of this collector, amounting to $I_t = 200,525$ €, is depicted in the pie chart in *Figure 31*. From the same figure, it is possible to observe that about 25% of the total cost is related to the PCU, 10% to the cost of mirrors and almost 50% to the cost of solar tracking and support structures. From this data, considering that this plant is characterised by a net peak electrical output power of about 32 kW_e and a reflector aperture area of $A_{n,0}$ = 106 m^2, it is possible to deduce the specific costs of both the installed plant and collector mirrors, equal to 6,266.41 €/kW_p and 188.68 €/m^2 respectively. Compared to the basic module, the other 5 dish-Stirling configurations studied differ only in the extension of the collector aperture areas. Thus, for the latter, the total installed cost was evaluated by only adjusting the amount related to the mirror surface area (evaluated by the unit cost estimated above). Moreover, the annual operation and maintenance costs were fixed to $M_t = 3,117.68$ €, based on the operation of the dish-Stirling unit of Palermo, and no costs for fuel consumption were considered ($F_t = 0$ €) since dish-Stirling systems do not need fossil fuel for operation [107].

Finally, for the LCOE computations, a discount rate value equal to $r = 7.5\%$ (as suggested for OECD - Organisation for Economic Co-operation and Development - countries [107]) and a plant lifespan of $n = 25$ year were used in *Equation (4.8)*.

As anticipated, the effect of the economies of scale, triggered by greater commercial penetration of this technology, should lead to a progressive reduction in the installed cost over several years similar to what happened for the other CSP technologies (parabolic troughs, Fresnel reflectors and solar towers).

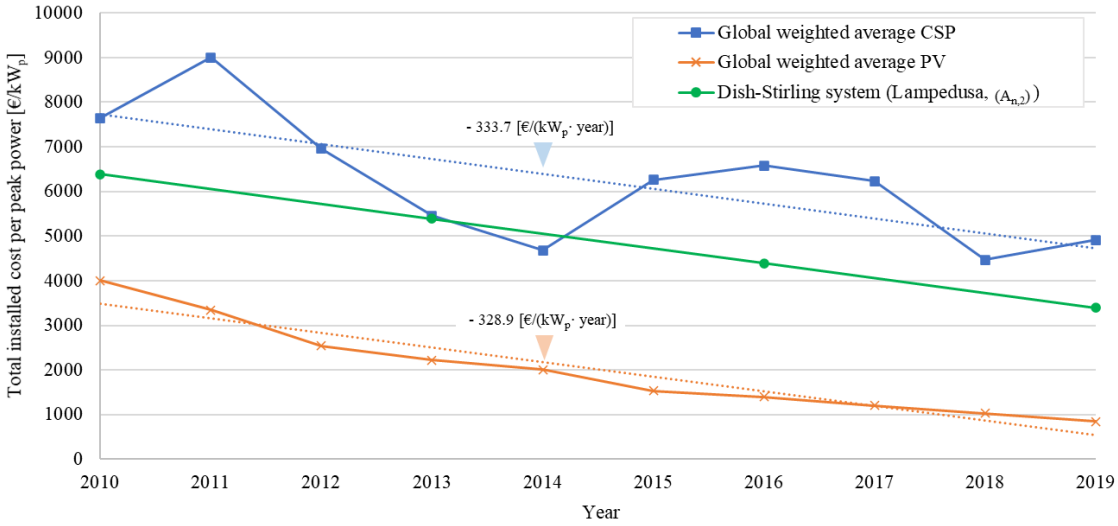

Figure 32. Global weighted average total installed costs of CSP and PV systems (2010-2019)

In *Figure 32*, the variations of the global average installed costs (per unit of peak electrical power) of both PV systems and CSP systems (excluding dish-Stirling concentrators) are shown for the last decade [107]. In this period, the annual cost reduction trend for CSP systems (indicated with the dotted line in *Figure 32*) was about 334 €/(kW$_p$·year). A similar trend was observed for PV systems in the same timespan (about 329 €/(kW$_p$·year)) although their installed costs were lower compared to that of CSP systems (see *Figure 32*).

Based on these considerations, this part of the thesis involved simulating the hypothetical time evolution that the LCOE of dish-Stirling systems would have if their installed cost reduction were the same as the other CSP technologies. Under this

hypothesis, 6 installed cost time variation functions corresponding to the 6 dish-Stirling configurations studied were defined (in *Figure 32* the cost function of the configuration with $A_{n,3}$ is plotted). All these functions have a reduction trend identical to that of the other CSP systems and an initial cost equal to the current cost of each plant configuration.

Following this approach, the LCOE variations in 10 years were simulated for the 6 collector configurations and all the analysed geographical locations. As mentioned above, a new incentive scheme, finalised to encourage the diffusion of dish-Stirling systems is introduced with this part of the thesis. To test this incentive scheme, the NPV and the DPBT were assessed for all the 42 studied cases. The *NPV* was calculated according to the following definition:

$$NPV = \sum_{t=1}^{n} \frac{CF_t}{(1+r)^t} \quad [€] \tag{4.9}$$

where: *n* is the lifespan of the plant (equal to 25 years), *t* is the *t-th* year of the lifetime of the project, CF_t [€] is the corresponding cash flow and *r* [-] is the interest rate (assumed equal to 7.5%). On the other hand, the *DPBT* [year], defined as the number of years *t* needed for the equivalent of the investment income to exceed the equivalent of the capital expenditure, was determined according to the following relation:

$$DPBT = t \quad | \quad \sum_{t=0}^{n} \frac{CF_t}{(1+r)^t} \geq 0 \quad [year] \tag{4.10}$$

In the above relationships, the cash flow, for year zero $(t = 0)$ was fixed to the investment plant cost, while for the years that followed $(t > 0)$, it was calculated considering the annual operation and maintenance costs of the plant and the revenue from the sale of the annual electric energy delivered to the national grid:

$$CF_t := \begin{cases} I_0 & for\, t = 0 \\ E_t \cdot T_{feed-in}^{(i)} - M_t & for\, t > 0 \end{cases} \quad [€] \tag{4.11}$$

where $T_{feed-in}^{(i)}$ [€] is the feed-in tariffs for a plant installed in the same calendar year *i* since the beginning of the incentive plan, and *t* is the number of plant operation years since the *i*-th year. The feed-in tariffs introduced in *Equation (4.12)* for the

calculation of both NPV and DPBT were defined according to the new incentive scheme for which the rationale is described below.

In order to take into account that the installation costs of the plants will reduce during the incentivization period, a decreasing over time feed-in tariff was defined. Thus, plants that will be built in a certain year *i* of the incentive period will benefit from a slightly lower feed-in tariff $T_{feed-in}^{(i)}$ than plants that were built the previous year $T_{feed-in}^{(i-1)}$, and so on. However, the designated feed-in tariff for plants that will be built in the same year will remain constant throughout the incentive period.

The following assumptions were made in order to construct the reduction function of the feed-in tariff over time: (1) the reduction trend of the installation cost over time is equal to that of the global weighted installed cost of CSP systems; (2) the DPBT is equal for all plants having the same collector opening area, regardless of the year of their construction. In other words, this proposed incentive mechanism aims to find a trade-off between the interests of CSP investors and those of the local governments providing the incentive: on the one hand, investors will be able to achieve a near-constant DPBT of their investments regardless of the year of plant construction; on the other hand, governments will be able to rationally reduce the economical charge of the incentive system over time, taking into account the reduction in the installed cost of the technology thanks to economies of scale. Thus, by manipulating *Equations (4.9)* and *(4.10)*, according to these assumptions, the feed-in tariff variations of plants falling under the incentive plan at the *i* -th year can be expressed as follows:

$$T_{feed-in}^{(\mathrm{i})} = \frac{I_0^{(\mathrm{i})}}{I_0^{(0)}} \cdot \left(T_{feed-in}^{(0)} - \frac{M_t}{E_t} \right) + \frac{M_t}{E_t} \quad \left[€ / \mathrm{kWh} \right] \tag{4.12}$$

where, $I_0^{(\mathrm{i})}$ is the plant installed cost at the *i*-th year from the entry into force of the incentive plan (e.g., the linear function already depicted in *Figure 32* for dish-Stirling concentrators).

It is worth noting from *Equation (4.12)* how general this incentive scheme is and how easily it can be specialized for different geographic macro-areas and for different dish-Stirling systems. In fact, while the variation of the $\frac{I_0^{(\mathrm{i})}}{I_0^{(0)}}$ ratio over time is essentially

a global decreasing trend (see *Figure 32*), the values of I_0, M_t and E_t depend both on the particular dish-Stirling system and the local availability of direct solar irradiation. Finally, the initial feed-in tariff $T_{feed-in}^{(0)}$ can be tuned to ensure an attractive DPBT for investors. This initial tariff can be also compared with that dedicated to other solar power systems.

In order to test the validity of this approach, the incentive scheme proposed above was calibrated for the Italian territory considering both the calculated energy productions for dish-Stirling plants installed in this geographical area and the structure of the old Italian incentive scheme dedicated to renewable energy sources [123]. According to this plan, which is no longer in force in Italy, the feed-in tariff for CSP systems was obtained as the sum of two components: a base incentive tariff T_b [€/kWh$_e$] (depending on the plant size) and a bonus $P_{r,solar}$ [€/kWh$_e$] (proportional to the solar integration fraction of the plant). In the new incentive scheme proposed in this study, the bonus component was maintained identical to that of the old decree for CSP systems ($P_{r,solar}$ =0.045 €/kWh$_e$), while the basic incentive tariff was increased and set to T_b =0.415 €/kWh$_e$. In this way, the feed-in tariff for the first calendar year of the incentive plan was set to $T_{feed-in}^{(0)}$ =0.46 €/kWh$_e$ which is equal to the feed-in tariff of the first Italian incentive plan dedicated to PV plants (decree of 28 July 2005 [124]). Thus, introducing both $T_{feed-in}^{(0)}$ and E_t as parameters in *Equation (4.12)* and assuming the installed cost functions $I_0^{(i)}$, already employed for LCOE analyses, it was possible to determine a $T_{feed-in}^{(i)}$ function for each of the 42 studied cases hereinafter defined. Then these functions were averaged in order to define a single regional feed-in tariff function. Finally, this function was introduced in *Equations (4.9)* and *(4.10)* to assess the NPV and DPBT of all the studied cases with the aim of testing the validity of the proposed incentive scheme.

4.3 Overview of analysed case studies

The procedure proposed above was used to assess the energy performance of dish-Stirling concentrators installed in different locations in the central Mediterranean. The dish-Stirling system that was chosen as a reference for the energy evaluations is a real

commercial collector currently operating at the facility test site at Palermo University and described in *Paragraph 2.5 "The reference dish-Stirling system"* of *Chapter 2* (see *Figure 33*).

Figure 33. The dish-Stirling plant of Palermo

Five additional dish-Stirling configurations were also considered for the study. These latter systems were hypothesised to have the same PCU (i.e., the same Stirling engine) as the real collector model from which they differ in both the reflector size (see *Figure 34*) and in the implementation of a receiver cooling system. This cooling device, assumed to be similar to that developed for the SBP EuroDish units [49], allows the dissipation of the solar energy surplus that is concentrated in the PCU receiver during the

peaks of solar irradiance. This energy surplus, in turn, is related to the fact that the reflector aperture areas of the modified configurations were assumed to be larger than the basic ones. The aperture areas of these five CSP systems are equal to $A_{n,1}$ = 116.6 m^2, $A_{n,2}$ = 127.2 m^2, $A_{n,3}$ = 137.8 m^2, $A_{n,4}$ = 148.4 m^2, $A_{n,5}$ = 159 m^2, respectively.

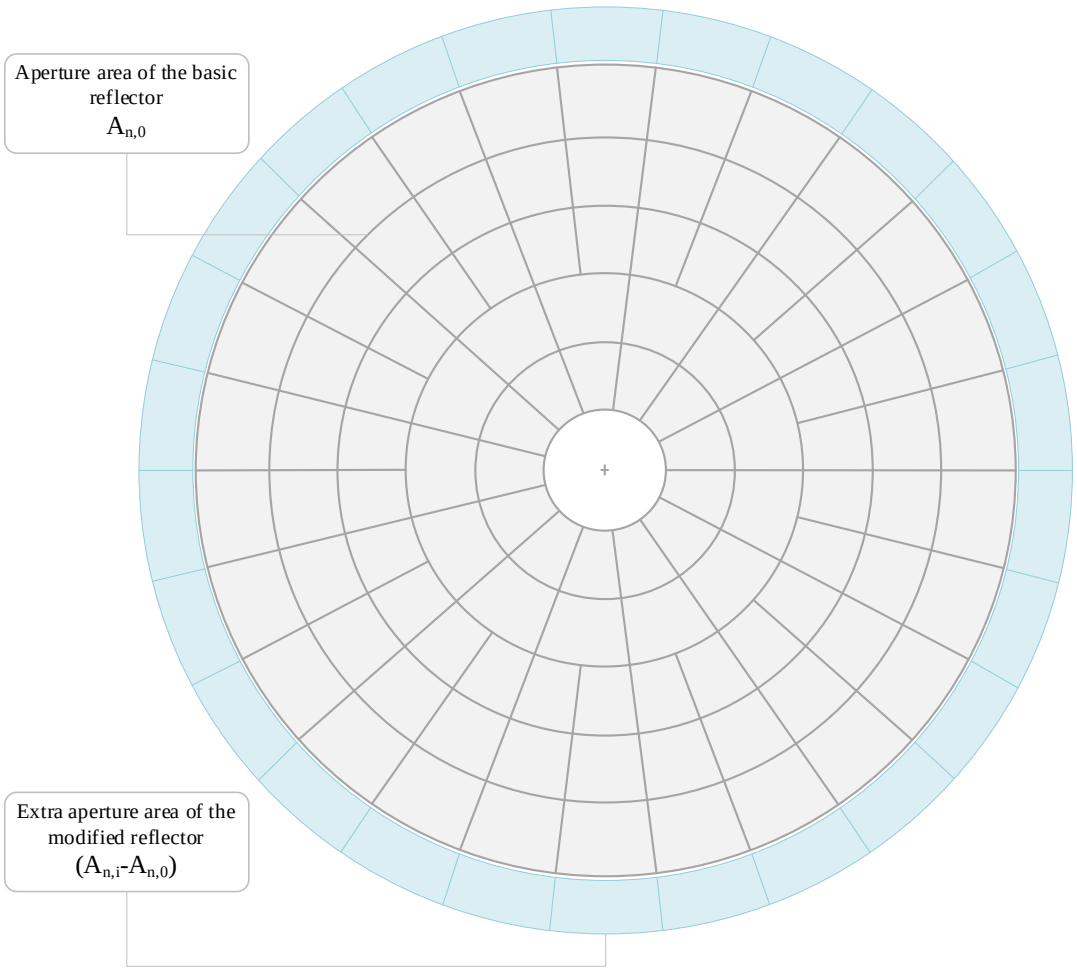

Figure 34. Representation of reflector aperture area for modified dish-Stirling system configurations

In order to evaluate the dish-Stirling energy production as a function of various solar irradiation levels, seven locations, each characterised by different hourly frequency distributions of DNI, were considered for the analyses (see *Figure 35*).

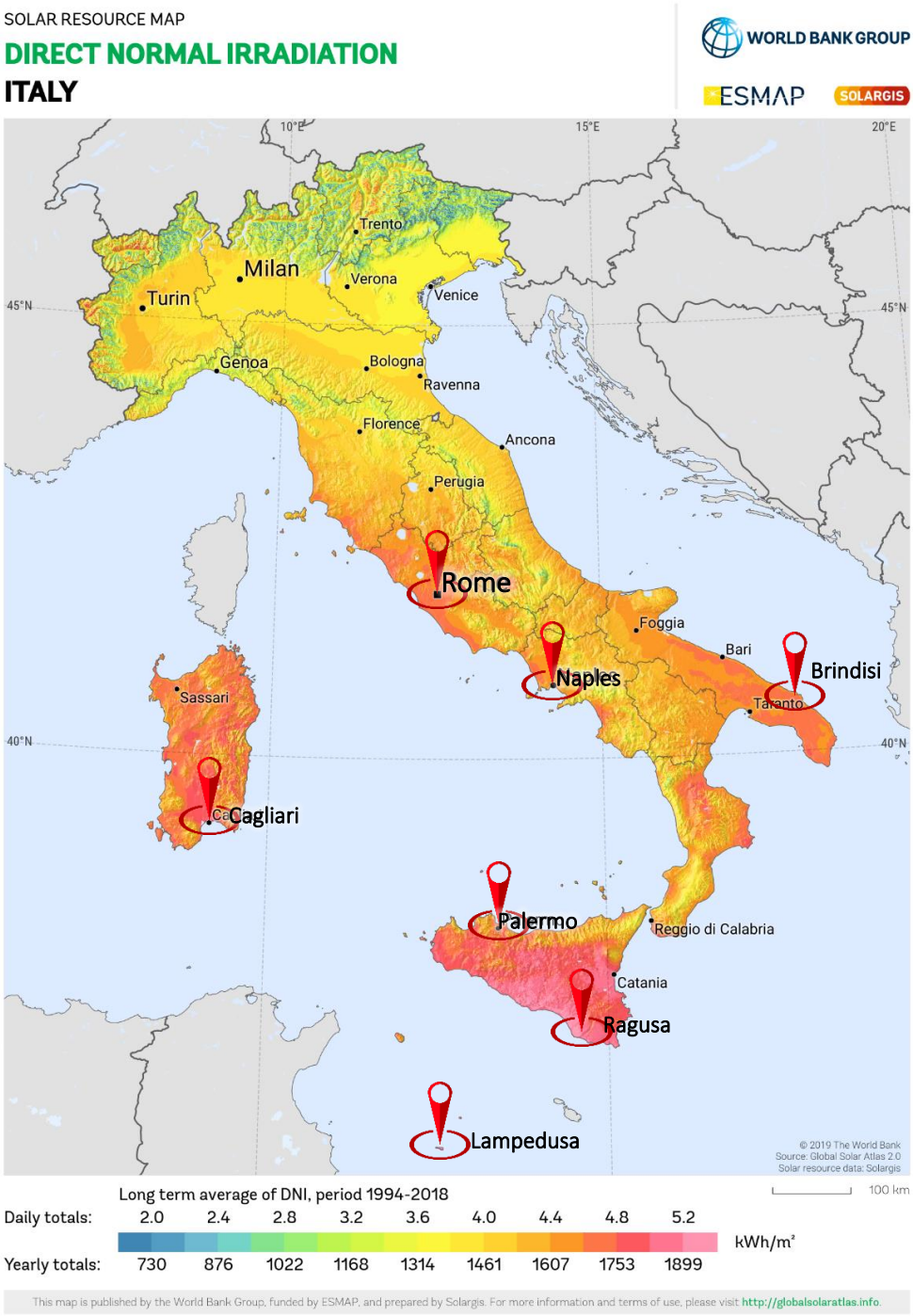

Figure 35. iso-map of DNI and locations of the studied CSP plants (source: https://globalsolaratlas.info/download/italy)

These plant locations, which are all on the southern side of the Italian territory (see *Figure 35*), are the following: Lampedusa, Cagliari, Ragusa, Palermo, Brindisi, Rome, and Naples. Considering the 6 collector configurations and the 7 plant locations,

the total number of case studies that are examined in this study amounts to 42. As described in more detail further on in this article, hourly-based numerical simulations were carried out in order to define the electric energy production of all these 42 studied cases. These simulations were performed assuming two different DNI time-series for each location as input.

Thus, using the methods described in the flowchart of *Figure 30*, it was possible to produce the following histograms:

- 14 frequency histograms of 1-hour DNI series were generated using the two solar datasets for each of the 7 locations. The average values of the air temperature of each bin were represented on the same graphs (following the calculation flow described by boxes (a), (c) and (e) in *Figure 30*).
- 84 histograms representing the net electric output energy of the 42 studied cases generated by the hourly-based calculation approach using the two solar datasets (following the calculation flow described by boxes (a), (b), (c) and (e) in *Figure 30*).
- 42 histograms representing the net electric output energy for all the 42 studied cases, using the simplified approach with the PVGIS dataset as input (following the calculation flow described by boxes (a), (c), (d) and (e) in *Figure 30)*.

4.4 Findings and discussion

Using the hourly series of DNI values provided by both the TMY of Meteonorm and satellite solar data of PVGIS (recorded between 2007 and 2016), the annual average direct solar irradiance values were obtained for all the studied locations, and these are summarised in *Table 11*. From the analysis of this data, it is possible to observe that the cumulative values of direct solar energy extrapolated from the two datasets deviate from each other by a relative mean percentage difference of about 12%, with a maximum value of about 30% (in the case of Rome). These differences are not only in the total values of energy but also in how these cumulated quantities are distributed over the different classes of DNI levels, as the data depicted in *Figure 36* and *Figure 37*.

Table 11. Annual direct solar irradiation for the studied locations (PVGIS and Meteonorm)

Location	**Longitude**	**Latitude**	**Direct annual solar irradiation (kWh/m²/year)**	
	(Decimal degrees)		PVGIS	Meteonorm
Brindisi	17.943	40.673	1840	1791
Cagliari	9.117	39.267	2009	1704
Lampedusa	12.617	35.503	2058	1948
Naples	14.330	40.844	1825	1615
Palermo	13.345	38.104	1819	1932
Ragusa	14.657	37.091	1975	2138
Rome	12.566	41.783	1810	1311

These figures, in fact, represent the frequency histograms of one-hour I_b series for the 7 considered locations. This data was elaborated by using the calculation method described in the flowchart of *Figure 30* fixing a bin width of $\Delta I_b = 50\,\mathrm{W/m^2}$. The histograms produced with PVGIS data (continuous lines in in *Figure 36* and *Figure 37*) show, for all the locations, an annual peak hourly frequency (ranging between $\bar{n}_{I_b} = 700$-800 hours per year) at DNI levels between 700 and 800 W/m^2. On the other hand, those deduced from Meteonorm data (dashed lines in *Figure 36* and *Figure 37*) show either flat distributions (e.g., for Brindisi, Cagliari, Rome and Naples) or distributions having peaks for DNI classes either below 700 W/m^2 (e.g., for Lampedusa and Palermo) or above 800 W/m^2 (e.g., for Ragusa).

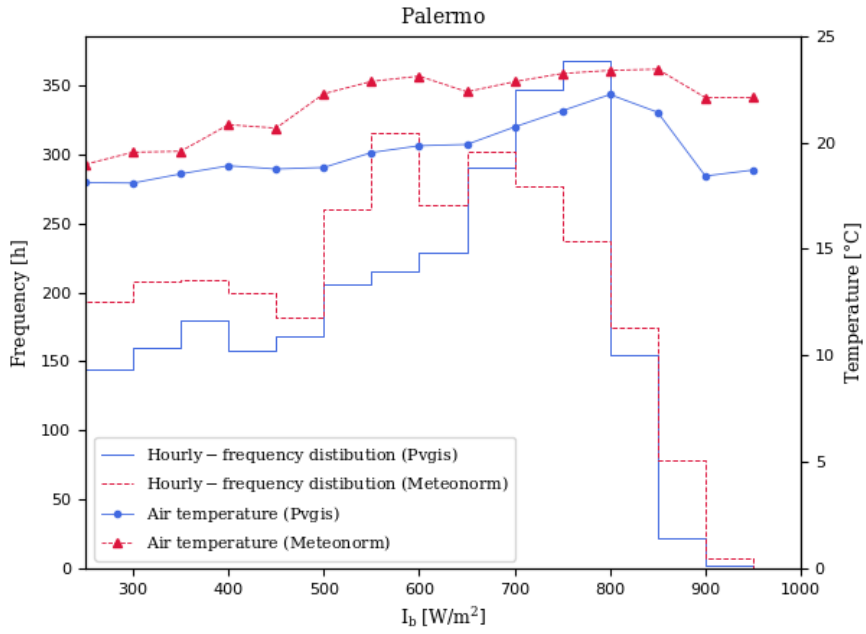

Figure 36. Frequency histograms of 1-hour I_b series and $\overline{T}_{air}$ bin values for the site of Palermo (elaborated using both Meteonorm and PVGIS datasets)

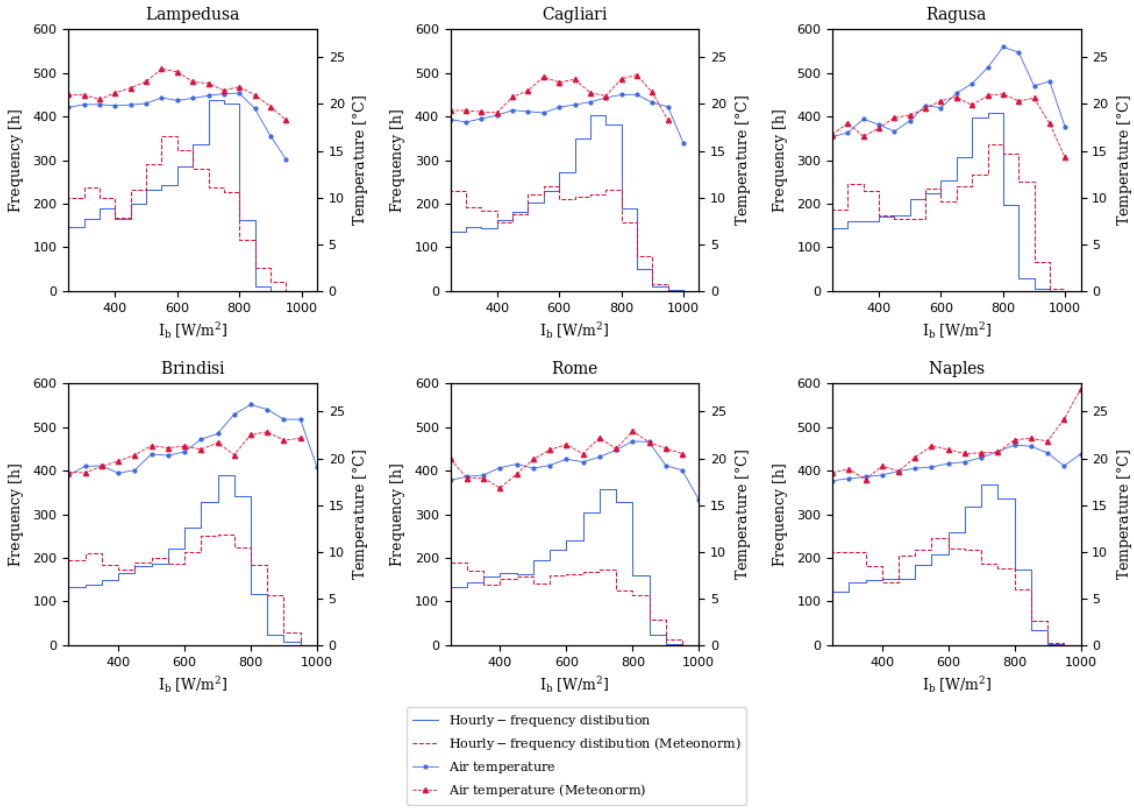

Figure 37. Frequency histograms of 1-hour I_b series and $\overline{T}_{air}$ bin values for 6 locations (elaborated using both Meteonorm and PVGIS datasets)

For example, in the case of Palermo (see *Figure 36*), even though the cumulative average annual energy deduced from the two solar databases differs only by 6% (see *Table 11*), the corresponding histograms show peaks at different I_b class intervals (about 700-800 W/m^2 for PVGIS and 550-700 W/m^2 for Meteonorm). In the same *Figure 36* and *Figure 37*, in each I_b bin, the annual average value of the air temperature $\overline{T}_{air}$ (calculated according to the approaches described by the flowchart in *Figure 30*) was also represented using both Meteonorm and PVGIS datasets. For all the locations analysed, these results generally show that $\overline{T}_{air}$ is an increasing function of I_b up to about I_b = 900 W/m^2, while for higher values of I_b, $\overline{T}_{air}$ decreases slightly. This behaviour can be justified by analysing the climate data that characterizes the central area of the Mediterranean basin, since:

- The hours for which I_b is between 250-400 W/m^2 are equally distributed across all seasons. During these periods the average air temperatures are between T_{air} =12 °C (winter) and T_{air} =24 °C (summer).
- The hours for which I_b is between 400-900 W/m^2 are mainly concentrated in the warmer seasons (spring and summer). During these periods, the average air temperature is about T_{air} = 20 °C
- Finally, the hours during which I_b is between 900-950 W/m^2 (according to days characterised by clear skies and low air turbidity) are mainly concentrated in spring and winter. During these periods, the average air temperature is about T_{air} = 18 °C.

For the basic collector configuration $A_{n,0}$ (corresponding to the existing dish-Stirling plant of Palermo), the annual net electric energy distributions, as a function of the different I_b classes, were calculated using the methods described in the flowchart in *Figure 30* and are represented by the histograms in *Figure 38* and *Figure 39* for each of the 7 plant locations. From the results represented in *Figure 38*, it is possible to observe that the productions calculated with the PVGIS solar dataset for the location of Palermo

through both the simplified method and the hourly method are practically identical (with an overall relative percentage error of around 0.03%). This result is particularly interesting because it demonstrates that it is possible to accurately simulate the annual electricity production of a dish-Stirling system from the frequency histograms of 1-hour I_b series only. This is possible also because the energy model described by *Equation (4.5)* is not particularly sensitive to the variations in T_{air} .

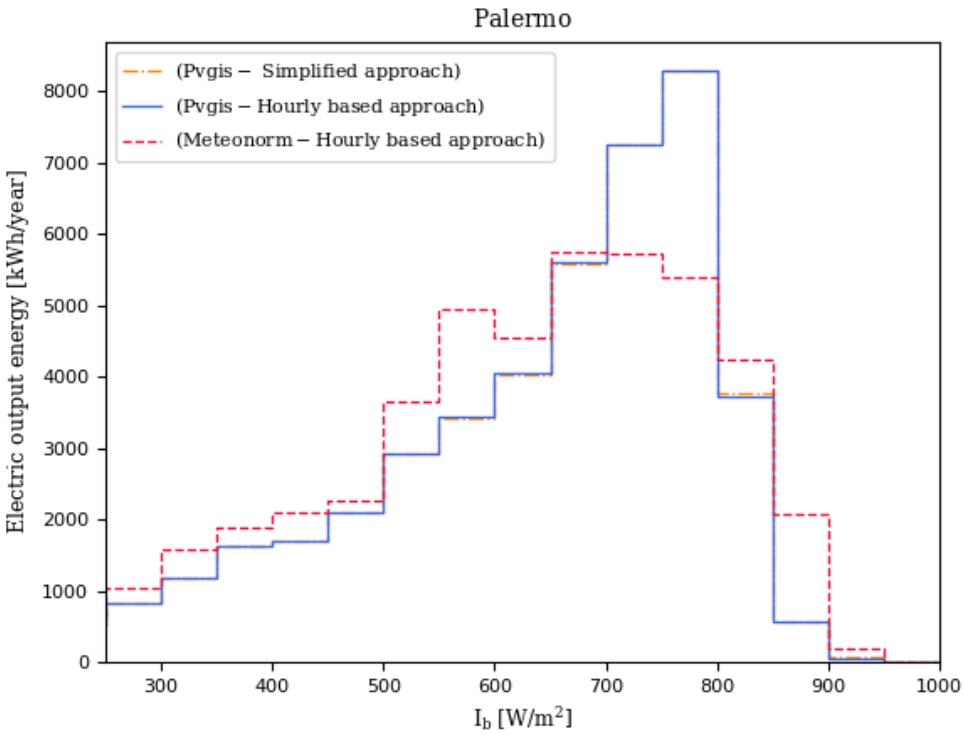

Figure 38. Annual electric output energy as a function of I_b classes for the dish-Stirling plant of Palermo ($A_{n,0}$ configuration)

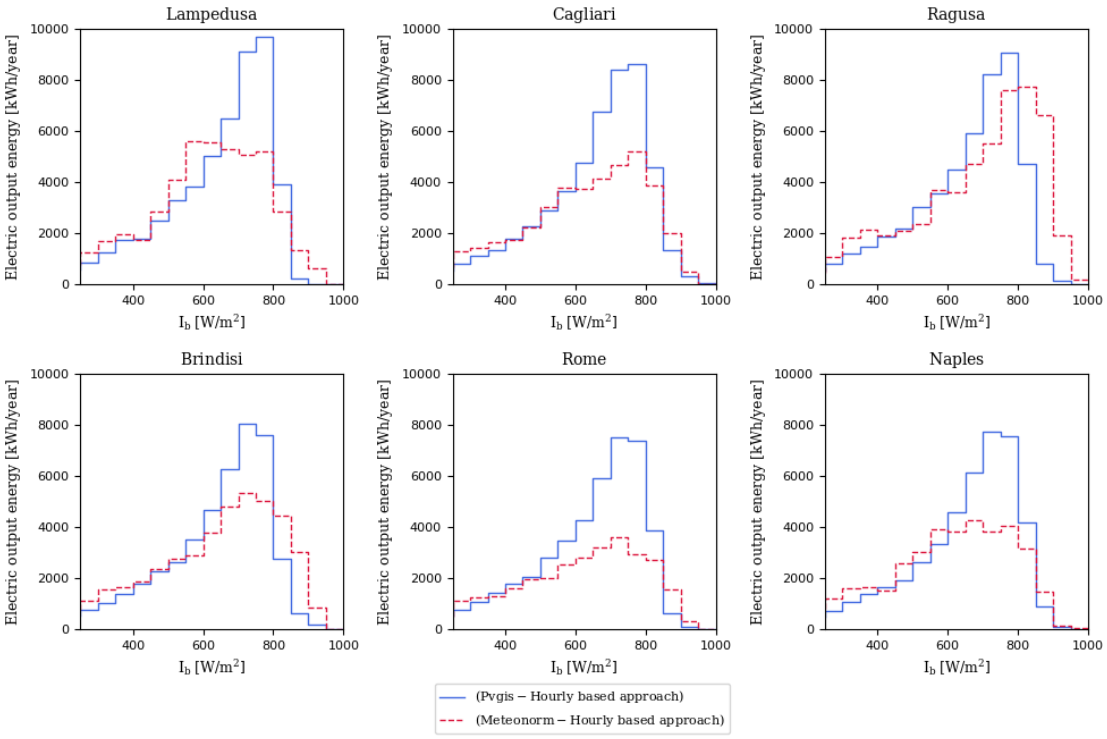

Figure 39. Annual electric output energy as a function of I_b classes for the $A_{n,0}$ dish-Stirling configuration at 6 different locations (elaborated using both Meteonorm and PVGIS datasets)

This new approach may be used, for example, to allow the collector optimization in a macro-climatic area using the typical frequency histograms of 1-hour I_b series that can be generated through suitable statistical methods. For what concerns, instead, the comparison between the results obtained with the hourly approach using the two solar datasets, it is possible to notice from *Figure 38* and *Figure 39*, that the differences between these results are essentially a consequence of the differences between the hourly frequency histograms of DNI (see *Figure 36* and *Figure 37*). Another interesting observation is that the differences between the annual electrical energies calculated using Meteonorm and PVGIS do not coincide with those between the direct annual solar irradiation values defined by the same datasets (see *Table 11*). For example, in the case of Palermo (see *Figure 38*), the annual net electrical energy output calculated by Meteonorm amounts to E_t = 46 MWh_e, while the corresponding energy value calculated by PVGIS amounts to E_t = 43.84 MWh_e. The percentage deviation between these values

is 4.8%, while that between the annual solar direct irradiation values for the same location calculated from *Table 11* is about 6%. The same comparative analysis was extended to the other 6 locations yielding similar qualitative results, as summarised in *Figure 40.*

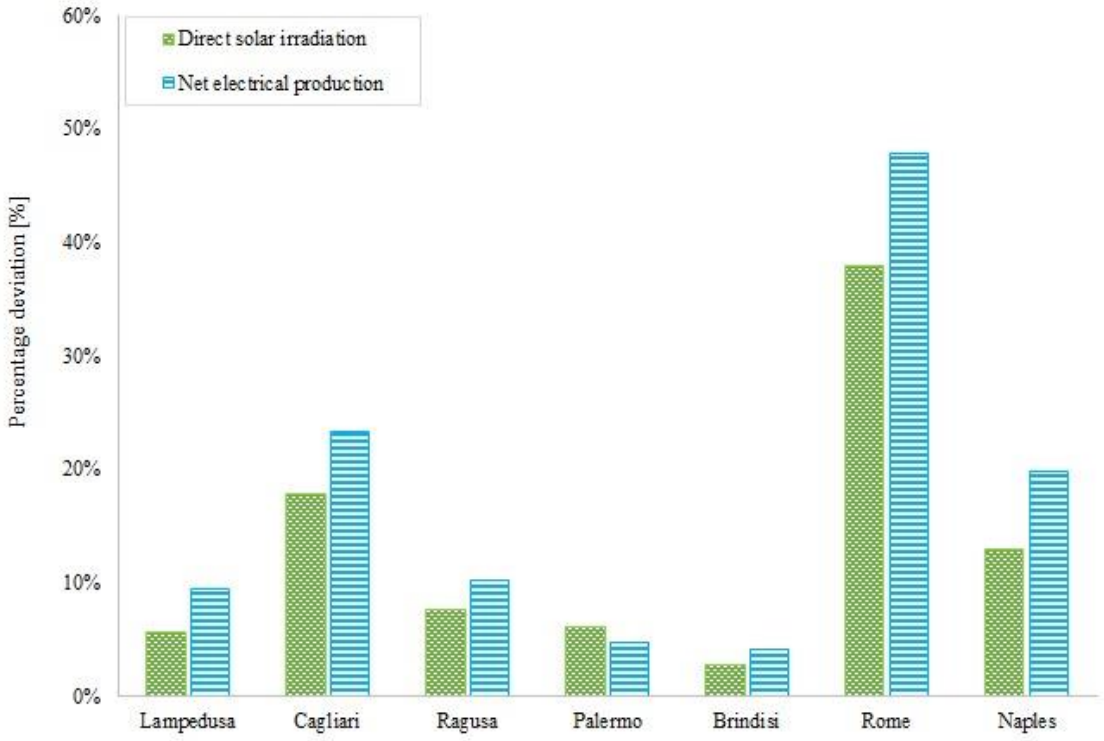

*Figure 40. P*ercentage deviations between the values of the annual DNI and E_t calculated using PVGIS and Meteonorm, respectively

From the data represented in this figure what stands out, for example in the case of Rome, is that where the percentage difference between the input solar irradiation values is about 38%, that between the production values is 47.8%. This non-proportionality between input and output energy differences is essentially related to the fact that the solar-to-electric conversion efficiency of a dish-Stirling system (calculated according to *Equation (4.6)*) weighs the various levels of input solar irradiance differently (see *Figure 41*). In summary, these first results underline what the impact could be of an incorrect definition of the DNI hourly frequency histograms on the energy prediction accuracy of a dish-Stirling system at a given location.

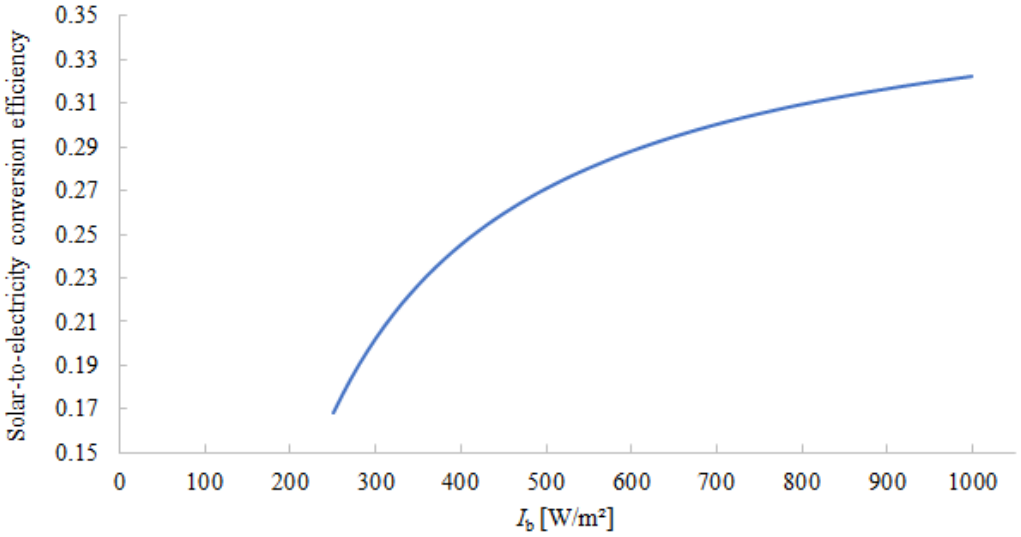

Figure 41. Instantaneous solar-to-electric conversion efficiency curve as a function of direct normal solar irradiance with T_{air} = 25 °C and clean mirrors (see *Equation (4.6)*)

Based on these considerations, for the analysis presented below, the DNI data deduced by PVGIS was considered more useful than that of Meteonorm, since:

- the solar data from PVGIS is based on real satellite measurements carried out over several years at the studied locations;
- the major uncertainties in this data mainly correspond to the lower levels of DNI (mostly on cloudy days). These solar irradiance levels have a negligible impact on the accuracy of the annual energy production determinations as it is possible to deduce from the efficiency curve in *Figure 41*.

Moreover, PVGIS data shows that the annual hourly frequency peaks of DNI, for all the considered locations, correspond to DNI values ranging between 700 and 800 W/m^2. However, the dish-Stirling configuration of Palermo was optimised for a peak power of I_b = 900 W/m^2, which is an irradiance level occurring only for a small number of hours per year in the Mediterranean area. Therefore, in this part of the thesis, following a strategy similar to that reported in the literature for the EuroDish systems [49], the possibility of reducing the I_b value corresponding to the peak output power of the Stirling engine by both increasing the collector aperture area A_n and using a thermal dissipater in

the receiver to manage $\dot{Q}_{S,in}$ greater than $\dot{Q}_{S,in}^{max}$ was investigated. The net electrical output powers as a function of I_b variations for the 6 collectors were calculated using *Equations* from *(4.1)* to *(4.6)* and these are depicted in *Figure 42*.

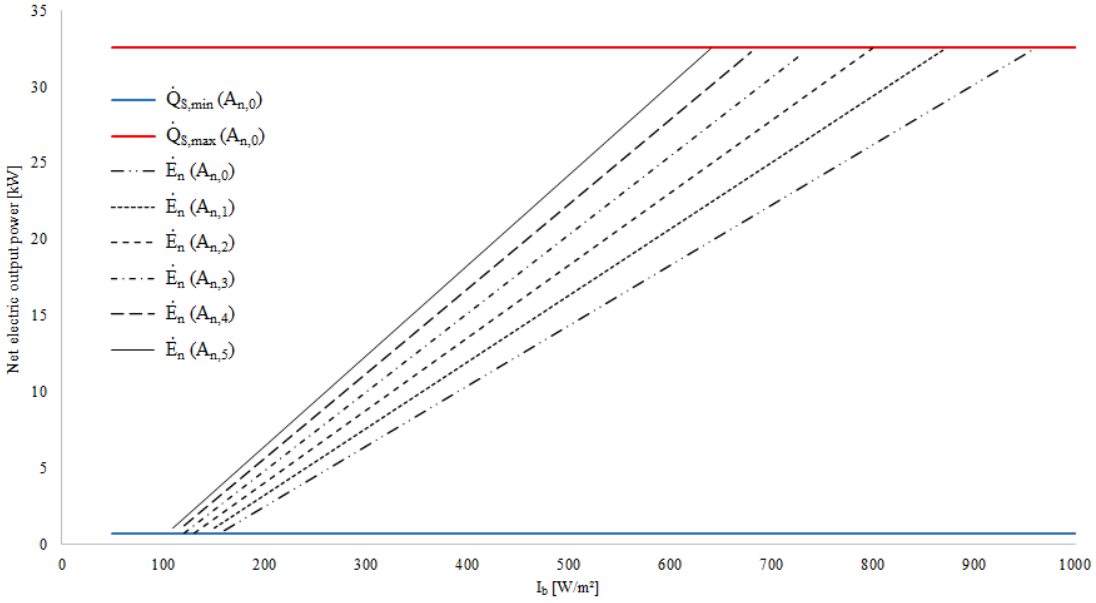

Figure 42. The net electric output power of the 6 dish-Stirling configurations as a function of direct normal solar irradiance at T_{air} = 25 [°C] and with clean mirrors

All the curves, in this picture, are limited by a minimum and a maximum power threshold corresponding to the output limits of the actual PCU mounted in the Palermo dish-Stirling plant. From these curves, it is evident, as anticipated, that the larger the collector aperture area the lower the solar irradiance corresponding to I_b^{max} (calculated by *Equation (4.2)*). Then for each value of I_b greater than I_b^{max}, the net electrical output power is kept constant through the action of the receiver fan cooler. The results of the numerical simulations in terms of annual net electrical energy production, for all the dish-Stirling configurations and considered locations, calculated using the PVGIS solar input data with the hourly based approach are reported in *Table 12*.

Table 12. Annual electric output energy (E_t) for all the 42 examined cases expressed in [MWh_e/year]

Location	$\mathbf{A_{n,0}}$	$\mathbf{A_{n,1}}$	$\mathbf{A_{n,2}}$	$\mathbf{A_{n,3}}$	$\mathbf{A_{n,4}}$	$\mathbf{A_{n,5}}$
Brindisi	44.08	50.01	55.70	60.10	63.27	65.72
Cagliari	49.13	55.63	61.48	65.88	69.09	71.55
Lampedusa	50.2	56.95	63.21	67.90	71.38	74.08
Naples	44.32	50.25	55.60	59.66	62.62	64.89
Palermo	43.84	49.75	55.19	59.28	62.37	64.78
Ragusa	47.85	54.27	60.32	64.72	67.96	70.46
Rome	43.47	49.31	54.67	58.74	61.77	64.12

Comparing *Table 11* to *Table 12*, it is possible to observe that, for fixed collector configuration, the annual electric production (E_t) is proportional to the annual direct solar irradiation values. Thus analysed, a linear correlation between the annual net electrical energy collector output and the annual direct solar irradiation emerges for each plant configuration. These functions are represented in *Figure 43* for all configurations ($A_{n,0}$, $A_{n,1}$, $A_{n,2}$, $A_{n,3}$, $A_{n,4}$ and $A_{n,5}$) and can be employed to make an initial estimate of the electrical production of a dish-Stirling concentrator as a function of the annual solar irradiation values of the plant installation site.

For example, in the case of the basic configuration of the dish-Stirling system ($A_{n,0}$), this production varies between about 40 and 50 MWh_e/year corresponding to annual direct solar irradiation values of between 1800 and 2060 kWh/(m^2·year).

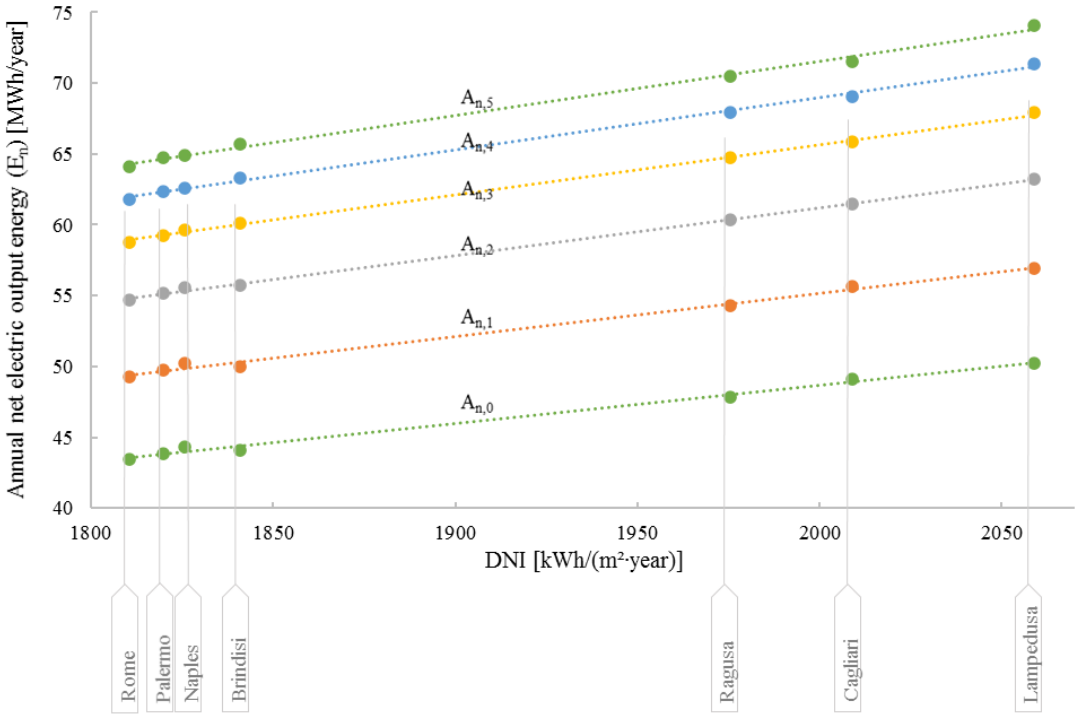

Figure 43. Linear correlations of the annual net electric output energy as a function of the annual DNI for different dish-Stirling configurations

On the other hand, independent of plant location, the annual energy production of dish-Stirling concentrators increases with the aperture area of the solar collectors, up to a maximum of about 47%, corresponding to a solar collector with an opening area increase of 50% ($A_{n,5}$ = 159 m^2). For example, in the case of the most productive site (Lampedusa) among the seven analysed, E_t increases from about 50 to 74 MWh$_e$/year going from the basic configuration to that characterised by the largest collector aperture area as depicted with the blue line in *Figure 44*. The same figure also shows the trend of the annual efficiency $\bar{\eta}_{sol-ele}$ calculated for the different configurations located in Lampedusa. From this data, it can be observed that this efficiency increases from a value of 24% for the basic configuration to a maximum of about 25% for the $A_{n,2}$ configuration and then decreases to about 23% for the $A_{n,5}$ configuration.

This interesting observation indicates the possibility of adopting a maximum annual $\bar{\eta}_{sol-ele}$ efficiency of the system as an optimisation criterion for dish-Stirling systems. Clearly, the maximum $\bar{\eta}_{sol-ele}$ depends on the technical characteristics of the

engine, the aperture area of the reflector and the hourly frequency distribution of direct solar radiation characteristics of the installation site. Therefore, for the purposes of the analyses that will be shown below in this part, the optimal configuration for Lampedusa is called $A_{n,2}$.

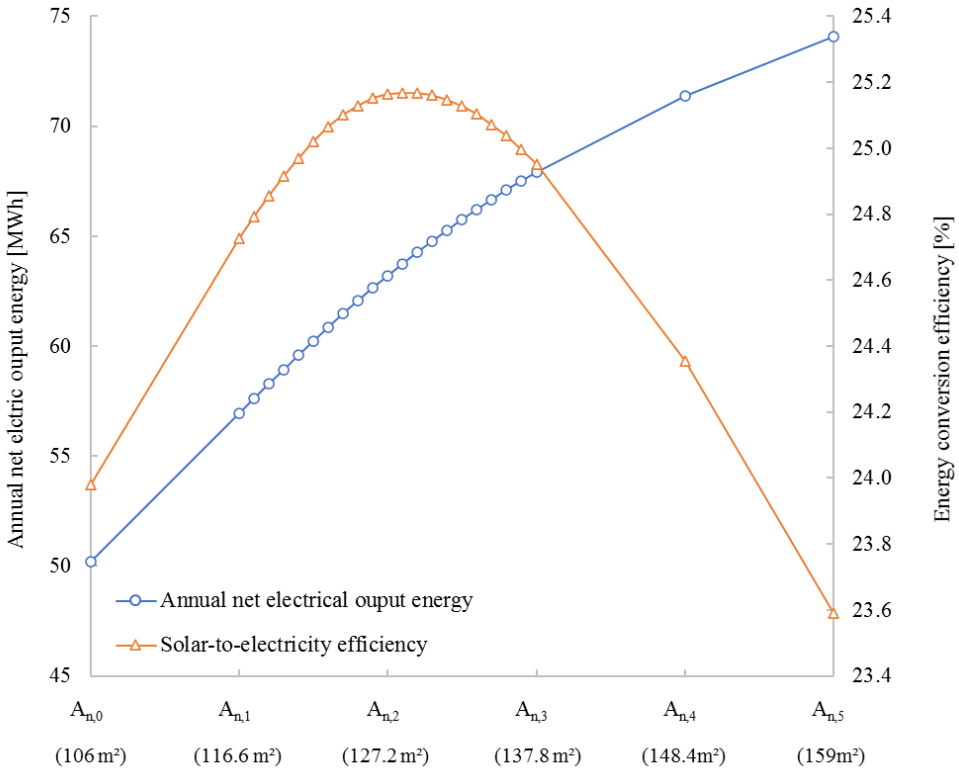

Figure 44. The annual net electricity output and the solar-to-electric conversion efficiency assessed for each of the investigated configurations of the dish-Stirling system located at Lampedusa

Once the energy production values for the different configurations of dish-Stirling concentrators were calculated it was possible to estimate their LCOE values using the expression described by *Equation (4.8)*. Lampedusa was considered as the reference location for these analyses, since, among those considered, it is the one characterised by the highest values of annual direct solar irradiation (about 2060 kWh/(m^2·year). For a basic collector ($A_{n,0}$) installed at this location, an LCOE = 0.47 €/kWh was deduced

assuming its current installed cost. For the $A_{n,2}$ configuration, instead, the LCOE value was reduced to 0.37 €/kWh, consistent with the fact that this configuration can generate more electric energy in one year (about E_t = 63.2MWh$_e$/year). The $A_{n,2}$ configuration, in fact, can be considered to be optimised for the typical solar radiation conditions of the central Mediterranean, as described above. Assuming then an annual installed cost reduction equal to that of the other CSP technologies in the last decade (about -334 kW$_p$/year) it was possible to simulate a feasible trend over time of the LCOE for the same plant configuration and location. The result of this analysis is represented in *Figure 45* along with the global weighted average of LCOE recorded for all the other solar technologies (CSP and PV) in the last decade [107].

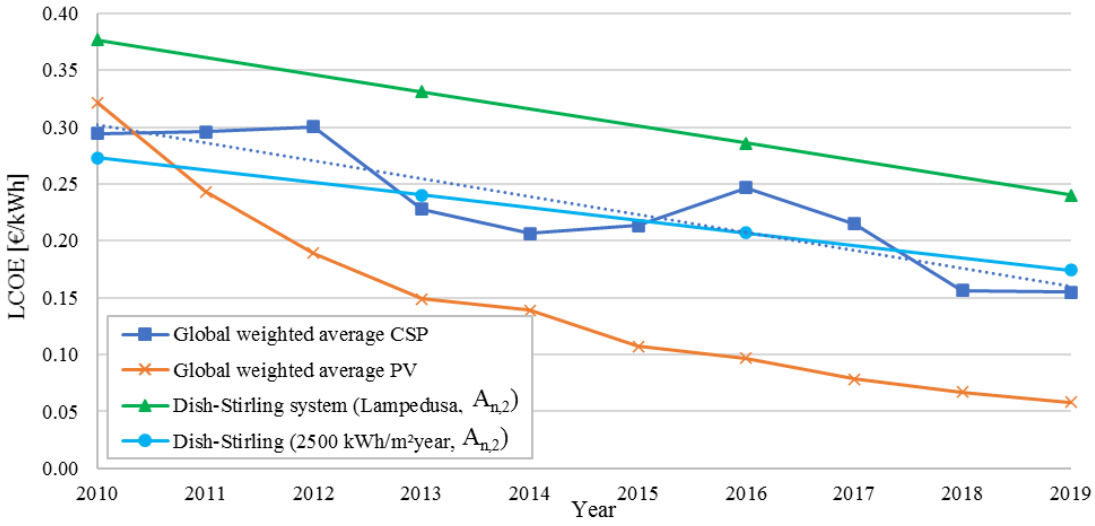

Figure 45. Comparison between the LCOE simulated for dish-Stirling systems and the global weighted average LCOE of the other solar technologies recorded between 2010-2019

These results show, for the considered dish-Stirling collector, an LCOE reduction tendency similar to that of the other CSP systems (dotted line in *Figure 45*) even though the LCOE values of the dish-Stirling are always higher than the other systems. In fact, after 10 years the dish-Stirling system of Lampedusa would be characterised by an LCOE = 0.24 €/kWh while for all the other CSP technologies this value is equal to about LCOE = 0.15 €/kWh. The results of this analysis confirm that the area of the Mediterranean investigated in this study is characterised by DNI levels (ranging between 1800-2000 kWh/(m^2·year)), which are at the lower limit of those considered of interest for power

generation through CSP systems. However, if the same analysis is conducted for a dish-Stirling plant located at a hypothetical geographical position characterised by annual DNI values of about 2500 kWh/(m^2·year), similar to those of the sites where CSP plants are typically built, lower values of the LCOE are obtained for dish-Stirling concentrators (see *Figure 45*). The electricity production used for this analysis was extrapolated from the linear correlation of *Figure 43* for the $A_{n,2}$ configuration corresponding to an annual DNI value of 2500 kWh/(m^2·year). The same approach was then repeated considering DNI variables between 2000 and 3000 kWh/(m^2·year) and assuming an installed cost of the $A_{n,2}$ configuration corresponding to that of the tenth year. The result of this calculation, plotted in *Figure 46*, shows an interesting outcome of this study: if the dish-Stirling systems, with optimised collector extensions, are realised in large numbers in geographical zones characterised by annual DNI values of between 2400 and 2700 kWh/(m^2·year), the expected current value of the LCOE of this technology would conform to that of other CSP systems.

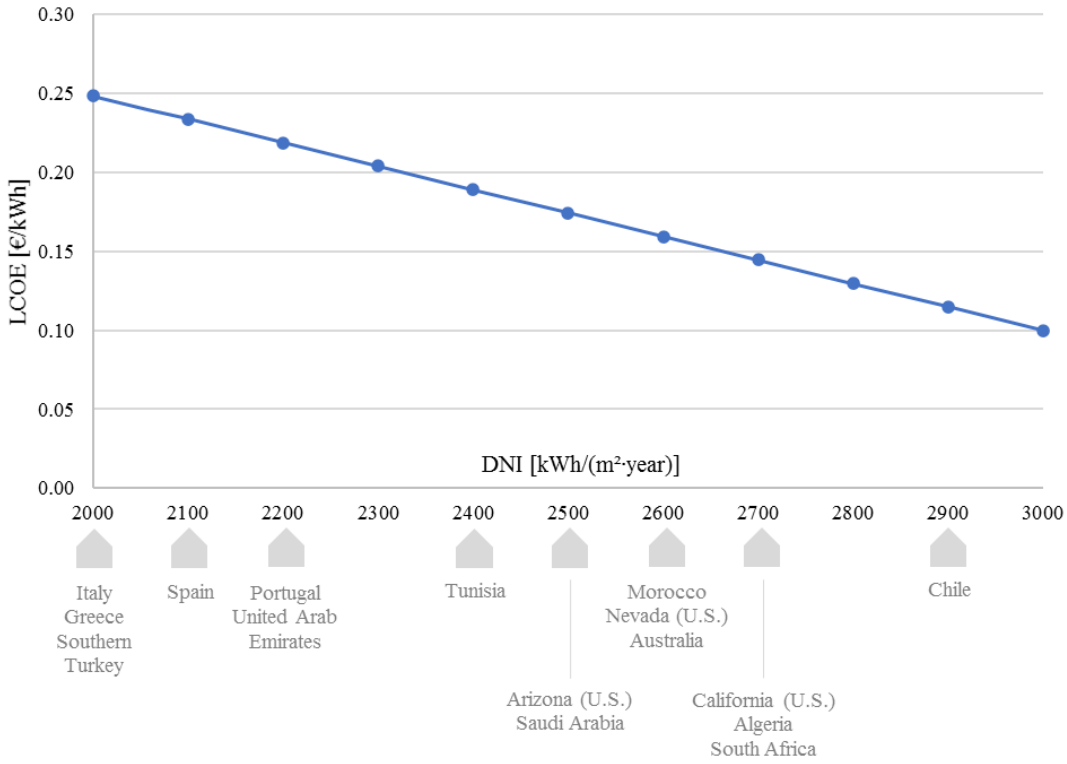

Figure 46. LCOE variations as a function of the DNI levels for $A_{n,3}$ configuration considering the installed cost assumed at the tenth year

Furthermore, assuming the same $I_0^{(i)}$ function already hypothesised for the LCOE analyses and considering the E_t of the 42 plants in *Table 12*, the new incentive scheme proposed in this study was verified. For each of these cases, in fact, the yearly variation of the feed-in tariff $T_{feed-in}^{(i)}$ was calculated using the expression described by *Equation (4.12)*. These functions were then averaged to define a single regional feed-in tariff function. This function represents the variations of the feed-in tariffs dedicated to plants falling under the incentive plan at the *i*-th calendar year after its entry into force. The result of these calculations (plotted in *Figure 47*) shows that the average tariff varies linearly passing from an initial value of $T_{feed-in}^{(0)}$ = 0.46 €/kWh to a final value of $T_{feed-in}^{(9)}$ = 0.27 €/kWh. By using this function, the DPBT of each of the 42 cases was calculated using *Equation (4.9)* and the main hypothesis of the proposed incentive scheme was verified, that is: the 42 DPBT values of *Table 13* remain, with a good approximation, constant regardless of the calendar year in which each plant is admitted to the incentive plan.

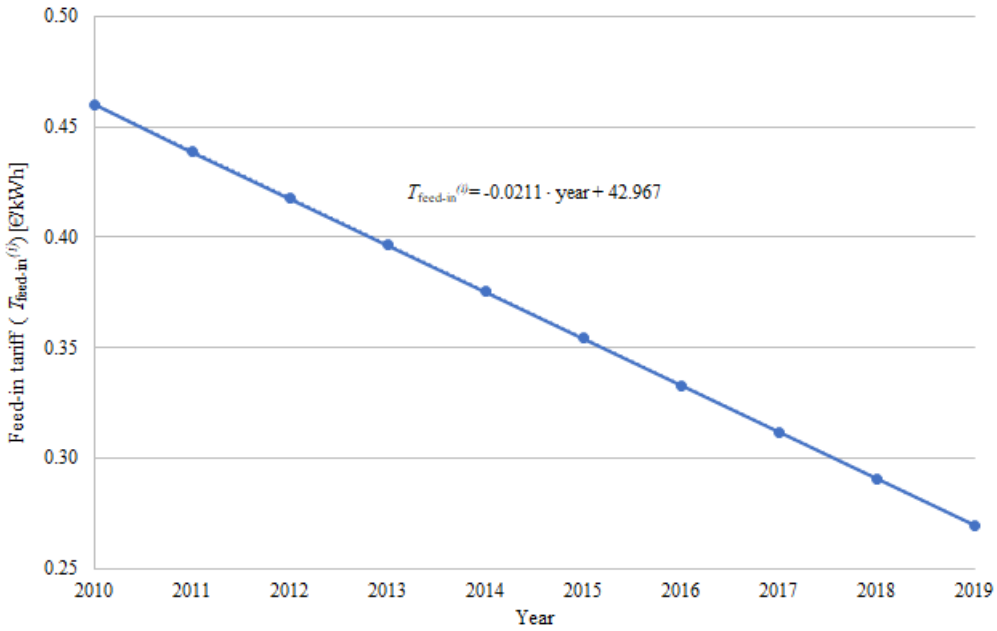

Figure 47. Feed-in tariff variation over 10 years according to the proposed incentive scheme

These DPBT values reported in *Table 13* for all the analysed cases show that the optimised dish-Stirling configuration ($A_{n,2}$) installed at the most productive location (e.g., Lampedusa) presents DPBT values ranging around 15 years.

Table 13. DPBT values calculated for the 42 analysed cases expressed in years.

DPBT$^{(1)}$	**$A_{n,0}$**	**$A_{n,1}$**	**$A_{n,2}$**	**$A_{n,3}$**	**$A_{n,4}$**	**$A_{n,5}$**
Brindisi	28.9	20.0	15.8	13.8	12.7	12.1
Cagliari	20.5	15.5	12.9	11.6	10.9	10.4
Lampedusa	19.3	14.8	12.4	11.1	10.3	9.9
Naples	28.3	19.7	15.9	14.0	13.0	12.4
Palermo	29.6	20.2	16.1	14.2	13.1	12.4
Ragusa	22.0	16.4	13.5	12.0	11.2	10.7
Rome	30.7	20.7	16.5	14.4	13.3	12.6
DPBT$^{(10)}$	**$A_{n,0}$**	**$A_{n,1}$**	**$A_{n,2}$**	**$A_{n,3}$**	**$A_{n,4}$**	**$A_{n,5}$**
Brindisi	30.6	20.2	15.8	13.8	12.8	12.2
Cagliari	20.4	15.3	12.8	11.5	10.8	10.4
Lampedusa	19.1	14.5	12.1	10.8	10.2	9.8
Naples	29.8	19.9	15.9	14.0	13.0	12.5
Palermo	31.4	20.5	16.2	14.2	13.2	12.5
Ragusa	22.1	16.2	13.3	11.9	11.1	10.7
Rome	32.9	21.1	16.5	14.5	13.4	12.8

Finally, by means of *Equation (4.9)*, the NPV values were calculated for all cases, considering their variations in the first ten years. The NPV values relative to the first and tenth years are shown for comparison in *Table 14*. These results show that the profitability of investments in plants falling under the incentive scheme in the tenth year since its entry into force is almost halved compared to those of plants incentivised since the first year.

Table 14. NPV values of the 42 analysed cases calculated at the first and tenth year since the entry into force of the incentives

NPV(1)	**$A_{n,0}$**	**$A_{n,1}$**	**$A_{n,2}$**	**$A_{n,3}$**	**$A_{n,4}$**	**$A_{n,5}$**
Brindisi	-€ 8,613	€ 17,768	€ 43,098	€ 62,207	€ 75,508	€ 85,322
Cagliari	€ 15,499	€ 44,607	€ 70,689	€ 89,793	€ 103,229	€ 113,136
Lampedusa	€ 20,598	€ 50,872	€ 78,937	€ 99,429	€ 114,170	€ 125,170
Naples	-€ 7,453	€ 18,871	€ 42,633	€ 60,103	€ 72,396	€ 81,340
Palermo	-€ 9,752	€ 16,482	€ 40,665	€ 58,313	€ 71,191	€ 80,826
Ragusa	€ 9,404	€ 38,195	€ 65,138	€ 84,279	€ 97,846	€ 107,912
Rome	-€ 10,225	€ 11,905	€ 32,117	€ 47,013	€ 57,613	€ 65,435
NPV(10)	**$A_{n,0}$**	**$A_{n,1}$**	**$A_{n,2}$**	**$A_{n,3}$**	**$A_{n,4}$**	**$A_{n,5}$**
Brindisi	-€ 5,932	€ 8,801	€ 22,916	€ 33,377	€ 40,424	€ 45,423
Cagliari	€ 8,235	€ 24,570	€ 39,127	€ 49,585	€ 56,711	€ 61,765
Lampedusa	€ 11,231	€ 28,251	€ 43,973	€ 55,246	€ 63,140	€ 68,836
Naples	-€ 5,251	€ 9,449	€ 22,643	€ 32,140	€ 38,596	€ 43,083
Palermo	-€ 6,602	€ 8,045	€ 21,486	€ 31,088	€ 37,888	€ 42,781
Ragusa	€ 4,654	€ 20,802	€ 35,866	€ 46,345	€ 53,549	€ 58,696
Rome	-€ 7,640	€ 6,842	€ 20,018	€ 29,571	€ 36,199	€ 40,934

Moreover, as indicated by the negative NPV values in *Table 14*, the investment in the basic configuration of the dish-Stirling $A_{n.0}$ collector (which is the one currently operating in Palermo) would not be profitable, from a financial point of view, not even for plants falling under the first year of incentives.

4.5 Outcomes

The annual solar-to-electric conversion efficiency of dish-Stirling systems can be increased by optimizing the size of the collector aperture area to the hourly frequency distributions of direct normal irradiance typical of the installation site. Here, a new energy model of the dish-Stirling concentrator capable of carrying out this kind of optimization

analysis is presented. The numerical model, calibrated with the real operating data of a 32 kW_p dish-Stirling system located in Palermo (Italy), was used to assess the annual energy production of six different plant configurations at seven different locations in the central Mediterranean. In this geographical area, the annual direct solar irradiation varies between 1800 and 2060 kWh/(m^2·year) with annual hourly frequency peaks of about 750 hours at DNI classes of between 700 and 800 W/m^2. The results of the numerical simulations show that the current dish-Stirling configuration presents an average annual solar-to-electric conversion efficiency of 24%, being able to produce between 40 and 50 MWh_e/year of electricity at the typical direct normal irradiance range at the analysed locations. On the other hand, an optimised configuration of the collector, designed by expanding the collector opening area by 20% to allow a peak power output of the Stirling engine at DNI = 700-800 W/m^2, can increase the energy production by about 26% at the most productive site. This configuration, which could be implemented with a modest increase in the installed costs, can also permit a reduction of the current estimated Levelized Cost of Energy of this technology from 0.47 to 0.37 €/kWh. The latter value of Levelized Cost of Energy would be further reduced to 0.24 €/kWh after 10 years if it is assumed that the installed cost reduction trend is similar to that of other concentrating solar power systems in the last decade (about -334 kW_p/year).

Interestingly, repeating the latter analysis for a geographical location with annual direct normal irradiation values similar to those of the zones where large concentrating solar power systems are typically built, results in a Levelized Cost of Energy of 0.17 €/kWh which is a value close to the current one of all the other concentrating solar power systems. In the analyses above, it is assumed that the reduction over time of installed costs of dish-Stirling systems is due to the effect of economies of scale triggered by a greater diffusion of these systems in the concentrating solar power generation market.

To this end, a new incentive scheme dedicated to dish-Stirling plants has been also proposed, structured to have a feed-in tariff that varies according to the year in which the plant falls under the incentive scheme and designed to guarantee that the discounted payback time of the investments is constant regardless of the year the plant is built. The proposed scheme was tested considering the energy production calculated for solar collectors in the central Mediterranean, demonstrating that it would be possible to obtain discounted payback time values of around 10 years for the optimised plant configuration

located in the most productive site. This scheme is characterised by a regional feed-in tariff variable from 0.46 €/kWh in the first year to 0.27 €/kWh in the tenth.

In future research, the analyses presented in this part of the thesis for dish-Stirling systems could be extended and specialised to geographical locations with direct normal irradiance levels higher than those in the central Mediterranean. With this aim, the new simplified calculation method that was developed in the thesis can be used. This method allows the simulation of the annual electricity production of a dish-Stirling system from the frequency histograms of 1-hour direct normal irradiance series. This new approach may also be used for the optimization of dish-Stirling systems using direct normal irradiance hourly frequency distributions that are generated through suitable statistical methods for a macro-climatic area.

Nomenclature

a_1	first parameter of the Stirling engine mechanical efficiency curve [-]
a_2	second parameter of the Stirling engine mechanical efficiency curve [W]
A_n	net effective aperture area of the reflector [m^2]
$A_{n,i}$	net effective aperture area of the reflector for the i-the configuration of 6 (*i* ranges from 0 to 5) [m^2]
A_r	receiver aperture area [m^2]
CF_t	cash flow of the *t-th* year of the lifetime of the project [€]
DNI_e	the annual effective direct solar irradiation [kWh/(m²·year)]
$\dot{E}_n$	net electric output power produced by a dish-Stirling system [W]
$(\dot{E}_n)_{hor}$	net electric power produced by the dish-Stirling system calculated by the hourly-based approach [W]
$\dot{E}_p^{ave}$	average value of the parasitic plant consumption [W]
E_s	solar direct normal energy corresponding to each I_b bin [kWh/m²]
E_t	amount of electricity produced in the year *t*-th [kWh]
$(E_t)_{hor}$	electricity produced in the year *t*-th calculated by the hourly-based approach [kWh]
$(\overline{E}_t)_{hor}$	annual average electricity calculated by the hourly-based approach [kWh]
$(E_t)_{sim}$	electricity produced in the year *t*-th calculated by the simplified approach [kWh]
$(\overline{E}_t)_{sim}$	annual average electricity calculated by the simplified approach [kWh]
$(\dot{E}_t)_{sim}$	average electric power output calculated according to the simplified approach [kWh]
F_t	fossil fuel cost [€]
h_r	receiver convective coefficient [W/(m²·K)]

i	*i*-th year since the beginning of the incentive plan
I_b	solar beam irradiance [W/m^2]
$\bar{I}_b$	the middle-point value of the I_b bin [W/m^2]
$I_b^{\max}$	upper limit of the direct solar irradiance [W/m^2]
$I_b^{\min}$	lower limit of the direct solar irradiance [W/m^2]
I_t	investment cost that occurs in the year t [€]
M_t	operation maintenance cost that occurs in the year t [€]
N	number of years of the time series of solar data [year]
n	lifetime of the power plant under consideration [year]
n_{I_b}	number of cases falling into each I_b bin [h]
$\bar{n}_{I_b}$	annual average values of n_{I_b} [h]
$P_{\text{r,solar}}$	bonus for integrated solar plant [€/kWh$_e$]
$\dot{Q}_{rej}$	heat power rejected from the receiver by a cooling fan [W]
$\dot{Q}_{r,\text{out}}$	heat loss power from the receiver [W]
$\dot{Q}_{S,in}$	thermal input power of the Stirling engine [W]
$\dot{Q}_{S,in}^{\max}$	upper limit of the thermal input power of the Stirling engine [W]
$\dot{Q}_{S,in}^{\min}$	lower limit of the thermal input power of the Stirling engine [W]
r	interest rate used for discounting expenditures and revenues [-]
R_T	temperature correction factor [-]
t	*t*-th year of the lifetime of the power plant
T_0	reference temperature [°C]
T_{air}	air temperature [°C]
$\bar{T}_{air}$	average air temperature of each I_b bin [°C]
T_{b}	base incentive tariff [€/kWh$_e$]
$T_{feed-in}^{(i)}$	feed-in tariff [€/kWh$_e$]
T_r^{ave}	average receiver temperature [°C]

T_{sky}	apparent sky temperature [°C]
$\dot{W}_S$	mechanical output power of the Stirling engine [W]

Greek letters

ΔI_b	width of each I_b bin [W/m^2]
ε_r	the effective emissivity of the receiver [-]
η_o	the optical efficiency of the system [-]
η_{cle}	the cleanliness index of the collector mirrors [-]
η_{cle}^{ave}	the average cleanliness index of the collector mirrors [-]
η_e	the electric efficiency of the alternator [-]
$\eta_{sol-ele}$	the instantaneous solar-to-electric energy conversion efficiency [-]
$\bar{\eta}_{sol-ele}$	the annual solar-to-electric energy conversion efficiency [-]
σ	the Stefan-Boltzmann constant [W/(m²·K^4)]

Acronyms

CO_2	Carbon dioxide
CSP	Concentrating Solar Power
DNI	Direct Normal Irradiance [W/m²]
DPBT	Discounted Payback Time [year]
GHG	Greenhouse Gases
LCOE	Levelized Costs of Electricity [€/kWh$_e$]
NPV	Net Present Value [€]
NREL	National Renewable Energy Laboratory
OECD	Organisation for Economic Co-operation and Development
PCU	Power Conversion Unit
PV	Photovoltaic
PVGIS	Photovoltaic Geographical Information System
SBP	Schlaich Bergermann und Partner

TMY Typical Meteorological Year

Chapter 5

A cogenerative layout for a dish-Stirling solar concentrator

This chapter investigates the possibility of modifying the operation mode of the dish-Stirling system from pure electric to cogenerative, exploiting the thermal energy recovered at low temperature through the Stirling engine cooling system. To this end, the energy and environmental benefits that could be obtained by integrating a dish-Stirling cogeneration concentrator into the energy systems used to satisfy the air conditioning demand of an office building are assessed. Therefore, two typical reference energy systems are explored and include, firstly, a natural gas boiler for heating and air-cooled chillers for cooling periods; secondly, a reversible heat pump for both heating and cooling. For both systems, a dish-Stirling concentrator is assumed to operate first in electric mode and then in a cogenerative mode.

5.1 Introduction

The use of renewable energy sources along with energy-saving measures are the two main routes to decarbonizing the building sector [125]. However, the integration of

renewable technologies with buildings is challenged by the need to align production and demand energy profiles, which often do not match [126]. In this regard, it is necessary to consider, on the one hand, the energy needs (in terms of electricity, energy for heating and cooling) of buildings which are largely variable over time, and, on the other hand, the aleatory nature of renewables such as solar and wind energy [127]. Then, to mitigate intermittency problems and to perform peak shaving, the use of renewable technologies cannot disregard the installation of efficient energy storage systems or energy auxiliary systems [128].

The dish-Stirling solar concentrator, which couples a paraboloidal reflector with a Stirling engine, is the newest CSP technology to be developed and the most efficient in solar-to-electricity conversion [49]. Furthermore, such systems, whose producibility is highly dependent on the level of normal solar irradiation of the installation site [22], can be employed in several applications [31]. This technology can be coupled with a thermal storage system [34], or it can be hybridized to extend the production period to hours of the day during which solar radiation is not available [35], it can be used in both centralized [37] and distributed power generation for electricity supplying remote rural areas [36], and it can also be combined with desalination systems to produce potable water [38].

Other interesting applications of dish-Stirling technology include the possibility to operate it in pure electric mode or cogenerative mode [32]. Referring to the pure electric mode, in [129], the authors analysed and compared the energy performance of a photovoltaic system and a dish-Stirling system integrated into a building located in Lebanon to meet the electricity demand. With the criterion of maximising the use of the building rooftop area, it was observed that the dish-Stirling system, with a peak electrical power of 25 kW_p, covers 68% of the total electric energy demand, compared to 12% obtained using the PV system (9.3 kW_p).

Regarding the cogenerative mode, research has shown the possibility of using a dish-Stirling system in the building sector to satisfy energy demand for heating, cooling, ventilation, domestic hot water, and electricity. In [33], energy, environmental and economic analyses of a dish-Stirling cogenerative system (10 kW_p), covering the electricity, heating, and cooling energy demands of a residential building, were carried out. Since the building energy requirements and the engine output power depend on the climatic conditions and the level of solar beam irradiation, the reference building was

considered to be located in five different cities in Iran achieving average primary energy savings of about 139 MWh/y. In [130], the modelling and optimization of a micro-CHP system with a solar-powered Stirling engine were carried out. This system achieved an energy-saving rate of 15% during most of the year for a reference building located in three different Iranian cities. In [120], a combined CHP plant is proposed for the first time, implementing a dish-Stirling collector field, a seasonal geothermal storage, and a water-to-water heat pump system. The cogeneration plant has been designed both to supply thermal energy to the heating system of a non-residential building at Palermo University and to produce electrical energy. The results of the simulations show that by installing a single dish-Stirling concentrator, it is possible to cover 59% of the building's annual thermal loads using the energy produced by the solar system, with a 55% reduction in CO_2 emissions.

5.2 Assessing the energy-saving potential of a dish-Stirling concentrator integrated into energy plants in the tertiary sector

The following part of the thesis assesses the benefits achievable by integrating the dish-Stirling concentrator into energy plants used to cover the energy demand of tertiary buildings. Two typical plants for space heating and cooling are identified to be eligible for the integration of this technology. The first one consists of systems that use natural gas and electricity, while the second one includes only electrically driven systems. Meanwhile, to improve the achievable energy savings, two alternative operating strategies of the solar concentrator are proposed. More specifically, a fully electric mode is compared to a cogenerative mode, where the heat recovered from the Stirling engine is used to meet heating demand. Two further contributions of the proposed manuscript could be identified as follows:

- The analysis proposes the integration of the detailed modelling of the dish-Stirling concentrator with the ones of the heat pump and chiller. Such an approach allows for a better understanding of the plant behaviour, along with a more reliable assessment of the energy-saving and avoided CO_2 emissions.

- The study investigates the feasibility of a cogeneration system based on the dish-Stirling technology, in localities characterized by Direct Normal Irradiation (DNI) lower than 2000 kWh/m²/y.

To explore these topics, an office building located in Palermo (Southern Italy) is assumed as a case study. Two energy plants commonly adopted in this sector are considered: (i) a natural gas (NG) boiler for meeting thermal demand during the winter and an air-cooled chiller during the summer; and (ii) a reversible heat pump (HP) for providing both heating and cooling. In both plants, the possibility to operate the concentrator in electric or cogenerative mode is investigated. The numerical model of the dish-Stirling systems was validated by experimental data collected during the monitoring of the facility test site of Palermo [22]. The energy demands of the selected case study were available from energy audits performed in the field. A simplified economic analysis is also carried out to highlight factors that could affect the economic viability of the proposed investments.

5.3.4 Technical features and modelling of main plant components

In this section, the models of the main plant components are explained in detail. Such models are then used to dynamically simulate the operation of the investigated energy plants. If to assess the annual energy production of the dish-Stirling solar concentrator it was used the reference numerical model presented in *Paragraph 3.1* and related *Equation (3.4)*, on the other hand, both operating models of the reversible air-to-water heat pump and an air-cooled chiller are shown below. The technical features of these reference systems are reported in *Table 15*. In particular, the cooling/heating capacities were selected based on the peak of the cooling/heating demand of the case study. For all of them, R410A is assumed as the refrigerant, and Electronic Expansion Valve (EEV) is used as the metering device. Brazed plate heat exchangers are used to heat and cool water. In the air-cooled chiller, a fin and tube heat exchanger with induced-draft fans is used on the condenser airside. Each unit is equipped with scroll compressors. The delivered cooling/heating capacity is controlled by activating/deactivating one compressor at a time for the air-cooled chiller. Conversely, a variable frequency drive is used on the heat pump.

Table 15. Main technical features of the air-cooled vapour compression chillers and reversible heat pump

	Reversible Heat Pump Cooling capacity* 56 kW Heating Capacity** 57 kW	**Air-Cooled Chiller*** Cooling capacity* 55 kW
Refrigerant	R410A	R410A
Condenser	Micro-Channels Heat Exchanger (Number of exchangers: 1; Surface 2.96 m^2, Fin pitch 1 mm) 2 Fan, 1.95 kW each (Air Flowrate per fan 16,388 m^3/h)	Fin and Tube Heat Exchanger (Tube diameter 9.2 mm, 3 tube rows, fin density 16 fins per inch) 2 Fan, 1.20 kW (Air Flowrate per fan 12,362 m^3/h)
Metering Device	Electronic Expansion Valve	Electronic Expansion Valve
Evaporator	Brazed Plate Heat Exchanger Dimension in (mm) Width=526, Height=119, Length 291 Number of plates 92 1 Pump, 1.0 kW (Water flow 9.2 m^3/h)	Brazed Plate Heat Exchanger Dimension in (mm) Width=526, Height=119, Length 291 Number of plates 92 1 Pump, 1.0 kW (Water flow 9.2 m^3/h)
Compressor Type	Scroll	Scroll
Swept Volume [cm^3/rev]	88.32	103.5
Compressors Power [kW]	9.44 (each)	12.4 (each)
Number of compressors	2	2
Oil Charge [dm^3]	6.6	7.2
Refrigerant Charge [kg]	15	19.9

[1] Heat Pump's cooling capacity refers to the following boundary conditions: variation of the water temperature in the evaporator: 12-7 °C, and outdoor air temperature equal to 35 °C (such boundary conditions are also used for the air-cooled chiller).
[2] Heat Pump's heating capacity refers to the following boundary conditions: variation of the water temperature in the condenser: 40-45 °C and outdoor air temperature equal to 7 °C.

Simulations of full-load and part-load operation were carried out using plant simulator IMST-ART v.3.80 [131]. This tool allows the performance of 1-D simulations for vapor-compression chiller systems, relying on detailed thermohydraulic modelling of heat exchangers, refrigerant lines, and accessories. Energy consumption and efficiency of

compressors were evaluated using the "catalogue data" option, which converts data from commercial compressor catalogues into efficiency and consumption curves. A constant 3 °C superheat at the evaporator outlet was assumed, thus replicating the operating mode of EEVs.

In *Figure 48*, the Coefficient of Performance (COP) and the Heating Capacity (HC) of the reversible heat pump are plotted versus the outdoor air temperature (ODT) and the part load ratio (PLR). The black points in *Figure 48* were obtained from the IMST-Art simulations at full (PLR=100) and part-load conditions (PLR<100).

Then, multivariable regression was adopted to model the dependence of COP and HC on the two mentioned variables. The resulting equations are shown in the cited figures along with the corrected R-square. Similar graphs were obtained for the cooling-mode of the HP and the air-cooled chiller, not shown here for the sake of brevity. However, it was not possible to check the accuracy of the results since experimental data were not available for the investigated systems. Nevertheless, some published papers investigated the accuracy of simulation results from IMST-Art for chiller systems [132] commercial freezers [133], and heat pumps [134]. As shown in [133], experimental cooling capacity and power consumption are predicted by the software within a ±10% error band. Furthermore, the experimental evaporation and condensation temperatures are predicted within an error band of ±3 K. Other validation studies can be found in the following reference [131].

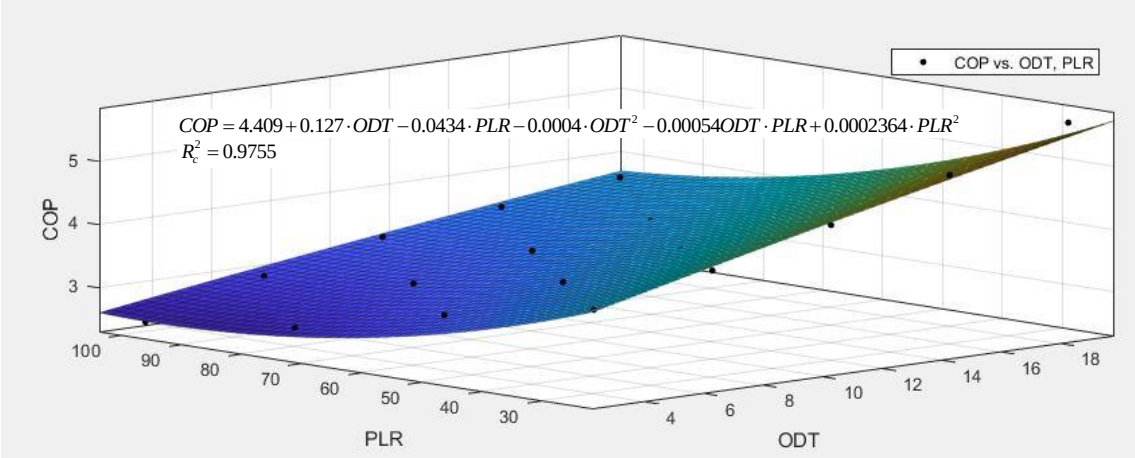

(a)

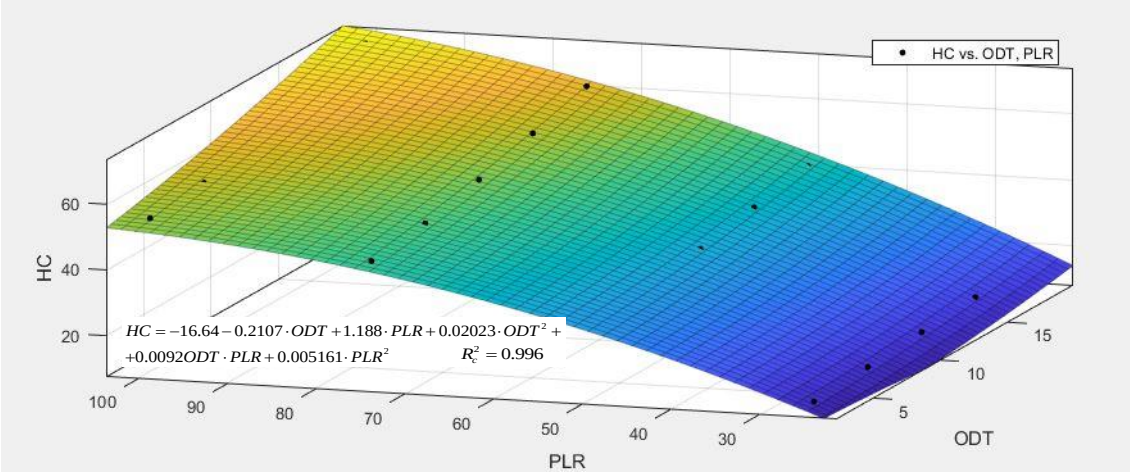

(b)

Figure 48. (a) Coefficient of Performance and (b) Heating Capacity of the reversible HP obtained from IMST-Art Simulations in case.

5.3.5 Description of the case study

An office building located in Palermo (Italy, 38.11°N; 13.36°E) was selected as a case study. In *Figure 49*, the following profiles are shown:

- the yearly cooling demand (Figure 49.a)
- the thermal demand which accounts for space-heating and domestic hot water (DHW) (*Figure 49.b*)
- the electricity demand related to the lighting system and office equipment operation (*Figure 49.c*).

Such profiles were available from energy audits performed in the framework of previous research [135].

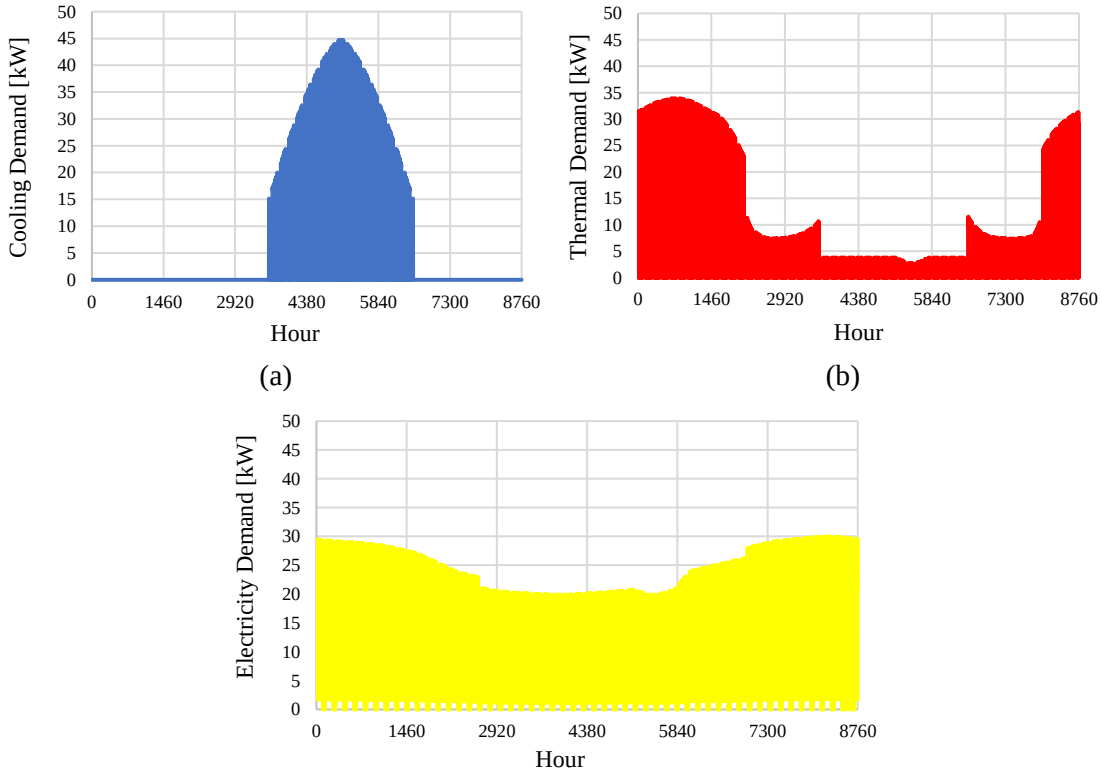

Figure 49. Hourly profiles of the case study: (a) cooling, (b) thermal, and (c) electricity demands [135]

The reference dish-Stirling concentrator is operating at the facility test site of the University of Palermo and described in *Paragraph 2.5* "*Reference dish-Stirling system*" and the most relevant technical data concerning the considered dish-Stirling system are summarized in *Table 1* reported in the same paragraph of this thesis. According to the energy model shown in *Paragraph 3.1* "*A validated energy model of a solar dish-Stirling system considering the cleanliness of mirrors*" [22], from *Equation (3.4)*, it is possible to deduce that the main variables influencing the producibility of the dish-Stirling system are the solar beam irradiation $\left(I_{\mathrm{b}}\right)$, the external air temperature $\left(T_{\mathrm{air}}\right)$, and the level of soiling of the mirrors $\left(\eta_{\mathrm{cle}}\right)$. *Figure 50* depicts the hourly frequency distribution of the solar beam irradiation with a bin of 50 W/m² and the average air temperature values

calculated for each interval, referred to Typical Meteorological Year (TMY) provided by the Meteonorm solar database for Palermo [78]. Meteonorm uses input data obtained by interpolating observed ground-based data, mainly global and diffuse radiation, along with the support of satellite images. Furthermore, the software takes into account the attenuation of direct solar radiation due to atmospheric turbidity, i.e. the presence of water vapour and aerosol particles, in the solar radiation modelling [136].

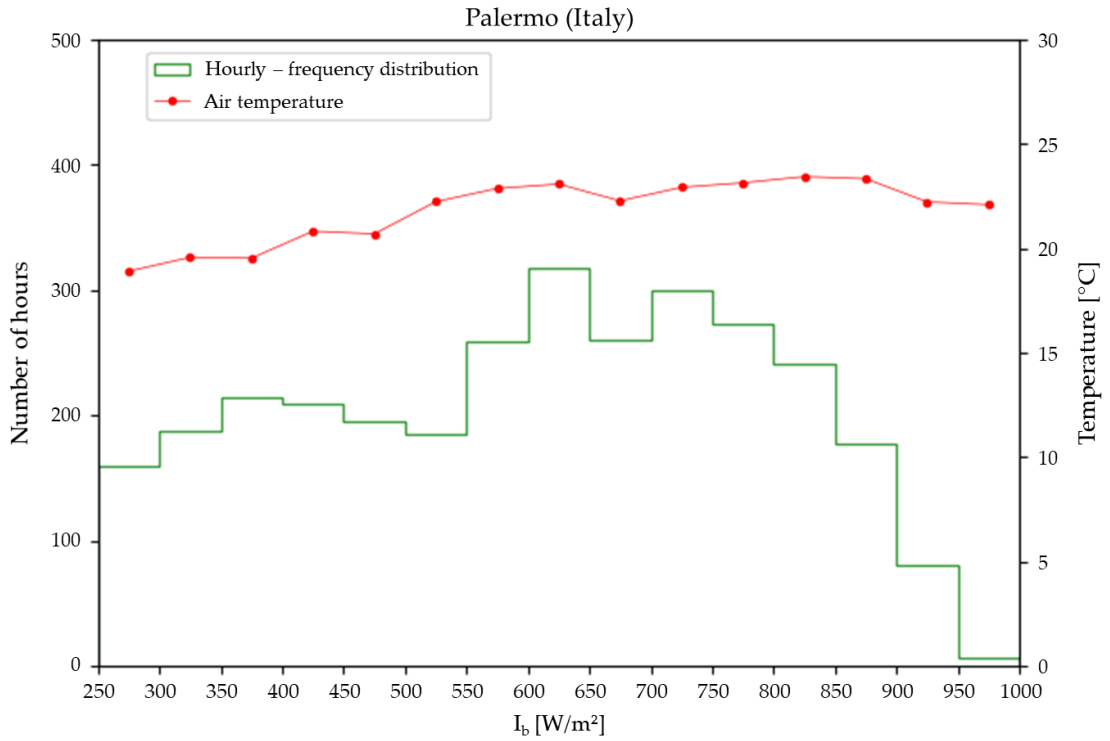

Figure 50. Hourly-frequency histogram (bin of 50 W/m²) of I_b and average air temperature for Palermo

As shown in *Figure 50*, the hourly frequency distribution of I_b for Palermo presents two peaks: one between 600 and 650 W/m² and the other one between 700 and 750 W/m². Both ranges are characterized by an average air temperature of approximately 23 °C. The annual normal solar irradiation value is equal to 1932.61 kWh/m²/y. Based on Meteonorm solar data and the reference energy model [22], the electrical production of the dish-Stirling system closely follows the seasonal trend of I_b, as shown in *Figure 51*. From simulations carried out in the present research, the cumulative annual production was found to be 46 MWh in Palermo.

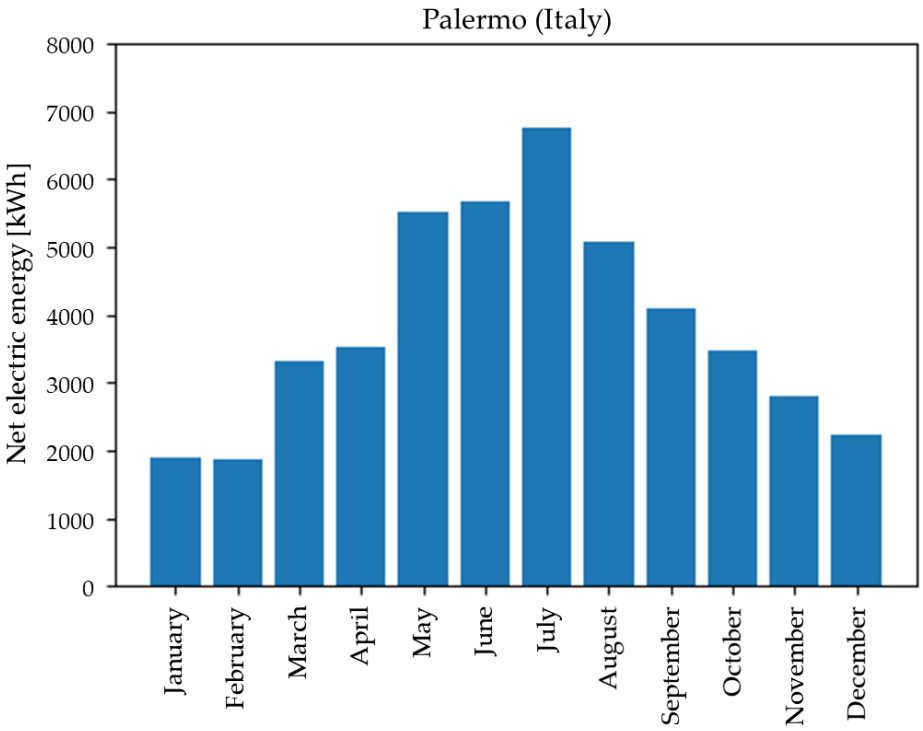

Figure 51. The monthly electric output energy of the dish-Stirling system at Palermo

5.3.5.1 Description of the investigated scenarios

Two alternative energy systems were assumed as reference plants to cover the demands of the case study. Such systems, here following indicated as System no. 1 and System no. 2, are representative of typical plants used in the tertiary sector for air-conditioning demand. Schemes of these are shown in *Figure 52*. Note that:

- In *System no. 1* (*Figure 52.a*), an NG boiler is used to cover the thermal demand during the winter. In particular, hot water at 65 °C is supplied to fan coil units, and hot water at 45 °C to meet the DHW demand. Conversely, an air-cooled chiller covers the cooling demand during the summer. The electricity consumed by the lighting, office equipment, and the air-cooled chiller is purchased from the local grid.
- In *System no. 2* (*Figure 52.b*), a reversible air-to-water HP covers both heating and cooling demands. Regarding DHW, electric heaters are used.

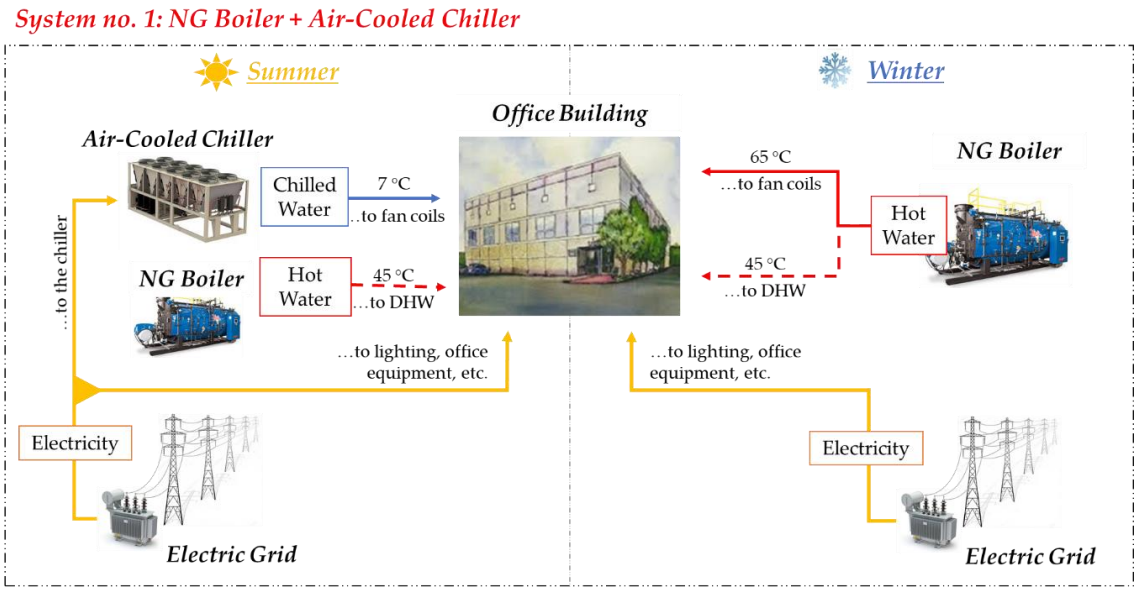

(a)

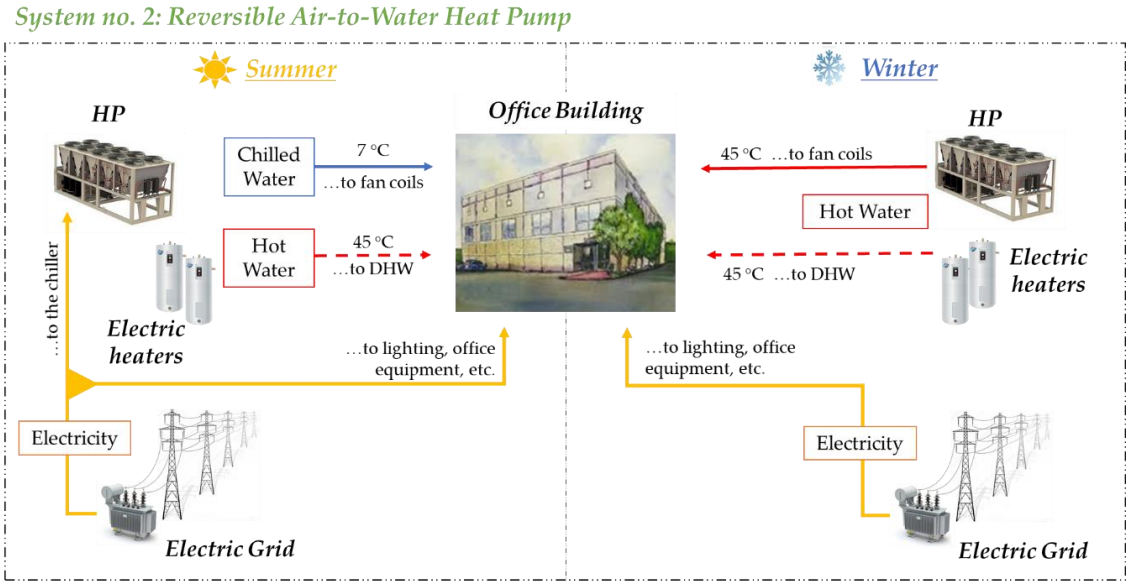

(b)

Figure 52. Schemes of the reference plants assumed for the case study: (a) System no. 1: NG boiler and air-cooled chiller, and (b) System no. 2: reversible heat pump

In both systems, it was assumed to integrate the reference dish-Stirling solar concentrator (see *Paragraph 2.5* "*Reference dish-Stirling system*") and the following operating strategies were examined:

- *Electric-mode*: the dish-Stirling system produces only electricity, and heat is not recovered.
- *Cogenerative-mode*: the dish-Stirling system produces both electricity and heat. To make such a heat flow useful for air-conditioning purposes, the temperature of the water exiting the cooler of the Stirling engine is increased from 40 °C to 50 °C. Such a temperature increase is achieved by shutting off the dry-cooler. A reduction in the efficiency and electric power of the solar concentrator is expected due to the higher compression temperature of the engine. However, the assumed increase of the Stirling-engine cold side temperature (about 10 °C) slightly affects the engine efficiency (about -0.05% is the observed reduction), according to the following experimental study [92].

Based on the previous management strategies, different scenarios could be conceived when the dish-Stirling system is integrated. For Systems no. 1, the schemes of the two scenarios are shown in *Figure 53*. Note that:

- *Scenario no. 1-A*: as shown in *Figure 53.a*, the dish-Stirling system produces only electricity which is used differently during the year. In particular, during the winter, such electricity is consumed by the lighting system and office equipment. Conversely, during the summer, it is also used to drive the air-cooled chiller. The thermal demand is covered using the NG boiler.
- *Scenario no. 1-B*: as shown in *Figure 53.b*, the dish-Stirling system produces both electricity and heat, used differently throughout the year. In particular, during the winter, the recovered heat is supplied to the air conditioning system. As a consequence, a fraction of thermal demand is not met by the boiler, and the amount of NG consumed decreases. Moreover, the produced electricity flow is consumed by the lighting system and office equipment. During the summer, the produced electricity is used to supply the air-cooled chiller, the lighting system, and office equipment. However, the heat flow recovered from the Stirling engine is at 40 °C since only DHW is needed. Indeed, it is not convenient to recover heat at a higher temperature which would reduce the electric power.

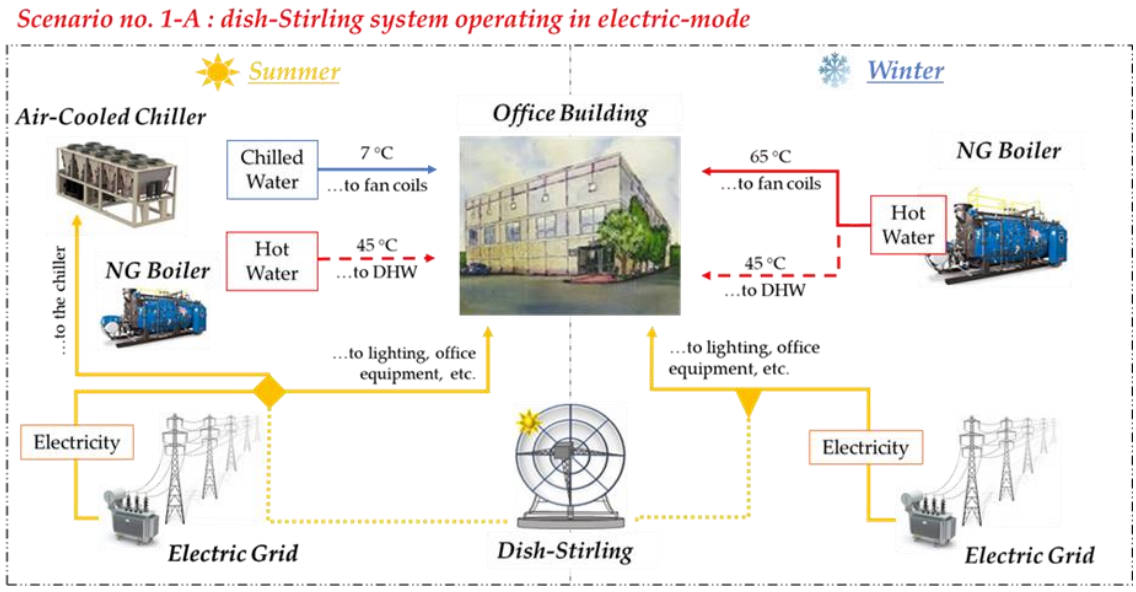

(a)

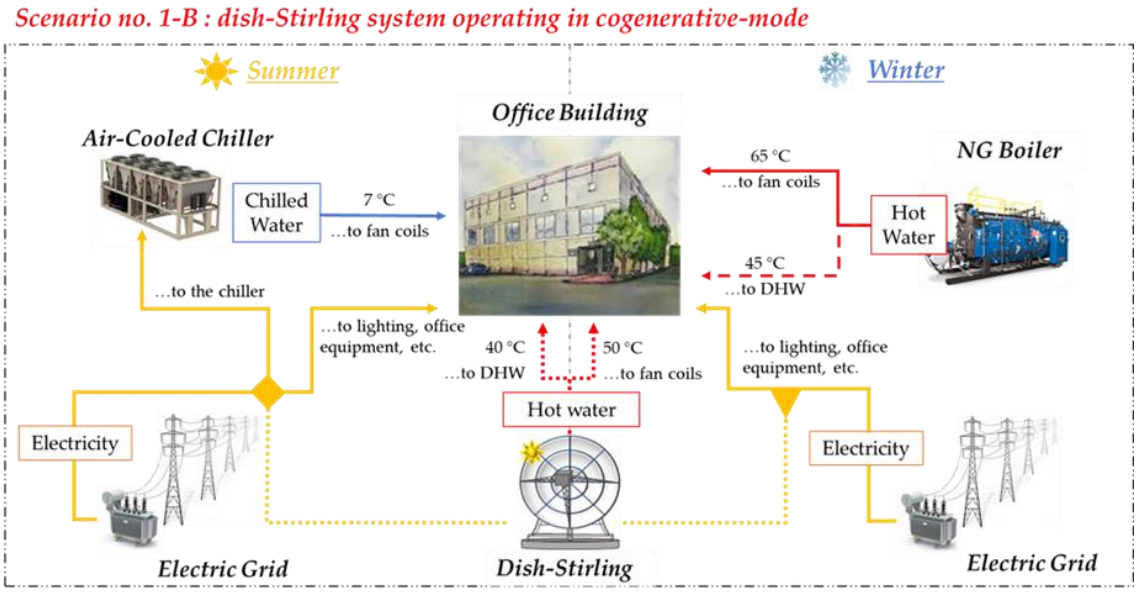

(b)

Figure 53. Improved scenarios for System no. 1: (a) dish-Stirling system operating in electric-mode, and (b) dish-Stirling system operating in cogenerative-mode

Like System no. 1, two scenarios were proposed for System no. 2, which are shown in *Figure 54*. Note that:

- *Scenario no. 2-A:* as shown in *Figure 54.a*, the dish-Stirling system produces only electricity which is used to operate the HP during the year. In those hours of low electricity demand, the electricity surplus is sold to the grid.
- *Scenario no. 2-B:* as shown in *Figure 54.b*, the dish-Stirling system operates in a cogenerative mode. In particular, like Scenario 1-B, during the winter, the recovered heat flow is used to supply the air-conditioning system, while the electricity is consumed mainly by the HP. Conversely, during the summer, the produced electricity is used to drive the HP, the lighting systems, and office equipment. Also, in this scenario, like Scenario 1-B the heat flow recovered from the Stirling engine is only used for DHW purposes.

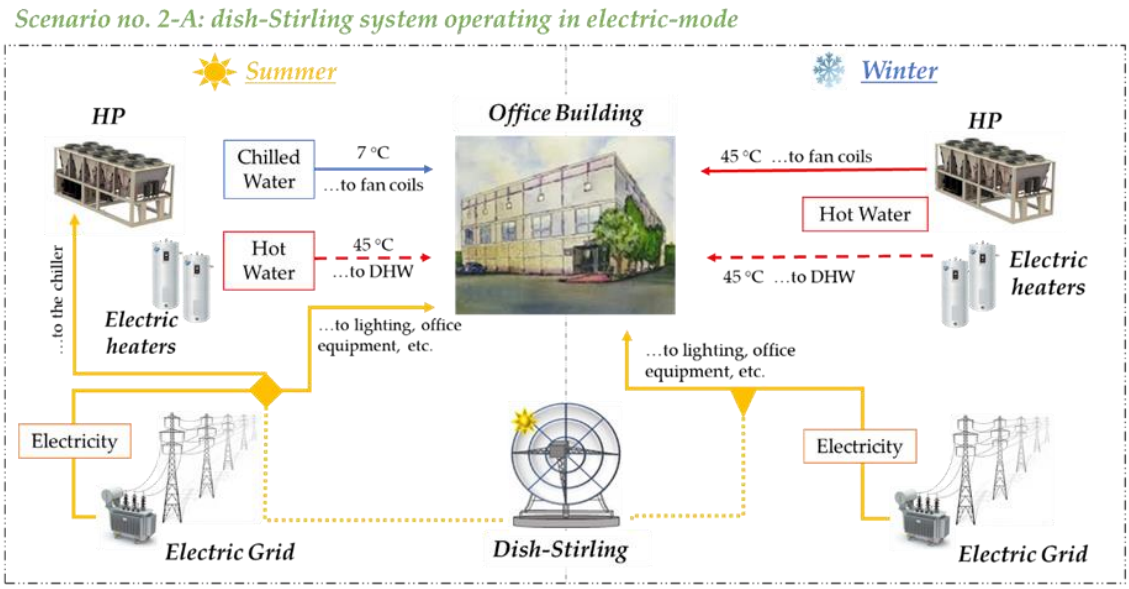

(a)

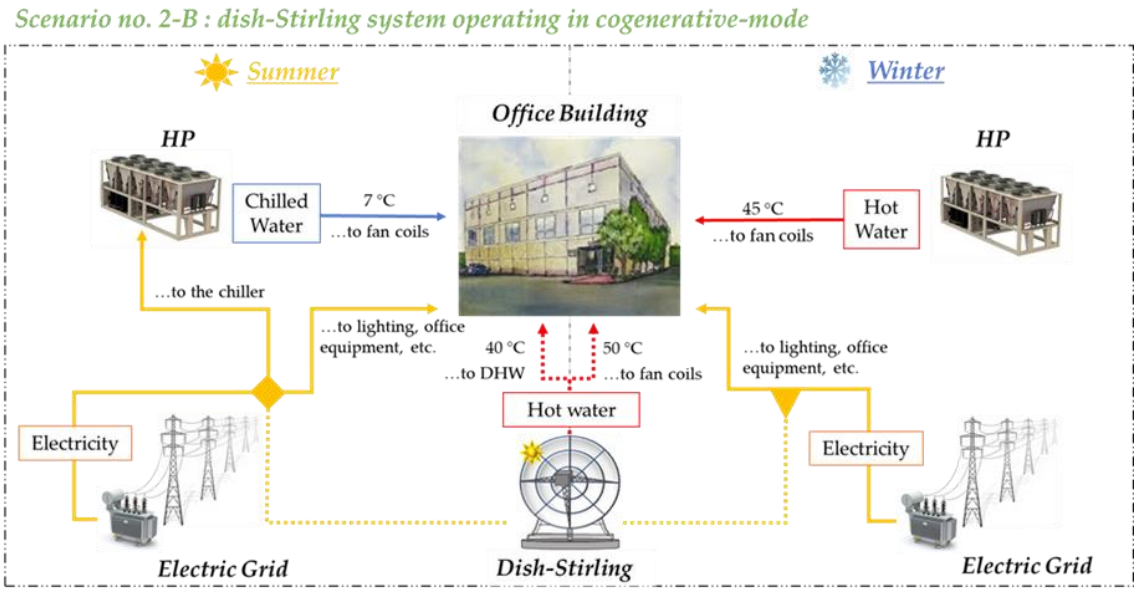

(b)

Figure 54. Improved scenarios for System no. 2: (a) dish-Stirling system operating in electric-mode, and (b) dish-Stirling system operating in cogenerative-mode

5.3.6 *Notes on performed simulations and definition of the environmental and economic indicators*

The models of the main plant components previously described were implemented and solved by TRNSYS [137] software. The dynamic simulation of the investigated plant configurations was performed on a one-hour step.

Concerning the achievable environmental benefits, only the reduction in CO_2 emissions was considered. Such a reduction was quantified by considering that the amount of electricity produced by the dish-Stirling system is not purchased from the electricity generation system of the country where the plant is operated anymore. *Equation (5.1)* was used for this purpose, where the emission factor $\left(\mu_e^{CO_2}\right)$ quantifies the kilograms of CO_2 emitted per kilowatt-hour of saved electricity $\left(E_{sav}\right)$. For instance, in Italy, according to [138], the emissions factor was estimated to be 0.485 kg_{CO_2}/kWh_{el}.

$$CO_2^{av} = \mu_e^{CO_2} \cdot E_{sav} \tag{5.1}$$

In *Equation (5.1)*, CO_2^{av} is measured in kilograms per year. The same approach was used to calculate the avoided CO_2 emissions resulting from the reduction in natural gas consumption. In this case, the emission factor $\mu_{NG}^{CO_2}$ was assumed to be 0.19 $kgCO_2/kWh$ NG.

The total installed cost of the dish-Stirling unit of Palermo amounted to 200,525 € (I_0). This cost was evaluated by taking into account the real costs incurred for the realization of this facility test site in 2017. To assess the economic feasibility of the four analyzed scenarios, the Net Present Value (*NPV*) and the Discounted Payback Time (*DPBT*) of the investment were assumed as economic and risk indicators. These indicators were determined by using the same equations stated in *Paragraph 4.2.3* "*LCOE analysis and definition of a new incentive scheme*" and for the reader's greater clarity they are shown again below.

The NPV was calculated according to Equation (5.2) as follows:

$$NPV = \sum_{t=1}^{n} \frac{CF_t}{(1+r)^t} \tag{5.2}$$

where: n is the useful lifetime of the plant set equal to 25 years, t is the t-th year of the lifetime of the plant, CF_t [€] is the corresponding cash flow and *r* [-] is the discount rate set to 5%. While the DPBT [y] is defined as the number of years (t) required for the initial total investment to be re-paid and was determined according to *Equation (5.3)*.

$$DPBT = t \quad | \quad \sum_{t=0}^{n} \frac{CF_t}{(1+r)^t} \geq 0 \tag{5.3}$$

5.3 Results and discussion

Results obtained for reference System no. 1 and System no. 2 are shown in *Table 16* and *Table 17*. It was found that:

- for System no 1 (see *Table 16*) the NG consumed to cover the thermal demand was equal to 3970.4 Sm^3/y. Conversely, electricity accounted for 63.64 MWh_e/y. The amount of CO_2 emitted for operating this plant was 38107 kg_{CO_2}/y. Almost

81% of these emissions were due to the electricity purchase from the grid, while 19% was due to NG consumed by the boiler;

- for System no. 2 (see *Table 17*), since a reversible HP covers both cooling and heating demand, only electricity was consumed throughout the year. The annual amount was found to be 71.45 MWh_e/y, which led in turn to the emissions of 34653 kg_{CO_2}/y of CO_2.

5.3.1 Results for improved System no. 1: Scenario no. 1-A and 1-B

Results for the improved configurations of Systems no. 1 shown in *Figure 55*, are presented and discussed in the following two subsections.

5.3.1.1 Results for Scenario 1-A

As shown in *Figure 53.a*, in this case, the dish-Stirling system is operated in electric-mode. In *Figure 55.a,* the annual electricity produced by the solar concentrator is plotted with the aggregated electricity demand of the case study (which accounts for the electricity consumed by the lighting systems, office equipment, and chiller). Note that:

- a large share of the aggregated electricity demand (yellow profile in *Figure 55.a*) is met by using the electricity produced from the dish-Stirling system (orange profile). The fraction of electricity demand which is not covered by the concentrator is purchased from the grid;
- focusing on a generic week in August in *Figure 55.b*, the hourly dish-Stirling output power is simultaneous to the office demand, thus indicating that storage should not be installed. Conversely, on non-working days when electricity is not needed, the electricity is sold to the grid.

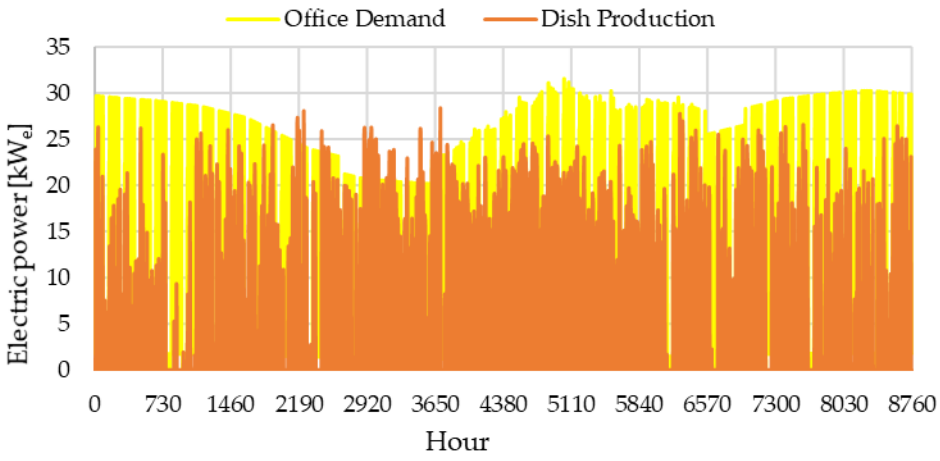

(a)

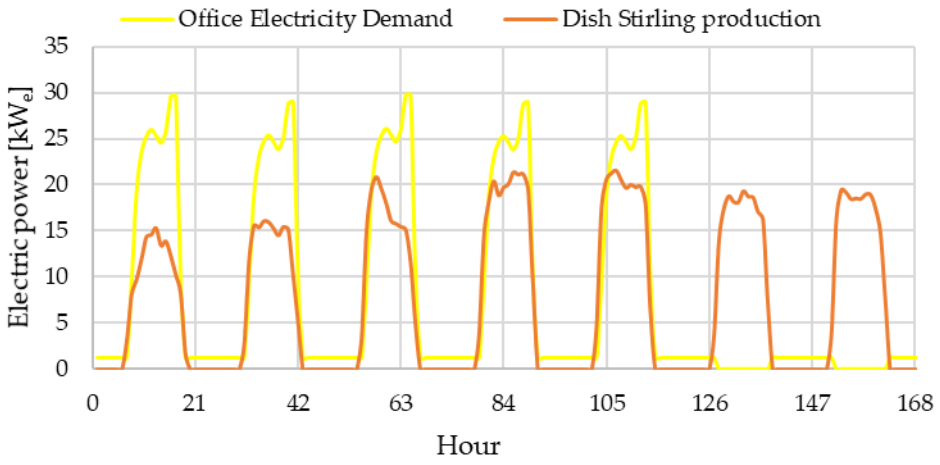

(b)

Figure 55. Scenario no. 1-A: (a) profiles of annual electricity demand and dish-Stirling production (b) weekly profiles of electricity demand and dish-Stirling production

Annual results for Scenario no. 1-A are shown in *Table 16*. Since no heat was recovered during the operation, the amount of NG consumed did not vary compared to reference System no.1. Only the amount of electricity purchased from the grid decreased from 63.64 MWh_e/y to 18.01 MWh_e/y, resulting in 71.7% electricity saving. As a consequence, the same percentage reduction in CO_2 emissions is observed.

5.3.1.2 *Results for Scenario 1-B*

In this scenario, the dish-Stirling system was operated in cogenerative-mode. In *Figure 56.a*, the profile of the electricity produced by the solar concentrator is plotted along with the aggregated electricity demand profile. In *Figure 56.b*, the electricity produced from the cogenerative dish-Stirling system is compared with the one obtained in electric mode. In *Figure 56.c*, the heat flow recovered is plotted along with the office thermal demand. Note that:

- as shown in *Figure 56.a*, the electricity produced by the concentrator (green profile) can cover a large share of the entire aggregated electricity demand (yellow profile).
- as shown in *Figure 56.b*, the profile of the electricity produced from the dish-Stirling system in electricity-mode and the one obtained for Scenario no. 1-B are compared. During the winter, the higher temperature of the cold side of the Stirling engine, required by the cogenerative asset, leads to a reduction in the electric output power (see dashed black contoured rectangle). From the simulation, it was found that such a reduction is about 15% of the corresponding output power in electricity-mode.
- as shown in *Figure 56.c*, the heat flow recovered covers at least half of the office thermal demand. Conversely, during the summer, a fraction of the recovered heat flow is used to cover the DHW demand.

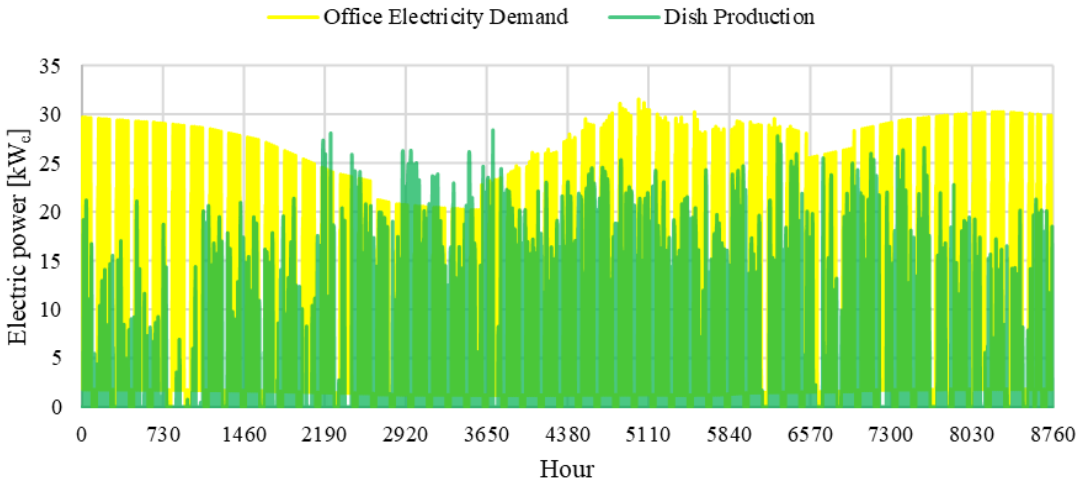

(a)

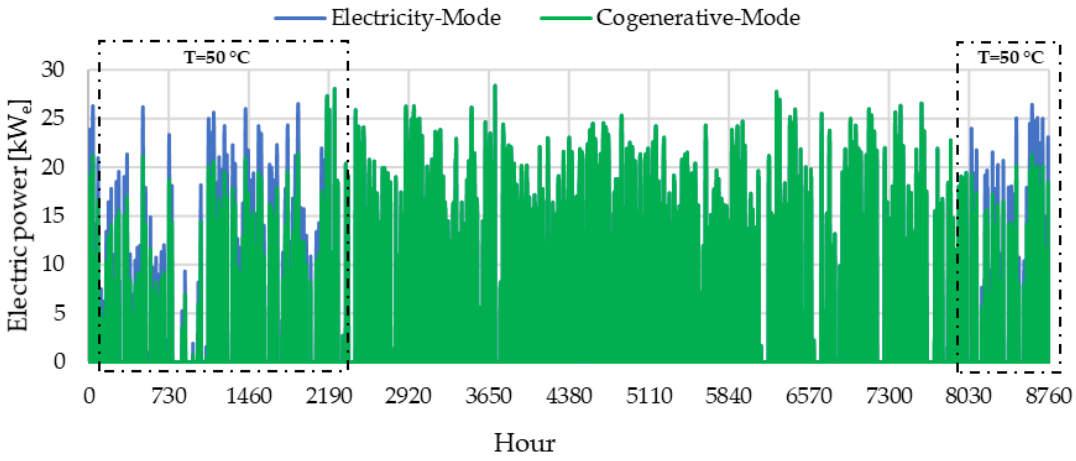

(b)

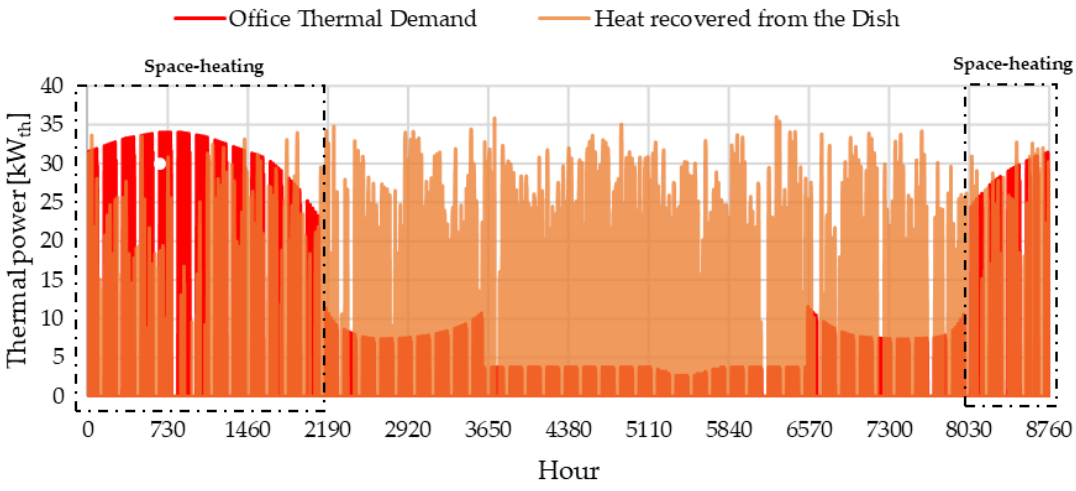

(c)

Figure 56. Scenario no. 1-B: (a) profiles of annual electricity demand and dish-Stirling production; (b) electricity profile of dish-Stirling production in electricity mode and the one obtained for cogenerative mode (c) profile of office thermal demand and heat recovered from dish-Stirling

Annual results for Scenario no. 1-B are shown in *Table 16*. Since heat is recovered from the Stirling engine during winter operation, the amount of NG consumed decreases by about 84.8% compared to the base case and Scenario no. 1-A. Conversely, the amount of electricity produced in Scenario no. 2-A reduces by about 4.6% compared to Scenario no. 1-A due to the lower electric output power of the dish-Stirling system during the

winter. However, such a reduction is fully justified by the lower NG consumption achieved. From an environmental viewpoint, a further 31.9% reduction in CO_2 emissions is observed passing from Scenario no. 1-A to Scenario no. 1-B.

Table 16. Annual results for System no. 1, Scenario no. 1-A, and Scenario no. 1-B

	System no. 1	**Scenario no. 1-A**	**Scenario no. 1-B**
NG consumption [Sm^3/y]	3970.4	3970.4	601.2
Electricity purchased from the grid [MWh_e/y]	63.64	18.01	20.14
Electricity produced by the dish-Stirling [MWh_e/y]	-	46.29	44.16
CO_2 Emissions [kg_{CO_2}/y]	38107	15976	10866

5.3.2 Results for improved System no. 2: Scenario no. 2-A and 2-B

In Scenario no. 2-A, it was assumed that the electricity produced by the dish-Stirling system was used to drive the HP in summer and winter. The yearly profile of the electricity produced by the dish-Stirling system is the same as the one shown in *Figure 55.a*. A reduction of the electricity purchased from the grid is achieved and, as shown in *Table 17*, it decreases from 71.45 MWh_e/y of the base case to 25.15 MWh_e/y (almost 65%). The same percentage reduction is observed in the amount of emitted CO_2.

In Scenario no. 2-B, it was assumed that the dish-Stirling system operates in a cogenerative-mode. In this scenario, the profile of the electricity and heat produced by the concentrator throughout the year is equal to that shown in *Figure 55.a* and in *Figure 55.c*. In *Table 17* the energy and environmental results are shown. Note that, when the heat is recovered, an additional 2.96 MWh_e/y of electricity are not purchased from the grid anymore, due to the lower amount of heating demand covered by using the HP. As a consequence, the amount of emitted CO_2 decreases from 12199 $kgCO_2/y$ to 11130 $kgCO_2/y$ (-8.8%).

Substantial improvements in both energy and environmental performances are observed passing from the base configuration of System no. 2 to Scenario no. 2-B.

Table 17. Annual results for System no. 2, Scenario no. 2-A, and Scenario no. 2-B

	System no. 2	**Scenario no. 2-A**	**Scenario no. 2-B**
Electricity Purchased from the grid [MWh_e/y]	71.45	25.15	22.95
Electricity produced by the dish-Stirling [MWh_e/y]	-	46.30	44.16
CO_2 Emissions [kg_{CO_2}/y]	34653	12199	11130

5.3.3 Economic results for the four analyzed scenarios

The economic feasibility of scenarios 1-A, 1-B, 2-A, and 2-B was assessed using the indicators described in subsection 3.3. The results of this analysis are shown in *Table 18*. Due to the high investment cost of the dish-Stirling system, it was observed that, with the current investment cost, in the absence of financial support, none of the investigated scenarios achieved a DPBT lower than 25 years.

It is worth considering that the feasibility of the proposed investment improves when the amount of energy saved is economically valued by an ad-hoc feed-in tariff (FIT). To this aim, the last available Italian mechanism supporting electricity production by renewable sources was assumed as a reference [139]. According to the cited decree, a FIT value was set equal to 0.369 €/kWh_e throughout the useful lifetime of the plant. The results of this analysis are shown in *Table 18.* Under this hypothesis, it was observed that the DPBT is equal to ~19 years for Scenarios 1-A and 2-A, with NPV equal to 35 k€ and 38 k€, respectively. Conversely, when the dish-Stirling system operates in the cogenerative mode for Scenarios 1-B and 2-B, the DBPT decreases to 14-17 years, and NPV is equal to 73 k€ and 45 k€, respectively.

It is of note that the previous indicators were calculated by assuming the same investment cost as the prototype installed in Palermo. In the case of a future full-commercial scale, a reduction in the installed cost is expected and a resulting improvement in the economic viability of the investment will be consequent. In this respect, assuming a 40% reduction of the capital cost (which corresponds to a total installed cost equal to 3,645 €/kW_p), the DPBT will be lower than 10 years for all the scenarios as shown in *Table 18.*

Table 18. Summary of NPV and DPBT values for the investigated scenarios

Assumptions	Economic indicators	Scenario no. 1-A	Scenario no. 1-B	Scenario no. 2-A	Scenario no. 2-B
(I_0, FIT)	NPV [€]	35,054	73,611	38,323	45,797
	DPBT [y]	18.6	14.6	18.1	17.2
($I_{reduced}$, *FIT)*	NPV [€]	111,445	150,002	114,713	122,187
	DPBT [y]	9.1	7.5	8.9	8.6

5.3.4 Brief comparative analysis of the key findings with other studies

In this paragraph, the key findings of the proposed research are compared with the results of some of the published papers focused on the integration of the dish-Stirling technology into the building sector.

In [129], the authors claimed that the combination of a photovoltaic system and a dish-Stirling system reduced the total energy consumption of a building located in Lebanon by about 68%, decreasing the dependence on the national power grid. Also, for the proposed case study in this analysis, the integration of the dish-Stirling allowed a reduction of 65-72% in the amount of electricity purchased from the local power grid for the case of energy plants relying only on electrically driven systems. These values confirm that, although dependence on other energy sources is inevitable, the integration of this technology could greatly contribute to achieving the self-sufficiency of buildings.

When a cogenerative mode is assumed, 85% percentage variation in the natural gas consumption is observed as well. A higher value of primary energy saving (about 97%) was found in [120], where the authors optimized the configuration of a dish-Stirling collector field, a seasonal geothermal storage, and a water-to-water heat pump system, supplying the heating system of a non-residential building in Palermo. The difference in the previous percentages could be related to the lack of an optimization routine in the present work compared to [120]. However, the achieved value suggests again that the cogenerative asset during the winter could be very promising for reducing energy consumption, also in places mainly characterized by cooling demand. Furthermore,

unlike [120], in the present analysis, any thermal energy storage was included in the plant layout.

In the end, the comparison of the proposed scenarios for the two energy plants suggests that promising energy-saving and avoided CO_2 emissions could be achieved when the energy demands of the served building are met by using both electricity and NG (i.e., 72% for Scenario 1-B). This result is totally in line with the key findings of [33] and [120], where the authors considered integrating such technologies to reduce the dependence on natural gas.

5.4 Outcomes

This part of the thesis investigated the energy and environmental benefits achievable by integrating a dish-Stirling system into an energy plant covering the air-conditioning demand of an office building located in Southern Italy. Two different plants were assumed as references, both representative of the typical systems used in this sector. The first one relied on the natural gas boiler for covering the thermal demand and on air-cooled chillers for cooling demand. The second one consisted of a reversible heat pump for covering both heating and cooling demands. For both systems, the benefits of operating the dish-Stirling concentrator in electricity-mode or cogenerative-mode were analysed. The detailed models adopted for all the main plant components were implemented into the TRNSYS environment and hourly-based simulations were carried out.

Starting from the first systems, it was found that the integration of the dish-Stirling concentrator allows for the reduction of the electricity purchased from 63.64 MWh_e/y to 18.01 MWh_e/y (about 72%), which also leads to a reduction in CO_2 emissions of about 58%. Even better energy performance was achieved by operating the dish-Stirling system in cogenerative-mode during the winter. In this last configuration, it was found that the amount of consumed natural gas decreases by about 85% compared to the base case. However, an increase in the purchased electricity is observed compared to the case of the dish-Stirling system operated in electricity-mode (+4.6%). However, such an increase is more than offset by the reduction in natural gas consumption.

For the second system which included a reversible heat pump, it was found that when the dish-Stirling system operates in electricity-mode, a 65% decrease in the amount of electricity purchased from the grid could be achieved, which passes from 71.45 MWh_e/y of the base case to 25.15 MWh_e/y. When heat is recovered, an additional 2.96 MWh_e/y of electricity is no longer purchased from the grid. Results of this analysis have shown that promising energy savings could be achieved by integrating dish-Stirling technology in conventional energy systems used in the tertiary sector to cover the energy demands. Moreover, the cogenerative asset could be very advantageous and environmentally friendly when heating demand still relies on fossil fuel consumption. Finally, the economic analysis of the four proposed system scenarios showed that the installation of a dish-Stirling system integrated into a building is only economically viable if financial support is considered. Then technological improvements and economies of scale will allow the reduction in total installed cost until it is competitive with that of other currently fully commercialized CSP technologies.

Nomenclature

a_1	first parameter of the Stirling engine mechanical efficiency curve [-]
a_2	second parameter of the Stirling engine mechanical efficiency curve [W]
A	area [m2]
CF	cash flow [€/y]
DPBT	Discounted Payback Time [y]
E	electric energy [kWh]
$\dot{E}$	electric power [W]
h	convective heat transfer coefficient [W/(m²·K)]
I	irradiance [W/m2]
I_0	total installed cost of the dish-Stirling unit [€]
n	useful lifetime of the plant [y]
NPV	Net Present Value
Q	thermal energy [kWh]
$\dot{Q}$	thermal power [W]
r	discount rate [%]
R	correction factor [-]
T	temperature [°C]
FIT	feed-in tariff [€/kWhe]
$\dot{W}$	mechanical output power [W]

Greek letters

ε	emissivity [-]
η	efficiency [-]
μ	emission facto [kgCO_2/kWh]
σ	the Stefan-Boltzmann constant [W/(m²·K^4)]

Subscripts

b	beam component of radiation
cle	cleanliness
e	electric
G	generation
in	inlet
n	net effective aperture area of the reflector CSP
p	parasitic component
o	optical
out	outlet
S	Stirling
sav	saving
r	receiver
t	t-th year of the lifetime of the plant [-]
T	Temperature
0	referred to the reference

Superscripts

av	avoided
ave	average

Acronyms

CO_2	Carbon Dioxide
COP	Coefficient of Performance
CSP	Concentrating Solar Power
DNI	Direct Normal Irradiation
GHG	Greenhouse Gases
HP	Heat Pump
HC	Heating Capacity

NG	Natural Gas
ODT	Outdoor Temperature
PCU	Power Conversion Unit
PLR	Part Load Ratio
TMY	Typical Meteorological Year

Chapter 6

A seasonal thermal energy storage system coupled with a dish-Stirling plant

In the previous chapter, a cogeneration plant was proposed. Now we investigate the possibility to join a dish-Stirling collector field, a seasonal geothermal storage and a water-water heat pump system. Specifically, the operation of this cogenerative plant would make it possible both to supply thermal energy to the heating system of one of the buildings of the Department of Engineering at Palermo (Italy) and to produce electricity. In the proposed layout, the thermal energy recovered at low temperature from the cooling system of the Stirling engine is stored in the ground during the summer season and then used to satisfy the winter thermal loads of the building. The operation of the system was simulated by varying the number of solar concentrators and the characteristic quantities of the geothermal field, by means of hourly simulations performed with Transient System Simulation Tool. Experimental data from a dish-Stirling pilot collector, located in the same area, were used to accurately calibrate the numerical model. Finally, energy, environmental and economic analyses made it possible to select the best configurations from the 1440 cases analysed.

6.1 Introduction

The exploitation of waste low-temperature heat from a Stirling engine could be used to cover the winter heating load of buildings [33]. It is, however, necessary to resolve the well-known temporal mismatch between the thermal energy production (summer) and the thermal energy demand periods (winter) through a Seasonal Thermal Energy Storage system (STES) [140]. In this framework, geothermal plants can be considered a promising residential heating source due to their high efficiency [141] for example installing a solar-assisted ground source heat pump as described in [142] and [143]. There are different types of STES systems [144], such as: Hot Water Thermal Energy Storage (HWTES); Gravel-Water thermal energy storage (GWTES); Aquifer Thermal Energy Storage (ATES); and Borehole Thermal Energy Storage (BTES).

HWTES systems store hot water inside a tank with a reinforced concrete structure which can be buried in the ground. The tank is provided with thermal insulation in order to minimise heat losses to the environment [144]. Similarly, GWTES systems store heat inside a reinforced concrete and thermally insulated tank, but contain a mixture of water and gravel [144]. This mixture is characterised by a lower specific heat compared to water and, therefore, considering the same thermal energy storage, GWTES systems are larger than HWTES systems [145]. ATES systems are an interesting alternative because it is not necessary to build a reinforced concrete tank nor to excavate a site in which to bury it as ATES heat storage exploits already existing aquifers in the subsoil [145]. Finally, BTES systems use soil as the storage medium. In this case, the heat is transferred to the soil by a system of distributed vertical geothermal exchangers [146]. The heat transfer fluid, usually a solution of water and glycol, flows along the borehole exchanger charging and discharging the soil creating a radial temperature gradient that reduces the external heat losses to the undisturbed cooler soil surrounding the storage volume. The BTES system can also be thermally insulated on the upper boundary surface in order to limit the influence of external climate conditions and to minimise the upper thermal losses [147].

Among the aforementioned sensible thermal energy storage systems, BTES systems are the most suited to be coupled with dish-Stirling CSP technology because of: the low operating temperature, the relative ease of installation, the moderate investment needed to realise the geothermal field [148], and the medium-high value of storage yield

[144], since thermal energy losses in the environment are limited as a result of the low enthalpy that characterises the storage process and therefore the low temperature of the heat transfer fluid used. BTES plants are already widely used worldwide [56]. In Sweden, several single-U boreholes have been installed in a parking lot and have been used for both summer and winter air conditioning in a university building since 2001 [149].

At present, it is possible to find in the literature studies on the use of a dish-Stirling system in a cogeneration setup [150], but there are no studies, in particular, investigating the possibility of coupling the dish-Stirling solar concentrator to the seasonal boreholes storage system. Examining the dish-Stirling system currently installed on the University campus of Palermo and Building 9 of the Engineering Department next to the site where the same production system is located, this part of the thesis proposes a layout of the Combined Heat and Power (CHP) plant in order to meet the space heating load of Building 9 through the low-temperature waste heat from the Stirling engine. The proposed plant layout includes: a number of dish-Stirling units for the production of electricity and heat; a BTES-type seasonal thermal storage system with a number of possible geometries; two heat pumps; and a thermal user consisting of Building 9 where the natural gas boiler is kept as an auxiliary system.

According to the research exposed in this part of the thesis, the proposed cogeneration plant layout would completely satisfy the thermal energy needs of the building considered, obtaining significant energy savings and large amounts of avoided CO_2 emissions. However, the economic feasibility of these systems is strongly correlated to the ability to optimise the plant configuration so that the proceeds of energy sales and the energy savings, obtained over the operating life of the plant, can balance the total cost of installation. For this reason, an incentivisation scheme is proposed in order to encourage commercial penetration in the residential sector of the examined CHP system.

6.2 Description of proposed cogenerative layout and its operation

The proposed system is essentially a combination of a Concentrating Solar Power (CSP) and a Borehole Thermal Energy Storage (BTES) system. The CSP plant produces electricity mainly during the summer period. The waste heat produced during the

operation of the CSP system is used to heat a volume of soil through a system of geothermal heat exchangers. The thermal energy stored during the summer period is partially recovered from the soil during the winter period and is used as a cold heat source for the heat pump system providing the heating of the building.

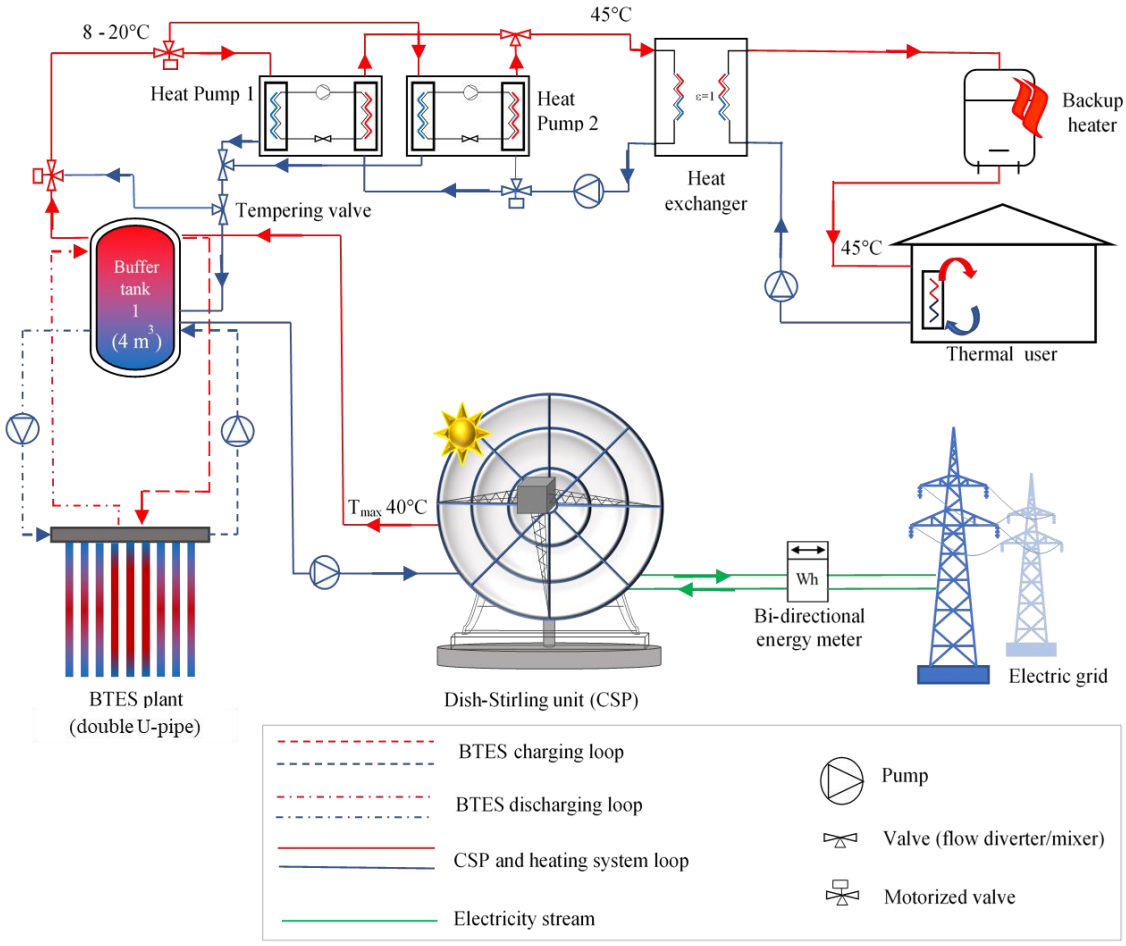

Figure 57. Schematic representation of the proposed CHP plant

Figure 57 shows the layout of the proposed system with its different components:

- A CSP collector system consists of dish-Stirling units. Each unit is characterised by a rated electrical output power of about 30 kW_e (corresponding to a rated DNI of about 960 W/m^2 [22]. The electric generators of the units are connected to the electric grid through a bi-directional energy meter, while the closed cooling circuits of the Stirling engines are connected to a Short-Term Thermal Energy Storage (STTES).

- A BTES system consists of a system of vertical ground-coupled heat exchangers with a double-U configuration, spatially distributed in the soil volume along concentric rings. The terminals of the closed circuit of the BTES exchanger pipes are connected to the STTES.
- Two water-to-water heat pumps are connected in parallel (with nominal heating capacities of 200 kW_{th} and 300 kW_{th} respectively). The cold side of this system is connected to the STTES while the hot side transfers heat to the heating system of the building through a thermal heat exchanger.
- A STTES (with a volume of about 4 m^3) acts as a hydraulic disconnector between the closed circuits of the Stirling engine's cooling system, the BTES, and the hot sides of the thermal exchangers of the heat pump evaporators.
- The closed circuit of the building's heating system is realised by connecting a heat exchanger to the condensers of the heat pumps, a conventional (gas-fired) backup boiler and hydronic terminals made with a system of fan coils.

The central element of the proposed plant is the system of dish-Stirling solar collectors generating the electricity that is injected into the national grid. The bidirectional meter is necessary because the CSP collectors during their operation, also consume a small amount of energy for the electrical parasitic absorption related to the operations of both the sun tracking system and the circulation pumps of the Stirling engine cooling system. The net electrical power produced by the dish-Stirling plant is usually linearly correlated to the value of DNI, as shown in the literature for this type of system [22]. On the other hand, data measured during an experimental campaign on the operation of the CSP model chosen for this study [22] has shown that the outlet temperature of the fluid in the cooling circuit of the Stirling engine is always around 40 °C independent of solar irradiation levels. This low-temperature thermal energy source in the studied layout is injected into the BTES, through the STTES mainly in the summer period when there is the highest energy production from the collectors.

In the winter period, when there is a heating demand from the building, the thermal energy stored in the BTES is transferred to the evaporators of the heat pumps. When the heating demand is simultaneous with the operations of the CSP system (e.g.,

on a cold winter day with clear skies), the thermal energy from the cooling of the Stirling engines is directly transferred to the heat pumps through the STTES. The water-to-water heat pump system is set to heat the water circulating in the heating circuit (user side) to a fixed temperature of 45 °C by means of a heat exchanger. As depicted in *Figure 58*, the BTES is essentially formed by a cylindrical portion of soil in which a number of vertical boreholes are drilled. In each borehole, a heat exchanger is installed, which is sealed by a grout mixture to guarantee the thermal contact between the soil and the pipes of the exchanger. In the configuration proposed, the heat exchangers, realised with double-U pipes are arranged on concentric rings. The heat exchangers placed in the inner ring are connected to each other in parallel. Then, each of these exchangers is connected in series to another exchanger placed in the next outer ring which, in turn, is connected to another one located in the next outer ring and so on.

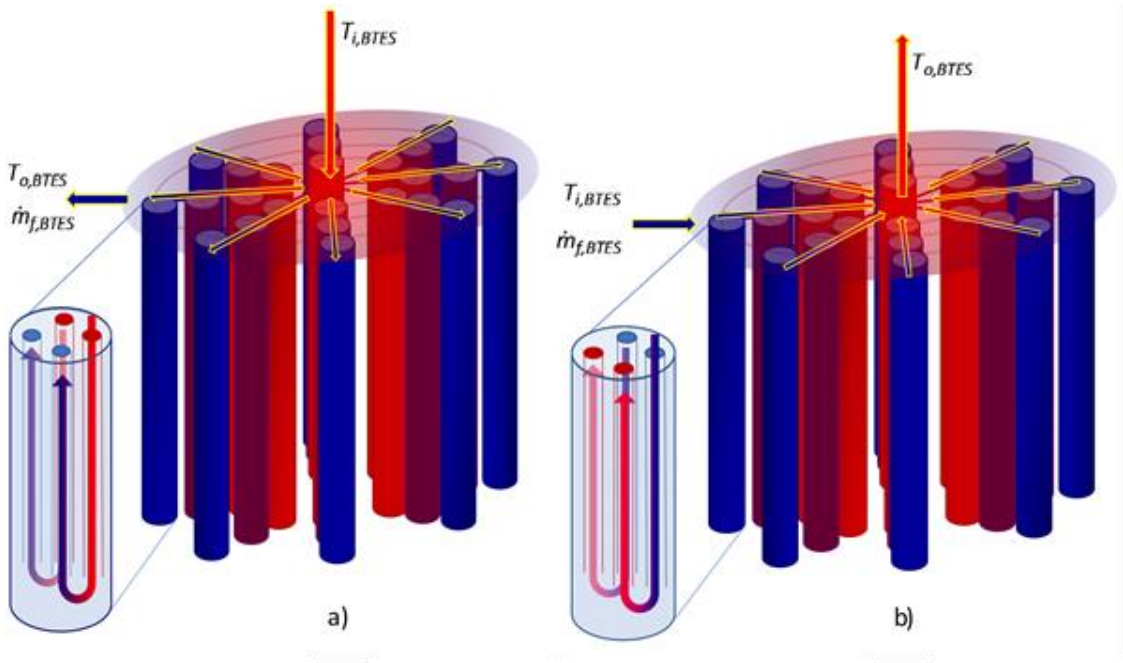

Figure 58. Operation of the BTES: a) charging phase (summer period) and b) discharging phase (winter period)

Finally, all the exchangers of the outermost ring are connected to each other in parallel. During this thermal charging, the hot fluid enters the central exchangers of the BTES and returns to the STTES from the more external ones (see *Figure 58.a*). Vice

versa, during the thermal discharge stage (winter period), the cold fluid coming from the STTES enters from the outermost BTES boreholes and returns, heated, to the central ones (see *Figure 58.b*). In this way it is possible to generate, over time, a radial thermal gradient (thermocline) in the BTES soil volume: the highest soil temperatures are localised in its central part and the lowest in its periphery. The thermocline formation increases the storage efficiency and reduces the thermal losses between the BTES soil volume and the cold soil surrounding it.

Finally, technical sheets of the heat pumps used for this analysis indicate that they can operate with cold source temperatures at the evaporators ranging from 8 °C to 20 °C. Therefore, to avoid the evaporator of the heat pumps getting water at a temperature higher than that allowed by the technical specifications, a tempering valve allows the mixing of hot water coming from STTES with cold water coming back from the evaporators so as to guarantee a maximum delivery temperature of 20 °C. Finally, when the renewable energy production system fails to fully cover the building's thermal loads, a natural gas-powered backup boiler is switched on to ensure that the fan coils are always fully operational. In this analysis, it is shown, through parametric analyses conducted with a dynamic numerical model, how the different components of the proposed CHP system can be optimised to minimise fossil fuel consumption, and, therefore, CO_2 emissions compared to a conventional heating system.

To assess the annual energy production of the dish-Stirling solar concentrator it was used the reference numerical model presented in *Paragraph 3.1* and the related *Equation (3.4)*. The models developed for the geothermal energy storage system and heat pumps are described in the following paragraphs.

6.2.1 Geothermal energy storage system model

The Duct Ground Heat Storage Model (DST) was used to simulate numerically the transient thermal response of the borehole system that constitutes the BTES. This model, implemented in the Transient System Simulation Tool (TRNSYS) Type 557, can be used successfully to analyse the seasonal storage of thermal energy in the soil [56]. According to the DST, the boreholes of the plant are uniformly distributed in a volume

of soil (arranged in a hexagonal pattern). The conventional volume of BTES defined by this system can be estimated as:

$$V_{BTES} = \pi \cdot H_b \cdot n_{b,t} \cdot \left(0.525 \cdot s_b\right)^2 \tag{6.1}$$

where H_b is the depth of the boreholes, $n_{b,t}$ is the total number of boreholes and s_b is the distance between two adjacent boreholes. The total number of boreholes, connected in series and in parallel, can be calculated through the following product:

$$n_{b,t} = n_{b,h} \cdot n_{b,s} \tag{6.2}$$

where $n_{b,h}$ is the number of boreholes in the innermost ring of the BTES and $n_{b,s}$ is the number of boreholes in each series.

The other input parameters required for the DST are the undisturbed soil temperature $T_{s,0}$, the average thermal conductive λ_s and heat capacity $C_{p,s}$ of the soil and the borehole thermal resistance R_b of the ground-coupled heat exchangers. The latter parameter is fundamental in order to define the heat transfer within the soil through these exchangers, and in the proposed model, it was defined by the following analytical equation proposed in the literature for double-U ground-coupled heat exchangers [151]:

$$R_b = \frac{1}{8\pi \cdot \lambda_g} \cdot \left[\ln\left(\frac{r_b}{r_{p,o}}\right) + 2\ln\left(\frac{r_b}{\sqrt{2} \cdot x_c}\right) + \ln\left(\frac{r_b}{2 \cdot x_c}\right) - \left(\frac{\lambda_g - \lambda_s}{\lambda_g + \lambda_s}\right) \cdot \ln\left(\frac{r_b^8 - x_c^8}{r_b^8}\right) \right] + \frac{R_p}{4} \tag{6.3}$$

In the above equation, r_b is the radius of the borehole, $r_{b,o}$ is the outer radius of each pipe, x_c is half of the shank spacing between the U-legs, λ_g is the thermal conductivity of the grout and R_p is the thermal resistance of a single pipe. The R_p, in turn, can be calculated as the sum of the conductive thermal resistance across the pipe and the fluid-pipe convective thermal resistance, by the following expression:

$$R_p = \frac{\ln\left(\frac{r_{p,o}}{r_{p,i}}\right)}{2 \cdot \pi \cdot \lambda_p} + \frac{1}{2 \cdot \pi \cdot r_{p,i} \cdot h_f} \tag{6.4}$$

where $r_{b,i}$ is the inner radius of the pipe, λ_p is the thermal conductivity of the pipe material and h_f is the convective heat transfer coefficient between the fluid and the pipe. The latter term, in the case of a circular pipe, can be obtained from the Nusselt number as:

$$h_f = \frac{Nu \cdot \lambda_f}{2 \cdot r_{p,i}} \tag{6.5}$$

where λ_f is the thermal conductivity of the fluid. To calculate the Nusselt number, the following correlation, valid for turbulent flow inside smooth pipes, provided by Gnielinski [152] was considered:

$$Nu = \frac{\left(\frac{f}{8}\right) \cdot (Re - 1000) \cdot Pr}{1 + 12.7 \cdot \left(\frac{f}{8}\right)^{1/2} \cdot \left(Pr^{2/3} - 1\right)} \tag{6.6}$$

where *Re* is the Reynolds number, *Pr* is the Prandtl number and *f* is the Darcy-Weisbach frictional factor. The Reynolds number, in turn, can be calculated as:

$$Re = \frac{2 \cdot \dot{m}_{f,U}}{\pi \cdot r_{p.i} \cdot \mu_f} \tag{6.7}$$

where $\dot{m}_{f,U}$ is the mass flow rate inside a single U-leg and μ_f is the dynamic viscosity of the fluid. The Prandtl number is defined as:

$$Pr = \frac{c_{p,f} \cdot \mu_f}{\lambda_f} \tag{6.8}$$

where $c_{p,f}$ is the specific heat of the fluid. Finally, for the friction factor the following correlation proposed by Haaland [153] was used:

$$f = \left[-1.8 \cdot \log\left(\left(\frac{\varepsilon_p}{7.4 \cdot r_{p,i}} \right)^{1.11} + \frac{6.9}{Re} \right) \right]^{-2} \tag{6.9}$$

where ε_p is the absolute roughness of the pipe surface. The possibility of considering the variations of R_b as a function of $\dot{m}_{f,U}$ due to *Equations* from *(6.3)* to *(6.9)*

, allows the model to be used for simulating the thermal response of the BTES with different fluid flow rates. During its operation, in fact, the BTES is alternatively connected both to the dish-Stirling and to the heat pumps and the total mass flow rate flowing inside the BTES $\left(\dot{m}_{f,BTES}\right)$ takes different values. From these different values, it is finally possible to define the different mass flow rates circulating inside each single U-leg of the thermal exchangers using the following expression:

$$\dot{m}_{f,\mathrm{U}} = \left(\frac{\dot{m}_{f,BTES}}{2 \cdot n_{b,h}} \right) \tag{6.10}$$

that was deducted considering the mass conservation equation of the fluid circulating inside the BTES. Using the above nomenclature, the thermal power that can be transferred or recovered from the BTES during its summer or winter operation is calculated from the global thermal balance of the system as:

$$\dot{Q}_{BTES} = \dot{m}_{f,BTES} \cdot c_{p,f} \cdot \left(T_{o,BTES} - T_{\mathrm{i},BTES} \right) \tag{6.11}$$

where $T_{\mathrm{o,BTES}}$ and $T_{\mathrm{i,BTES}}$ are the outlet and inlet temperatures of the BTES, respectively. Moreover, considering that during the years of operation of the system, the BTES will be subject to numerous thermal loading and unloading cycles, it is possible to calculate the total thermal energy charged into the BTES by the following integral:

$$E_{BTES,in}(n_y) = \sum_{i=1}^{n_y} \left(\int_{charge,i} \dot{Q}_{BTES} dt \right) \tag{6.12}$$

where n_{y} is the number of years of plant operation and *charge,i* is the interval of time during which the BTES is charged every year. Similarly, the total thermal energy recovered from the BTES can be calculated as:

$$E_{BTES,out}(n_y) = \sum_{i=1}^{n_y} \left(\int_{discharge,i} \dot{Q}_{BTES} dt \right) \tag{6.13}$$

where *discharge,i* is the interval of time during which the BTES is discharged every year. Using these energies, it is possible to calculate the total thermal storage efficiency of the system, after a number of years n_{y}, as:

$$\eta_{BTES}(n_y) = \frac{E_{BTES,out}(n_y)}{E_{BTES,in}(n_y)} \tag{6.14}$$

As shown in the analysis of the results in this part, efficiency η_{BTES} was used to assess which of the proposed BTES configurations performs the best.

The calibration parameters of the model used to simulate the thermal behaviour of the BTES are summarised in *Table 19*. More specifically:

- the thermal characteristics of the soil are those typical of the facility test area at the University of Palermo (Sicily);
- the thermal conductivity of the grout was estimated assuming it is made with a mixture of 10% Bentonite/90% Quartzite sand [151];
- the radius of the pipes and the distances between the U-legs are those typical of the commercial products used for ground-coupled heat exchangers;
- the conductivity of the exchanger tubes is that of high-density polyethylene.

Finally, regarding the thermal properties of the water used to calculate h_f, the values corresponding to the average temperature of the fluid entering and leaving the BTES were used. All the remaining parameters of the model (such as $n_{b,h}$, $n_{b,s}$, s_b) were set to perform the optimisation analysis described below.

Table 19. Parameters defined for the BTES model

Parameters	Value	Units
Borehole depth H_b	25	m
Undisturbed soil temperature, $T_{s,o}$	18	°C
Thermal conductivity of the soil, λ_s	1.75	W/(m K)
Volumetric heat capacity of the soil, $C_{p,s}$	2.72	GJ/(m^3·K)
Thermal conductivity of the grout, λ_g	2	W/(m ·K)
Thermal conductivity of the pipes, λ_p	0.45	W/(m ·K)

Parameters	Value	Units
Radius of the boreholes, r_b	0.075	m
Inner radius of the pipes, $r_{b,i}$	0.016	m
Outer radius of the pipes, $r_{b,o}$	0.020	m
Half shank spacing between the U-legs, x_c	0.040	m
Absolute roughness of the pipe surface, ε_p	$2 \cdot 10^{-5}$	m

6.2.2 Heat pump numerical model

As regards the modelling of the water-to-water heat pump system, a simple black-box model was considered, which was defined by interpolating the operating data provided by the manufacturer [56]. The first heat pump (HP1) and the second heat pump (HP2) have a rated heating capacity of 200 kW_{th} and 300 kW_{th} respectively. The technical data of these pumps, for a fixed hot-side outlet temperature of $T_{h,o}$= 45 °C, are summarised in *Table 20*, as a function of the inlet cold-side temperature of $T_{c,i}$ (8 < $T_{c,i}$ < 20 °C). In these tables $\dot{Q}_{FH}$ is the (full-load) heating power, $\dot{Q}_C$ is the cooling power, $\dot{E}_H$ is the electric power consumption and COP_{FL} is the coefficient of performance. When the heating power demand $\dot{Q}_{PH}$ is lower than the heat power output $\dot{Q}_{FH}$ that the heat pump can provide at $T_{c,i}$, there is a degradation of the coefficient of performance due to this partialisation. In this case, the current value of the coefficient of performance can be calculated as:

$$COP_{PL} = PLF \cdot COP_{FL}(T_{h,i}) \tag{6.15}$$

where *PLF* is the partial load factor that is defined as [56], [154]:

$$PLF = \frac{PLR}{C_c \cdot PLR + (1 - C_c)} \tag{6.16}$$

C_c is a degradation coefficient (that is assumed equal to C_c=0.90) and *PLR* is the partial load ratio, defined as:

$$PLR = \frac{\dot{Q}_{PH}}{\dot{Q}_{FH}(T_{c,i})} \tag{6.17}$$

Table 20. Operating technical data of HP1 (model WW 302.B200) and HP2 (model WW 302.B300)

$T_{h,o}$= 45 °C								
$T_{c,i}$ (°C)	$\dot{Q}_{FH}$ [kW$_{th}$]		$\dot{Q}_{C}$ [kW$_{th}$]		$\dot{E}_{ele,hp}$ [kW$_{e}$]		COP_{FL}	
	HP1	HP2	HP1	HP2	HP1	HP2	HP1	HP2
8	159	248	123	191	39.1	60.2	4.07	4.12
10	175	276	139	219	39.4	60.5	4.44	4.56
15	198	306	159	248	39.8	61.0	4.97	5.02
20	221	346	182	288	40.3	61.4	5.48	5.64

From the value of the COP_{PL} (evaluated by Equations from (6.15) to (6.17)) it is lastly possible to calculate the electric absorption of the heat pumps. The outlet cold-side temperature from the heat pumps can be calculated as:

$$T_{c,o} = T_{c,i} - \frac{\dot{Q}_c}{\dot{m}_{c,HP} \cdot c_{p,f}} \tag{6.18}$$

where $\dot{m}_{c,HP}$ is the mass water flow rate at source-side of each heat pump. From technical sheets, the mass flow rates considered for the calculations are $\dot{m}_{c,HP}$=25,376 [kg/h] and $\dot{m}_{c,HP}$=41,968 [kg/h] for the HP1 and HP2, respectively. An algorithm was implemented in the control system to minimise the partialisation of heat pump operation by alternating or parallel starting of the heat pumps as a function of the heating demand levels of the building [56].

6.2.3 Transient system simulation tool implementation of the plant model

The models describing the energy balance of the different components of the proposed plant were developed with reference to the literature and then numerically implemented using TRNSYS [137]. This software allowed the numerical analysis of a

large number of different layout configurations to be performed through a series of transient hourly-based simulations. With this aim, the hourly data time series of the air temperature and Direct Normal Irradiance (DNI) were defined using the Typical Meteorological Year (TMY) generated by Meteonorm [155] and were used as input variables of the model.

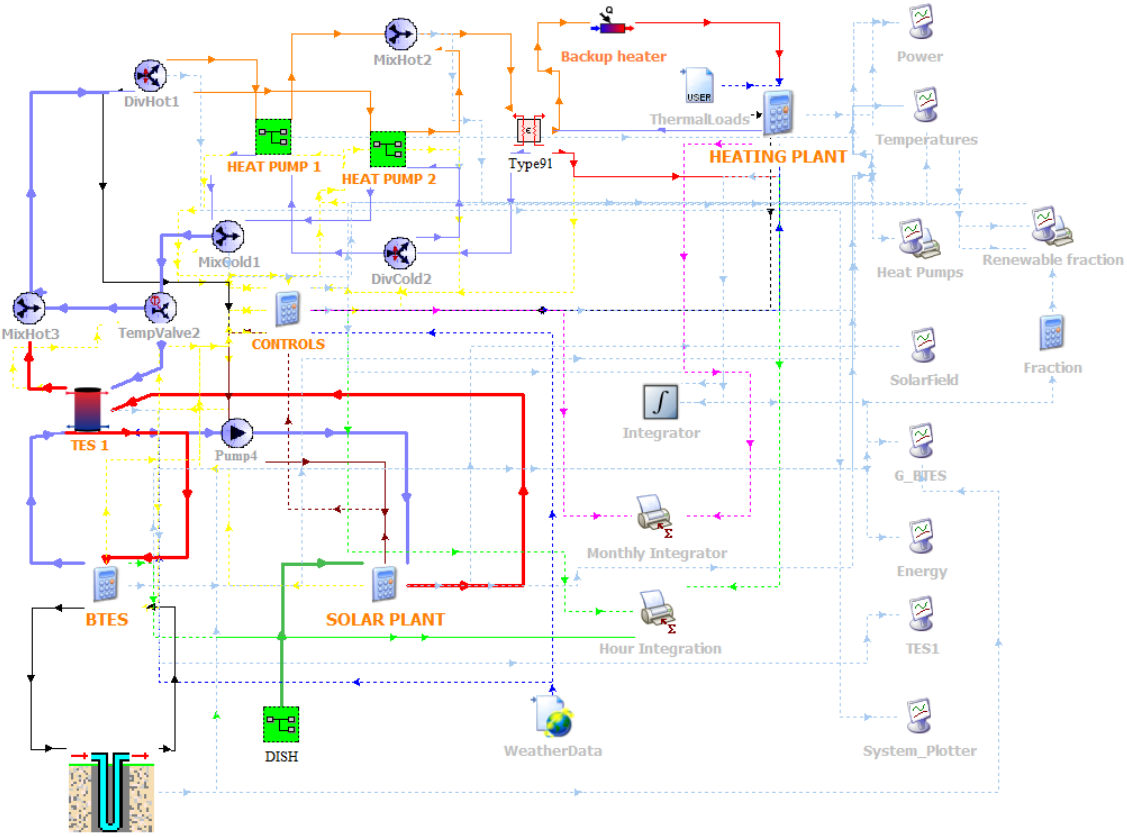

Figure 59. TRNSYS layout of the plant model

The simulation period was set to 25 years to fully characterise the thermal evolution of the BTES from the beginning of its operation until the achievement of its pseudo-stationary condition. For each of these years the same TMY dataset was used. *Figure 59* shows the structure of the TRNSYS layout in which all the connections between the different elements constituting the system were modelled (including all the valves, heat exchangers, circulation pumps, etc.). Moreover, all the equations representing the model of each plant component already described were implemented

using equation TRNSYS types and for the dish-Stirling and the heat pump, special macros were developed for this purpose.

6.3 Multi-criteria analysis

A series of different configurations of the same plant layout was studied in order to identify the one performing best one in terms of energy, environment and economics. Referring to *Figure 60*, the different analysed configurations were obtained by varying the following parameters that characterise the previously presented layout:

- the number of dish-Stirling units n_{dish}, (varying from 1 to 4 with a step of 1)
- the number of head boreholes $n_{b,h}$, (varying from 15 to 20 with a step of 5)
- the number of boreholes in series $n_{b,s}$, (varying from 3 to 4 with a step of 1)
- the spacing of boreholes in series s_b, (varying from 2 to 12 m with a step of 2 m)
- the deep of the boreholes H_b, (varying from 10 to 100 m with a step of 10 m)

In this way, 1440 different plant system configurations were obtained whose transient operation during their useful lifetime (25 years) was simulated using the TRNSYS numerical model. All these simulations were carried out keeping the evaluated space heating load of the building E_{load} unchanged. Each simulation generated the time variations of about 40 variables, giving rise to a result matrix characterised by 40 columns and 219000 rows. Thus, the performed simulations produced a total number of items in the result dataset equal to about $1.26 \cdot 10^{10}$. This significant amount of data required the adoption of particular manipulation techniques through the creation of a MySQL database that, properly optimised, allows the efficient management and examination of almost 57 GB of data. For each studied configuration, it was possible to calculate, from the results of the simulation, the fraction of building heating load that is covered by the thermal energy provided by the heat pump system, as:

$$f_{hp} = \frac{E_{hp}}{E_{load}} \tag{6.19}$$

where E_{hp} is the thermal energy produced by the two heat pumps in one year and E_{load} is the heating energy load required by the building during the same year.

Furthermore, considering that, in general, the electricity required by heat pumps is not necessarily produced from renewable sources, the following definition of the annual renewable fraction was adopted for each studied configuration:

$$f_r = \frac{E_{load} - \left(E_{ele,hp} + E_{\text{gas,boiler}}\right)}{E_{load}} = f_{hp} \cdot \left(1 - \frac{1}{COP_{hp}}\right) \tag{6.20}$$

where $E_{\text{ele,hp}}$ is the annual electric energy absorbed by the heat pumps, $E_{\text{gas,boiler}}$ is the thermal energy annually delivered by the gas boiler backup heater and COP_{hp} is the coefficient of performance of the heat pump system. If the $E_{\text{ele,hp}}$ is fully provided by the electricity annually produced by the dish-Stirling it follows that *Equation (6.19)* is a sufficient indicator of the annual renewable fraction of the plant.

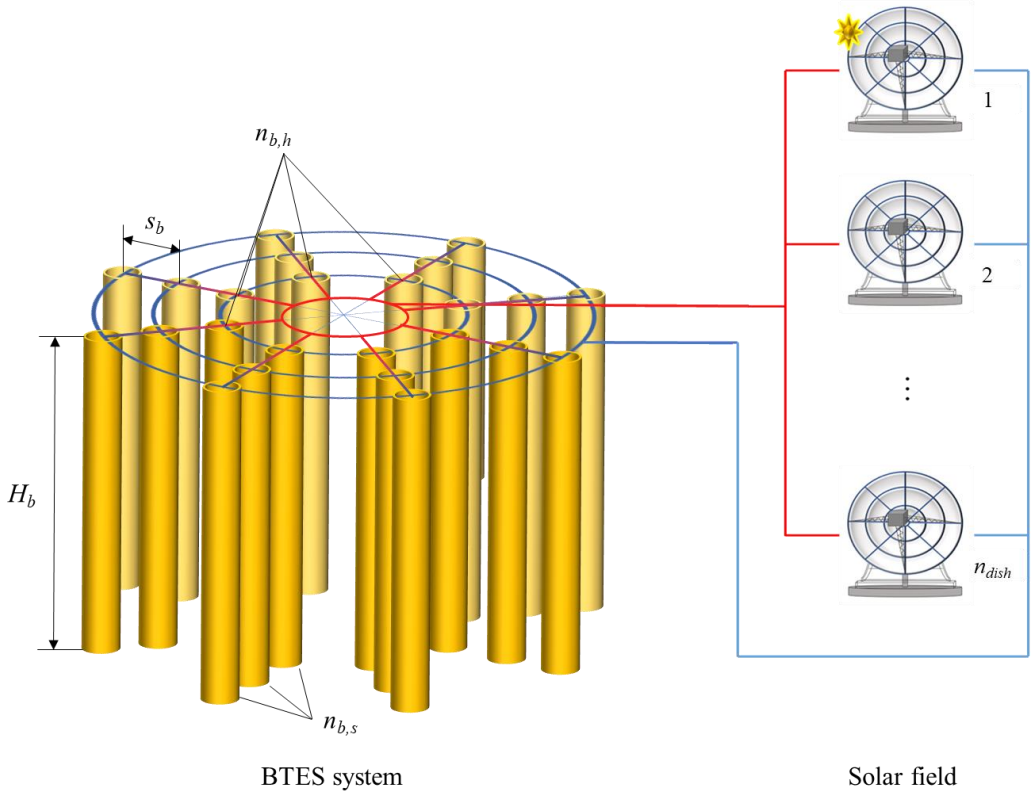

Figure 60. Decision variables of plant layout optimisation

However, even under this hypothesis, the coefficient f_{r} can be considered a good indicator of the more or less renewable fraction of the plant, as the higher the value of f_{r}, the lower the fraction of heating loads covered by the backup heater, the lower the amount

of electricity absorbed by the heat pumps and, thus, the greater the fraction of electricity, produced by the solar field, left free to cover other consumption.

6.3.1 Economic analysis

Knowing the annual renewable fraction of each of the 1440 plant configurations, an economic analysis was performed taking into account several possible scenarios. According to estimates, the initial cost of investment necessary to build the entire plant consists of: the cost of a single dish-Stirling solar concentrator (C_{dish}), including installation and maintenance costs over the lifetime of the system, amounts to € 278,000; the cost of realisation of a single geothermal probe expressed per unit of length (C_{BTES}) amounts to 60 €/m; the total cost necessary to purchase the two selected water-to-water heat pumps (C_{HP}) amounts to €50,000.

The initial overall cost of investment (I) for a generic CHP configuration plant depends on the number of installed solar concentrators (n_{dish}) and the total length of boreholes L_{tot} making up the thermal storage system which is equal to the product of the total number of boreholes ($n_{b,t}$) for the depth of a single borehole (H_b). The economic analysis was conducted on the basis of a "constant currency approach" considering the plant's useful lifetime being equal to 25 years, and the initial cash flow includes only the investment related to the examined configuration. For subsequent years, the cash flow was evaluated considering the following revenues and costs.

The incentivised sale of the electricity produced by the concentrating solar power field to the national electricity grid ($I_{el,\,sold}$). The dish-Stirling system of Palermo benefits from the national incentivisation mechanism no longer in force since December 2017 [139]. According to this decree, the feed-in tariff (T_f) is granted to a power plant with an electric capacity up to 500 kW for 25 years and is determined as follows:

$$T_f = T_b + Pr_{solar} \quad \left(\frac{€}{MWh}\right) \tag{6.21}$$

where, T_b is the basic incentive tariff that depends on the size of the power plant equal to 324 €/MWh, and Pr_{solar} is the bonus corresponding to the solar integration fraction that characterises the considered power plant. For the generation plant in issue,

this bonus is equal to 45 €/MWh since the fraction of solar integration is 1. Overall, the feed-in tariff amounts to 369 €/MWh. The incentive for the replacement of a conventional heating plant with a new heating plant equipped with geothermal heat pumps (I_{hp}) [123]. This income has a duration of 5 years and was calculated as follows:

$$I_{hp} = P_n \cdot Q_{uf} \cdot \left(1 - \frac{1}{COP_{hp}}\right) \cdot C_i \quad \left(\frac{€}{year}\right) \tag{6.22}$$

where: P_n indicates the nominal heat output of the installed heat pump expressed in kW_{th}; Q_{uf} indicates the utilisation coefficient dependent on climate zone; COP_{hp} is the coefficient of performance of the installed heat pump; and C_i is the coefficient of valorisation of the thermal energy produced expressed in €/kWh. The incentive calculated by referring to the two heat pumps planned for the cogeneration plant described in this document is: I_{hp}=23,483.73 €/year

The natural gas savings resulting from the use of renewable heat pumps $\left(S_{natural\ gas}\right)$ are calculated as:

$$S_{natural\ gas} = E_{load} \cdot f_r \cdot \left(\frac{c_{\substack{natural \\ gas}}}{\eta_{\substack{gas \\ boiler}}} - \frac{c_{electricity}}{COP_{hp}}\right) \quad \left(\frac{€}{year}\right) \tag{6.23}$$

where: E_{load} is the yearly heating energy demand of the building expressed in (kWh/year); f_r is the annual renewable fraction of the examined CHP plant; $c_{\substack{natural \\ gas}}$ (0.112 €/kWh) and $c_{electricity}$ (0.170 €/kWh) are unit costs of natural gas and electricity respectively, expressed in (€/kWh); $\eta_{\substack{gas \\ boiler}}$ is the overall yield of the existing gas boiler; COP_{hp} is coefficient of performance of the two renewable heat pumps.

The income resulting from the monetisation of avoided CO_2 emissions $\left(I_{CO_2}\right)$ can be calculated as:

$$I_{CO_2} = \frac{se_{CO_2} \cdot E_{load} \cdot f_r}{10^6} \cdot C_{CO_2} \quad \left(\frac{€}{year}\right) \tag{6.24}$$

where: se_{CO_2} indicates the specific emissions of CO_2 related to the thermal energy production using natural gas, expressed in (gCO_2/kWh_{th}); E_{load} is the yearly heating energy demand of the building expressed in (kWh/year); f_r is the annual renewable fraction of the examined CHP plant and C_{CO_2} is the unit revenue related to the amount of CO_2 avoided expressed in (€/t_{CO2}). Ultimately, taking into account the four monetary items listed above, the cash flow for the *t*-th year (CF_t) for the facility can be expressed as follows:

$$CF_t = I_{el,sold} + I_{hp} + S_{natural\,gas} + I_{CO_2} \quad \left(\frac{€}{year}\right) \tag{6.25}$$

6.3.2 Design of new mechanism of incentivisation

In Italy, there is currently no national incentive mechanism for CHP plants that exploit renewable sources by innovative technologies, such as the dish-Stirling solar concentrator. Although the energy efficiency of this technology is widely acclaimed [156], [22,49,72], the main factor limiting the spread of the dish-Stirling concentrator is the initial investment which is still too high compared to other solar technologies fully developed and marketed. Assuming that the incentive scheme described in the previous paragraph can continue to be used even if the reference decrees are partly no longer in force, this document suggests a new incentive mechanism through which a percentage of the initial investment is necessary for the realisation of a cogeneration project is financed. Four strategies of incentivisation are proposed, each with a different percentage of initial investment financed: 0% (I_0), 15% (I_A), 35% (I_B) and 45% (I_C). In order to assess the economic feasibility of the proposed cogeneration plant and to identify the most robust solution, the four strategies of incentivisation were investigated by varying the discount rate. As shown in *Figure 61* below, three values of discount rate were fixed obtaining 12 possible financial scenarios.

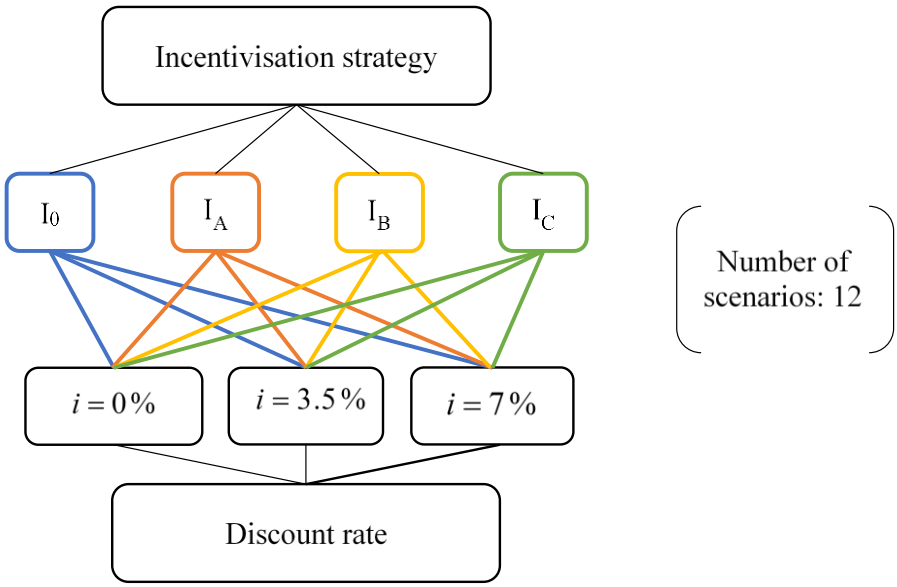

Figure 61. Schematic representation of all possible financial scenarios investigated

Referring to the 1440 plant configurations, all the financial scenarios schematically illustrated in *Figure 61* were analysed by investigating several economic indicators. In particular, the Net Present Value (NPV) and the Profitability Index (PI) were calculated in order to assess the profitability of the investment, while the Discounted Payback Time (DPBT) and Internal Rate of Return were determined to assess the investment risk. The NPV and PI were calculated according to *Equation (6.26)*:

$$\begin{cases} NPV = \sum_{t=1}^{N} \frac{CF_t}{(1+i)^t} \\ PI = \frac{NPV}{I} \end{cases} \tag{6.26}$$

where: CF_t is the cash flow of t-th year of the useful lifetime of the project; i is the discounted rate; and I is the initial overall cost of investment. The DPBT, defined as the number of years (t) needed for the equivalent of the investment income to exceed the equivalent of the capital expenditure, was determined according to *Equation (6.27)*:

$$DPBT = t \quad | \quad \sum_{t=0}^{N} \frac{CF_t}{(1+i)^t} \geq 0 \tag{6.27}$$

The IRR represents the percentage or interest rate (i) earned on the unrecovered part of an investment and it was calculated according to *Equation (6.28)*:

$$IRR = i \quad | \quad NPV = \sum_{t=1}^{N} \frac{CF_t}{(1+i)^t} = 0 \tag{6.28}$$

All these economic indicators were normalised in order to make them comparable, using the min-max normalisation as in *Equation (6.29)*:

$$z = \frac{x - min(x)}{max(x) - min(x)} \tag{6.29}$$

where: z is the normalised value of the set of observed values of x; $max(x)$ and $min(x)$ are maximum and minimum values of the same set of values. The obtained Boolean variables were indicated as $NPV_{normalised}$, $PI_{normalised}$ and $DPBT_{normalised}$. It was then possible to calculate the Overall Economic Viability Evaluation (OEVE) index, which graphically represents the area of a triangle whose vertices are the aforementioned economic variables as shown in *Figure 62*.

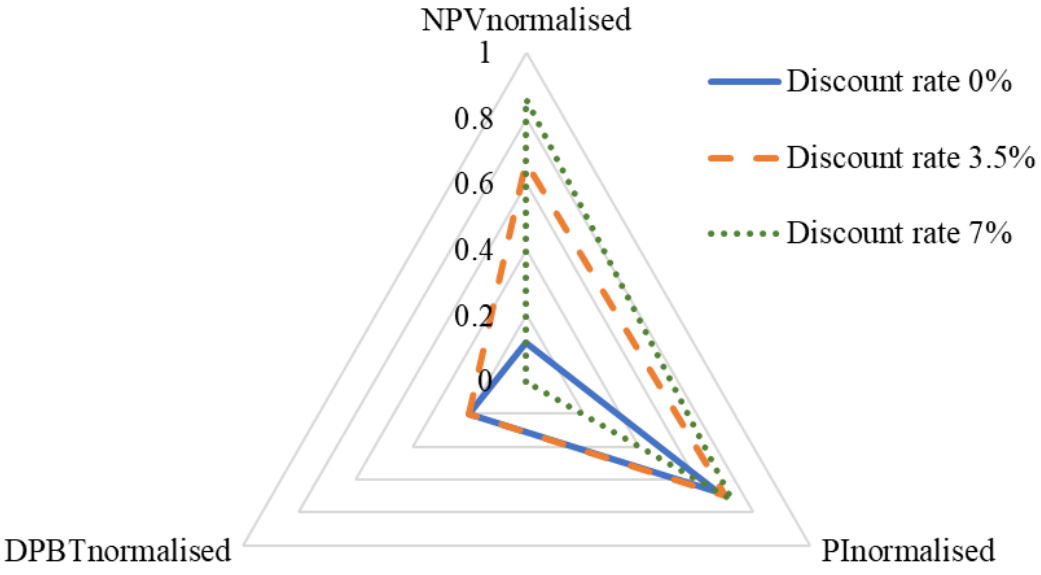

Figure 62. Radar diagram with normalised economic indexes of the configuration ID261

The higher the OEVE index is, (larger area in *Figure 62*) the more profitable the investment required to realise the corresponding CHP system configuration.

6.3.3 Evaluation of CO_2 emissions

The realisation of the CHP plant proposed and analysed in this part of the thesis would undoubtedly bring an environmental benefit in terms of avoided CO_2 emissions. The amount of CO_2 emissions avoided which corresponds to the operation of the various optimal configurations of the CHP system can be quantified as follows:

$$AE_{CO_2} = \frac{S_{\substack{thermal \\ energy}} \cdot se_{CO_2}}{ULT} \qquad \left[\frac{t_{CO_2}}{year}\right] \tag{6.30}$$

where: $S_{\substack{thermal \\ energy}}$ indicates the thermal energy savings, i.e. the thermal energy required by the building no longer supplied by the existing gas boiler but supplied through the renewable heat pumps over the lifetime of the CHP plant; se_{CO_2} indicates the specific emissions of CO_2 related to the thermal energy production using natural gas, expressed in (gCO_2/kWh_{th}); and ULT indicates the lifetime of the examined plant, which is 25 years in this case study.

6.4 Case study

As an application of the proposed methodology, reference has been made to one of the non-residential buildings of the University campus of Palermo: Building 9 of the Department of Engineering. According to the Italian standard UNI 10349 concerning climate data, Palermo falls into the B climate zone characterised by 751 Heating Degree Days (HDD) and the legal period for space heating ranges from 1 December to 31 March, for 8 hours per day [157]. Palermo has a Mediterranean climate characterised by a temperate-wet winter with an average temperature range from 8 °C to 14 °C, and by a hot-dry summer with an average temperature range from 21 °C to 28 °C, with peaks of above 35-40 °C [158]. The existing heating system of the building includes two gas boilers that feed a series of radiators. The heating volume is 14,500 m^3 and there is a conventional heating system with gas boilers with a total nominal power of 600 kW. *Figure 63* reports the thermal load demand of Building 9 during a typical week of each month of the conventional heating period. According to historical and measured data, the

monthly heating load energy demand of the considered building is: 59489 kWh in January, 38702 kWh in February, 6264 kWh in March and 62090 kWh in December. The overall yearly heating load energy demand is: E_{load}=166545 kWh. Finally, the hourly-based climate data input was defined using the Typical Meteorological Year (TMY) generated by Meteonorm [155] for Palermo (38.11°N; 13.36°E).

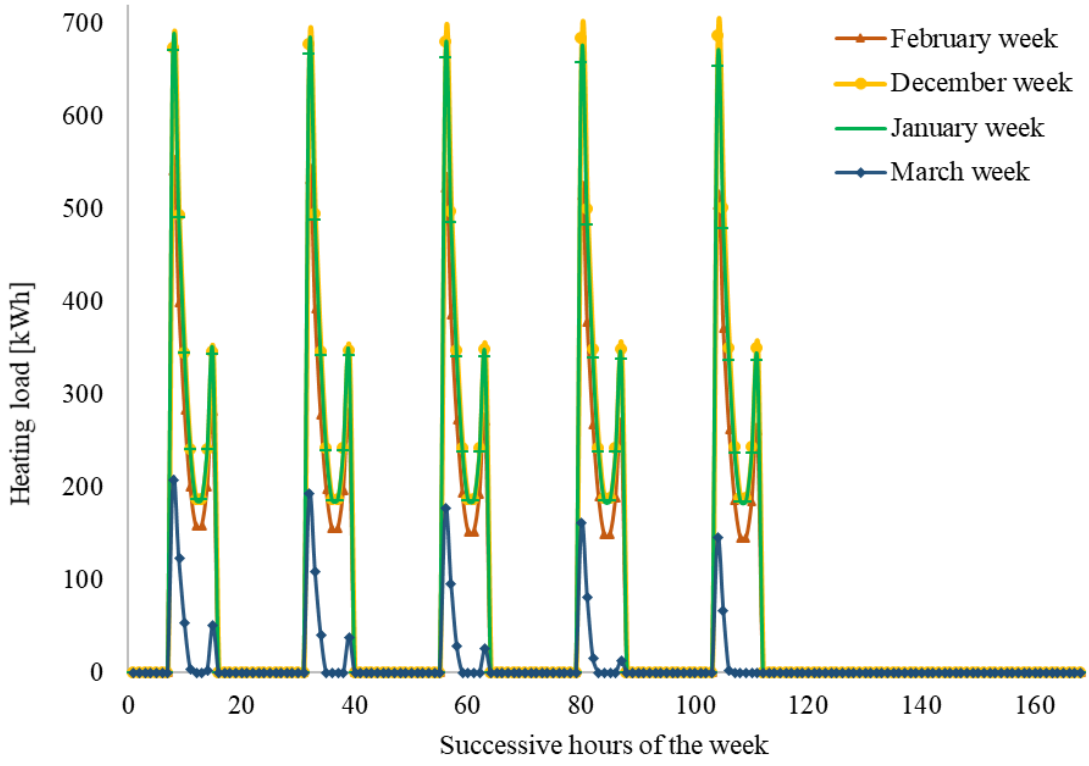

Figure 63. Weekly profile of heating load energy demand of Building 9 during the conventional heating period of a year

6.5 *Findings and discussion*

As already described, the dish-Stirling system represents the central element of the proposed cogeneration layout. *Table 21* shows the cumulative monthly values of the electrical and thermal energies produced by a single unit located in Palermo [155]. In *Table 21*, the following monthly cumulated quantities are indicated: the solar energy collected by the solar concentrator (E_{sun}), the gross and net electrical energies produced

by the solar plant (E_g, E_n), the parasitic electrical absorption of the solar plant (E_p) and the thermal output energy rejected from the Stirling engine ($E_{S,out}$). In the following paragraphs, the results will be discussed and analysed more in detail.

6.5.1 Energy balance of the cogenerative plant

Values calculated using the numerical model of the dish-Stirling collector show a peak in energy production occurring in July. In this month, the net electric and the thermal efficiencies are equal to 24% and 44%, respectively. The total annual net production of electric energy amounts to 40.8 MWh/year while the thermal energy rejected from the Stirling engine, is about 88.7 MWh/year. The corresponding net electric and thermal annual efficiencies are 20% and 44%, respectively. Since all these calculated quantities significantly depend on the direct solar irradiation, it was necessary to accurately select a *DNI* database representative of the micro-climatic conditions for the studied location. For this purpose, several solar databases were compared to each other to check whether the Meteonorm solar dataset could be representative of the *DNI* conditions of Palermo. Moreover, since the real operating data of dish-Stirling systems show that their performances can be considerably reduced by the soiling of the collector mirrors [22], for the presented calculations, an annual average cleanliness index equal to $\eta_{cle}^{ave} = 0.9$ was assumed. This value was carefully defined by processing the real operational data of the dish-Stirling unit installed in Palermo, assuming the possibility of periodic washings of the collector mirrors.

Thus, taking into account both the good predictive accuracy of the proposed numerical model (already discussed with the introduction of the MAPE and ζ metrics) and the quality of the input data (DNI and average cleanliness index), it is possible to reasonably assert that the energy outputs of *Table 21* accurately represent the monthly producibility of a dish-Stirling plant located in Palermo.

Table 21. Monthly and annual values of energy amounts involving a single dish-Stirling plant like that installed at Palermo

Month	E_{sun}	E_g	E_p	E_n	E_{th}
			(MWh)		
January	8.99	2.30	1.19	1.11	4.07
February	8.21	2.20	1.08	1.12	3.65
March	14.28	3.87	1.19	2.68	6.32
April	15.28	4.13	1.15	2.98	6.77
May	23.23	6.44	1.19	5.25	10.19
June	24.58	6.75	1.15	5.60	10.82
July	28.65	8.03	1.19	6.84	12.51
August	22.60	6.18	1.19	4.99	9.97
September	17.84	4.90	1.15	3.75	7.86
October	15.10	4.14	1.19	2.94	6.66
November	12.31	3.32	1.15	2.17	5.46
December	9.94	2.63	1.19	1.44	4.44
Annual	**201.01**	**54.88**	**14.02**	**40.87**	**88.72**

As already mentioned, to eliminate this temporal mismatch, a BTES was introduced into the plant layout. In order to show the annual energy balance of the proposed layout and the energy fluxes between its different components, the data from the simulation results relative to a representative plant configuration is described below. This studied configuration (ID90), is one of the best performing among all that have been analysed using the multi-criteria optimisation process and is characterised by the following geometrical parameters:

- the number of dish-Stirling units n_{dish}=2
- the number of head boreholes $n_{b,h}$, =25
- the number of boreholes in series $n_{b,s}$=4

- the spacing of boreholes in series s_b=6 m
- the depth of the boreholes H_b=60 m.

For this configuration, the daily average values of the BTES soil temperature and the cumulative input and output thermal energies corresponding to a simulation period of 25 years are depicted in *Figure 64*. The input energies to BTES are those supplied by the solar system during the charging stages while the output energies are those transferred from the BTES to the evaporators of the heat pump system during the discharge stages. From the results of *Figure 64*, it is possible to observe that the average soil temperature increases during the successive years of plant operation until it reaches a pseudo-stationary condition at around the 25th year. This gradual soil temperature increase is related to the fact that the annual amount of thermal energy produced by the two solar collectors, and then stored in the BTES, is greater than the energy demanded by the heat pumps.

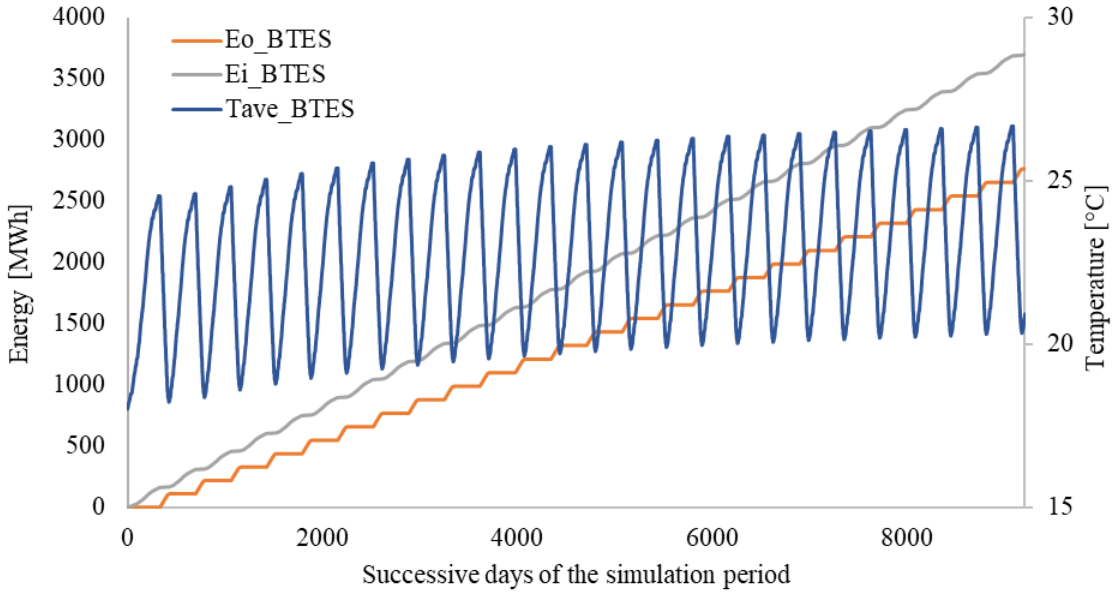

Figure 64. Average BTES temperature and cumulative input and output energy exchanged by the boreholes during the 25th year of operations (ID90 configuration)

From these results, it is also possible to calculate that the storage efficiency of the BTES reaches a value of about η_{BTES}=0.75 at the end of the studied period. This

inefficiency is due both to the variations in the internal energy of the BTES soil volume (which results in the increase of the average soil temperature) and to the thermal losses from the boundaries of the same volume. These thermal losses are clearly proportional to the difference between the average temperatures of the BTES and the surrounding soil. When the system reaches its stationary configuration, at around the 25th year, the difference between the energies annually entering and leaving the BTES essentially equals its thermal losses.

The thermal energy balance of the plant during its 25th year of operation can be verified using the monthly energy values that have been summarised in *Table 22*. These energies are: the space heating loads of the building (E_{load}), the waste heat from the solar collector ($E_{S,out}$), the input and output energies of the BTES ($E_{BTES,in}$, $E_{BTES,out}$), the heat delivered to the heat pump evaporators ($E_{e,HP}$), the heat supplied by heat pumps to the building heating system ($E_{c,HP}$) and the energy provided by the backup heater ($E_{gas\ boiler}$).

The data in *Table 22* show that during the months when there is no heating demand from the building and the availability of the solar resource is greater, the waste heat from the two solar collectors is totally transferred to the BTES. This energy, for the studied configuration, amounts to $E_{S,out}$=140.33 MWh and, as already mentioned, corresponds to about 80% of annual thermal energy produced by the solar collectors (equal to $E_{S,out}$=177.21 MWh).

In the winter season, 86% of heat energy required by heat pumps for their operation ($E_{e,HP}$=133.33 MWh) is recovered from the soil ($E_{BTES,out}$=115.12 MWh) while the remaining 14% is directly supplied from the solar system ($E_{S,out}$=18.21 MWh). The residual energy produced in this period of the year by the solar systems is directly transferred into the BTES ($E_{BTES,in}$ =18.67 MWh). The latter energy represents about 11% of the thermal energy that annually charges the geothermal storage.

These results show an interesting aspect of the operation of the proposed system: during the winter season, it is often possible that days with clear skies occur. During these days, the direct solar irradiation levels may be sufficient for the activation of the solar collectors. Thus, if this energy collection is contemporary with the building heating demand hours, it can be directly delivered to the heat pump evaporators. Otherwise, for example at weekends, it can be stored in the BTES as during the summer season.

Finally, from the data of *Table 22*, it is possible to observe that the studied configuration of the proposed system is able to cover up to 97% of the annual heating demand of the building (E_{load}=166.55 MWh) while the remaining 3% is covered by the energy delivered by the gas boiler backup heater ($E_{gas\ boiler}$=5.45 MWh).

Table 22. Monthly thermal energy values at 25th year (ID90 configuration)

Month	E_{load}	$E_{S,out}$	$E_{BTES,in}$	$E_{BTES,out}$	$E_{e,HP}$	$E_{c,HP}$	$E_{gas\ boiler}$
	[MWh]						
January	59.49	8.10	2.87	41.95	47.21	56.98	2.58
February	38.70	7.29	3.09	27.63	31.85	38.62	0.10
March	6.26	12.63	9.80	2.22	4.97	6.13	0.14
April	0	13.51	13.53	0	0	0	0
May	0	20.39	20.34	0	0	0	0
June	0	21.62	21.59	0	0	0	0
July	0	25.01	24.96	0	0	0	0
August	0	19.93	19.91	0	0	0	0
September	0	15.68	15.67	0	0	0	0
October	0	13.29	13.27	0	0	0	0
November	0	10.88	10.87	0	0	0	0
December	62.09	8.86	2.91	43.33	49.31	59.51	2.63
25th year	**166.55**	**177.21**	**158.79**	**115.12**	**133.33**	**161.24**	**5.45**

The electric energy balance of the plant during its 25th year of operation can be verified using the monthly energy values that have been summarised in *Table 23*, where are described: the net electric energy produced by the dish-Stirling plant (E_n), the electric energy absorbed by the heat pump system ($E_{ele,hp}$), the parasitic electric absorptions of the plant ($E_{plant,p}$), the net electricity exchanged with the grid ($E_{ele,net}$), the coefficient of

performance of the heat pumps (COP_{hp}) and the global coefficient of performance considering all the parasitic electric consumptions of the plant (*COP*).

Table 23. Monthly electric energy and COP values at 25th year (ID90 configuration)

Month	E_n	$E_{ele,hp}$	$E_{plant,p}$	$E_{ele,net}$	COP_{hp}	COP
	[MWh]				[-]	
January	2.21	10.33	0.87	-9.00	5.51	5.08
February	2.24	7.15	1.07	-5.98	5.40	4.70
March	5.37	1.24	0.56	3.57	4.94	3.40
April	6	0	0.38	6	0	0
May	11	0	0.45	10	0	0
June	11	0	0.46	11	0	0
July	14	0	0.49	13	0	0
August	10	0	0.46	10	0	0
September	7	0	0.39	7	0	0
October	6	0	0.38	6	0	0
November	4	0	0.35	4	0	0
December	2.89	10.79	0.90	-8.80	5.51	5.09
25th year	**81.73**	**29.52**	**6.75**	**45.46**	**5.46**	**4.45**

The analysis of the results of *Table 23,* shows that the heat pumps reach an annual COP_{hp}=5.51 which reduces to *COP*=4.4 if all the parasitic consumptions related to operations of the hydraulic circulators of the plant are considered. The interesting result from this data is that considering the electric grid as an energy storage system, 44% of the electric energy annually produced by the solar field can be used to cover the total electric consumption of the heating plant (36.27 MWh). The remaining 56% (amounting to 45.46 MWh) can, for example, be used either to cover the remaining electricity

consumption of the building or simply be sold to the electric national grid. Under these assumptions, the renewable fraction of the heating system would reach the extremely high value of f_r=97 % which would correspond to a total annual reduction of emissions of $\Delta e_{CO_2} = 96\%$.

These very high values of the system efficiency were achieved through the optimisation process of the BTES geometry. In this regard, the BTES inlet and outlet temperatures and the average soil temperature are depicted in *Figure 65* as a function of the successive days of the 25th year of plant operation.

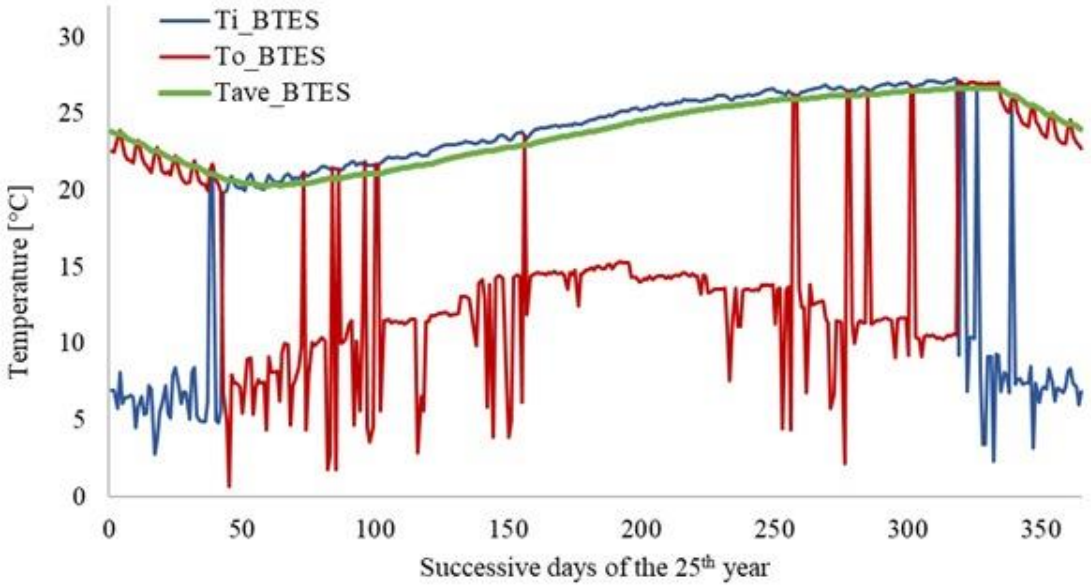

Figure 65. Daily averaged values of the input, output and soil temperatures of the BTES at the 25th year of operation (ID90 configuration*)*

As is shown in *Figure 65*, during the winter discharging phases, the temperature of the fluid exiting the BTES (red line) is always higher than the inlet temperature (blue line). During the charging phase, instead, this situation is reversed. The large temperature differences of the outlet and inlet temperature with respect to the average soil temperature (green line), during the discharging and charging phases respectively, indicate the generation of local high thermal gradients around the boreholes of the BTES.

The results generated by the numerical model and presented above asses both the technical feasibility and the efficiency of the proposed CHP plant if it were located in a central Mediterranean location. However, it was not possible to compare the accuracy of these numerical results with experimental data, since there are no pilot installations of this kind currently built. To overcome this problem, the accuracy of the solutions of each plant component was assessed, assuming that this was sufficient to demonstrate the accuracy of the overall model. Detailed information on the calibration of the dish-Stirling model and its predictive capability has already been provided, while regarding the accuracy of the BTES model, which represents the second key element of the proposed layout, it is possible to provide the following additional information:

i) the TRNSYS Type 557 was used to study the dynamic response of different BTES configurations. This Type implements the widely used Duct Ground Heat Storage Model (DST), which is considered state-of–the-art for these kinds of simulations [159]
ii) the values of the soil thermal properties that were used as input for the DST model have a narrow range of possible variations which, therefore, would not lead to substantial changes in the numerical results of the simulations presented in this analysis.

6.5.2 Analysis of the optimised combined heat and power system configurations

Through the optimization process, 4 configurations were selected among 1440 analysed. The best performing cases were selected by extracting from the dataset the configurations that maximise either the OEVE index or the ratio f_r. The first group represents the most economically advantageous configurations, while the second represents those characterised by a higher fraction of energy covered by a renewable source. The results of this process are summarised in *Table 24*, where the configuration identification number, the OEVE and f_r. indexes, the BTES geometric parameter, the system COP and the corresponding storage efficiency are reported. This data shows that optimised configurations refer to systems layout with a maximum of two dish-Stirling collectors. This is essentially related to the fact that the thermal energy generated by two

collectors is more than sufficient to cover the thermal loads required by the heat pumps and the number of the collectors significantly affects the investment cost required to build the system

Table 24. Selected optimum CHP system configurations

Criteria:	**highest renewable fraction**		**most cost-efficient**	
Simulation ID number	236	90	261	397
OEVE	13.15	0.15	**21.50**	**11.26**
f_r	**0.59**	**0.78**	0.43	0.72
n_{dish}	1	2	1	2
s_b (m)	8	2	12	12
$n_{b,s}$	4	4	4	3
$n_{b,h}$	15	25	20	15
H_b (m)	30	60	10	50
L_{tot} (m)	1800	6000	800	2250
V_{BTES} (m^3)	99752	20782	99752	280552
COP_{hp}	4.14	5.37	4.44	4.48
COP	3.56	4.43	3.72	3.90
f_{hp}	0.78	0.96	0.55	0.92
η_{BTES}	0.99	0.75	0.52	0.60

Moreover, the analysis of data in *Table 24* suggests a second relevant observation: for a fixed number of solar collectors, the configurations that are more economically advantageous (ID261 and ID397) are those with the lowest fraction of energy covered by the renewable energy source (ID236 and ID90). This trade-off can be easily explained, since: the higher the value of L_{tot} the higher the f_r ratio and the lower the OEVE index (since the investment cost of the BTES is higher). The most cost-effective configuration,

for example, is the ID261 which refers to a layout with a single collector and is characterised by an f_r =0.43 and a renewable fraction equal to f_{hp}=0.55. The configuration ID90 with two solar collectors (whose results have already been discussed in detail above) is characterised, instead, by the highest renewable fraction (f_{hp} =0.96) while it presents the lowest value of the OEVE index among all the others. To conclude the discussion of these results, it is interesting to underline that the configurations with two solar collectors are those that are characterized by higher COP_{hp} values compared to those with one solar collector. The higher efficiency of the former is due to the instance where the surplus of thermal energy, with respect to the heat pump demand, determines a greater increase of the BTES temperature during the charging stages. This higher soil thermal level determines a greater efficiency of the heat pumps when the BTES is discharged.

More specifically, with regard to the environmental indicators of the 4 optimum configurations, with respect to the case of a conventional heating system powered by a gas boiler, reference can be made to the quantities shown in *Table 25*.

Table 25. Environmental indicators of the optimum configurations

Simulation ID number	$S_{thermal\ energy}$	AE_{CO_2}	Δe_{CO_2}
	(MWh/year)	(t_{CO2}/year)	(%)
261	91.4	18.4	54.9
236	129.6	26.1	77.8
397	153.2	30.9	92.0
90	159.9	32.2	96.0

From the analysis of these quantities, it can be deduced that the installation of the proposed CHP plant would result in percentage emission reductions, compared to the conventional plant, ranging from 55% (for the ID261) to 96% (for the ID90). The configuration with the highest f_r ratio (ID90) would allow savings of almost 160 MWh produced from fossils per year.

With regard to the financial analysis, the DPBT values for the 4 analysed configurations, according to the 12 hypothesised financial scenarios, have been reported in *Table 26*. From this data, it is possible to notice that, for all the 4 configurations, assuming both a discount rate of 7% and no initial investment financing (financial scenario I_0), the incentivised sale of electricity produced by the CHP plant would not be sufficient to amortise the investment costs within 25 years (i.e., the useful life of the cogeneration plant).

Table 26. DPBT of the optimum configurations

Number of simulation	I_0	I_A	I_B	I_C	Discount rate
261	11.2	8.8	5.6	4.5	0%
	15.2	11.4	6.9	5.0	3.5%
	25	16.7	8.9	6.2	7%
236	12.0	9.6	6.4	4.9	0%
	16.6	12.6	7.9	5.9	3.5%
	25	19.2	10.3	7.3	7%
397	14.2	11.7	8.4	6.7	0%
	20.5	15.8	10.4	8.1	3.5%
	25	25	14.2	10.3	7%
90	18.9	15.7	11.4	9.3	0%
	25	25	15.2	11.8	3.5%
	25	25	25	16.8	7%

This, obviously, would represent the worst possible scenario. If, on the other hand, considering an initial investment financing of 35% (scenario I_B), the payback times of the configurations with one and two concentrators would be reduced by 10 and 15 years, respectively. Assuming the same scenario I_B, the investment risk for most of the 4

configurations analysed would be significantly reduced compared to the worst-case scenario, as shown by the IRR data reported in *Table 27*.

Table 27. IRR of the optimum configurations

	Simulation ID number			
Scenario	236	90	261	397
I_0	6.07%	2.20%	6.67%	4.70%
I_A	8.21%	3.80%	8.96%	6.55%
I_B	12.43%	6.80%	13.53%	10.12%
I_C	15.64%	8.97%	17.03%	12.75%

It is, also, reasonable to assume that the necessary reduction in the initial investment costs (i.e., 40%) must not be exclusively related to the financing mechanism (included in the incentive scheme), but also to a possible cost reduction in the technology itself. Such reduction could result because greater commercial diffusion of these systems could trigger economies of scale. Dish-Stirling collectors, for example, although the most efficient among all the solar systems, have not yet reached commercial maturity comparable to that of the other CSP systems.

6.6 Outcomes

In this part of the thesis, a heat and electric power cogeneration plant that combines a field of dish-Stirling collectors, seasonal geothermal storage and a system of water-to-water heat pumps, was proposed for the first time. The cogeneration plant has been designed both to supply thermal energy to the heating system of a non-residential building and to produce electricity. The operation of the plant has been tested by means of hourly-based numerical simulations that have been carried out using a numerical model implemented with TRNSYS. Building 9 of the Department of Engineering on the Palermo University campus was used as a case study and the real operational data of a pilot dish-

Stirling collector, located in the same area, was used to carefully calibrate the numerical model. Using energy and economic performance indicators, it was, finally, possible to optimise both the number of solar collectors and the geometry of the seasonal thermal storage. The best performing configuration consists of two dish-Stirling collectors and 100 geothermal exchangers, each 60 m long and 2 m apart. The two solar collectors annually generate 82 MWh of electrical energy and 177 MWh of thermal energy. 80% of the thermal energy annually produced by the Stirling engines is stored in the soil since it is generated in summer, when the heating system of the building is off. 75% of this stored energy is, then, recovered during the winter season and transferred to the evaporators of the heat pumps. 14% of all heat energy annually required by the heat pumps is directly supplied by the solar collectors whenever the energy generation is simultaneous with the heating demands of the building. With this configuration, the heat pump system can cover about 97% of the total heating demand of the building which annually amounts to 166 MWh. The annual average value coefficient of performance of the heat pump systems is equal to 5.37, while that of the whole plant, considering all the electric consumption, is equal to 4.43. Under these conditions, if it is further assumed that the electric grid is used as seasonal storage, it would be possible to cover all the electric requests from the heat pump employing about 44% of the total electric energy produced by the solar field during one year. In this way, a very high value, about 96%, of thermal energy for heating the building from renewable sources could be achieved which would correspond to annual savings of 32 t_{CO2}. In addition, there would remain about 45 MWh/year of electric energy produced by the solar system that could be used either to cover all the other consumptions of the building or be sold to the national electric grid. Thus, the results of this model demonstrate the technical feasibility of the new proposed cogeneration layout by also quantifying the thermal and electrical efficiency values for a plant built in the Southern Mediterranean basin. However, further economic analyses, based on a plant's useful lifetime of 25 years, show that the commercial penetration of these types of systems should be strongly supported by a national incentive scheme capable of including both a feed-in tariff of about 369 €/MWh and an initial investment financing of at least 40%. Then, a greater commercial penetration could trigger economies of scale capable to reduce in the installation cost of the plant itself. Dish-Stirling collectors, for example,

although are the most efficient among all the solar systems, have not yet reached commercial maturity comparable to that of the other CSP systems.

Nomenclature

a_1	first parameter of the Stirling engine mechanical efficiency curve [-]
a_2	second parameter of the Stirling engine mechanical efficiency curve [W]
AE_{CO_2}	amount of avoided CO_2 emissions [ton/year]
A_n	net effective surface area of the dish collector [m^2]
A_r	receiver aperture area [m^2]
C_{BTES}	unit cost of geothermal well [€/m]
C_{CO_2}	unit revenue related to the amount of CO_2 avoided [€/t_{CO2}]
C_c	degradation coefficient of the heat pump [-]
C_{dish}	unit cost of the dish-Stirling solar concentrator [€/concentrator]
$c_{electricity}$	unit cost of electricity [€/kWh]
CF_t	cash flow for the t-th year [€/year]
C_{HP}	total cost of the two selected water-to-water heat pumps [€/m]
C_i	valorisation coefficient of the thermal energy produced [-]
$c_{natural\ gas}$	unit cost of natural gas [€/kWh]
COP_{hp}	coefficient of performance of the heat pumps system [-]
COP	global coefficient of performance of the CHP plant [-]
COP_{FL}	full-load coefficient of performance of the heat pump [-]
COP_{PL}	partial-load coefficient of performance of the heat pump [-]
$C_{p,s}$	volumetric heat capacity of the soil [W/(m^3·K)]
$c_{p,f}$	specific heat of the heat transfer fluid in the pipes [W/(kg·K)]
$E_{BTES,\ in}$	thermal energy charged into the BTES [kWh]
$E_{BTES,\ out}$	thermal energy discharged from the BTES [kWh]
$E_{c,HP}$	heat supplied by the heat pumps condensers [kWh]
$E_{e,HP}$	heat delivered to the heat pump evaporators [kWh]
$\dot{E}_{ele,hp}$	electric power absorption of the heat pump [W]
$E_{ele,net}$	net electricity exchanged between the CHP plant and national electric grid [kWh]

$\dot{E}_g$	gross electric power output of the CSP collector [W]
$\dot{E}_{gas,boiler}$	thermal energy produced by the gas boiler [W]
E_{hp}	thermal energy produced by the two heat pumps [kWh]
E_{load}	heating energy demand of the building [kWh]
$\dot{E}_n$	net electric power output of the CSP collector [W]
$\dot{E}_p$	parasitic electric absorption of the system [W]
$\dot{E}_p^{ave}$	average value of the parasitic electric absorption of the system [W]
$E_{\text{plant,p}}$	parasitic electric absorptions of the CHP plant [kWh]
E_{sun}	solar energy collected by the concentrator [kWh]
$E_{S,out}$	thermal energy produced by the concentrator [kWh]
f	Darcy-Weisbach frictional factor [-]
f_r	annual renewable fraction [%]
h_{f}	convective fluid-to-pipe heat exchange coefficient [W/(m^2·K)]
h_{r}	convective heat exchange coefficient of the receiver [W/(m^2·K)]
H_{b}	deep of the boreholes of the BTES [m]
i	discount rate [%]
I	total initial investment of CHP plant [€]
I_{b}	solar beam radiation [W/(m^2)]
I_{CO_2}	income from the amount of avoided CO2 emissions [€/year]
$I_{el,\ sold}$	income from the incentive sale of renewable electricity [€/year]
I_{hp}	income from the installation of renewable heat pumps [€/year]
L_{tot}	total length of boreholes [m]
M	median function
$\dot{m}_{c,HP}$	cold-side mass flow rate of the heat pump [kg/s]
$\dot{m}_{f,\text{BTES}}$	mass flow rate of the fluid inside the U-leg exchanger [kg/s]
$\dot{m}_{f,U}$	mass flow rate of the fluid inside the U-leg exchanger [kg/s]
n	pair number of predicted values and actually measured values
$n_{b,\text{h}}$	number of boreholes in the innermost ring of the BTES [-]
$n_{b,\text{s}}$	number of boreholes in each series of the BTES [-]

$n_{b,t}$	total number of boreholes of the BTES [-]
n_{dish}	number of dish-Stirling solar concentrator [-]
Nu	Nusselt number of the heat transfer fluid in the pipes [-]
PLF	Partial load factor of the heat pump [-]
PLR	Partial load ratio of the heat pump [-]
P_n	Nominal heat output of the heat pump [W]
Pr	Prandtl number of the heat transfer fluid in the pipes [-]
Pr_{solar}	bonus corresponding to the solar integration fraction of plant [€/MWh]
Q	accuracy ratio
$\dot{Q}_{BTES}$	heat power exchanged with the BTES [W]
$\dot{Q}_C$	cooling power of the heat pump [W]
$\dot{Q}_{FH}$	full-load heating power of the heat pump [W]
$\dot{Q}_{PH}$	current heating power of the heat pump [W]
$\dot{Q}_{r,in}$	heat power absorbed by the receiver [W]
$\dot{Q}_{r,\mathrm{out}}$	heat loss power from the receiver [W]
$\dot{Q}_{S,in}$	thermal input power of the Stirling engine [W]
$\dot{Q}_{S,\mathrm{out}}$	thermal output power of the Stirling engine [W]
Q_{uf}	utilisation coefficient of the heat pump[-]
Re	Reynolds number of the heat transfer fluid in the pipes [-]
r_b	radius of each borehole of the BTES [m]
$r_{p,i}$	inner radius of each pipe of the U-leg thermal exchanger [m]
$r_{p,o}$	outer radius of each pipe of the U-leg thermal exchanger [m]
R_b	thermal resistance of the borehole [(m·K)/W]
R_p	total thermal resistance of a pipe of the U-leg thermal exchanger[(m·K)/W]
R_T	temperature correction factor of Eq. 6 [-]
se_{CO_2}	specific emission of CO_2 [gCO_2/kWh_{th}]
s_b	spacing between boreholes [m]
$S_{natural\ gas}$	natural gas savings [€/year]

$S_{\substack{thermal \\ energy}}$	thermal energy savings of building [kWh_{th}]
T_{air}	temperature of the air [°C]
$T_{ave,BTES}$	inlet temperature to the BTES [°C]
T_b	basic incentive tariff [€/MWh]
$T_{c,i}$	cold-side inlet temperature to the heat pump [°C]
$T_{c,o}$	cold-side outlet temperature from the heat pump [°C]
T_f	feed-in tariff [€/MWh]
$T_{h,i}$	hot-side inlet temperature to the heat pump [°C]
$T_{h,o}$	hot-side outlet temperature from the heat pump [°C]
$T_{i,BTES}$	inlet temperature to the BTES [°C]
$T_{o,BTES}$	outlet temperature from the BTES [°C]
T_r	temperature of the receiver [°C]
T_0	reference temperature [°C]
$T_{s,0}$	undisturbed temperature of the soil [°C]
T_{sky}	apparent sky temperature [°C]
ULT	lifetime of the plant [year]
V_{BTES}	conventional volume of the BTES [m^3]
$\dot{W}_S$	mechanical output power of the Stirling engine [W]
x_c	half of the shank spacing between U-legs [m]
x_i	actually measured value of the *i*-th pair
y_i	predicted value of the *i*-th pair

Greek letters

Δe_{CO_2}	total annual reduction of emissions [%]
ε_p	absolute roughness of the pipe surface [m]
ε_r	emissivity of the receiver [-]
ζ	median symmetric accuracy
$\eta_{\substack{gas \\ boiler}}$	overall yield of the existing gas boiler [-]
η_{BTES}	storage efficiency of the BTES [-]

η_{cle}	cleanliness index of the collector mirrors [-]
η_{cle}^{ave}	average value of the cleanliness index of the collector mirrors [-]
η_e	electrical efficiency of the alternator [-]
η_o	optical efficiency of the collector with clean mirrors [-]
$\eta_{S,M}$	mechanical efficiency of the Stirling engine [-]
$\eta_{S,T}$	thermal efficiency of the Stirling engine [-]
λ_f	thermal conductivity of the heat transfer fluid [W/(m·K)]
λ_g	thermal conductivity of the borehole grout [W/(m·K)]
λ_p	thermal conductivity of the pipe material [W/(m·K)]
λ_s	average thermal conductivity of the soil [W/(m·K)]
μ_f	dynamic viscosity of the fluid [kg/(m·s)]
σ	Stefan-Boltzmann constant, $5.67 \cdot 10^{-8}$ [W/(m^2·K^4)]

Acronyms

ATES	Aquifer Thermal Energy Storage
BTES	Boreholes Thermal Energy Storage
CHP	Combined Heat and Power
CO_2	Carbon dioxide
COP	Coefficient of Performance of a heat pump
CSP	Concentrating Solar Power
DNI	Direct Normal Irradiance
DPBT	Discounted Payback Time
DST	Duct Ground Heat Storage Model
GHG	Greenhouse Gases
GHI	Global Horizontal Irradiance
GWTES	Gravel-Water thermal energy storage
HDD	Heating Degrees Days
HP	Heat Pump
HWTES	Hot Water Thermal Energy Storage
IRR	Internal Rate of Return

MAPE	Mean Absolute Percentage Error
NPV	Net Present Value
OEVE	Overall Economic Viability Evaluation
PCU	Power Conversion Unit
PI	Profitability Index
RES	Renewable Energy Sources
STES	Seasonal Thermal Energy Storage
STTES	Short-Term Thermal Energy Storage
TMY	Typical Meteorological Year

Chapter 7

Life Cycle Sustainability Assessment of a dish-Stirling concentrating solar power plant

In this chapter, a Life Cycle Sustainability Assessment of the existing dish-Stirling system located in southern Italy is presented. This part of the thesis allows the assessment of the system in the three dimensions of sustainability: environmental, economic, and social, as well as a detailed and careful analysis of the entire life cycle of the CSP system providing a clear representation of the holistic sustainability performance of solar electricity production.

7.1 Introduction

Energy systems are undergoing a worldwide transformation due to their high pollution impacts in terms of carbon and other toxic discharges. The transition toward low carbon emissions and an energy-efficient society are being promoted especially by Goal 7 (Affordable and clean energy), Goal 12 (Responsible consumption and production) and Goal 13 (Climate action) of the Sustainable Development Goals (SDGs)

[160]. The concepts such as an increase in energy savings and the development of alternative energy technologies, aimed at reducing greenhouse gas (GHG) emissions, are the current focus of public debate and hence become key elements of the energy policies of any industrialized country. The ongoing exploitation of non-renewable energy resources is unsustainable in perspective to future generations – across the three dimensions of sustainability: economic, environmental, and social. In 2014, the European Union published their targets to significantly increase the use of renewable energy sources for electric energy generation in the 2030 framework for Climate and Energy policies [161]. This strong commitment is essential to achieve the goal of reducing CO_2 emissions related to the generation of electrical energy and avoid a temperature rise above 2 °C in 2050 [162]. Due to the prevalent use of fossil fuels and the permanent growth in energy demand, the electricity sector is closely linked to global warming-related emissions. Among the different renewable energy sources, solar energy represents an abundant source of energy with the highest exploitation potential of all energy sources to satisfy a substantial portion of the world's future energy demand [163].

In the last decade, there has been a significant increase in solar-based electricity generation, exemplarily shown by the use of Concentrating Solar Power (CSP) plants. CSP technologies enable the indirect conversion of solar radiation into electricity, by first converting thermal energy into mechanical energy using a working fluid that evolves according to a thermodynamic cycle and then transforming the latter energy into electricity using a power generator [164]. The International Energy Agency (IEA) expects the CSP technology to be highly competitive by 2030, assuming exploitation of the full potential of CSP. By 2050, 11.3% of total global electricity could be provided by the mentioned plants, leading to a reduction in CO_2 emission of 2.1 Gt per year [165]. Among CSP systems, dish-Stirling systems have several advantages such as the highest efficiency in converting solar energy into electricity. In addition, from the environmental point of view, these systems produce electrical energy without releasing greenhouse gases or pollutants into the atmosphere. Yet, like most of the common technologies in the renewable energy sector, the dish-Stirling system is responsible for most of the environmental impacts in its production and installation phases. Both steps may involve high energy consumption and the use of raw materials. Considering the social and economic sustainability dimensions, CSP systems could result in further potentially

positive effects compared to other technologies using different energy sources. Life Cycle Sustainability Assessment (LCSA) is a framework combining and measuring all three pillars of sustainability. A detailed and careful analysis of the entire life cycle of the CSP system could provide a clear representation of the holistic sustainability performance of the electricity production from the solar energy source.

The goal of the following part of the thesis was to analyse an existing dish-Stirling concentrating solar power plant, supplying energy into the grid, in terms of its sustainability performance. Far more impact indicators than only Global Warming Potential (GWP) were reported for an improved environmental assessment and the explicit description of individual components allows the author and reader to identify the emission hotspots. Additionally, for the first time, critical raw materials used for the dish-Stirling production have been assessed as part of S-LCA.

7.2 Life Cycle Sustainability Assessment

LCSA is a framework combining all three pillars of sustainability. LCSA extends the scope of the analysis from mostly product-related questions to sector-related questions [166]. The LCSA framework was developed by Kloepffer and Finkbeiner et al. [167,168]. It can be described with the formal *Equation (7.1)* – being ISO-14040-consistent [169]:

$$LCSA = LCA + LCC + (S - LCA) \tag{7.1}$$

where Life Cycle Assessment (LCA) is the environmental assessment of a product's life cycle [169], Life Cycle Costing (LCC) is the cost of a product's life cycle [170] and S-LCA is the Social Life Cycle Assessment of a product [171,172]. To implement LCSA, a contemporary and complementary implementation of the three techniques (LCA, LCC and S-LCA) to the same functional unit (FU) and an equivalent system boundary must be carried out. It is a method for sustainability assessment of both positive and negative impacts, whereby the social pillar, in particular, can have a positive influence on the overall sustainability assessment [171–173]. The framework does not include any weighting between the three pillars and none compensation between the pillars is allowed [168].

The advantage of LCSA is the transparency and the identification of potential trade-offs between the pillars [174]. LCA offers a detailed approach for assessing different processes and systems as well as a quantification of the potential environmental impacts. For the life cycle of a product or service, potential environmental impacts are considered in pre-defined system boundaries based on quantitative data on raw material consumption and emissions of all respective relevant processes. According to the ISO standard 14040, LCA includes a systematic investigation of the environmental impacts for all stages of a product's life cycle [169,175,176]. LCC is a methodology encompassing and assessing all costs related to a product arising in all life cycle stages from cradle-to-grave [177,178]. The LCC methodology is used for various purposes in a high number of different sectors, nevertheless, there is no uniform and distinct definition for LCC except the ISO reference standard for buildings [179]. S-LCA is the most recent of the three sustainability assessment techniques presented. It is not yet available for all products standardized. S-LCA as a complementary evaluation approach to LCA and LCC evaluates the social impact of a product considering the same functional unit and an equivalent system boundary [171–173].

7.2.1 Present LCSA studies on dish-Stirling systems

Few publications on LCSA of solar concentrators/dish-Stirling have been published so far. Further LCSA studies have dealt mainly with photovoltaic systems [180–183] or have individually considered one or two of the three named sustainability pillars, not fully meeting the LCSA framework. In detail, Ehtiwesh et al. [184], and Lamnatou and Chemisana [185] analyzed the environmental aspects related to the CSP technology. Two publications, conducted on dish-Stirling systems, were presented by Bravo et al., and Cavallaro and Ciraolo, which respectively illustrated a comparative environmental assessment between the dish-Stirling technology and a photovoltaic (PV) plant with equal power [186] and a preliminary LCA analysis [187]. Benacloche et al. [188] conducted an LCA analysis and a socio-economic Multiregional Input-Output analysis for the estimation of environmental impacts, production services and employment creation, on a parabolic solar concentrator coupled to a biomass system. Corona et al. [189] focused their attention on the social aspect of an LCSA, suggesting a new classification and characterization model based on previous methodological

developments. Naves et al. [190] focused their review study on the evaluation of sustainability in the economic domain of the solar energy sector.

Three publications dealt with LCSA and CSP technology in detail, whereof two studies published all key factors (e.g., system boundaries, functional unit etc.) – see *Table 28.*

The paper by Corona & San Miguel, published in 2019, investigated a novel hybrid solar energy technology (HYSOL) in Spain [191]. The primary objective of this article was to respond to the need expressed by the scientific community to test the use of LCSA for different products and in different sectors. The focus was not on the sustainability results, as the main goal was on identifying the operationalization of LCSA. The relevant framework conditions, such as system boundaries, functional unit and analyzed indicators, can be taken from *Table 28,* as can the presentation of results. The LCSA application itself was described in detail. Further, Corona & San Miguel focused on the presentation and visualization of LCSA to support decision-makers. A visualization proposal, named Sustainability Crown was presented [191]. The second study on LCSA for a fictional CSP plant was published by Ko et al. in 2018 [192]. The framework conditions, tools used, and main results are shown in *Table 28.* As a third publication, the study by Rodríguez-Serrano et al., a sustainability assessment of a solar thermal power generation facility in Mexico was conducted using the Framework for Integrated Sustainability Assessment (FISA). FISA, like LCSA, considers all three pillars of sustainability [193]. Nonetheless, this study did not detail key factors, which is why it was not included in *Table 28*.

Table 28. LCSA studies on CSP systems

	Corona & San Miguel, 2019 [191]	**Ko et al., 2018** [192]
Goal	test the use of life cycle-based sustainability analysis	cradle-to-grave analysis of the environmental performance of a CSP tower plant in selected impact categories
Product	novel type of hybrid concentrating solar power (CSP) plant designed to operate using both solar energy and auxiliary fuels	concentrating solar power (CSP) tower plants

	Corona & San Miguel, 2019 [191]	**Ko et al., 2018** [192]
FU	1 MWh of electricity poured into the grid	1 kWh net electricity fed to the grid
System boundaries	cradle-to-gate	cradle-to-grave use phase: use of grid electricity is included
Data assessed by	two engineering companies	primary data from a project is used, combined with manufacturer data GaBi database
Comparison made with other product(s)	yes: CSP PTC	no
Assumed energy production per year	800 GWh/year	585 GWh/year
Assessed lifetime	n.a.	30 years
LCA indicators	Climate change: kg CO_2e /MWh Water stress: m3/MWh	GWP ADP EP net caloric primary energy demand (PED n.-r. and PED r.) blue water consumption (BWC) land occupation
LCA software and database	SimaPro 8.0.3 & ReCiPe	GaBi & CML2001
LCC indicators	**similar system boundaries** Life Cycle Cost: €/MWh (not clear what is part of it) Costs balance per functional unit Net value added Multiplier effect	**cradle-to-use** (personnel costs excluded) NPV
LCC tools	n.a.	n.a.
S-LCA indicators	**similar system boundaries** Employment creation (person-year) (h/MWh) Social Risk (SHBD) Social Performance of the promoter	LCWE (Life Cycle Working Environment) Distribution of working time (s/country) Lethal and non-lethal accidents
S-LCA tools	SHDB	SHDB
Calculation of EPBT	by CED v9 method	n.a.
Recycling considered	yes	yes

	Corona & San Miguel, 2019 [191]	**Ko et al., 2018** [192]
LCA Climate Change Results	Climate Change: CSP Bio: 45.9 kg CO_2e /MWh CSP GN: 294 kg CO_2e /MWh	Life Cycle: 24.3g CO_2e /kWh Construction: 12g CO_2e /kWh Use: 15.2g CO_2e /kWh EoL: -2.9 CO_2e /kWh
EPBT Results	CSP Bio: 6.1 months CSP GN: 22 months	n.a.
LCC Results	CSP Bio: 211 €/MWh CSP GN: 154 €/MWh	Construction cost: 478 m€ Annual operation costs: 892 t€ NPV: 43,4 m€ (5 % discount rate, 30 years, 66.5 €/MWh)
S-LCA Results	CSP Bio: 454,090 person-year CSP GN: 158,106 person-year Person-year = employment generated	Total working time: 19,398,646s (5388h; 673d – with 8 h each day)

7.2.2 Delimitation of the present study

The differences between the two studies synthetically described in *Table 28* and the present LCSA consist of:

- the actual study refers to a real existing dish-Stirling CSP system located in Italy (Palermo), manufactured in Sweden, and described in *Paragraph 2.5* "*Reference dish-Stirling system*";
- the reference dish-Stirling system supplies electricity to the national electric grid;
- the system boundary was defined as cradle-to-use;
- the functional unit was defined to be the CSP system itself and not a definite amount of energy generated;
- the use-phase and End-of-Life phase were not considered;
- the lifetime of the CSP system was expected to be 25 years, and
- hydrogen as a heat transfer fluid was used (instead of HYSOL technology or heat transfer fluid).

The LCA results obtained were more detailed (impact assessment as well as results presented) compared to those obtained from the above-mentioned studies. Explicit descriptions of the components and their contributions to the total emissions were given

and more impact indicators rather than just carbon dioxide equivalents were assessed. Regarding LCC, the kind of labour, as well as components required to build the CSP plant, were given. The S-LCA, based on the Social Hotspot database, was presented with additional details (specific labour hours from real data). The current part of the thesis is including the European framework for critical raw materials in processes and supply chain.

In the following, the LCSA study for a solar dish-Stirling system is presented, including a complete LCA case study carried out with the software GaBi [194]; a full LCC carried out in accordance with ISO 14040/44 and considering the production and maintenance costs; and a S-LCA which focuses on the risk analysis of raw materials up until their extraction.

7.2.3 Case study: the reference dish-Stirling concentrating solar power plant of Palermo

A grid-connected dish-Stirling solar concentrator with a nominal power of 33 kW located at the campus of the University of Palermo (Italy) was analysed. The dish-Stirling system is a CSP technology performing an efficient conversion of direct normal irradiation into electricity.

The electrical producibility of the dish-Stirling system has been analysed through a numerical model [22] (by *Equation (3.4)*) implemented in the TRNSYS environment [137] and described in *Paragraph 3.1.2* "*A linear model of dish-Stirling electric power generation*". According to the reference numerical model, the electrical production of the dish-Stirling system depends essentially on the solar beam radiation and the air temperature that characterize the installation site, as well as the level of cleanliness of the mirrors. Based on the Meteonorm solar database, Palermo is characterized by an annual normal solar irradiation value of 1,932.61 kWh/m²/y. *Figure 66* shows the monthly values of the cumulative solar beam irradiation and the average air temperature for the installation site (Palermo, Italy) [195].

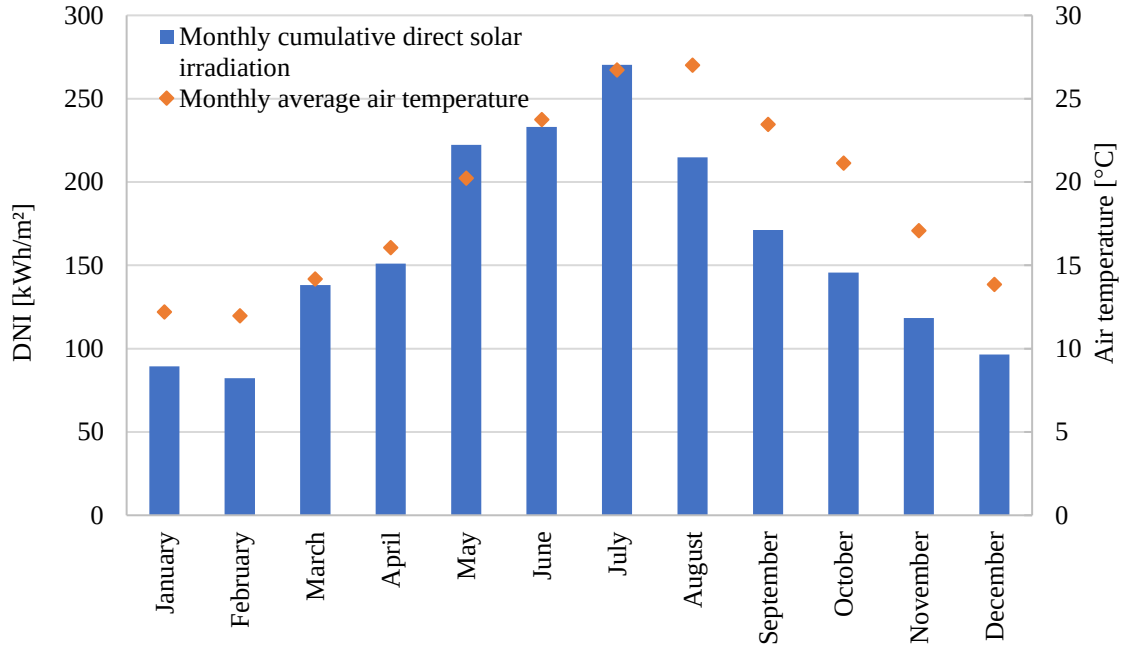

Figure 66. Monthly values of the cumulative solar beam irradiation and the average air temperature typical of Palermo (Italy)

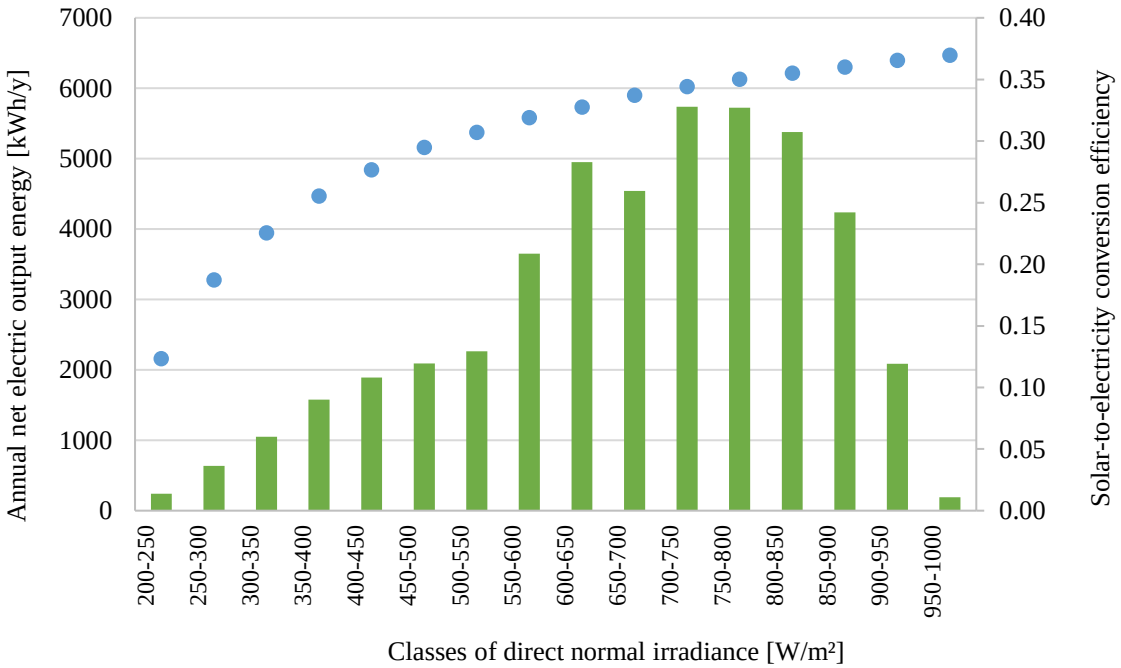

Figure 67. Annual net electric energy produced (green bars) for each class of DNI and the corresponding average value of solar-to-electricity conversation efficiency (light blue dots) [195]

The annual net electricity production of the reference dish-Stirling system amounts to approximately 46 MWh in Palermo. From *Figure* 67, showing the annual net electricity production of the dish-Stirling concentrator distributed per DNI classes (DNI intervals of 50 W/m²), it can be observed that the energy production of the concentrator increases as the DNI level increases, and so does the solar-to-electricity conversion efficiency. Excluding the dish reflector optical losses, the highest average value of the conversion efficiency is about 36% for DNI levels ranging from 950 to 1000 W/m² [195].

7.3 Life Cycle Assessment

A Life Cycle Assessment provides a structured approach to evaluate processes and systems and quantify their potential environmental emissions and impacts. LCA was harmonized with the standards ISO 14040 and ISO 14044, which led to a common structure of LCA including four steps:

- the Goal and Scope of the assessment, including the definition of the FU and the system boundaries,
- the Life Cycle Inventory Analysis (LCI),
- the Life Cycle Impact Assessment (LCIA) and finally,
- the Interpretation [169,175,176].

7.3.1 Goal and Scope

The goal of this LCA, as part of LCSA, was to provide a comprehensive and actual LCA for the production (cradle-to-use) of the dish-Stirling concentrating solar power plant located in Palermo. The FU was set to one power plant. The LCA, especially LCI and LCIA were based on primary data and secondary data from GaBi and Ecoinvent databases. Additional assumptions had to be made in order to obtain as a realistic result as possible. During the use phase, a certain amount of hydrogen would have to be added regularly to the solar plant due to unstoppable leakage of the gas. We assumed that about 95% of all hydrogen was being produced from natural gas and coal [196], inferring the GaBi process *DE: Hydrogen peroxide (100 %; H_2O_2) (Hydrogen from steam cracker) ts*

to be suitable. The software GaBi SP40, its professional database and the Ecoinvent database 3.5 were used. Across various plans, for the sake of improved clarity, the complete engine was modelled, shown in the following process diagram (see *Figure 68*).

Figure 68 distinguishes the following macro-components of the solar concentrator:

- the PCU equipment, comprising the receiver, the Stirling engine and the electric generator;
- the tripod, that is the lattice structure that, anchored to the supporting structure of the paraboloidal reflector, supports the PCU;
- the mirror, i.e. the dish reflector;
- the circle structure on which all mirrors of the reflector are fixed;
- the dish-carrier, that is the lattice structure on which the circle structure is fixed; and
- the elevation tracker and the turntable constituting the biaxial tracking system.

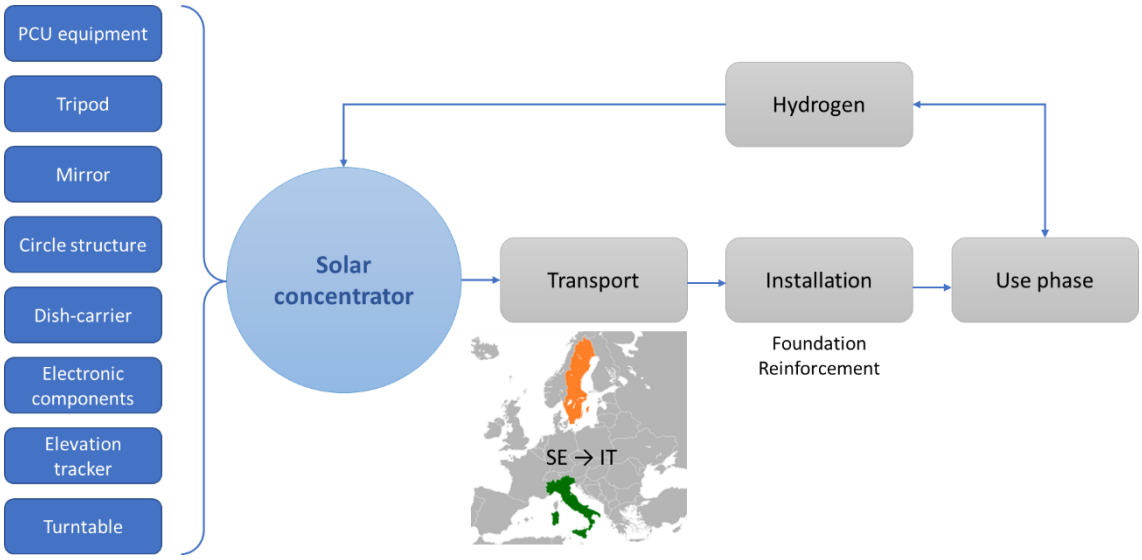

Figure 68. Simplified Process Diagram – System boundaries

The solar concentrator was assembled in Sweden and trucked to Palermo, Italy. Calculations and assumptions relating to the transport have been determined in accordance with the European Automobile Manufacturers Association (2019) [197] and integrated into the model with the GaBi Process *GLO: Truck, Euro 4, 28 - 32t gross*

weight / 22t payload capacity virtually driving 10,473 km, fed with 2,297 kg diesel (*EU-28: Diesel mix at refinery*) (see *Table A 1* in *Appendix*). When it arrived in Italy, a foundation, made of concrete and reinforcing steel (see *Table A 2* in *Appendix*), was cast on-site to securely install the solar concentrator.

7.3.2 Life Cycle Inventory Analysis

Within the LCI, quantitative statements about the input and output variables of the components were collected. Raw materials used and energy, required to produce the individual components and to produce the entire solar concentrator, were collected and combined. Data about the transport route was included. The tables in *Appendix* (form *Table A 1* to *Table A 10*) show the selected databases and processes for the individual components. A brief explanation of why the process was selected and what function it contains is given.

Additionally, the following assumptions have been made. Since only the main materials from the actual Stirling engine (see *Table 29*) and no further production details were available, the processes in the database were taken as reference processes. From the Ecoinvent database the *GLO* process *"Stirling heat and power co-generation unit construction, 3kW electrical feature"* was selected for the Stirling engine as general default, initially used by Kuenlin et al. [198]. However, since the Ecoinvent process described an engine with the power of 3 kW and a total mass of up to 495.96 kg, further assumptions had to be made to get closer to the actual case study. As alredy underlined before, the Stirling engine of the present LCA is characterized by a peak electric power of 33 kW, a total mass of 734.1 kg and four cylinder-piston units. Therefore, since the Stirling engine in the database and the reference engine differ in total mass by 238.14 kg, all the masses of the various constituent materials must be appropriately scaled and changed in the Ecoinvent process. For example, considering the ceramic cavity, it has a mass of 19.5 kg of the total mass equal to 734.1 kg, representing a share of 2.7% of the materials used in the Stirling engine (see *Table 29*), so each material has been updated according to the corresponding share.

Table 29. Materials used for Stirling engine of reference concentrator

Element	Material	Quantity [kg]	Share [%]
Heat exchanger	Nickel alloy	15.6	2.1
Cylinder/piston	Steel	400	54.5
Connecting rods	Steel	130	17.7
Electric generator	Steel	65	8.9
	Copper	65	8.9
Regenerator	Steel	39	5.3
Ceramic cavity	Ceramics	19.5	2.7
Total		**734.1**	

The upscaling procedure (see *Table 30*) did not result in a system that fully represented the actual solar concentrator, but it was the most appropriate approach since detailed data on primary production were not available (see *Table A 5* in *Appendix*).

Table 30. Mass upscaled values

Material	Real mass share [%]	Share of difference [kg]	Assigned to Ecoinvent	New value in GaBi [kg]
Nickel alloy	2.1	5.1	*GLO: nickel, 99,5 %*	5.1
Steel (cylinder/piston, electric generator (steel), regenerator)	68.7	163.5	*GLO: sheet rolling, steel [allocatable product]*	299.5
Steel (connecting rods)	17.7	42.2	*GLO: reinforcing steel [allocatable product]*	178.2
Copper (electric generator)	8.9	21.1	*GLO: copper [allocatable product]*	25.6
Ceramic cavity	2.7	6.3	*GLO: ceramic tile [allocatable product]*	6.8
Other (see Appendix)				218.9
Total				**734.1**

Furthermore, in the actual reference CSP system, two axial gear motors are installed. The GaBi process "*Manufacturing electric motor (<=10 kW); assembling*

electric motor; production mix, at plant; <=10 kW (en)" appeared to correspond to reality. Due to the black-box structure of GaBi, this process could not be accessed directly, which was why the following assumptions and modelling have been made. The percentages given in the description of GaBi e.g. motor assembled from electrical steel (45.1 %), mechanical steel sheet (10.7 %) etc. were copied in a "new" model. To a large extent, the processes could be reconstructed and thus rebuilt (see *Table A 6* in *Appendix*).

However, the original process did not provide any information on the required production energy, hence this must be added as another estimation from further sources to avoid neglecting emissions. Boughanmi et al. [199] did a LCA for a 10 kW engine using the same materials as named by the GaBi process "*Manufacturing electric motor"*. These results could be referred to as a baseline scenario for our calculation of the required production energy.

The production line included materials and transportation, but excluded the energy needed for production. This value needed to be assumed to meet the defined system boundaries and to fully assess the production process. Primary data and exact measurements were not given in this case, so it was necessary to make use of literature data: Boughanmi et al. [199] divided the specified environmental impacts, such as the cumulated energy demand (CED) of a 10 kW electric engine, respect to their life cycle emissions – which was quite similar to the actual one assessed. Boughanmi et al. [199] estimated the CED for the production with 3,481 MJ (see difference value in *Table 31*) – including already the production energy needed [199].

The actual "Italian" CED represented the energy needed for the production line excluding the energy needed – resulting in 2,161 MJ (see CED value, not including electricity, in *Table 31*). In order to assume this missing energy aspect, the difference (1,320 MJ) was estimated and inserted in the process "*FR: Electricity grid mix*", since Boughanmi et al. [199] used French data in their study. Remodelling Boughanmi et al. [199] with the current Italian-CED-basis, the total production CED (incl. energy needed) resulted in 5,644 MJ (see *Table 31*).

Table 31. Calculation Production Energy [199]

Difference	**CED excl. electricity**	**Required production energy**	**CED incl. electricity grid mix**	**Calculated loss factor for the electricity mix in France**	**Energy production**
[MJ]	**[MJ]**	**[MJ]**	**[MJ]**		**[MJ]**
3,483	2,161	1,320	5,644	2.64	500.56

On the basis of the calculated energy loss factor, the real energy demand for the production of the engine was estimated by dividing 1,320 MJ by the value of 2.64 (see *Table 31*). This value of 2.64 was calculated as the *Difference* divided by the *Required production energy*. A plausibility check of the calculated 500.56 MJ, which represented the required amount of production energy, led to the same CED given by Boughanmi et al. [199]. With this CED, scaling up the process to two motors with a total weight of 24.6 kg of the actual "Italian" engine, the calculated assumptions could be integrated into the GaBi model (see *Table A 6* in *Appendix*).

Further assumptions, based on secondary data, had also been made for the required production energy of the dish. The amount of energy needed in the manufacturing process has not been published due to confidentiality agreements [186,187], therefore some assumptions had been made. According to Ordóñez Barreiro et al. [200], the ratio of required energy of different thermal solar systems (dish-Stirling, central power and parabolic trough) throughout the life cycle is seen to be comparable. As only manufacturing data for the object itself was missing, the energy demand in manufacturing was estimated to be 0.037 MJ/kWh, according to Burkhardt et al. [201]. This amount represented the energy assumed for the manufacturing of the solar plant. With a life expectancy of 25 years and an annual electricity generation of 46 MWh (at Palermo, Italy), a total energy of 1,150 MWh was expected at the end of the use phase. With the given information, the total energy demand for all manufacturing processes of the dish was expected at 42.550 MJ.

Besides the unknown amount of production energy (see *Table 31*), the type of energy remained unclear. Within this analysis, the total energy demand was assumed of being provided by the electricity grid in Sweden (GaBi process: *SE: Electricity grid mix*),

as the entire manufacturing operation took place in Sweden. Cut off criteria were applied for few components within the framework of this LCA due to missing process data (see *Table A 4* in *Appendix*).

7.3.3 Life Cycle Impact Assessment (LCIA)

The purpose of the LCIA is to classify and characterize the data collected in the inventory with regard to certain environmental effects, so-called impact categories. The CML 2001 (2016) method was selected for this analysis. The LCI-processes listed in *Table 29, Table 30* and in the tables of *Appendix* were modelled as cradle-to-use assessment in LCIA with GaBi SP40 (part four of [169,175]). A Global Warming Potential (GWP) of 35 t CO_2e was assessed for the functional unit of one dish Stirling engine (see *Table 32*).

Table 32. LCIA Results

Impact Category	**Result**	**Unit**
Climate Change (Global Warming Potential)	34,772	[kg CO_2e]
Acidification Potential	135	[kg SO_2e]
Eutrophication Potential	42	[kg PO_4e]
Photochemical Ozone Creation Potential	22	[kg C_2H_4e]
Abiotic Depletion Potential (fossil)	0.4	[GJ]
Abiotic Depletion Potential of Resource	369,098	[kg Sbe]
Ozone Layer Depletion Potential	0.00	[kg R11e]

Focusing on the total emissions of 35 t CO_2e, it became evident that 21% of all emissions were attributable to the elevation tracker. Both the dish-carrier and the electronic components led to 16% of the total emissions of CO_{2e}. The foundation accounted for 12% of the greenhouse gas emissions, while a total of 11% was attributed to the PCU equipment (see *Figure 69*). Similarly, other emissions were broken down in

detail to assign the occurring emissions. Thus, it emerged that the three main drivers for all indicators were:

- The electronic components,
- the elevation tracker, and
- the PCU equipment,

followed by the dish, the turntable, and the tripod. When considering materials, 54% of total GWP emissions and 43% of the energy needed were caused by the use of steel. The absolute emissions of the Acidification Potential (AP) were 135 kg SO_2 eq./Solar Dish, 31% driven by the PCU equipment (42 kg SO_2e) and 26% by the electronic components (35 kg SO_2e) (see *Figure 70*). In total, 46% of the Eutrophication Potential (EP) was driven by electronic components and 34% by PCU equipment (see *Figure 71*).

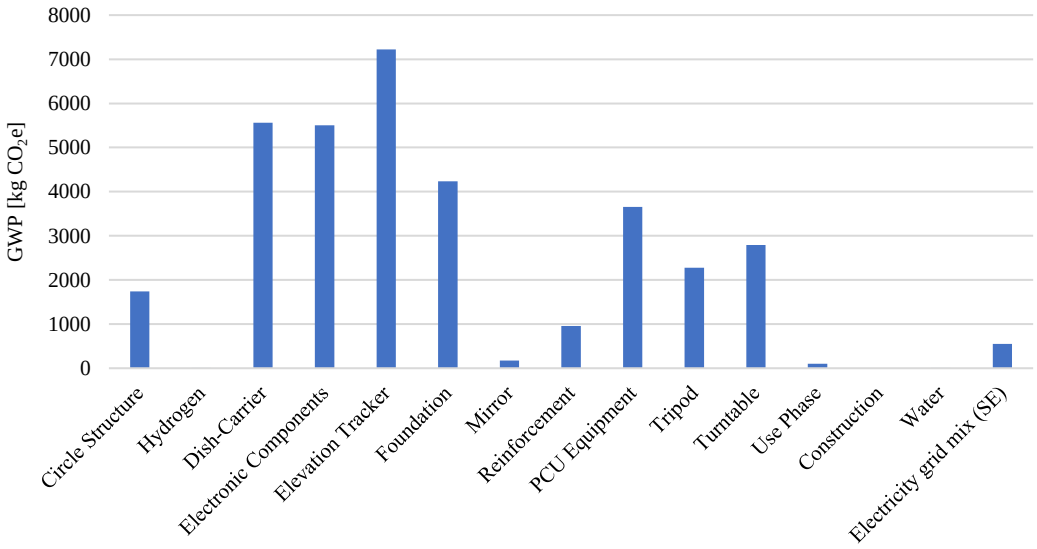

Figure 69. GWP emissions

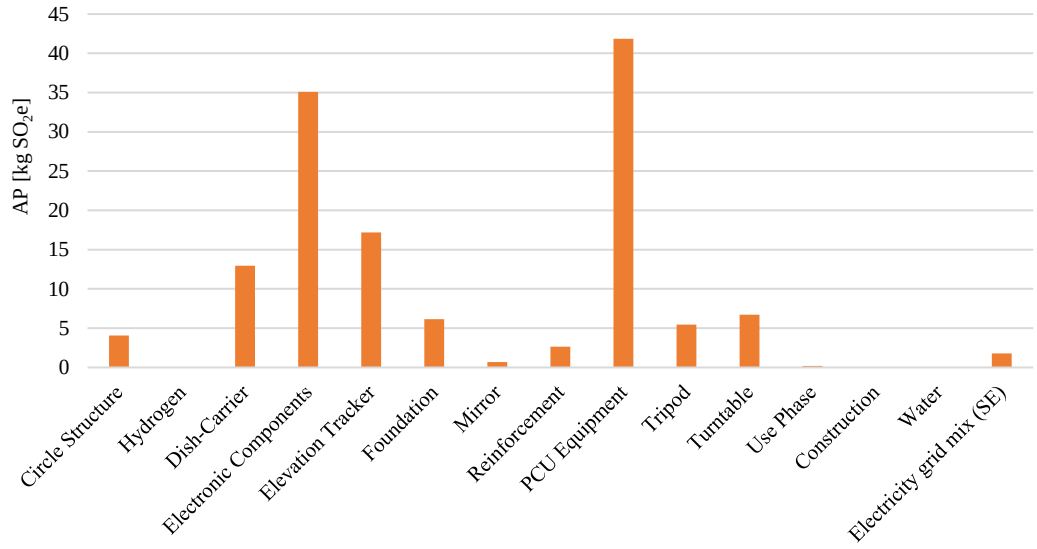

Figure 70. AP emissions

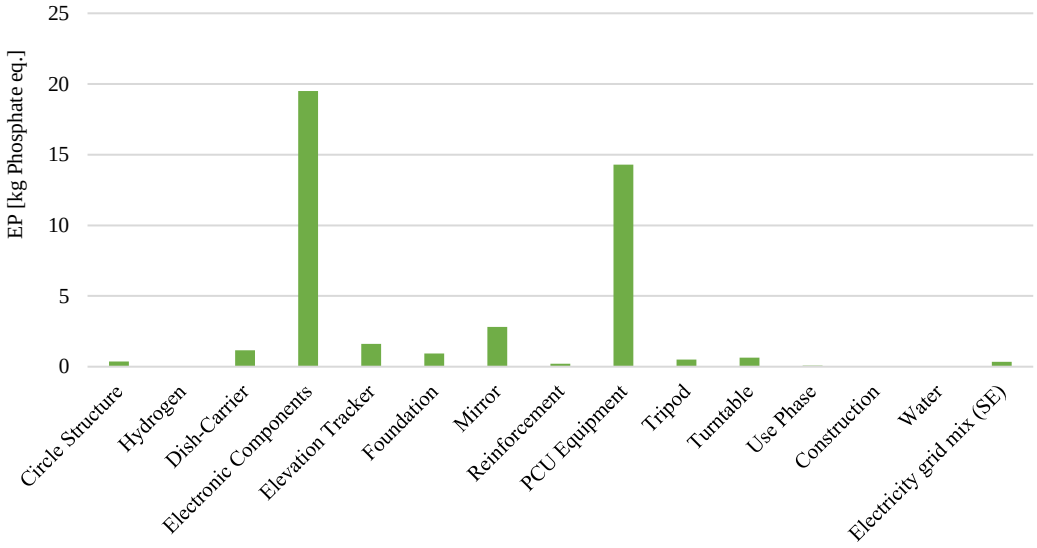

Figure 71. EP emissions

The Photochemical Ozone Creation Potential (POCP) was influenced by 48% by the electronic components in its total emissions of 22 kg Ethene eq. (see *Figure 72*). The electronic components accounted for 61% (see *Figure 73*) for the elementary Abiotic Depletion Potential (ADPe) and 54% for Ozone Layer Depletion Potential (ODP) (see *Figure 74*). The fossil Abiotic Depletion Potential (ADPf), however, was only influenced by 21% by the electronic components. A further 21% was accounted for by the elevation tracker and 13% was attributable to the PCU equipment (see *Figure 74*).

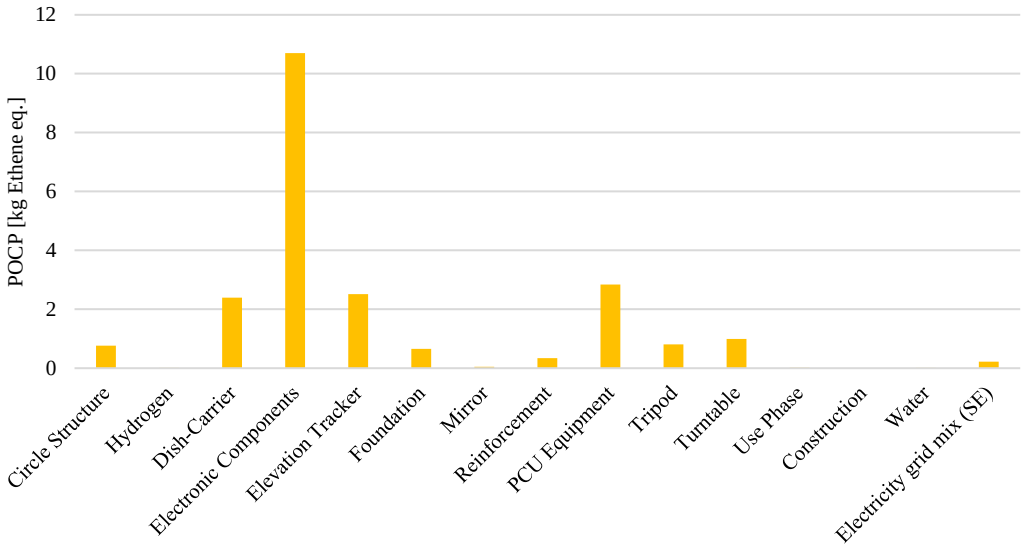

Figure 72. POCP emissions

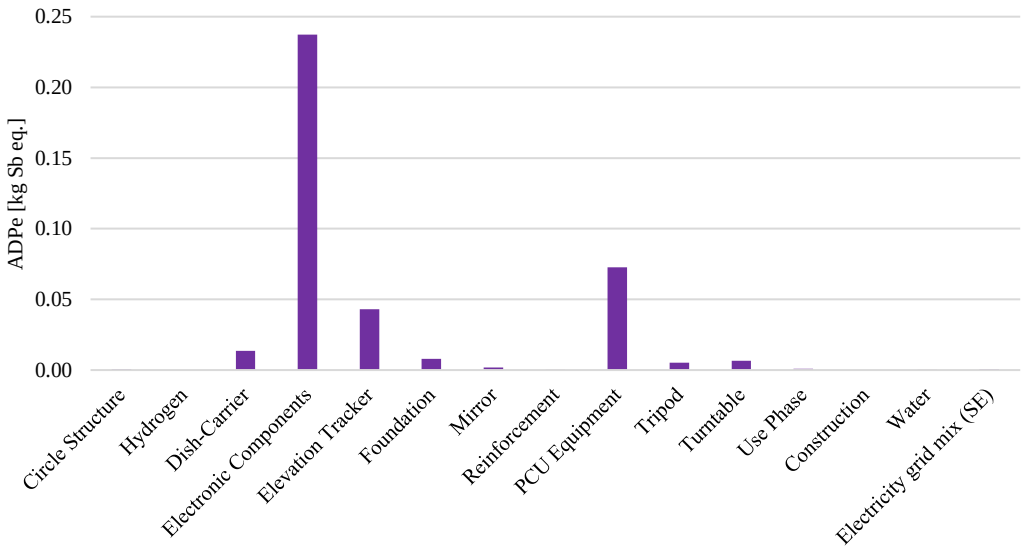

Figure 73. ADPe emissions

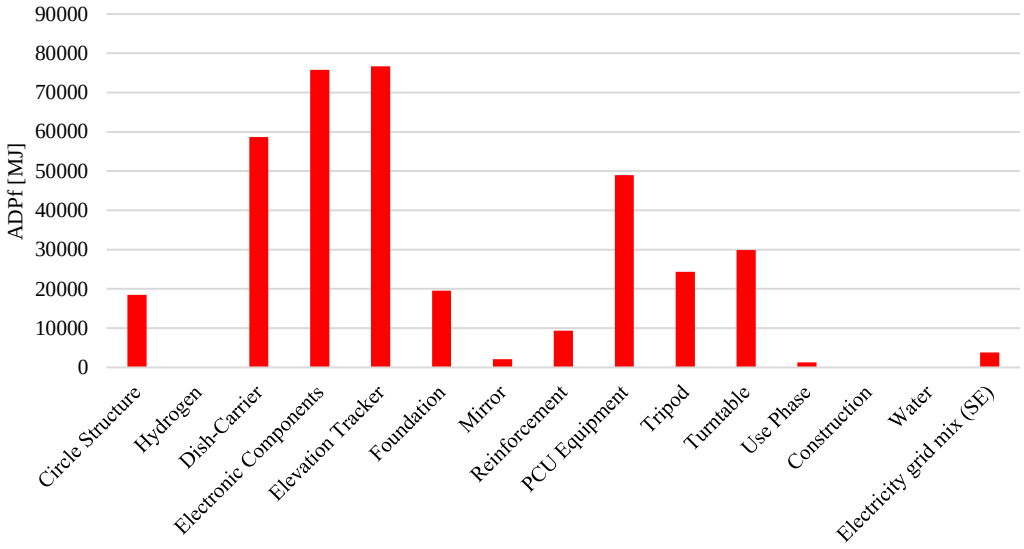

Figure 74. ADPf emissions

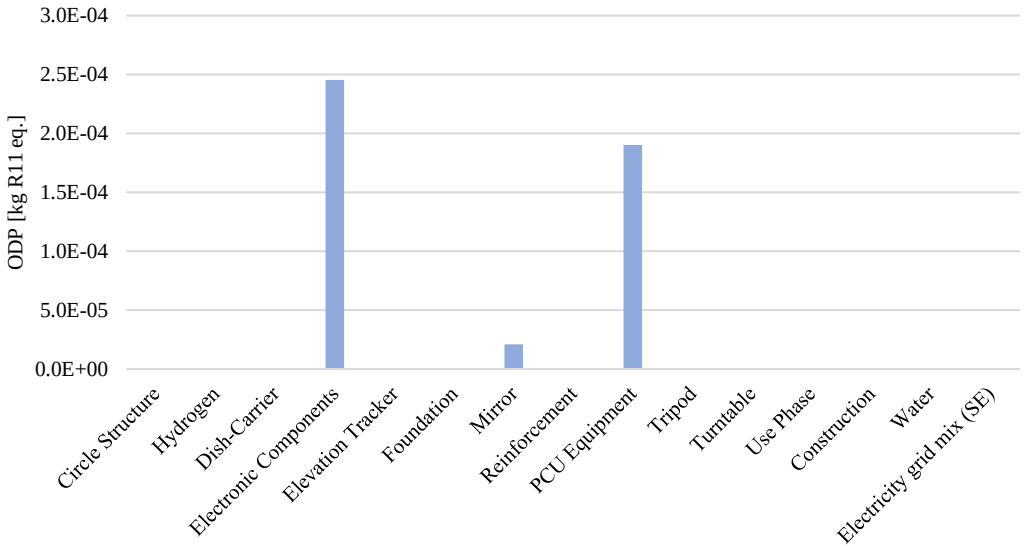

Figure 75. ODP emissions

Since hydrogen has to be replenished regularly and water is required to ensure frequent cleaning, an explicit LCA for the use phase was conducted, resulting in a value of GWP equal to 102 kg CO_2e. All other indicators accounted for only a very small portion of the total emissions of the use phase, being AP = 0.2 kg SO_2 eq., EP = 0.1 kg Phosphates eq., POCP = 0.1 kg Ethenes eq., ADPe = 0 kg Sb eq., ADPf = 1,281 MJ, and

ODP = 0 kg R11 eq. For all indicators, water was the driving factor and accounted for at least 95% of total emissions. If the use phase would be excluded from the emissions and only the cradle-to-gate system boundaries would have been considered, GWP would result in 34,669 kg CO_2e.

Compared to the two LCSA studies on solar dishes mentioned before [191,192], the following became evident: both studies have selected 1 kWh or 1 MWh of produced energy as FU (see *Table 28*). Setting the actually modelled and calculated value of 34,772 kg CO_2e (see *Figure 69*) in relation to the absolute amount of energy produced over a lifetime of 25 years (1,150 MWh total), a GWP value per MWh produced was obtained (from their ratio) equal to:

$$GWP = 30.24 \frac{kg_{CO_{2eq.}}}{MWh}$$

Considering the system boundaries cradle-to-gate, respectively the value would be 30.15 kg CO_2e/MWh. The cradle-to-use figure of 30.24 kg CO_2e/MWh or 30.24 g CO_2e/kWh was quite similar to the values in both comparison studies: Ko et al. [192] obtained 36.3 g CO_2e/kWh for cradle-to-gate and 51.5 g CO_2e/kWh for cradle-to-use. When comparing the cradle-to-use balance, a significant difference became evident (51.5 vs. 20.24 g CO_2e/kWh).

The study by Corona & San Miguel (2019) [191] presented two values of 45.9 kg CO_2e/MWh and 294 kg CO_2e/MWh (see *Table 28*). The study by Rodriguez-Serrano et al. [193], which had hardly any key factors and thus made comparability much more difficult, showed a GWP value of 24 g CO_2e/kWh.

7.3.4 Energy Payback Time (EPBT)

Any solar concentrator aims to generate electricity. However, energy was also required for the construction and production of the solar concentrator. The Energy Payback Time (EPBT) is defined as the time needed to generate as much electricity as needed throughout the life cycle of the solar concentrator, for production, construction, and demolition. Since this study did not consider the End-of-Life-phase, demolition was not included within the EPBT. Literature, e.g. Lamnatou & Chemisana [185] and Varun et al. [202], showed one year or less as expected EPBT. The estimated EPBT of one year

corresponds to the equivalent of 54.188 MWh. The EPBT for the actual dish-Stirling was calculated using the following *Equation (7.2)*:

$$EPBT = \frac{CED}{E_t} \tag{7.2}$$

where, *CED* is the cumulative energy demand for the system boundaries (cradle – to – use) expressed in MJ and was calculated using GaBi SP40, and E_t is the annual electricity generation of the reference dish-Stirling solar concentrator. A calculated CED of $52.08 \cdot 10^4$ [MJ] and an annual electricity generation of 46 [MWh] (=165,600 [MJ]) led to the calculated EPBT of 3.14 years. Compared to the study mentioned above [191] (see *Table 28*) and to other literature values [185,202], the EPBT of 3.14 years is comparatively high.

7.3.5 Life Cycle Costing

Life Cycle Costing (LCC), as the second pillar of LCSA, belongs to the group of sustainability instruments that focus on the flows related to the production and consumption of goods and services. In contrast to LCA, LCC represents the economic approach, which summarizes the total costs of a product discounted over its entire life cycle. LCC is based on a purely economic assessment that considers different costs associated with a product. External costs are neglected in this approach.

In general, LCC follows the four steps of ISO 14040/44. The definition of objectives and scope is analogous to LCA. It is notable that both assessments (LCA and LCC) focus on a consistent definition of the product system. One challenging aspect of LCC is the proposed capture of all costs over the entire life cycle, while costs are borne by different actors, which can lead to contradictions. In contrast to LCA, there is no comparable phase of impact assessment in LCC, since all inventory data comprise a single unit of measurement: currency. Characterization of the inventory data is therefore not necessary. Aggregated cost data provide a direct measure of the financial impact [170]. LCC differs from the traditional cost accounting system, known in the business, in that the costs and revenues of a cost object are tracked over several calendar periods and not just over one cost period.

To comply with the conventional LCC approach and to follow the ISO 14040/44 standard, the framework of the previously analysed LCA was adopted: FU was set to one dish-Stirling solar power plant, the system boundaries were classified as cradle-to-use. The LCC was calculated via Excel

7.3.5.1 Life Cycle Costing Results

The conventional LCC approach was being applied. External costs were not included in the calculations. The conventional costs explicitly considered the costs of purchased and used components, transportation costs, installation phase costs and maintenance costs (see *Table 33*, *Table 34*, and *Table 35*). In particular, regarding the maintenance phase, it is essential to mention that a life cycle of 25 years or 219,000 operation hours for the dish-Stirling engine was assumed. Due to confidentiality agreements, the individual component costs such as inverters or filters (first column, *Table 33*) could not be broken down and reproduced in detail. The total costs of these components resulted in 180,000 € (*Table 33*).

Table 33. Costs in Euro (*will be shown in separate tables)

Component:	**Description**	**Cost**
Costs of each component:		**180,000 €**
Inverter	Variable Frequency Drive; Pure Sine Wave Inverter	
Rectifier	Active Front End	
Reactor	Standard Reactor	
Filter	Standard Filters	
Energy meter	Direct connected electricity meter	
Actuator	Linear actuator	
Solar instruments	Solar monitoring system; Pyranometer; Pyrheliometer	
Conditioning	Air conditioner cabinet	
Circulator	Water Circulator	

Electric panel fan	Axial fan	
Coaxial gear-motor	Tacking motor	
Alternator	Electric motor	
Dry cooler	Dry cooler	
Costs of components transport (Sweden to Italy)		**10,000 €**
Detailed costs of the installation phase:		**25,525 €**
	Labor and Machines*	18,325 €*
	Concrete	3,200 €
	Iron	3,000 €
	Copper	1,000 €
Weather Station		**15,000 €**
Costs of maintenance phase*		**77,942 €***
Total incl. maintenance		**308,467 €**
Total (cradle-to-use)		**230,525 €**

Including maintenance, the largest driver of the total costs were the components themselves, which accounted for 58 % (180,000 €). Maintenance costs followed by 25 % of total costs over the entire lifetime of 25 years (*Figure 76*).

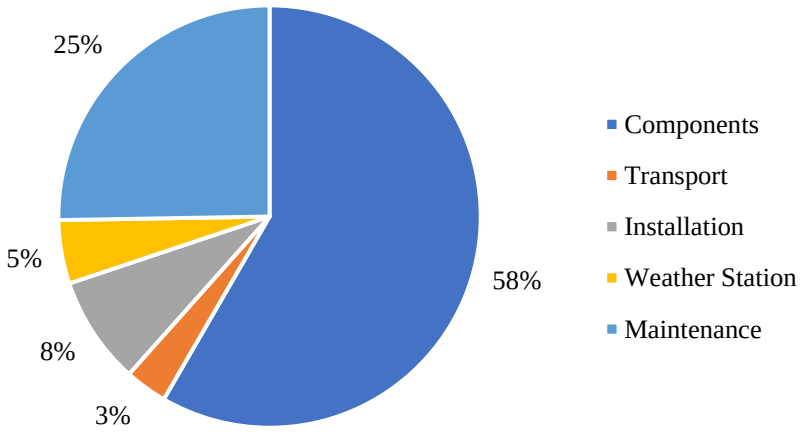

Figure 76. Costs in % (of total incl. maintenance)

Maintenance costs were broken down in *Table 35*, where it became evident that the upkeep of the Stirling power concentrator accounted for the largest share of maintenance costs. However, over a period of 25 years, the annual maintenance costs were at 3,118 €/year. In total, 8% of the costs were attributable to the detailed costs of the installation phase. At 18,325 €, the costs for labor and machines accounted for 71% of this specific cost factor (25,525 €). Splitting up these 71%, while 74% of the total amount were personnel costs with 13,525 € and 16% accounted for installation machinery (*Table 34*). The weather station itself accounted for 5 % of the total costs incl. maintenance (7% excl. maintenance). Transport expenditure and components filled the remaining 3% (incl. maintenance; 4% excl. maintenance). The cost of labor and machinery (total of 18,325 €) were divided into labor and machinery costs. The labor outlay was distinguished between skilled and unskilled workers and furthermore calculated according to the unit expenditure and the number of days worked. Additionally, five different machines were explicitly listed. The total costs were calculated from the unit costs (€ per day) and the number of days of use (*Table 34*).

Table 34. Costs of labor and machines

	Unit cost [€/day]	**n° Days**	**Total [€]**
Skilled labor	150	50.5	7,575
Labor	100	59.5	5,950
Cherry picker	150	14	2,100
Bob cat	100	7	700
Excavator	200	2	400
Mobile cranes	150	4	600
Cranes	1000	1	1,000
Total cost			**18,325**

The total maintenance costs of 77,942 € were depicted in *Table 35*. The information about the calculated lifetime of the dish-Stirling engine was of significant

importance (assumed lifetime of 25 years or 219,000 operating hours). The frequency per lifetime considers how often a replacement/cleaning has to be done within the entire lifetime – for example as shown in column 1 and row 1 of *Table 35*, the engine seals have to be replaced every 6,000 operating hours. Therefore, the number of replacements required throughout the life span of the installation, shown in the second-to-last column of *Table 35*, was calculated by dividing the total number of hours of operation (219,000 h) by the hourly frequency of the maintenance operation considered (6,000 h). In the same table, the last column presents the total summed costs (*Total [€]*) and refers to frequency and outlay per component. The component costs (*Component cost [€]*) were known and given. Data is taken from past invoices as well as empirical values from the operating accounting in Palermo, Italy. The calculation of the labor costs differed, as these were determined from the hourly rates per unskilled and skilled worker. The daily rates from *Table 34* were divided by an estimated amount of eight working-hours per day and multiplied by the assumed hours required per activity. As shown exemplarily in the first column of *Table 35*.

Table 35. Maintenance costs

Operating hours	Components replaced	Working hours	People employed	Qualificat. people	Labor cost [€]	Component cost [€]	Unit cost [€]	Times	Total [€]
Stirling power concentrator									
6,000	Engine seals	3.25	1	skilled labor	101.56	720	821.56	36.5	29,987
	Gas valve seats								
	Thermal insolation		1	unskilled labor					
	Oil and oil filters								
42,000	Heater quadrant	7	1	skilled labor	218.75	4,850	5,068.75	5.2	26,430
	Cylinder liners								
	Piston rods								
	Gears								
	Thermal couplers		1	unskilled labor					
	Bearings								
2,000	Yearly corrective maintenance	2.4	1	skilled labor	45	15	60	109.5	6,570

4.54 times per year	Hydrogen bottle (40 liters, 200 bar)	0.15	1	unskilled labor	1.875	55	56.88	112.5	6,398
Mirror									
Every 2 weeks (360 hours)	100 liters water	0.5	1	unskilled labor	6.25			608.3	3,802
Tracker System									
5,000	Yearly corrective maintenance	2.2	1	skilled labor	41.25	50	91.25	43.8	3,997
Preventive maintenance (every 10 years)	Backup batteries	0.25	1	unskilled labor	3.125	300	303.13	2.5	758
Total maintenance costs									**77,942**

To conclude the subject matter, a cost of the generated energy of 268 €/MWh was derived. This value was obtained by dividing the total cost of the reference dish-Stirling system (including maintenance costs over the useful life of the plant of 77.942 € (see *Table 35*) by the energy produced over the 25-year useful life (equal to 1,150 MWh, being Et = 46 MWh/a). This value is comparably higher than the one calculated by Corona & San Miguel [191] (211 €/MWh) and significantly higher than the one reported by Ko et al. [192] (*Table 28* and *Table 40*). Considering average energy prices for private households in the EU or exclusively Italy or Germany, the published values differ: Eurostat (2020) [203], and IEA (2020) [204] indicated around 280 €/MWh (Italy) and 353 €/MWh (Germany) in 2018. For the first half of 2020, Germany and Italy charged comparatively high prices in comparison to other EU states. The average value for the EU in the first half-year of 2020 was defined at 213 €/MWh [203,204]. No explicit prices for green energy were given, thus no accurate comparison could have been made.

7.3.6 Social Life Cycle Assessment

S-LCA is the most recent of the three sustainability assessment instruments presented. The use of the same functional unit and similar system boundaries are of critical weight. Again, the assessment should follow the four steps of LCA according to ISO 14040/44 [169,175].

Despite this common assessment framework, there are differences between LCA and S-LCA assessments: The definition and selection of stakeholders is a relevant aspect as the results of the S-LCA depend heavily on these stakeholders. Moreover, the S-LCA allows assessments of both negative and positive impacts, whereas LCA shows emissions, mostly negative. In addition, S-LCA is strongly dependent on local conditions and company behavior, less on the production process itself [171,172,205,206]. In the context of this study, a complete S-LCA according to UNEP guidelines [171,172] was not conducted. To quantify the social impacts of the dish-Stirling engine a detailed risk analysis of critical raw materials via the Social Hotspot Database (SHDB) [207] was prepared for individual components and their respective raw material and mining countries, manufacture and assembly. The database aims to foster collaboration to improve social conditions worldwide. The SHDB provides data and tools needed to improve the visibility of social hotspots in product supply chains of products. It contains a comprehensive list of indicators on e.g., labor rights and community infrastructure. The database covers 140 countries and regions and 57 economic sectors [207]. This allows identifying increased risks to the community and human health, as well as other categories of relevance. Results are presented in the following sub-chapter.

In addition to the risk analysis, the work environment of the installation phase was closely examined. The installation of the dish-Stirling system took a total of 46.5 days, which equals 372 hours (1,339,200 seconds), assuming each working day accounted for eight hours. These approximately 1.5 months of full-time work could be divided into work steps (see *Table 36*), such as the casting of the foundation, the assembly of the dish-Stirling system, the commissioning of the system and the calibration of the mirrors. The assembly of the system was close to a full working month while the foundation took nine days to be completed. The work was arranged to be outdoors. Both skilled and unskilled employees have worked on the construction (see *Table 36*). Skilled workers have spent

50.5 days of 8 hours on the construction site (404 hours or 1,454,400 seconds), unskilled workers have spent 59.5 days of 8 hours on the construction (476 hours or 1,713,600 seconds). The wage costs were considered which had already been processed in LCC, so 150 € per skilled labor force or 100 € for the unskilled employee per working day and worker were calculated. Resulting in an hourly wage of 18.75 €/h (skilled) or 12.5 €/h (unskilled) for an eight-hour day.

In Italy there is no minimum wage [208]. The wage of 12.5 €/h for unskilled workers in the construction of the dish-Stirling engine was above the highest European minimum wage. In 2019, the average weekly working time in Italy was 40.7 h. This corresponds to 8.14 h/d/worker in a five-day week. The applied 8 h/d/worker for the installation of the dish-Stirling were slightly below the 2019-average for Italy, which is positive to note. Comparing these results with the other two LCSA studies mentioned, the present result is significantly lower (fewer working seconds). However, in the case of working days, in particular, reference must be made to the narrower system boundaries, which explains the lower total working days.

Table 36. Labor installation phase

Phase	Days	Sub-phase	Days	Type of work	Days	Skilled worker	Man/ days	Unskilled worker	man/ days
Foundation	9		9						
				Excavation	1	1	1	1	1
				Foundation floor	1	1	1	1	1
				Shuttering	2	1	2	2	4
				Concrete reinfor cement	3	1	3	2	6
				Concrete casting	1	1	1	1	1
				Earthing system	1	1	1	1	1
Assembly of the dish Stirling system	31.5								
		Dish	17						
				Preparation and pre-assembly	1	1	1	2	2

Phase	Days	Sub-phase	Days	Type of work	Days	Skilled worker	Man/ days	Unskilled worker	man/ days
				Welding of the structure	5	1	5	1	5
				Welding of rings and brackets	5	1	5	1	5
				Finishing and painting of welds	1			1	1
				Mirrors assembly	3	1	3	2	6
				Mirrors calibration	2			2	4
		Arches and cage	5.5						
				Welding of arches	1	2	2	1	1
				Assembly of turntable	1	1	1	2	2
				Assembly of turntable and arches	1	1	1	2	2
				Installation of cooler	0.5	1	0.5	2	1
				Laying of the track	0.5	1	0.5	1	0.5
				Installation of pre-assembled electric panels	0.5	1	0.5	2	1
				Installation of azimuth and elevation motors	1	1	1	2	2
		Elevation	2						
				Installation of engine on the tripod	1	1	1	2	2
				Assembly of dish and tripod - before its elevation					
				Elevation of dish with engine					
				Installation of platforms and fairleads	1	1	1	2	2

Phase	Days	Sub-phase	Days	Type of work	Days	Skilled worker	Man/ days	Unskilled worker	man/ days
		Electrical system	5						
				Installation of sensors	1	1	1	1	1
				Wiring	3	1	3	1	3
				Installation of weather station	1	1	1		
		Water system	2						
				Installation of the cooling system	1	1	1	1	1
				Installation of the hydrogen supply system	1	1	1	1	1
Commissioning of the system	4		4						
				Calibration	2	1	2	1	2
				Testing the movement of the parts	1	3	3		
				Filling and testing the water system					
				Commissioning of Stirling engine					
				Testing the hydrogen system					
				Removal of films	1	1	1	1	1
Calibration of the mirrors	2		2		2	3	6		0
Total days	**46.5**		**46.5**		**46.5**		**50.5**		**59.5**

7.3.6.1 Social Hotspot Analysis of critical raw materials involved

The most economically important raw materials with a simultaneous high supply risk were referred to as critical raw materials. There are warnings that Europe's transition to climate neutrality could shift the current dependence on fossil fuels to raw materials. These raw materials are largely sourced abroad and imported. Every three years the list of critical raw materials is revised and published. In 2020, 83 materials were examined, with economic importance and supply risk being relevant parameters, leading to a list of 30 critical raw materials (CRM) [209].

Based on the previous LCA of the dish-Stirling, relevant and also critical input raw materials were defined based on the EU report [209]:

- magnesium: magnesium oxide used for parts of the mirror;
- bauxite: aluminium oxide used for mirror parts and
- coking coal: needed in the steel process, used for the turntable and final assembly.

Further, one could assume the need of:

- beryllium for electronic components and
- fluorspar for the steel production.

Even it can be said for a fact whether these commodities were actually included in the dish-Stirling system, it is possible to make this assumption to estimate additional risks.

The main producer and supplier countries for the EU could be defined [209]. Since the dish-Stirling was produced in Sweden and constructed in Italy, it was assumed the purchase entirely from outside of the EU. The main producers were not necessarily considered the same as the main suppliers for the EU: this was the case with Bauxite, while the EU obtains the largest share from Guinea, even this country is not one of the largest Bauxite producers worldwide. In the case of Beryllium, there was no information on the EU's main supplier country [209] (*Table 37*).

Table 37. CRM dish-Stirling - Relevant Countries

	Main Producer			**Main Supplier EU**		
CRM	1	2	3	1	2	**Main sector**
Magnesium	China (89 %)	US (4 %)	-	China (93 %)		Electro. Equipm.
Bauxite	Australia (28 %)	China (20 %)	Brazil (13 %)	Guinea (64 %)	**Brazil (10 %)**	Electro. Equipm.
Coking Coal	China (55 %)	Australia (16 %)	Russia (7 %)	Australia (24 %)		Ferrous Metals
Beryllium	**US (88 %)**	China (8 %)	Madagascar (2 %)	-	-	Electro. Equipm.
Fluorspar	China (65 %)	Mexico (15 %)	Mongolia (5 %)	Mexico (25 %)		Ferrous Metals

The Social Hotspot Analysis for the five critical raw materials was performed via the SHDB (access and analysis in January 2021). In case the EU main supplier was one of the main producers in the world, this country has been assumed to be the country of origin for the raw materials. In the case of Bauxite, this didn't apply – so Guinea and Brazil were analysed as the main supplier countries. In the case of Beryllium, there was no explicit information on supplier countries. The US has been assumed to be the main supplier for the required materials (*Table 38*: written in bold).

Within the SHDB the search could not be conducted directly, as for raw materials and products themselves, sectors had to be selected [207]. The classification of the five identified CRM resulted in two main sectors:

- electronic equipment and
- ferrous metals (Table 38).

All five categories:

- Labor Rights and Decent Work,
- Health and Safety,
- Human Rights,
- Governance and

- Community,

including all subcategories and one exemplary indicator, each had been selected in the SHDB. The CRM was evaluated for six producing and supplying countries (*Table 39*). The assessed risk has been classified from low (white) to very high (red) and subjectively rated from low (1) to high (4). The categories *no data* and *no evidence* are shown without color and numerical values.

In order to finally obtain a general country impression per category, we calculated an average value across the given data: as an example, the category Health and Safety showed two indicators for the US which were given as risk factors. Summed to a total of six and in the following divided by the total number of indicators, this led to a mean of three – high risk (*Equation (7.3)*; *Table 38*). The detailed analyses are shown in the Appendix: from *Table A 1* to *Table A 10.*

$$\frac{2(USDALYs)+4(US\ Fatal\ Injuries\ by\ sector)}{2(Number\ of\ Indicators)}=3(Mean) \qquad (7.3)$$

Table 38. Health & Safety Social Risk

CRM	Sector	Country	Health & Safety		
			Occupational Toxics & Hazards	Injuries and Fatalities	
			Overall Occupational Cancer Risk - loss of life (DALYs)	Fatal injuries by sector	**Mean**
Magnesium	Electro. Equip.	China	4		4
Bauxite	Electro. Equip.	Guinea			
Bauxite	Electro. Equip.	Brazil	2		2
Beryllium	Electro. Equip.	US	2	4	3
Coking Coal	Ferrous Metals	Australia	1	2	2

Fluor Spar	Ferrous Metals	Mexico	2	3	3

Considering the summary from the individual analyses, it became evident that no country, no sector and no category could be rated low risk with regard to social hotspots. All risks considered were rated medium to high. China and Guinea in particular posed high risks for the social factors at the country level, with Governance and Health & Safety being considered critical in both countries. These two categories were generally considered to be of high risk (see *Table 39*).

Table 39. Overall Social Risk

CRM	Sector	Country	Labor Rights & Decent Work	Health & Safety	Human Rights	Governance	Community	Overall Mean
Magnesium	Electro. Equip.	China	3	4	2	3	2	**3**
Bauxite	Electro. Equip.	Guinea	3	-	3	4	3	**3**
Bauxite	Electro. Equip.	Brazil	2	2	2	3	2	**2**
Beryllium	Electro. Equip.	US	2	3	2	2	2	**2**
Coking Coal	Ferrous Metals	Australia	2	2	1	2	2	**2**
Fluor Spar	Ferrous Metals	Mexico	3	3	1	4	2	**2**
Overall Mean			**2**	**3**	**2**	**3**	**2**	

7.4 Life Cycle Assessment

The objective of this part of the thesis was to conduct an outright LCSA of a dish-Stirling Concentrating Solar Power Plant located in Palermo.

The data reflected a challenge in the present study: there was little or no primary data on raw materials or production steps. Assumptions had to be made for modelling the LCA. However, these assumptions were cross-checked with indicators such as the EPBT

or further g CO_2e/kWh results from other studies. The results are comparable (see *Table 40*), which indicates reliable data and assumptions.

Table 40. Comparison with existing LCSA studies

	Corona & San Miguel, 2019	**Ko et al., 2018**	**Actual Study**
Product	Novel type of hybrid CSP plant	CSP tower plants	CSP plant
FU	1 MWh of electricity poured into grid	1 kWh net electricity fed to the grid	1 CSP plant
System boundaries (LCA)	cradle-to-gate	cradle-to-grave	cradle-to-gate
Data assessed by	two engineering companies	primary data & GaBi database	few primary data, literature & GaBi
Assumed energy production/year	800 GWh/year	585 GWh/year	46 MWh/year
Assessed lifetime	n.a.	30 years	25 years
LCA indicators	**2** indicators: Climate change Water stress	**6** indicators: GWP ADP EP PED BWC land occupation	**7** indicators: GWP ADPf ADPe EP AP POCP ODP
LCA software and database	SimaPro 8.0.3 & ReCiPe	GaBi & CML2001	GaBi & CML2001
LCC tools	n.a.	n.a.	Excel
S-LCA tools	SHDB	SHDB	SHDB & EU critical raw materials
EPBT	CSP Bio: 6.1 months CSP GN: 22 months	-	3.14 years
Recycling considered	Yes	Yes	No
LCA GWP Results	**cradle-to-gate** CSP Bio: 45.9 kg CO_2e/MWh CSP GN: 294 kg CO_2e /MWh	**cradle-to-gate** 36.3 g CO_2e /kWh	**cradle-to-gate** 30.15 g CO_2e /kWh
	cradle-to-use	**cradle-to-use**	**cradle-to-use**

	Corona & San Miguel, 2019	Ko et al., 2018	Actual Study
	-	51.5 g CO_2e /kWh	30.24 g CO_2e /kWh
LCC Results	**cradle-to-gate** CSP Bio: 211 €/MWh CSP GN: 154 €/MWh	**cradle-to-use** 66.5 €/MWh	**cradle-to-gate** 268 €/MWh
S-LCA Results	**cradle-to-gate** Employment creation CSP Bio: 454,090 person-year CSP GN: 158,106 person-year	**cradle-to-use** Total working time 19,398,646s	**cradle-to-use** Total working time Skilled Worker 1,454,400 s Unskilled Worker 1,713,600 s
Visualization used	-	-	-

For LCC, the conventional cost approach was chosen, which is utterly similar to business administration approaches. Costs are not considered for a period of one year, but over the entire lifetime: in this case 25 years. Detailed life cycle-assumptions were not given in comparative studies. The costs per MWh could anyhow be compared, whereof the actual costs per MWh were comparatively high. Externalities were not included in this model, which could be seen as a limitation. Regarding LCC and S-LCA, the system boundaries were defined as equivalent to the ones used for LCA – which was not given by both comparative studies (*Table 40*). A comparison of results was attempted; it should be noted that assumptions about system boundaries and calculated data had to be made for comparison. This makes reliable and completely valid analogy difficult (*Table 40*).

It was not possible to perform a full S-LCA due to a lack of information. However, an analysis of wages and working hours and the risk analysis provided an alternative solution. Both, the working hours per day and the wages in Italy for the installation of the dish-Stirling showed positive values, compared to other European countries. Moreover, the values were compared to the values given by one of the comparative studies (*Table 40*). The results of the risk analysis gave a detailed idea of the social risk of producing and supplying countries. None of the indicators could be assigned with low risks; reliable

data still remains an obstacle. For the social pillar, it should be pointed out that data and even contacts were limiting factors, which influenced the implementation of a detailed survey and the complete tracking of the full supply chain. Without a sufficient timeframe and contact with all relevant stakeholders, a comprehensive S-LCA is rather imprecise.

Even though the most relevant limitation was the data, a complete LCSA has been conducted. According to the approach by Finkbeiner and Kloepffer [167,168], no weighting of the individual pillars is allowed, nor can any of the pillars affect the performance of another pillar with its performance. The LCSA-results are independent of each other and can only be reported individually. At this point, further challenges of LCSA emerged, namely interpretation and communication. There are various visualization tools or approximation approaches to make the LCSA more understandable to non-experts – such as the Life Cycle Sustainability Triangle (LCST) [167], the Life Cycle Sustainability Dashboard (LCSD) [210], the Sustainability Crowns [191] or the Tiered Approach [174]. None of these approaches was used (*Table 40*), as it was difficult to relate the results of the individual pillars. Finally, it was not possible to conclude how the columns relate to each other and to what extent the social component could have an impact on the environmental or economic part and whether an improvement of any kind could be achieved at certain levels, such as wages or lower production costs. The mentioned limitations of the general LCSA led to the conclusion that a general and optimized interpretation and communication approach must be found in a timely manner. By this way, the results of these analyses no longer stand for themselves but lead to general understanding and contribute to the optimization of all sustainability dimensions of products and services.

7.5 Outcomes

Among different renewable energy sources, solar energy represents an abundant source of energy with the highest future potential to satisfy a substantial portion of the worlds' energy demand. In the field of solar electricity generation, the Concentrating Solar Power plants are called a highly competitive technology [163,165]. Yet, the dish-Stirling is responsible for environmental impacts caused during its production and installation. The LCSA system boundary was defined as cradle-to-use, the functional unit

was the CSP plant itself. The LCA is based on data available in GaBi (SP40) and Ecoinvent 3.5 resulting in seven midpoint indicators using the CML2001 methodology. In terms of greenhouse gas emissions, 35 t CO_2e were calculated. Other emission indicators than CO_2e and a detailed split up concerning driving process steps were given in the actual study. The three main drivers for all indicators were the electronic components, the elevation tracker and the PCU equipment – mainly driven by steel as material. The conventional LCC resulted in 308,467.00 € as total costs, which lead to 268.00 € per MWh (0.268 €/kWh) of generated energy (*Table 40*). The European average energy prices verified the result calculated and represented their plausibility. For S-LCA, workdays, wages, and a risk analysis via the SHDB were assessed. The wage of 12.5 €/h for unskilled workers was slightly above the highest European minimum wage. Based on LCA, relevant and critical input raw materials were defined, following the EU report [209]. No country, no sector and no category could be with low risk for this technology. The LCSA-pillar-results stand on their own, interpretation and communication remain challenging. Limitations further were data availability, uniform system boundaries and comparability of results. A holistic statement about the sustainability performance of the dish-Stirling engine could not be defined, resulting in the future need for a general and optimized interpretation and communication approach for LCSA.

Appendix

Table A 1. Production Processes and Assumptions

Component	Part of the solar concentrator	Database	Process	Database explanation (original text from the documentation), either GaBi or Ecoinvent
Stainless steel tube, welded, Ø60,3x 2,9mm; 717 kg	Circle structure	GaBi (SP40)	EU: Steel welded pipe worldsteel	The data set represents an average european welded pipe with data from worldsteel. The steel is being produced in the blast furnace route.
Steel; 2,200 kg	Dish	GaBi (SP40)	EU: Steel welded pipe worldsteel	The data set represents an average european welded pipe with data from worldsteel. The steel is being produced in the blast furnace route.
Screws; 66 kg	Dish	GaBi (SP40)	EU-28: Fixing material screws galvanized	The life cycle analysis of steel screws contains all material and energetic needs for the production of a steel billet (with alloying elements) and its further processing (rolling, hardening, electroplating) to galvanized and hardened steel screws. Refined-zinc mix (industrial data from different sites) is used for electroplating. Transports from the factory to the construction site are not considered and have to be incorporated in a system approach.
Inverter; 1 piece	Electronic components	Ecoinvent 3.5	RER: inverter production, 2.5 kW	Production of an inverter (2500 W) with an efficiency of 93.5% (total efficiency factor which includes MPP-Tracking) for photovoltaic plant.
Inductor; 95 kg	Electronic components	Ecoinvent 3.5	GLO: inductor production, ring core choke type	Standard inductor, set to the total mass of 95 kg since in the original inductor the following materials were used: copper 80 kg, steel 13 kg, and plastic 2 kg.
Filter; 1 piece	Electronic component	GaBi (SP40)	GLO: Filter SAW (25 mg) 3*7*1	The most important groups of so called passive electronic components are regarded, which are different types of capacitors, resistors, inductions/coils, oscillators and electronic switches. The respective processes provide a

Component	Part of the solar concentrator	Database	Process	Database explanation (original text from the documentation), either GaBi or Ecoinvent
				representative component, which is based on a typical, respective
Conditioner; 58 kg	Electronic components	GaBi (SP40)	Direct expansion air conditioner (per 1 kW) (EN15804 A1-A3)	The data represents the production of a classical split and multi-split systems for air conditioning. The system consists of an outdoor unit (compressor and condenser) and of one indoor unit (evaporators and fan). These systems operate in a power range of up to 20 kW.
Rectifier	Electronic components	-	-	No process in the databases available.
Energy meter	Electronic components	-	-	No process in the databases available.
Actuator	Electronic components	-	-	No process in the databases available.
Steel; electrogalvanized; 2,750 kg	Elevation tracker	GaBi (SP40)	EU: Steel electrogalvanized steel worldsteel	This dataset includes raw material extraction (e.g. coal, iron, ore, etc.) and processing, e.g. scrap, coke making, sinter, blast furnace, basic oxygen furnace, hot strip mill, galvanizing process. Details on the steel product manufacturing route can be found in Appendix 1 of the 2017 worldsteel LCA Methodology Report. The steelmaking processes are shown in the flow diagram. Inputs included in the Life Cycle Inventory relate to all raw material inputs, including steel scrap, energy, water, and transport. Outputs include steel and other co-products, emissions to air, water and land. Further information is given in the 2017 worldsteel LCA Methodology Report.

Component	Part of the solar concentrator	Database	Process	Database explanation (original text from the documentation), either GaBi or Ecoinvent
Screws; 150 kg	Elevation tracker	GaBi (SP40)	EU-28: Fixing material screws galvanized	The life cycle analysis of steel screws contains all material and energetic needs for the production of a steel billet (with alloying elements) and its further processing (rolling, hardening, electroplating) to galvanized and hardened steel screws. Refined-zinc mix (industrial data from different sites) is used for electroplating. Transports from the factory to the construction site are not considered and have to be incorporated in a system approach.
Silicon dioxide (SO2); 191.7 kg	Mirror	GaBi (SP40)	DE: Silica sand (Excavation and processing)	Quartz is mined from a quarrel by using construction machines (excavators, dumpers etc.). The quartz mined is then transported from the quarrel to the processing plant for further processing steps (cleaning, grinding, screening). The stones are cleaned in dry processes and crushed into small particles by using crushers or ball mills. Screening and separation is done to achieve the desired grain size, it is carried out by using sieves or vibration screens.
Sodium oxide (NaO); 37.8 kg	Mirror	Ecoinvent 3.5	RER: sodium oxide production	Used as an intermediate product in the production of sodium peroxide, in the production of glass, for polymerization and as a drying agent for dry inorganic solvents.
Calcium oxide (CaO); 21.6 kg	Mirror	GaBi (SP40)	EU-28: Lime (CaO; quicklime lumpy) (EN15804 A1-A3)	Quicklime (CaO) is manufactured technically by deacidifying limestone (CaCO3) at temperatures over 900 ◦C. Different kinds of shaft kilns are used. The fuels that are added to the limestone are either in lumps (coke or briquets), which move through the kiln from the top to the bottom, and/or fuels like natural gas or heating oil, which are put into the oven at specific positions. The most important types of shaft kilns today are direct current-reverse current-regenerative

Component	Part of the solar concentrator	Database	Process	Database explanation (original text from the documentation), either GaBi or Ecoinvent
				ovens and ring shaft kilns. In addition to this, rotary tubular kilns are used. These are fired with coal dust or heating oil.
Magnesium oxide (MgO); 10.8 kg	Mirror	Ecoinvent 3.5	RER: magnesium oxide production	This dataset represents the production of magnesium oxide. Magnesium oxide forms colorless, green or brown crystals. Industrially used magnesium oxide consists mainly of sintered (sintered magnesia) for use as refractory material in the steel industry. Other forms of magnesium oxide that are used include calcinated material (caustic magnesia), which is used for agriculture, as well as the pulp and paper and the building industry, and fused magnesia. Magnesium oxide is produced from natural magnesite (MgCO3), from dolomite (CaCO3 and MgCO3), from seawater or from brines. This dataset represents the production of caustic magnesium obtained by mining magnesite in an open-pit mine. This is followed by a beneficiation step, which comprises crushing and gravity separation. Finally, the material is fed into a feeder to end up with caustic magnesium oxide. The inventory in this dataset is based on extrapolations based on similar processes.
Aluminum oxide (Al2O3); 5.4 kg	Mirror	GaBi (SP 40)	EU-28: Aluminium oxide mix (alumina, Al2O3)	The process used for the production of aluminum oxide is the Bayer Process. First, the bauxite ore is grinded into powder. The powder is the mixed with a caustic soda solution and heated to 175 ◦C, then put into a digester vessel which is operating at above atmospheric pressure. In the vessel, the aluminum oxide is converted into water- soluble sodium aluminate. The slurry leaves the digester at temperatures above its atmospheric boiling point and is cooled by flashing- off steam as the pressure is

Component	Part of the solar concentrator	Database	Process	Database explanation (original text from the documentation), either GaBi or Ecoinvent
				reduced in several stages. The steam is used to heat the slurry for the digestion. The non– soluble residues in the aluminate solution are separated by precipitation and filtration, sometimes lime is added as a precipitation agent to remove undesired soluble components like silica. The dissolved aluminate is removed by supersaturating the solution and seeding aluminum hydroxide crystals. The aluminum hydroxide is calcined at temperatures of 980 ◦C yielding aluminum oxide.
FeO; 2.7 kg	Mirror	Ecoinvent 3.5	GLO: ilmenite - magnetite mine operation	Ilmenite and magnetite mining from hard-rock ore. Based on Tellnes mine (Norway) and Lac Allard mine (Canada). Comments on modelling. All the flows related to energy consumption are based on U.S. Department of Energy survey from 2007 on Mining Industry.
Steel pipe; 64.77 kg	Steering equipment	GaBi (SP40)	EU-28: Steel pipe (EN15804 A1-A3)	Steel pipe for the installation of heating and gas supply. According to VDI guideline 2067 for steel pipes an average life span of 40 years can be assumed for heating, gas supply and cold water and 25 years for warm water. Steel production: The preparation of the iron ore includes mainly the crushing. The average iron content in the iron ore is 60%. Pellets are small crystallized balls of iron ore. The palletization process consists of grinding and drying, balling and induration followed by screening and handling.
Pump;7 kg	Steering equipment	GaBi (SP40)	EU-28: Circulating pump 250–1000 W (EN15804 A1-A3)	Circulating pump for heating systems with a capacity of 250–1000 W. According to VDI guideline 2067 for buffers an average life span of 10 years can be assumed.

Table A 2. Transport Processes and Assumptions

Component	Part of the solar concentrator	Database	Process	Database explanation (original text from the documentation), either GaBi or Ecoinvent
Truck transport; 10,473 km	Transport	GaBi (SP40)	GLO: Truck, Euro 4, 28–32 t gross weight / 22 t payload capacity	Average truck age in the European union is according to the ACEA Report Vehicles in use Europe 2019 12.4 years. In 2006/2007 was the truck engine standard euro IV mandatory, therefore euro IV is assumed for the truck.
Diesel; 2,297 kg	Transport	GaBi (SP40)	EU-28: Diesel mix at refinery	Average European diesel. Fuel consumption is estimated by GaBi.

Table A 3. Final Assembly Processes and Assumptions

Component	Part of the solar concentrator	Database	Process	Database explanation (original text from the documentation), either GaBi or Ecoinvent
Sand; 6.8 m3 = 10,452 kg	Foundation	GaBi (SP40)	EU_28: Sand (grain size 0/2) (EN15804 A1-A3) (dried)	The extraction of the material is a technology mix of the wet extraction and the dry extraction process. In the wet process, the sand in rivers or ground water layers is extracted by excavators. In the dry process, the sand of dry layers above the ground water level is excavated. The preparation of the raw mineral begins with the washing of the stone grains that have been extracted from the repository. By adding clean water, the raw mineral is released from elutriated constituents such as loam and clay and from foreign substances such as wood, kaolin, coal, metal etc. in various washing stages. It is then sorted by size in vibration sieves or in an upstream classifier.

Component	Part of the solar concentrator	Database	Process	Database explanation (original text from the documentation), either GaBi or Ecoinvent
Water; 100 L	Final assembly	GaBi (Sp40)	EU-28: Water (deionized)	This process describes the reverse osmosis process. Deionized water is produced by forcing the salt-containing water (groundwater) through a semipermeable membrane under pressure.
Gravel; 13.4 m3 = 23,852 kg	Foundation	GaBi (SP40)	EU-28: Gravel 2/32	The life cycle assessment of sand and gravel covers the quarrying of stone and its preparation. The preparation of the raw mineral begins with the washing of the stone grains that have been extracted from the repository. By adding clean water, the raw mineral is released from elutriated constituents such as loam and clay and from foreign substances such as wood, kaolin, coal, metal etc. in various washing stages. It is then sorted by size in vibration sieves or in an upstream classifier.
Water, 2,512.5 L	Foundation	GaBi (SP40)	IT: Tap water from groundwater	The following operations were modelled for drinking water purification: Screening (Solids/Rejects elimination): Rough and fine particles, e.g. sand or plankton, are detained by racks and micro strainers. Sedimentation: Soluble particles deposit in sedimentation basins. Very fine particles are deposited by flocculation process. For Coagulation/Flocculation Aluminum- and ferric salt are used: FeCl3, Fe2(SO4)3, AlCl3, Al2(SO4)3 and An(OH)mCl3n-m. Water softening (decarbonization): This step includes the reduction of water hardness (carbon hardness). Part of the hardness forming lime Ca(HCo3)2 is firstly flocculated and eliminated afterwards through the addition of slaked lime. Disinfection: Following the flocculation separation ozonation is done. Ozone serves for disinfection as well as the improvement of filterability. After the stage of

Component	Part of the solar concentrator	Database	Process	Database explanation (original text from the documentation), either GaBi or Ecoinvent
				ozonation follows a stage of filtration. Chlorination is the last step of drinking water purification. In this case chlorine, sodium hypochlorite and chlorine dioxide is used. This is used for the aborticide respectively deactivation of germs. Filtration: Slow sand filter and quick sand filter separate suspend particles; products of precipitation and other residues. Quick sand filter detains contaminants mechanically. Sand and flint serve as filter materials. Slow sand filters are used to simulate the natural ground filtration. The back flush from filters happen with air and water alternately. Up to now filter rinsing water (waste water) are drained immediately in receiving waters respectively the public main sewer, depending on the local conditions. The accumulating sludge is led in the waste water treatment plant for further treatment.
Cement; 5,863 kg	Foundation	GaBi (SP40)	EU-28:Cement (CEM II 32.5) (EN15804 A1-A3)	The main processes in cement production consist of raw material extraction, production of clinker, and cement grinding. The extraction of the main raw material from the quarry normally takes place in the immediate area of the cement works. Portland cement (CEM I) is primarily made up of finely ground clinker cement and a smaller amount of ground materials. Other cements may also include constituents such as slag sand (CEM III), natural pozzolan such as trass (CEM IV), fly ash, oil shale burn-out or limestone. The most important agent is the blast furnace cement (CEM III). Coagulation is controlled with the help of minor constituents, such as calcium sulphate to facilitate its optimal processing in the concrete production. Clinker cement is made up of a mixture of primary products of mainly calcium oxide, silica,

Component	Part of the solar concentrator	Database	Process	Database explanation (original text from the documentation), either GaBi or Ecoinvent
				aluminum oxide, and iron oxide. Limestone, chalk and clay (or their naturally occurring mixture of limestone marl) provide these chemical constituents. The raw material mixture is heated to approximately 1450 ◦C in a rotary furnace until sintering. New bonds are created from the source material, these are known as the clinker phases. These are specific calcium silicates and calcium aluminates that give the cement its characteristic property of hardening in the presence of water.
Reinforcement steel; 417 kg	Reinforcement	GaBi (SP40)		This dataset includes raw material extraction (e.g. coal, iron, ore, etc.) and processing, e.g. scrap, coke making, sinter, blast furnace, basic oxygen furnace, electric arc furnace, rolling mill. Details on the steel product manufacturing route can be found in Appendix 1 of the 2017 worldsteel LCA Methodology Report. The steelmaking processes are shown in the flow diagram. Inputs included in the Life Cycle Inventory relate to all raw material inputs, including steel scrap, energy, water, and transport. Outputs include steel and other co-products, emissions to air, water and land. Further information is given in the 2017 worldsteel LCA Methodology Report.

Table A 4. Cut-Offs

Cut-Offs – to be named explicitly
Special color called: Korro Aqua 2741 15-30µ – GRAY. dish paint used as substitute in model. Nut, lock nut and washer named as necessary for the dish. Just screws were considered in model. Rectifier not included, no process available. Energy meter not included, no process available. Linear actuator not included, no process available.

Table A 5. Stirling engine – Adjusted Process

Process	**Amount**	**Unit**
AU: electricity, low voltage [allocatable product]	1.506434985	MJ
AU: electricity, medium voltage [allocatable product]	6.754585875	MJ
CA-QC: heat, district or industrial, natural gas [17300: Steam and hot water]	14.29098059	MJ
Europe without Switzerland: electricity, low voltage [allocatable product]	25.17345356	MJ
Europe without Switzerland: electricity, medium voltage [allocatable product]	113.2399324	MJ
Europe without Switzerland: heat, central or small-scale, other than natural gas [allocatable product]	3.971978256	MJ
Europe without Switzerland: heat, district or industrial, natural gas [allocatable product]	437.563895	MJ
Europe without Switzerland: waste mineral wool [Waste]	-3.48980327	kg
Europe without Switzerland: waste polyethylene/polypropylene product [Waste]	-3.564218005	kg
Europe without Switzerland: waste polyvinylchloride product [Waste]	-0.335826614	kg
From unspecified [Transformation]	0.044	sqm
GLO: aluminium, wrought alloy [allocatable product]	2.4	kg
GLO: building, hall, steel construction [allocatable product]	0.012	sqm
GLO: building, multi-storey [allocatable product]	0.073	m^3
GLO: cast iron [allocatable product]	148	kg
GLO: ceramic tile [allocatable product]	6.83	kg
GLO: copper [allocatable product]	25.59	kg
GLO: heating and sanitary equipment, mini CHP plant [allocatable product]	0.75	pcs.
GLO: lead [allocatable product]	0.12	kg

Process	Amount	Unit
GLO: nickel, 99.5% [allocatable product]	5.12	kg
GLO: polyethylene, high density, granulate [allocatable product]	12.6	kg
GLO: polyvinylchloride, emulsion polymerised [allocatable product]	0.153192	kg
GLO: polyvinylchloride, suspension polymerised [allocatable product]	1.046808	kg
GLO: reinforcing steel [allocatable product]	178.19	kg
GLO: sheet rolling, aluminium [allocatable product]	2.4	kg
GLO: sheet rolling, chromium steel [allocatable product]	31	kg
GLO: sheet rolling, steel [allocatable product]	307.94	kg
GLO: steel, chromium steel 18/8, hot rolled [allocatable product]	31	kg
GLO: stone wool, packed [allocatable product]	12	kg
GLO: tin [allocatable product]	0.26	kg
GLO: wire drawing, copper [allocatable product]	4.2	kg
GLO: zinc [allocatable product]	0.04	kg
NZ: electricity, medium voltage [allocatable product]	2.19	MJ
RAF: electricity, low voltage [allocatable product]	4.381038381	MJ
RAF: electricity, medium voltage [allocatable product]	21.61405098	MJ
RAS: electricity, low voltage [allocatable product]	66.77194127	MJ
RAS: electricity, medium voltage [allocatable product]	310.1797678	MJ
RLA: electricity, low voltage [allocatable product]	8.378164738	MJ
RLA: electricity, medium voltage [allocatable product]	41.59294145	MJ
RNA: electricity, low voltage [allocatable product]	31.3825017	MJ
RNA: electricity, medium voltage [allocatable product]	145.5256223	MJ

Process	Amount	Unit
RoW: electricity, low voltage [allocatable product]	0.011926598	MJ
RoW: electricity, medium voltage [allocatable product]	0.055322655	MJ
RoW: heat, central or small-scale, other than natural gas [allocatable product]	278.0280217	MJ
RoW: heat, district or industrial, natural gas [allocatable product]	821.1451245	MJ
RoW: inert waste, for final disposal [Waste]	-0.525	kg
RoW: transport, passenger car [allocatable product]	400,000	m
RoW: waste mineral wool [Waste]	-8.51019673	kg
RoW: waste polyethylene/polypropylene product [Waste]	-9.035781995	kg
RoW: waste polyvinylchloride product [Waste]	-0.864173386	kg
RoW: wastewater, from residence [Waste]	-0.427	m^3
RU: electricity, low voltage [allocatable product]	6.115284066	MJ
RU: electricity, medium voltage [allocatable product]	29.32993106	MJ

Table A 6. Axial Gear Motor - Adjusted Process.

Database	Process	Amount	Unit
GaBi (SP40)	EU-28: Aluminium ingot (AlSi10Mg(a)) sec.	4.526	kg
GaBi (SP40)	DE: Cast iron component (EN15804 A1-A3)	2.116	kg
GaBi (SP40)	EU-28: Copper Wire Mix (Europe 2015)	3.469	kg
GaBi (SP40)	SE: Electricity grid mix	166.4	MJ
GaBi (SP40)	RER: Epoxy resin	0.1205	kg
GaBi (SP40)	DE: Glass fibres	0.1033	kg

Database	Process	Amount	Unit
GaBi (SP40)	DE: Polyester Resin unsaturated (UP)	0.4182	kg
Ecoinvent 3.5	RER: steel, low-alloyed, at plant	11.65	kg
GaBi (SP40)	GLO: Steel cold rolled coil	2.764	kg
GaBi (SP40)	EU-15: No. 1 steel - scrap credit (open loop)	-0.6863	kg

Table A 7. Human Rights Social Risk

CRM	Sector	Country	**Human rights Indig. Rights**	**Gender Equity**	**High Conflict Zones**	**Human Health Issues Non community**	**Human Health Issues community.**	Mean
			Overall risk of indig. rights being infringed	**Gender Inequality Index (GII), UNDP**	**High Conflict UNDP**	**Overall Non-communicable Diseases and other health risks**	**Age-standardized mortality rates from communicable diseases**	
Magnesium	Electro. Equip.	China	2	1	4	2	1	2
Bauxite	Electro. Equip.	Guinea	3	3	2	3	3	3
Bauxite	Electro. Equip.	Brazil	1	3	3	1	1	2
Beryllium	Electro. Equip.	US	2	2	4	1	1	2
Coking Coal	Ferrous Metals	Australia	1	1	3	1	1	1
Fluor Spar	Ferrous Metals	Mexico	1	2	2	1	1	1

Table A 8. Governance Social Risk

CRM	Sector	Country	Governance Legal System	Corruption	Mean
			Overall Fragility in Legal System	Overall Corruption	
Magnesium	Electro. Equip.	China	3	3	3
Bauxite	Electro. Equip.	Guinea		4	4
Bauxite	Electro. Equip.	Brazil	2	4	3
Beryllium	Electro. Equip.	US	2	1	2
Coking Coal	Ferrous Metals	Australia	2	1	2
Fluor Spar	Ferrous Metals	Mexico	3	4	4

Table A 9. Community Social Risk

CRM	Sector	Country	Community Access to Improved Drinking Water % Total Access to an Improved Source of Drinking Water	Access to Improved Sanitation	Children out of School	Access to Hospital Beds	Smallholder vs. Commercial Farms	Mean
				% Total Access to an Improved source of Sanitation	Percent of Children Out of Primary School, total	Number of Hospital Beds per 1000 population	Percentage of family-owned farms in country	
Magnesium	Electro. Equip.	China	1	2	3	2		2
Bauxite	Electro. Equip.	Guinea	3	4	3	3		3
Bauxite	Electro. Equip.	Brazil	1	2	3	3		2
Beryllium	Electro. Equip.	US	1	1		3		2
Coking Coal	Ferrous Metals	Australia	1	1	2	2		2
Fluor Spar	Ferrous Metals	Mexico	1	2	1	3		2

Table A 10. Labor Rights and Decent Work Social Risk.

CRM	Sector	Country	Wage Assessments	Poverty	Child Labor	Forced Labor		Freedom of Association, Collective Bargaining, Right to Strike	Migrant Labor	Social Benefits	Labor Laws/Conventions	Discrimination and equal opportunity	Unemployment	Mean
			Risk that Avg Wage is Below Country Minimum Wage	Percent of population living under the relevant poverty line	Risk of Child Labor by Sector (quali.)	Overall Forced Labor in Country	Percent of Population working > X hrs per week, greater than60 hrs per week	Freedom of Association Rights, Collective Bargaining Rights, Right to Strike Qualitative	Evidence of Risk to Migrant Workers –Quali.	Overall risk of inad. Social benefits	Number of Labor Laws by Sector	Prevalence of discrimination in the workplace (qualitative)	Average of Unemp. % at the country level	
Magnesium	Electro. Equip.	China	1	2	3	2								2
Bauxite	Electro. Equip.	Guinea	3	4	3	3								3
Bauxite	Electro. Equip.	Brazil	1	2	3	3								2
Beryllium	Electro. Equip.	US	1	1		3								2
Coking Coal	Ferrous Metals	Australia	1	1	2	2								2
Fluor Spar	Ferrous Metals	Mexico	1	2	1	3								2

Nomenclature

Abbreviations

ADPe	elementary Abiotic Depletion Potential
ADPf	fossil Abiotic Depletion Potential
AP	Acidification Potential
BWC	Blue Water Consumption
CED	Cumulated Energy Demand
CML	Centrum voor Milieukunde (Name of assessment methodology)
CRM	Critical Raw Materials
CSP	Concentrating Solar Power
DNI	Direct Normal Irradiance
EP	Eutrophication Potential
EPBT	Energy Payback Time
FU	Functional Unit
GHG	Greenhouse Gas
GWP	Global Warming Potential
HYSOL	Hybrid Solar Energy Technology
IEA	International Energy Agency
LCA	Life Cycle Assessment
LCC	Life Cycle Costing
LCI	Life Cycle Inventory Analysis
LCIA	Life Cycle Impact Assessment
LCSA	Life Cycle Sustainability Assessment
LCSD	Life Cycle Sustainability Dashboard
LCST	Life Cycle Sustainability Triangle
LCWE	Life Cycle Working Environment
ODP	Ozone Layer Depletion Potential
PCU	Power Conversion Unit
PED	Primary Energy Demand
POCP	Photochemical Ozone Creation Potential

PV	Photovoltaic
SDG	Sustainable Development Goal
SHDB	Social Hotspot DataBase
S-LCA	Social Life Cycle Assessment

Closure and future remarks

Research presented in this thesis has been focused on the modelling, optimisation and energy, economic and environmental analysis of dish-Stirling power concentration solar systems, considering the demonstration plant installed within the university campus of Palermo (Italy) as a reference system.

Like all solar systems, the aleatory nature of the solar energy source represents the main affecting factor of the reliability and continuity of the electricity production of dish-Stirling systems. Therefore, it is necessary to have reliable models that are sensitive to the main factors influencing their operation and able to efficiently predict thermal energy and electricity production. The development of accurate and dynamic energy predictive models could enable a push towards greater deployment of systems such as parabolic dish concentrators, driving a rapid and robust transition from fossil energy production toward energy generation from renewables to reduce CO_2 emissions. Firstly, a correct energy assessment of power plants would allow outlining the right direction for optimisation and improvement, especially of promising and not yet fully mature technologies such as CSP, towards cost-efficiency reduction. Secondly, an accurate knowledge of the energy performance of no-fossil fuelled power plants would allow making a realistic evaluation of their economic recoverability, making the investment safe and encouraging more cautious investors also.

Starting from the energy model developed by our research group, according to which the net electric power produced by the system and the direct normal irradiation are linearly correlated, the analysis presented in *Chapter 3* aims to test and optimise a forecasting model for the energy performance of a dish-Stirling solar concentrating plant

based upon the use of artificial neural networks. Contrary to most of the models already tested in the most recent literature in this scientific sector, the data used for the training and validation phases of the networks are real experimental data obtained by a monitoring campaign of an operating plant on the university campus in Palermo. Several neural networks characterised by different architectures and sizes were also tested to better appreciate the relationship between the complexity and quality of the obtained results. A further novelty of the research is the introduction among the input variables of information regarding the cleaning of the reflector mirrors, which has never before been tested in this type of model. The results made it possible to appreciate the good performance of the Multi-Layer Perceptron models compared to the Radial Basis Function models, traditionally characterised by better performance in the approximation of functions. With respect to a modern analytical model already developed, the best of the developed neural models achieved an even higher index of determination between the predicted and calculated results, with a value of 0.98. The results prove the highest reliability of the developed ANN models; the availability of the dataset and the used Python scripts allow, thanks to the exclusive use of open software, maximum transparency, and replicability. Finally, it should be noted that the results of the best of the neural networks tested are better, in terms of coefficient of determination than one of the most advanced and best performing analytical models already developed. Further enhancement of the performance of the neural network models could be achieved by using different activation functions and different optimisers.

Several studies and energy, economic and environmental analyses of the dish-Stirling system have been addressed, with the aim of optimising energy generation and exploring other possible ways of operating this system.

The low commercial penetration of dish-Stirling systems in the renewable solar power generation market can be partially attributed to the fact that these systems are more difficult to combine with thermal energy storage with respect to the other CSP systems. Furthermore, the presence of a thermal storage system would reduce the cost of electricity produced thanks to the continuity of operation during night-time hours. Moreover, the fact that Stirling engines are not produced on a large scale and have a relatively high initial cost is certainly another strong barrier to the commercial penetration of this technology. A novel strategy to encourage greater commercial diffusion of dish-Stirling

systems is outlined and proposed in *Chapter 4*. This approach combines the optimization of the collector size to the solar radiation conditions of the installation site with the definition of a new incentive scheme. The results of the numerical simulations showed that the current dish-Stirling configuration (designed for a peak net electrical output power at DNI = 960 W/m^2) presents an average annual solar-to-electric conversion efficiency of 24%, being able to produce between 40 and 50 MWh$_e$/year of electricity at the typical direct normal irradiance range at seven analysed locations. On the other hand, an optimised configuration of the collector, designed by expanding the collector opening area by 20% to allow a peak power output of the Stirling engine at DNI = 700-800 W/m^2, can increase the energy production by about 26% at the most productive site (Lampedusa, Italy). This configuration, which could be implemented with a modest increase in the installed costs, can also permit a reduction of the current estimated Levelized Cost of Energy of this technology from 0.47 to 0.37 €/kWh. The latter value of Levelized Cost of Energy would be further reduced to 0.24 €/kWh after 10 years if it is assumed that the installed cost reduction trend is similar to that of other concentrating solar power systems in the last decade (about -334 kWp/year). In future research, the analyses presented in *Chapter 4* for dish-Stirling systems could be extended and specialised to geographical locations with direct normal irradiance levels higher than those in the central Mediterranean. With this aim, the new simplified calculation method that was developed in the thesis can be used. This method allows the simulation of the annual electricity production of a dish-Stirling system from the frequency histograms of 1-hour direct normal irradiance series. This new approach may also be used for the optimization of dish-Stirling systems using direct normal irradiance hourly frequency distributions that are generated through suitable statistical methods for a macro-climatic area.

In the framework of the decarbonisation of the building sector using renewable energy sources, *Chapter 5* investigates the option of integrating energy plant of a tertiary building with dish-Stirling systems capable of operating in pure electric mode or in cogenerative mode. Two typical plants for space heating and cooling are identified to be eligible for the integration of this technology. The first one used the natural gas boiler for covering the thermal demand and air-cooled chillers for cooling demand. The second one included a reversible heat pump for covering both heating and cooling demands. Meanwhile, to improve the achievable energy savings, the possibility to operate the

concentrator in electric or cogenerative mode is investigated. More specifically, a fully electric mode is compared to a cogenerative mode, where the heat recovered from the Stirling engine is used to meet heating demand. The detailed models developed for all the main plant components in the TRNSYS environment allowed hourly-based simulations to be carry out, by which it was found that the integration of the dish-Stirling concentrator allows for the reduction of the purchased electricity of about 72%, which also leads to a reduction in CO_2 emissions of about 58%. Even better energy performance was achieved by operating the dish-Stirling system in cogenerative-mode during the winter. In this last configuration, it was observed that the amount of consumed natural gas decreases by about 85% compared to the base case. However, an increase in the purchased electricity is observed compared to the case of the dish-Stirling system operated in electricity-mode (+4.6%). This increase is, however, more than offset by the reduction in natural gas consumption. For the second system, which included a reversible heat pump, the results showed that when the dish-Stirling system operates in electricity-mode, a 65% reduction in the amount of electricity purchased from the grid could be achieved. When heat is recovered, an additional 4% of electricity is no longer purchased from the grid. The results of this analysis have shown that promising energy savings could be obtained by integrating dish-Stirling technology in conventional energy systems used in the tertiary sector to cover the energy demands. Moreover, the cogenerative asset could be very advantageous and environmentally friendly when heating demand still relies on fossil fuel consumption. Finally, the economic analysis of the four proposed system scenarios showed that the installation of a dish-Stirling system integrated into a building is only economically viable if financial support is considered. Then technological improvements and economies of scale will allow the reduction in total installed cost until it is competitive with that of other currently fully commercialized CSP technologies.

In *Chapter 6,* it was investigated the possibility to couple a dish-Stirling collector field with a seasonal geothermal storage and a water-to-water heat pump system. Specifically, the operation of this cogenerative plant would make it possible both to supply thermal energy to the heating system of one of the buildings of the Department of Engineering at Palermo (Italy) and to produce electricity. In the proposed layout, the low-temperature thermal energy recovered from the cooling system of the Stirling engine is stored in the ground during the summer season and then used to satisfy the winter thermal

loads of the building. The cogeneration plant has been designed both to supply thermal energy to the heating system of a non-residential building and to produce electricity. Building 9 of the Department of Engineering on the Palermo University campus was used as a case study and the real operational data of a pilot dish-Stirling collector, located in the same area, was used to carefully calibrate the numerical model implemented in TRNSYS. By using energy and economic performance indicators, it was, finally, possible to optimise both the number of solar collectors and the geometry of the seasonal thermal storage. Among 1440 layout configurations analysed, the best performing configuration consists of two dish-Stirling collectors and 100 geothermal exchangers, each 60 m long and 2 m apart. The two solar collectors annually generate 82 MWh of electrical energy and 177 MWh of thermal energy. Moreover, 80% of the thermal energy annually produced by the Stirling engines is stored in the soil since it is generated in summer, when the heating system of the building is off. 75% of this stored energy is, then, recovered during the winter season and transferred to the evaporators of the heat pumps. 14% of all heat energy annually required by the heat pumps is directly supplied by the solar collectors whenever the energy generation is simultaneous with the heating demands of the building. With this configuration, the heat pump system can cover about 97% of the total heating demand of the building which annually amounts to 166 MWh. The annual average value coefficient of performance of the heat pump systems is equal to 5.37, while that of the whole plant, considering all the electric consumption, is equal to 4.43. Under these conditions, if it is further assumed that the electric grid is used as a seasonal storage, it would be possible to cover all the electric requests from the heat pump employing about 44% of the total electric energy produced by the solar field for one year. In this way, a very high value, about 96%, of thermal energy for heating the building from renewable sources could be achieved which would correspond to annual savings of 32 tons of CO_2. In addition, there would remain about 45 MWh/year of electric energy produced by the solar system that could be used either to cover all the other consumptions of the building or be sold to the national electric grid. Thus, the results of this model demonstrate the technical feasibility of the new proposed cogeneration layout by also quantifying the thermal and electrical efficiency values for a plant built in the Southern Mediterranean basin. However, further economic analyses, based on a plant's useful lifetime of 25 years, show that the commercial penetration of these types of systems should be strongly

supported by a national incentive scheme capable of including both a feed-in tariff of about 369 €/MWh and an initial investment financing of at least 40%. Although this study also demonstrates the technological feasibility and the energy and environmental benefits that can be obtained by coupling dish-Stirling systems with borehole thermal energy storage systems, it still confirms that the initial investment cost required for the installation of such CSP systems is the main constraint for market deployment.

Finally, *Chapter 7* evaluated the reference dish-Stirling existing plant with a Life Cycle Sustainability Assessment. This part of the thesis allows the assessment of the system in the three dimensions of sustainability: environmental, economic, and social, as well as a detailed and careful analysis of the entire life cycle of the CSP system offering a clear representation of the holistic sustainability performance of solar electricity production. The LCSA system boundary was defined as cradle-to-use, the functional unit was the CSP plant itself. The LCA is based on data available in GaBi (SP40) and Ecoinvent 3.5 resulting in seven midpoint indicators using the CML2001 methodology. In terms of greenhouse gas emissions, 35 t CO_{2e} were calculated. Other emission indicators than CO_{2e} and a detailed split up concerning driving process steps were given in the actual study. The three main drivers for all indicators were the electronic components, the elevation tracker and the PCU equipment – mainly driven by steel as material. The conventional LCC resulted in 308,467.00 € as total costs, which lead to 268.00 € per MWh (0.268 €/kWh) of generated energy. Average European energy prices verified the calculated result and represented their plausibility. For S-LCA, working days, wages, and a risk analysis through the SHDB were evaluated. The wage of 12.5 €/h for unskilled workers was slightly above the highest European minimum wage. Based on LCA, relevant and critical input raw materials were defined, following the EU report [209]. No country, no sector and no category could be with low risk for this technology. The results of the LCSA pillar are independent, but interpretation and communication remain challenging. Limitations also relate to data availability, uniform system boundaries and comparability of results. A holistic statement about the sustainability performance of the dish-Stirling engine could not be defined, resulting in the future need for a general and optimized interpretation and communication approach for LCSA.

The research undertaken during the last doctoral period and addressed here can still be extended and further investigated, especially as regards the possibility to operate the dish-Stirling system in cogeneration mode. This solution could give this technology greater development and market penetration.

Publications on journals with IF

Guarino, S., Buscemi, A., Messineo, A., & Lo Brano, V. (2022). "Energy and Environmental Assessment of a Hybrid Dish-Stirling Concentrating Solar Power Plant". Sustainability, 14, 6098
https://doi.org/10.3390/su14106098

Buscemi, A., Guarino, S., Ciulla, G., & Lo Brano, V. (2021). "A methodology for optimisation of solar dish-Stirling systems size, based on the local frequency distribution of direct normal irradiance".
Applied Energy, 303, 117681.
https://doi.org/10.1016/j.apenergy.2021.117681

Bonomolo, M., Zizzo, G., Ferrari, S., Beccali, M., & Guarino, S.. (2021). "Empirical BAC Factors Method Application to Two Real Case Studies in South Italy."
Energy, 236,121498.
https://doi.org/10.1016/j.energy.2021.121498

Backes, J. G., D'Amico, A., Pauliks, N., Guarino, S., Traverso, M., & Lo Brano, V. (2021). "Life Cycle Sustainability Assessment of a dish-Stirling Concentrating Solar Power Plant in the Mediterranean area".
Sustainable Energy Technologies and Assessments, 47, 101444.
https://doi.org/10.1016/j.seta.2021.101444

Manno, D., Cipriani, G., Ciulla, G., Di Dio, V., Guarino, S., & Lo Brano, V. (2021). “Deep learning strategies for automatic fault diagnosis in photovoltaic systems by thermographic images”.

Energy Conversion and Management, 241, 114315.

https://doi.org/10.1016/j.enconman.2021.114315

Guarino, S., Catrini, P., Buscemi, A., Lo Brano, V., & Piacentino, A. (2021). “Assessing the energy-saving potential of a dish-Stirling concentrator integrated into energy plants in the tertiary sector”.

Energies, 14(4).

https://doi.org/10.3390/en14041163

Cipriani, G., D’Amico, A., Guarino, S., Manno, D., Traverso, M., & Di Dio, V. (2020). “*Convolutional Neural Network for Dust and Hotspot Classification in PV Modules”*.

Energies, 13(23), 1–17.

https://doi.org/10.3390/en13236357

Guarino, S., Buscemi, A., Ciulla, G., Bonomolo, M., & Lo Brano, V. (2020). “A dish-Stirling solar concentrator coupled to a seasonal thermal energy storage system in the southern Mediterranean basin: A cogenerative layout hypothesis”.

Energy Conversion and Management, 222, 113228.

https://doi.org/10.1016/j.enconman.2020.113228

References

[1] Kirk-Davidoff D. The Greenhouse Effect, Aerosols, and Climate Change. Green Chem An Incl Approach 2018:211–34. https://doi.org/10.1016/B978-0-12-809270-5.00009-1.

[2] Kumar A, Singh P, Raizada P, Hussain CM. Impact of COVID-19 on greenhouse gases emissions: A critical review. Sci Total Environ 2022;806:150349. https://doi.org/10.1016/J.SCITOTENV.2021.150349.

[3] Graham F. COP26: Glasgow Climate Pact signed into history. Nature 2021.

[4] HOME - UN Climate Change Conference (COP26) at the SEC – Glasgow 2021 n.d.

[5] IPCC, 2018: Global Warming of 1.5°C.An IPCC Special Report on the impacts of global warming of 1.5°C above pre-industrial levels and related global greenhouse gas emission pathways, in the context of strengthening the global response to the threat of clim. n.d.

[6] 2021 UCC conference U. COP26: The Glasgow climate pact. 2021.

[7] Gielen D, Gorini R, Leme R, Prakash G, Wagner N, Janeiro L, et al. World Energy Transitions Outlook: 1.5° C Pathway 2021.

[8] Khan J, Arsalan MH. Solar power technologies for sustainable electricity generation – A review. Renew Sustain Energy Rev 2016;55:414–25. https://doi.org/10.1016/j.rser.2015.10.135.

[9] Regmi G, Subramaniam V. Chapter 5 - Introduction to photovoltaics and alternative materials for silicon in photovoltaic energy conversion. In: Fraga MA, Amos D, Sonmezoglu S, Subramaniam V, editors. Sustain. Mater. Solut. Sol. Energy Technol., Elsevier; 2021, p. 131–73. https://doi.org/https://doi.org/10.1016/B978-0-12-821592-0.00004-2.

[10] Lovegrove K, Stein W. Concentrating Solar Power Technology: Principles, Developments and Applications. Woodhead Publushing; 2012. https://doi.org/10.1533/9780857096173.

[11] Fuqiang W, Ziming C, Jianyu T, Yuan Y, Yong S, Linhua L. Progress in concentrated solar power technology with parabolic trough collector system: A comprehensive review. Renew Sustain Energy Rev 2017;79:1314–28. https://doi.org/10.1016/j.rser.2017.05.174.

[12] Aqachmar Z, Ben Sassi H, Lahrech K, Barhdadi A. Solar technologies for electricity production: An updated review. Int J Hydrogen Energy 2021;46:30790–817. https://doi.org/10.1016/j.ijhydene.2021.06.190.

[13] REN21. Renewables 2021 Global Status Report. Paris: 2021.

[14] IRENA (2020). Renewable Power Generation Costs in 2020. Abu Dhabi: n.d.

[15] Bahar H, Bojek P. Concentrating Solar Power (CSP) 2020.

[16] International energy agency (IEA). Global Energy Review: CO2 Emissions in 2020 2021.

[17] Schiel W, Keck T. 9 - Parabolic dish concentrating solar power (CSP) systems. In: Lovegrove K, Stein W, editors. Conc. Sol. Power Technol., Woodhead Publishing; 2012, p. 284–322. https://doi.org/10.1533/9780857096173.2.284.

[18] Salameh Z. Chapter 5 - Emerging Renewable Energy Sources. In: Salameh Z, editor. Renew. Energy Syst. Des., Boston: Academic Press; 2014, p. 299–371. https://doi.org/10.1016/B978-0-12-374991-8.00005-2.

[19] Backes JG, D'Amico A, Pauliks N, Guarino S, Traverso M, Lo Brano V. Life Cycle Sustainability Assessment of a dish-Stirling Concentrating Solar Power

Plant in the Mediterranean area. Sustain Energy Technol Assessments 2021;47:101444. https://doi.org/10.1016/j.seta.2021.101444.

[20] Manno D, Cipriani G, Ciulla G, Di Dio V, Guarino S, Brano V Lo. Deep learning strategies for automatic fault diagnosis in photovoltaic systems by thermographic images. Energy Convers Manag 2021;241:114315.

[21] Cipriani G, D'Amico A, Guarino S, Manno D, Traverso M, Dio V Di. Convolutional Neural Network for Dust and Hotspot Classification in PV Modules. Energies 2020;13:1–17.

[22] Buscemi A, Lo Brano V, Chiaruzzi C, Ciulla G, Kalogeri C. A validated energy model of a solar dish-Stirling system considering the cleanliness of mirrors. Appl Energy 2020. https://doi.org/10.1016/j.apenergy.2019.114378.

[23] Blanco M, Santigosa LR. Advances in concentrating solar thermal research and technology. Woodhead Publishing; 2016.

[24] Islam MT, Huda N, Abdullah AB, Saidur R. A comprehensive review of state-of-the-art concentrating solar power (CSP) technologies: Current status and research trends. Renew Sustain Energy Rev 2018;91:987–1018. https://doi.org/10.1016/J.RSER.2018.04.097.

[25] National Renewable Energy Laboratory. Concentrating Solar Power Projects n.d. https://solarpaces.nrel.gov/.

[26] Asif M. Fundamentals and Application of Solar Thermal Technologies. Encycl Sustain Technol 2017:27–36. https://doi.org/10.1016/B978-0-12-409548-9.10093-4.

[27] Dincer I, Bicer Y. 4.23 Solar Thermochemical Energy Conversion. Compr Energy Syst 2018;4–5:895–946. https://doi.org/10.1016/B978-0-12-809597-3.00440-5.

[28] Coventry J, Andraka C. Dish systems for CSP. Sol Energy 2017;152:140–70. https://doi.org/10.1016/J.SOLENER.2017.02.056.

[29] Desideri U, Zepparelli F, Morettini V, Garroni E. Comparative analysis of concentrating solar power and photovoltaic technologies: Technical and

environmental evaluations. Appl Energy 2013;102:765–84. https://doi.org/https://doi.org/10.1016/j.apenergy.2012.08.033.

[30] Meyer R, Schlecht M, Chhatbar K. Solar resources for concentrating solar power (CSP) systems. Conc Sol Power Technol 2012:68-e2. https://doi.org/10.1533/9780857096173.1.68.

[31] Singh UR, Kumar A. Review on solar Stirling engine: Development and performance. Therm Sci Eng Prog 2018;8:244–56. https://doi.org/10.1016/J.TSEP.2018.08.016.

[32] Ferreira AC, Nunes ML, Teixeira JCF, Martins LASB, Teixeira SFCF. Thermodynamic and economic optimization of a solar-powered Stirling engine for micro-cogeneration purposes. Energy 2016;111:1–17. https://doi.org/10.1016/j.energy.2016.05.091.

[33] Moghadam RS, Sayyaadi H, Hosseinzade H. Sizing a solar dish Stirling micro-CHP system for residential application in diverse climatic conditions based on 3E analysis. Energy Convers Manag 2013;75:348–65. https://doi.org/10.1016/j.enconman.2013.06.008.

[34] Andraka CE. Dish Stirling advanced latent storage feasibility. Energy Procedia 2014;49:684–93. https://doi.org/10.1016/j.egypro.2014.03.074.

[35] Monné C, Bravo Y, Moreno F, Muñoz M. Analysis of a solar dish-Stirling system with hybridization and thermal storage. Int J Energy Environ Eng 2014;5:1–5. https://doi.org/10.1007/s40095-014-0080-x.

[36] Kadri Y, Hadj Abdallah H. Performance evaluation of a stand-alone solar dish Stirling system for power generation suitable for off-grid rural electrification. Energy Convers Manag 2016;129:140–56. https://doi.org/10.1016/j.enconman.2016.10.024.

[37] Abbas M, Boumeddane B, Said N, Chikouche A. Dish Stirling technology: A 100 MW solar power plant using hydrogen for Algeria. Int J Hydrogen Energy 2011;36:4305–14. https://doi.org/10.1016/j.ijhydene.2010.12.114.

[38] Al-Dafaie AMA, Dahdolan ME, Al-Nimr MA. Utilizing the heat rejected from a solar dish Stirling engine in potable water production. Sol Energy 2016;136:317–26. https://doi.org/10.1016/j.solener.2016.07.007.

[39] Bumataria RK, Patel NK. Review of Stirling Engines for Pumping Water using Solar Energy as a source of Power. Int J Eng Res Appl 2013;3:864–8.

[40] Zayed ME, Zhao J, Elsheikh AH, Li W, Sadek S, Aboelmaaref MM. A comprehensive review on Dish/Stirling concentrated solar power systems: Design, optical and geometrical analyses, thermal performance assessment, and applications. J Clean Prod 2021;283:124664. https://doi.org/10.1016/J.JCLEPRO.2020.124664.

[41] Steinfeld A, Palumbo R. Solar thermochemical process technology. Encycl Phys Sci Technol 2001;15:237–56.

[42] Siva Reddy V, Kaushik SC, Tyagi SK. Exergetic analysis and performance evaluation of parabolic dish Stirling engine solar power plant. Int J Energy Res 2013;37:1287–301. https://doi.org/10.1002/er.2926.

[43] Thakkar V, Doshi A, Rana A. Performance analysis methodology for parabolic dish solar concentrators for process heating using thermic fluid. J Mech Civ Eng 2015;12:101–14.

[44] Dähler F, Wild M, Schäppi R, Haueter P, Cooper T, Good P, et al. Optical design and experimental characterization of a solar concentrating dish system for fuel production via thermochemical redox cycles. Sol Energy 2018;170:568–75. https://doi.org/10.1016/J.SOLENER.2018.05.085.

[45] Schiel W, Keck T. Chapter 9 - Parabolic dish concentrating solar power systems. In: Lovegrove K, Stein W, editors. Conc. Sol. Power Technol. (Second Ed. Second Edi, Woodhead Publishing; 2021, p. 311–55. https://doi.org/https://doi.org/10.1016/B978-0-12-819970-1.00007-4.

[46] Dincer I, Bicer Y. Fundamentals of energy systems. Integr Energy Syst Multigeneration 2020:33–83. https://doi.org/10.1016/B978-0-12-809943-8.00002-9.

[47] Poullikkas A, Kourtis G, Hadjipaschalis I. Parametric comparative study for the installation of solar dish technologies in Cyprus. 7th Mediterr. Conf. Exhib. Power Gener. Transm. Distrib. Energy Convers. (MedPower 2010), 2010, p. 1–8.

[48] Li Y, Liu G, Liu X, Liao S. Thermodynamic multi-objective optimization of a solar-dish Brayton system based on maximum power output, thermal efficiency and ecological performance. Renew Energy 2016;95:465–73. https://doi.org/10.1016/J.RENENE.2016.04.052.

[49] Mancini T, Heller P, Butler B, Osborn B, Schiel W, Goldberg V, et al. Dish-stirling systems: An overview of development and status. J Sol Energy Eng Trans ASME 2003;125:135–51. https://doi.org/10.1115/1.1562634.

[50] Perozziello C, Grosu L, Vaglieco BM. Free-Piston Stirling Engine Technologies and Models: A Review. Energies 2021;14:7009.

[51] Zare S, Tavakolpour-Saleh A. Free piston Stirling engines: A review. Int J Energy Res 2020;44:5039–70.

[52] Dincer I, Zamfirescu C. 1.5 Thermodynamic Aspects of Energy. Compr Energy Syst 2018;1–5:153–211. https://doi.org/10.1016/B978-0-12-809597-3.00105-X.

[53] Selcuk MK, Fujita T. A nomographic methodology for use in performance trade-off studies of parabolic dish solar power modules 1984.

[54] Lopez CW, Stone KW. Performance of the Southern California Edison Company Stirling Dish. NASA STI/Recon Tech Rep N 1993;94.

[55] Lemmon EW, Bell IH, Huber ML, McLinden MO. NIST Standard Reference Database 23: Reference Fluid Thermodynamic and Transport Properties-REFPROP, Version 10.0, National Institute of Standards and Technology. Stand Ref Data Program, Gaithersbg 2018.

[56] Panno D, Buscemi A, Beccali M, Chiaruzzi C, Cipriani G, Ciulla G, et al. A solar assisted seasonal borehole thermal energy system for a non-residential building in the Mediterranean area. Sol Energy 2018. https://doi.org/10.1016/J.SOLENER.2018.06.014.

[57] Stine WB. Experimentally Validated Long-Term Energy Production Prediction Model for Solar Dish/Stirling Electric Generating Systems. In: D.Y. Goswami, L.D. Kannberg, T.R. Mancini, S. Somasundaram eds., editor. Proc. Intersoc. Energy Convers. Eng. Conf. vol. 2, New York, NY, USA: American Society of Mechanical Engineers; 1995, p. 491–5. https://doi.org/AC04-94AL85000.

[58] Igo J, Andraka CE. Solar dish field system model for spacing optimization. Proc. Energy Sustain. Conf. 2007, 2007. https://doi.org/10.1115/ES2007-36154.

[59] Nepveu F, Ferriere A, Bataille F. Thermal model of a dish/Stirling systems. Sol Energy 2009;83:81–9. https://doi.org/https://doi.org/10.1016/j.solener.2008.07.008.

[60] Mendoza Castellanos LS, Galindo Noguera AL, Carrillo Caballero GE, De Souza AL, Melian Cobas VR, Silva Lora EE, et al. Experimental analysis and numerical validation of the solar Dish/Stirling system connected to the electric grid. Renew Energy 2019. https://doi.org/10.1016/j.renene.2018.11.095.

[61] Schiel W, Schweiber A, Stine WB. Evaluation of the 9-kw e dish/stirling system of schlaich bergermann und partner using the proposed iea dish/stirling performance analysis guidelines. Intersoc. Energy Convers. Eng. Conf. 1994, 1994.

[62] Andraka CE. Cost/performance tradeoffs for reflectors used in solar concentrating dish systems. 2008 Proc. 2nd Int. Conf. Energy Sustain. ES 2008, 2009.

[63] Sciortino L, Agnello S, Barbera M, Bonsignore G, Buscemi A, Candia R, et al. Direct sunlight facility for testing and research in HCPV. AIP Conf. Proc., vol. 1616, 2014, p. 158–61.

[64] Kallos G, Astitha M, Katsafados P, Spyrou C. Long-Range Transport of Anthropogenically and Naturally Produced Particulate Matter in the Mediterranean and North Atlantic: Current State of Knowledge. J Appl Meteorol Climatol 2007;46:1230–51. https://doi.org/10.1175/JAM2530.1.

[65] Kallos G, Spyrou C, Astitha M, Mitsakou C, Solomos S, Kushta J, et al. Ten-year operational dust forecasting – Recent model development and future plans. IOP

Conf. Ser. Earth Environ. Sci., vol. 7, 2009, p. 12012. https://doi.org/10.1088/1755-1307/7/1/012012.

[66] Kallos G, Solomos S, Kushta J, Mitsakou C, Spyrou C, Bartsotas N, et al. Natural and anthropogenic aerosols in the Eastern Mediterranean and Middle East: Possible impacts. Sci Total Environ 2014;488–489:389–97. https://doi.org/10.1016/j.scitotenv.2014.02.035.

[67] Spyrou C, Kallos G, Mitsakou C, Athanasiadis P, Kalogeri C. The Effects of Naturally Produced Dust Particles on Radiative Transfer. Adv. Meteorol. Climatol. Atmos. Phys., Springer; 2013, p. 317–23.

[68] Hachicha AA, Yousef BAA, Said Z, Rodríguez I. A review study on the modeling of high-temperature solar thermal collector systems. Renew Sustain Energy Rev 2019. https://doi.org/10.1016/j.rser.2019.05.056.

[69] Pavan AM, Mellit A, De Pieri D. The effect of soiling on energy production for large-scale photovoltaic plants. Sol Energy 2011;85:1128–36.

[70] Gostein M, Stueve B, Chan M. Accurately measuring PV soiling losses with soiling station employing PV module power measurements. 2017 IEEE 44th Photovolt. Spec. Conf. PVSC 2017, 2017. https://doi.org/10.1109/PVSC.2017.8366169.

[71] Badescu V. Modeling solar radiation at the earth's surface. vol. 1. Springer; 2014.

[72] Stine W. DR. A Compendium of Solar Dish/Stirling Technology. Sandia Natl Lab 1994:SAND 93-7026.

[73] Law EW, Kay M, Taylor RA. Evaluating the benefits of using short-term direct normal irradiance forecasts to operate a concentrated solar thermal plant. Sol Energy 2016;140:93–108. https://doi.org/https://doi.org/10.1016/j.solener.2016.10.037.

[74] Gueymard CA, Ruiz-Arias JA. Extensive worldwide validation and climate sensitivity analysis of direct irradiance predictions from 1-min global irradiance. Sol Energy 2016;128:1–30.

https://doi.org/https://doi.org/10.1016/j.solener.2015.10.010.

[75] Vignola F, Harlan P, Perez R, Kmiecik M. Analysis of satellite derived beam and global solar radiation data. Sol Energy 2007;81:768–72. https://doi.org/10.1016/j.solener.2006.10.003.

[76] Larrañeta M, Moreno-Tejera S, Lillo-Bravo I, Silva-Pérez MA. A methodology for the stochastic generation of hourly synthetic direct normal irradiation time series. Theor Appl Climatol 2018;131:1517–27. https://doi.org/10.1007/s00704-017-2188-4.

[77] Roesch A, Wild M, Ohmura A, Dutton EG, Long CN, Zhang T. Assessment of BSRN radiation records for the computation of monthly means. Atmos Meas Tech 2011;4:339–54.

[78] Meteonorm. Meteonorm global meteorological database--Handbook Part II: Theory, Version 7.1.7.21517 2015.

[79] Suri M, Huld T, Dunlop ED, Cebecauer T. Geographic aspects of photovoltaics in Europe: contribution of the PVGIS website. IEEE J Sel Top Appl Earth Obs Remote Sens 2008;1:34–41.

[80] Remund J. Quality of meteonorm version 6.0. Europe 2008;6:389.

[81] Amillo AG, Huld T, Müller R. A new database of global and direct solar radiation using the eastern meteosat satellite, models and validation. Remote Sens 2014;6:8165–89. https://doi.org/10.3390/rs6098165.

[82] Psiloglou BE, Kambezidis HD, Kaskaoutis DG, Karagiannis D, Polo JM. Comparison between MRM simulations, CAMS and PVGIS databases with measured solar radiation components at the Methoni station, Greece. Renew Energy 2020;146:1372–91. https://doi.org/10.1016/j.renene.2019.07.064.

[83] Yang S, Wan MP, Chen W, Ng BF, Dubey S. Model predictive control with adaptive machine-learning-based model for building energy efficiency and comfort optimization. Appl Energy 2020;271:115147.

[84] Korkmaz D. SolarNet: A hybrid reliable model based on convolutional neural

network and variational mode decomposition for hourly photovoltaic power forecasting. Appl Energy 2021;300:117410.

[85] Chen Z, Yu H, Luo L, Wu L, Zheng Q, Wu Z, et al. Rapid and accurate modeling of PV modules based on extreme learning machine and large datasets of IV curves. Appl Energy 2021;292:116929.

[86] Elsheikh AH, Sharshir SW, Abd Elaziz M, Kabeel AE, Guilan W, Haiou Z. Modeling of solar energy systems using artificial neural network: A comprehensive review. Sol Energy 2019;180:622–39. https://doi.org/10.1016/j.solener.2019.01.037.

[87] Khosravi A, Syri S, Pabon JJG, Sandoval OR, Caetano BC, Barrientos MH. Energy modeling of a solar dish/Stirling by artificial intelligence approach. Energy Convers Manag 2019;199:112021. https://doi.org/10.1016/j.enconman.2019.112021.

[88] Zaaoumi A, Bah A, Ciocan M, Sebastian P, Balan MC, Mechaqrane A, et al. Estimation of the energy production of a parabolic trough solar thermal power plant using analytical and artificial neural networks models. Renew Energy 2021;170:620–38. https://doi.org/10.1016/j.renene.2021.01.129.

[89] Ahmadi MH, Sorouri Ghare Aghaj S, Nazeri A. Prediction of power in solar stirling heat engine by using neural network based on hybrid genetic algorithm and particle swarm optimization. Neural Comput Appl 2013;22:1141–50. https://doi.org/10.1007/s00521-012-0880-y.

[90] Liao T, Lin J. Optimum performance characteristics of a solar-driven Stirling heat engine system. Energy Convers Manag 2015;97:20–5.

[91] Beltrán-Chacon R, Leal-Chavez D, Sauceda D, Pellegrini-Cervantes M, Borunda M. Design and analysis of a dead volume control for a solar Stirling engine with induction generator. Energy 2015;93:2593–603.

[92] Vahidi Bidhendi M, Abbassi Y. Exploring dynamic operation of a solar dish-stirling engine: Validation and implementation of a novel TRNSYS type. Sustain Energy Technol Assessments 2020;40:100765.

https://doi.org/10.1016/j.seta.2020.100765.

[93] Zayed ME, Zhao J, Elsheikh AH, Zhao Z, Zhong S, Kabeel AE. Comprehensive parametric analysis, design and performance assessment of a solar dish/Stirling system. Process Saf Environ Prot 2021;146:276–91. https://doi.org/10.1016/j.psep.2020.09.007.

[94] Zayed ME, Zhao J, Li W, Elsheikh AH, Abd Elaziz M, Yousri D, et al. Predicting the performance of solar dish Stirling power plant using a hybrid random vector functional link/chimp optimization model. Sol Energy 2021;222:1–17.

[95] Gulli A, Kapoor A, Pal S. Deep learning with TensorFlow 2 and Keras: regression, ConvNets, GANs, RNNs, NLP, and more with TensorFlow 2 and the Keras API. Packt Publishing Ltd; 2019.

[96] Singh P, Manure A. Learn TensorFlow 2.0: Implement Machine Learning and Deep Learning Models with Python. Springer; 2020.

[97] Brownlee J. Deep learning with Python: develop deep learning models on Theano and TensorFlow using Keras. Machine Learning Mastery; 2016.

[98] Brownlee J. Machine learning mastery with python. Mach Learn Mastery Pty Ltd 2016;527:100–20.

[99] Moolayil J, Moolayil J, John S. Learn Keras for Deep Neural Networks. Springer; 2019.

[100] Tian Z, Zhang Y, Liu K, Zhao J. Topic Knowledge Acquisition and Utilization for Machine Reading Comprehension in Social Media Domain. China Natl. Conf. Chinese Comput. Linguist., 2021, p. 161–76.

[101] José C. Principe, Neil R. Euliano WCL. Neural and Adaptive Systems: Fundamentals through Simulations. Wiley; 1999.

[102] Jiang Q, Zhu L, Shu C, Sekar V. An efficient multilayer RBF neural network and its application to regression problems. Neural Comput Appl 2021. https://doi.org/10.1007/s00521-021-06373-0.

[103] He X, Xu S. Process neural networks: Theory and applications. Springer Science \& Business Media; 2010.

[104] Bilogur A. Radial Basis Networks and Custom Keras Layers 2018. https://www.kaggle.com/residentmario/radial-basis-networks-and-custom-keras-layers.

[105] NREL. National Renewable Energy Laboratory. Concentrating Solar Power Projects with Operational Plants n.d. https://solarpaces.nrel.gov/ (accessed July 17, 2020).

[106] Hernández-Moro J, Martínez-Duart JM. Analytical model for solar PV and CSP electricity costs: Present LCOE values and their future evolution. Renew Sustain Energy Rev 2013;20:119–32. https://doi.org/https://doi.org/10.1016/j.rser.2012.11.082.

[107] IRENA (2020). Renewable Power Generation Costs in 2019. International Renewable Energy Agency, Abu Dhabi.: n.d.

[108] Thombare DG, Verma SK. Technological development in the Stirling cycle engines. Renew Sustain Energy Rev 2008. https://doi.org/10.1016/j.rser.2006.07.001.

[109] Zhang HL, Baeyens J, Degrève J, Cacères G. Concentrated solar power plants: Review and design methodology. Renew Sustain Energy Rev 2013;22:466–81. https://doi.org/10.1016/j.rser.2013.01.032.

[110] Sharma A, Shukla SK, Rai AK. Finite time thermodynamic analysis and optimization of solar-dish Stirling heat engine with regenerative losses. Therm Sci 2011;15:995–1009. https://doi.org/10.2298/TSCI110418101S.

[111] Guarino S, Catrini P, Buscemi A, Lo Brano V, Piacentino A. Assessing the Energy-Saving Potential of a Dish-Stirling Con-Centrator Integrated Into Energy Plants in the Tertiary Sector. Energies 2021;14. https://doi.org/10.3390/en14041163.

[112] Su B, Han W, Zhang X, Chen Y, Wang Z, Jin H. Assessment of a combined

cooling, heating and power system by synthetic use of biogas and solar energy. Appl Energy 2018;229:922–35. https://doi.org/https://doi.org/10.1016/j.apenergy.2018.08.037.

[113] Desideri U, Campana PE. Analysis and comparison between a concentrating solar and a photovoltaic power plant. Appl Energy 2014;113:422–33. https://doi.org/https://doi.org/10.1016/j.apenergy.2013.07.046.

[114] Janjai S, Laksanaboonsong J, Seesaard T. Potential application of concentrating solar power systems for the generation of electricity in Thailand. Appl Energy 2011;88:4960–7. https://doi.org/https://doi.org/10.1016/j.apenergy.2011.06.044.

[115] Heller P, Baumüller A, Schiel W. Eurodish the next milestone to decrease the costs of Dish/Stirling System towards competitiveness. Sol Paces Symp Sydney 2000:2–7.

[116] Keck T, Schiel W. EnviroDish and EuroDish System and Status. Proc. ISES Sol. world Congr., 2003.

[117] Chaves-Avila JP, Banez-Chicharro F, Ramos A. Impact of support schemes and market rules on renewable electricity generation and system operation: The Spanish case. IET Renew Power Gener 2017;11:238–44. https://doi.org/10.1049/iet-rpg.2016.0246.

[118] Izquierdo S, Montanes C, Dopazo C, Fueyo N. Analysis of CSP plants for the definition of energy policies: The influence on electricity cost of solar multiples, capacity factors and energy storage. Energy Policy 2010;38:6215–21.

[119] European Commission. Roadmap 2050. Policy 2012:1–9. https://doi.org/10.2833/10759.

[120] Guarino S, Buscemi A, Ciulla G, Bonomolo M, Lo Brano V. A dish-stirling solar concentrator coupled to a seasonal thermal energy storage system in the southern mediterranean basin: A cogenerative layout hypothesis. Energy Convers Manag 2020;222:113228. https://doi.org/10.1016/j.enconman.2020.113228.

[121] Hernández-Moro J, Martínez-Duart JM. CSP electricity cost evolution and grid

parities based on the IEA roadmaps. Energy Policy 2012;41:184–92. https://doi.org/10.1016/j.enpol.2011.10.032.

[122] Baker E, Fowlie M, Lemoine D, Reynolds SS. The Economics of Solar Electricity. Annu Rev Resour Econ 2013;5:387–426. https://doi.org/10.1146/annurev-resource-091912-151843.

[123] D. M. 16 Febbraio 2016. Incentivazione della produzione di energia termica da impianti a fonti rinnovabili ed interventi di efficienza energetica di piccole dimensioni 2016:65–71.

[124] D. M. 28 luglio 2005. "Criteri per l'incentivazione della produzione di energia elettrica mediante conversione fotovoltaica della fonte solare." 2005.

[125] Lund H. Renewable energy strategies for sustainable development. Energy 2007;32:912–9. https://doi.org/https://doi.org/10.1016/j.energy.2006.10.017.

[126] Kousksou T, Bruel P, Jamil A, Rhafiki] T [El, Zeraouli Y. Energy storage: Applications and challenges. Sol Energy Mater Sol Cells 2014;120:59–80. https://doi.org/https://doi.org/10.1016/j.solmat.2013.08.015.

[127] Alharbi F, Csala D. Saudi Arabia's solar and wind energy penetration: Future performance and requirements. Energies 2020;13:588.

[128] Mazzoni S, Ooi S, Nastasi B, Romagnoli A. Energy storage technologies as techno-economic parameters for master-planning and optimal dispatch in smart multi energy systems. Appl Energy 2019;254. https://doi.org/10.1016/j.apenergy.2019.113682.

[129] El-Bayeh CZ, Alzaareer K, Laraki M, Brahmi B, Panchabikesan K, Venturini WA, et al. A Comparison between PV and Dish Stirling Systems Towards Self-Sufficient Energy Building in Lebanon. 2020 5th Int. Conf. Renew. Energies Dev. Ctries., 2020, p. 1–6. https://doi.org/10.1109/REDEC49234.2020.9163860.

[130] Khoshbazan M, Ahmadi MH, Ming T, Tabe Arjmand J, Rahimzadeh M. Thermo-economic analysis and multi-objective optimization of micro-CHP Stirling system for different climates of Iran. Int J Low-Carbon Technol 2018;13:388–403.

https://doi.org/10.1093/ijlct/cty050.

[131] IMST-Group Instituto de Ingeniería Energética Universidad Politécnica de Valencia. IMST-Art 2017.

[132] Illán-Gómez F, García-Cascales JR, Hidalgo-Mompeán F, López-Belchí A. Experimental assessment of the replacement of a conventional fin-and-tube condenser by a minichannel heat exchanger in an air/water chiller for residential air conditioning. Energy Build 2017;144:104–16. https://doi.org/https://doi.org/10.1016/j.enbuild.2017.03.041.

[133] Pisano A, Martínez-Ballester S, Corberán JM, Mauro AW. Optimal design of a light commercial freezer through the analysis of the combined effects of capillary tube diameter and refrigerant charge on the performance. Int J Refrig 2015;52:1–10. https://doi.org/https://doi.org/10.1016/j.ijrefrig.2014.12.023.

[134] Blanco Castro J, Urchueguía JF, Corberán JM, Gonzálvez J. Optimized design of a heat exchanger for an air-to-water reversible heat pump working with propane (R290) as refrigerant: Modelling analysis and experimental observations. Appl Therm Eng 2005;25:2450–62. https://doi.org/https://doi.org/10.1016/j.applthermaleng.2004.12.009.

[135] Piacentino A, Barbaro C. A comprehensive tool for efficient design and operation of polygeneration-based energy μgrids serving a cluster of buildings. Part II: Analysis of the applicative potential. Appl Energy 2013;111:1222–38. https://doi.org/10.1016/J.APENERGY.2012.11.079.

[136] Suri M, Remund J, Cebecauer T, Hoyer-Click C, Dumortier D, Huld T, et al. Comparison of direct normal irradiation maps for Europe. Sol. Paces, 2009.

[137] Klein Sa, Beckman A, Mitchell W, Duffie A. TRNSYS 17-A TRansient SYstems Simulation program. Sol Energy Lab Univ Wisconsin, Madison 2011.

[138] ISPRA Istituto Superiore per la, Ambientale P e la R. Fattori di emissione atmosferica di CO2 e altri gas a effetto serra nel settore elettrico 2017.

[139] D.M. 23 giugno 2016. Incentivazione dell'energia elettrica prodotta da fonti

rinnovabili diverse dal fotovoltaico. 2016.

[140] Li G, Zheng X. Thermal energy storage system integration forms for a sustainable future. Renew Sustain Energy Rev 2016;62:736–57. https://doi.org/10.1016/j.rser.2016.04.076.

[141] Yao J, Liu W, Zhang L, Tian B, Dai Y, Huang M. Performance analysis of a residential heating system using borehole heat exchanger coupled with solar assisted PV/T heat pump. Renew Energy 2020.

[142] Esen H, Esen M, Ozsolak O. Modelling and experimental performance analysis of solar-assisted ground source heat pump system. J Exp Theor Artif Intell 2017;29:1–17.

[143] Li H, Bi Y, Qin L, Zang G. Absorption solar-ground source heat pump: Life cycle environmental profile and comparisons. Geothermics 2020;87:101850.

[144] Pavlov GK, Olesen BW. Seasonal solar thermal energy storage through ground heat exchangers. Review of systems and applications. Proceedings, 2011.

[145] Schmidt T, Mangold D, Müller-Steinhagen H. Central solar heating plants with seasonal storage in Germany. Sol Energy 2004;76:165–74. https://doi.org/10.1016/j.solener.2003.07.025.

[146] Sørensen PA, Schmidt T. Design and construction of large scale heat storages for district heating in Denmark. 14th Int. Conf. Energy Storage, 2018, p. 25–8.

[147] Dinçer I, Rosen MA. Thermal Energy Storage. Systems and applications. Wiley; 2011.

[148] Chen Y, Wang J, Lund PD. Sustainability evaluation and sensitivity analysis of district heating systems coupled to geothermal and solar resources. Energy Convers Manag 2020;220:113084.

[149] Andersson O. BTES for heating and cooling of the Astronomy House in Lund. Therm. Energy Storage Sustain. Energy Consum., Springer; 2007, p. 229–33.

[150] Ferreira AC, Nunes ML, Teixeira JCF, Martins LASB, Teixeira SFCF, Nebra SA.

Design of a solar dish Stirling cogeneration system: Application of a multi-objective optimization approach. Appl Therm Eng 2017;123:646–57. https://doi.org/https://doi.org/10.1016/j.applthermaleng.2017.05.127.

[151] Conti P, Testi D, Grassi W. Revised heat transfer modeling of double-U vertical ground-coupled heat exchangers. Appl Therm Eng 2016;106. https://doi.org/10.1016/j.applthermaleng.2016.06.097.

[152] Incropera FP, DeWitt DP, Bergman TL, Lavine AS. Fundamentals of Heat and Mass Transfer 5th Edition with IHT2.0/FEHT with Users Guides. Wiley; 2001.

[153] Massey BS. Mechanics of fluids. Chapman & Hall; 1989.

[154] Wang X, Zheng M, Zhang W, Zhang S, Yang T. Experimental study of a solar-assisted ground-coupled heat pump system with solar seasonal thermal storage in severe cold areas. Energy Build 2010;42:2104–10. https://doi.org/10.1016/J.ENBUILD.2010.06.022.

[155] Meteonorm: Meteonorm, Global Meteorological Database. 2015:Handbook part II: theory, version 7.1.7.201517.

[156] Droher JJ, Squier SE. Performance of the Vanguard Solar Dish-Stirling Engine Module. Final report n.d.

[157] Ciulla G, Lo Brano V, D'Amico A, Ciulla G, Lo Brano V, D'Amico A, et al. Modelling relationship among energy demand, climate and office building features: A cluster analysis at European level. Appl Energy 2016;183:1021–34. https://doi.org/10.1016/j.apenergy.2016.09.046.

[158] Brano V Lo, Orioli A, Ciulla G, Culotta S. Quality of wind speed fi tting distributions for the urban area of Palermo , Italy. Renew Energy 2011;36:1026–39. https://doi.org/10.1016/j.renene.2010.09.009.

[159] Kjellsson E, Hellström G, Perers B. Optimization of systems with the combination of ground-source heat pump and solar collectors in dwellings. Energy 2010. https://doi.org/10.1016/j.energy.2009.04.011.

[160] United Nations. The 17 Goals 2015.

[161] European Commission. A policy framework for climate and energy in the period from 2020 to 2030. 2014.

[162] European Commission. COP21 UN Climate Change Conference, Paris 2015.

[163] Yılmaz İH, Mwesigye A. Modeling, simulation and performance analysis of parabolic trough solar collectors: A comprehensive review. Appl Energy 2018;225:135–74. https://doi.org/10.1016/j.apenergy.2018.05.014.

[164] Ogunmodimu O, Okoroigwe EC. Concentrating solar power technologies for solar thermal grid electricity in Nigeria: A review. Renew Sustain Energy Rev 2018;90:104–19. https://doi.org/https://doi.org/10.1016/j.rser.2018.03.029.

[165] International Energy Agency. Technology Roadmap - Concentrating Solar Power. 2010.

[166] Guinée JB. Life Cycle Sustainability Assessment: What Is It and What Are Its Challenges? In: Clift R, Druckman A, editors. Tak. Stock Ind. Ecol., Clift, Roland Druckman, Angela; 2015, p. 1–362. https://doi.org/10.1007/978-3-319-20571-7.

[167] Finkbeiner M, Schau EM, Lehmann A, Traverso M. Towards life cycle sustainability assessment. Sustainability 2010;2:3309–22. https://doi.org/10.3390/su2103309.

[168] Kloepffer W. Life cycle sustainability assessment of products (with Comments by Helias A. Udo de Haes, p. 95). Int J Life Cycle Assess 2008;13:89–95. https://doi.org/10.1065/lca2008.02.376.

[169] ISO 14040. Environmental management – Life cycle assessment – Principles and framework. 2006.

[170] SETAC. Environmental Life Cycle Costing: A Code of Practice. 2011.

[171] UNEP. Guidelines for social life cycle assessment of products. 2009.

[172] UNEP. Guidelines for Social Life Cycle Assessment of Products. Management 2020;15:104.

[173] Benoît C, Norris GA, Valdivia S, Ciroth A, Moberg A, Bos U, et al. The guidelines

for social life cycle assessment of products: Just in time! Int J Life Cycle Assess 2010;15:156–63. https://doi.org/10.1007/s11367-009-0147-8.

[174] Neugebauer S, Martinez-Blanco J, Scheumann R, Finkbeiner M. Enhancing the practical implementation of life cycle sustainability assessment - Proposal of a Tiered approach. J Clean Prod 2015;102:165–76. https://doi.org/10.1016/j.jclepro.2015.04.053.

[175] ISO 14044. Environmental management – Life cycle assessment – Requirements and guidelines. 2018.

[176] Kloepffer W, Grahl B. Life Cycle Assessment - A Guide to Best Practice. 2014.

[177] Hoogmartens R, Van Passel S, Van Acker K, Dubois M. Bridging the gap between LCA, LCC and CBA as sustainability assessment tools. Environ Impact Assess Rev 2014;48:27–33. https://doi.org/10.1016/j.eiar.2014.05.001.

[178] Hunkeler D, Lichtenvort K, Rebitzer G. Environmental Life Cycle Costing. vol. 53. Society of Environmental Toxicology and Chemistry (SETAC); 2008.

[179] ISO 15686-5. INTERNATIONAL STANDARD ISO 15686-5. Buildings and constructed assets — Sercive life planning. Part 5: Life-cycle costing. 2017;2017.

[180] Li T, Roskilly AP, Wang Y. A Regional Life Cycle Sustainability Assessment Approach and its Application on Solar Photovoltaic. Energy Procedia 2017;105:3320–5. https://doi.org/10.1016/j.egypro.2017.03.757.

[181] Yu M, Halog A. Solar photovoltaic development in Australia-a life cycle sustainability assessment study. vol. 7. 2015. https://doi.org/10.3390/su7021213.

[182] Hosseini-Fashami F, Motevali A, Nabavi-Pelesaraei A, Hashemi SJ, Chau K wing. Energy-Life cycle assessment on applying solar technologies for greenhouse strawberry production. Renew Sustain Energy Rev 2019;116:109411. https://doi.org/10.1016/j.rser.2019.109411.

[183] Ghasemi-Mobtaker H, Mostashari-Rad F, Saber Z, Chau K wing, Nabavi-Pelesaraei A. Application of photovoltaic system to modify energy use, environmental damages and cumulative exergy demand of two irrigation systems-

A case study: Barley production of Iran. Renew Energy 2020;160:1316–34. https://doi.org/10.1016/j.renene.2020.07.047.

[184] Ehtiwesh IAS, Coelho MC, Sousa ACM. Exergetic and environmental life cycle assessment analysis of concentrated solar power plants. Renew Sustain Energy Rev 2016;56:145–55. https://doi.org/10.1016/j.rser.2015.11.066.

[185] Lamnatou C, Chemisana D. Concentrating solar systems: Life Cycle Assessment (LCA) and environmental issues. Renew Sustain Energy Rev 2017;78:916–32.

[186] Bravo Y, Carvalho M, Serra LM, Monné C, Alonso S, Moreno F, et al. Environmental evaluation of dish-Stirling technology for power generation. Sol Energy 2012;86:2811–25. https://doi.org/10.1016/j.solener.2012.06.019.

[187] Cavallaro F, Ciraolo L. A life cycle assessment (LCA) of a paraboloidal-dish solar thermal power generation system. 2006 1st Int Symp Environ Identities Mediterr Area, ISEIM 2006:260–5. https://doi.org/10.1109/ISEIMA.2006.344933.

[188] Banacloche S, Herrera I, Lechóna Y. Towards energy transition in Tunisia: Sustainability assessment of a hybrid concentrated solar power and biomass plant. Sci Total Environ 2020;744. https://doi.org/10.1016/j.scitotenv.2020.140729.

[189] Corona B, Bozhilova-Kisheva KP, Olsen SI, San Miguel G. Social Life Cycle Assessment of a Concentrated Solar Power Plant in Spain: A Methodological Proposal. J Ind Ecol 2017;21:1566–77. https://doi.org/10.1111/jiec.12541.

[190] Naves AX, Barreneche C, Fernández AI, Cabeza LF, Haddad AN, Boer D. Life cycle costing as a bottom line for the life cycle sustainability assessment in the solar energy sector: A review. Sol Energy 2019;192:238–62. https://doi.org/10.1016/j.solener.2018.04.011.

[191] Corona B, San Miguel G. Life cycle sustainability analysis applied to an innovative configuration of concentrated solar power. Int J Life Cycle Assess 2019;24:1444–60. https://doi.org/10.1007/s11367-018-1568-z.

[192] Ko N, Lorenz M, Horn R, Krieg H, Baumann M. Sustainability Assessment of Concentrated Solar Power (CSP) Tower Plants - Integrating LCA, LCC and

LCWE in One Framework. Procedia CIRP 2018;69:395–400. https://doi.org/10.1016/j.procir.2017.11.049.

[193] Rodríguez-Serrano I, Caldés N, Rúa C de la, Lechón Y. Assessing the three sustainability pillars through the Framework for Integrated Sustainability Assessment (FISA): Case study of a Solar Thermal Electricity project in Mexico. J Clean Prod 2017;149:1127–43. https://doi.org/10.1016/j.jclepro.2017.02.179.

[194] Sphera. GaBi Software 2020.

[195] Meteonorm. Meteonorm global meteorological database. Handboo Part II: Theory. Version 7.1.7.21517. 2015.

[196] Kakoulaki G, Kougias I, Taylor N, Dolci F, Moya J, Jäger-Waldau A. Green hydrogen in Europe – A regional assessment: Substituting existing production with electrolysis powered by renewables. Energy Convers Manag 2020. https://doi.org/10.1016/j.enconman.2020.113649.

[197] European Automobile Manufacturers Association. Vehicles in use Europe 2018. Eur Automob Manuf Assoc 2019:1–19.

[198] Kuenlin A, Augsburger G, Gerber L, Maréchal F. Life cycle assessment and environomic optimization of concentrating solar thermal power plants. Proc 26th Int Conf Effic Cost, Optim Simul Environ Impact Energy Syst ECOS 2013 2013.

[199] Boughanmi W, Manata JP, Roger D, Jacq T, Streiff F. Life cycle assessment of a three-phase electrical machine in continuous operation. IET Electr Power Appl 2012;6:277–85. https://doi.org/10.1049/iet-epa.2011.0219.

[200] Ordóñez Barreiro I, Jiménez Tirado N, Silva Pérez M a. Life cycle environmental impacts of electricity production by Dish/Stirling systems in Spain. SolarPaces Conf 2009:1–8.

[201] Burkhardt III JJ, Heath GA, Turchi CS. Life cycle assessment of a parabolic trough concentrating solar power plant and the impacts of key design alternatives. Environ Sci Technol 2011;45:2457–64.

[202] Varun, Bhat IK, Prakash R. LCA of renewable energy for electricity generation

systems—A review. Renew Sustain Energy Rev 2009;13:1067–73. https://doi.org/10.1016/j.rser.2008.08.004.

[203] eurostat. Electricity price statistics 2020.

[204] iea. Energy Prices 2020 2020.

[205] Benoît Norris C. Data for social LCA. Int J Life Cycle Assess 2014;19:261–5. https://doi.org/10.1007/s11367-013-0644-7.

[206] Traverso M, Bell L, Saling P, Fontes J. Towards social life cycle assessment: a quantitative product social impact assessment. Int J Life Cycle Assess 2018;23:597–606. https://doi.org/10.1007/s11367-016-1168-8.

[207] shdb. Social Hotspot Database 2019.

[208] Lohn-Info. Gesetzliche Mindestlöhne in anderen Staaten 2020.

[209] European Commission. Widerstandsfähigkeit der EU bei kritischen Rohstoffen: Einen Pfad hin zu größerer Sicherheit und Nachhaltigkeit abstecken. 2020.

[210] Traverso M, Finkbeiner M, Jørgensen A, Schneider L. Life Cycle Sustainability Dashboard. J Ind Ecol 2012;16:680–8. https://doi.org/10.1111/j.1530-9290.2012.00497.x.